Part 3: Weak Gravitational Lensing

P. Schneider

1 Introduction

Multiple images, microlensing (with appreciable magnifications) and arcs in clusters are phenomena of *strong lensing*. In *weak gravitational lensing*, the Jacobi matrix $\mathcal{A}$ is very close to the unit matrix, which implies weak distortions and small magnifications. Those cannot be identified in individual sources, but only in a statistical sense. Because of that, the accuracy of any weak lensing study will depend on the number of sources which can be used for the weak lensing analysis. This number can be made large either by having a large number density of sources, or to observe a large solid angle on the sky, or both. Which of these two aspects is more relevant depends on the specific application. Nearly without exception, the sources employed in weak lensing studies up to now are distant galaxies observed in the optical or near-IR passband, since they form the densest population of distant objects in the sky (which is a statement both about the source population in the Universe and the sensitivity of detectors employed in astronomical observations). To observe large number densities of sources, one needs deep observations to probe the faint (and thus more numerous) population of galaxies. Faint galaxies, however, are small, and therefore their observed shape is strongly affected by the Point Spread Function, caused by atmospheric seeing (for ground-based observations) and telescope effects. These effects need to be well understood and corrected for, which is the largest challenge of observational weak lensing studies. On the other hand, observing large regions of the sky quickly leads to large data sets, and the problems associated with handling them. We shall discuss some of the most important aspects of weak lensing observations in Sect. 3.

The effects just mentioned have prevented the detection of weak lensing effects in early studies with photographic plates (e.g., Tyson et al. 1984); they are not linear detectors (so correcting for PSF effects is not reliable), nor are they sensitive enough for obtaining sufficiently deep images. Weak lensing research came through a number of observational and technical advances.

Schneider P (2006), Weak gravitational lensing. In: Meylan G, Jetzer Ph and North P (eds) Gravitational lensing: Strong, weak, and micro. Saas-Fee Adv Courses vol 33, pp 269–451
DOI 10.1007/3-540-30309-X_3

Soon after the first giant arcs in clusters were discovered (see Sect. 1.2 of Schneider, this volume; hereafter referred to as IN) by Soucail et al. (1987) and Lynds and Petrosian (1989), Fort et al. (1988) observed objects in the lensing cluster Abell 370 which were less extremely stretched than the giant arc, but still showed a large axis ratio and was aligned in the direction tangent to its separation vector to the cluster center; they termed these images 'arclets'. Indeed, with the spectroscopic verification (Mellier et al. 1991) of the arclet A5 in Abell 370 being located at much larger distance from us than the lensing cluster, the gravitational lens origin of these arclets was proven. When the images of a few background galaxies are deformed so strongly that they can be identified as distorted by lensing, there should be many more galaxy images where the distortion is much smaller, and where it can only be detected by averaging over many such images. Tyson et al. (1990) reported this statistical distortion effect in two clusters, thereby initiating the weak lensing studies of the mass distribution of clusters of galaxies. This very fruitful field of research was put on a rigorous theoretical basis by Kaiser and Squires (1993) who showed that from the measurement of the (distorted) shapes of galaxies one can obtain a parameter-free map of the projected mass distribution in clusters.

The flourishing of weak lensing in the past ten years was mainly due to three different developments. First, the potential of weak lensing was realized, and theoretical methods were worked out for using weak lensing measurements in a large number of applications, many of which will be described in later sections. This realization, reaching out of the lensing community, also slowly changed the attitude of time allocation committees, and telescope time for such studies was granted. Second, returning to the initial remark, one requires large fields-of-views for many weak lensing application, and the development of increasingly large wide-field cameras installed at the best astronomical sites has allowed large observational progress to be made. Third, quantitative methods for the correction of observations effects, like the blurring of images by the atmosphere and telescope optics, have been developed, of which the most frequently used one came from Kaiser et al. (1995). We shall describe this technique, its extensions, tests and alternative methods in Sect. 3.5.

We shall start by describing the basics of weak lensing in Sect. 2, namely how the shear, or the projected tidal gravitational field of the intervening matter distribution can be determined from measuring the shapes of images of distant galaxies. Practical aspects of observations and the measurements of image shapes are discussed in Sect. 3. The next two sections are devoted to clusters of galaxies; in Sect. 4, some general properties of clusters are described, and their strong lensing properties are considered, whereas in Sect. 5 weak lensing by clusters is treated. As already mentioned, this allows us to obtain a parameter-free map of the projected (2-D) mass distribution of clusters.

We then turn to lensing by the inhomogeneously distributed matter distribution in the Universe, the large-scale structure. Starting with Gunn (1967), the observation of the distortion of light bundles by the inhomogeneously distributed matter in the Universe was realized as a unique probe to study the

properties of the cosmological (dark) matter distribution. The theory of this cosmic shear effect, and its applications, was worked out in the early 1990's (e.g., Blandford et al. 1991). In contrast to the lensing situations studied in the rest of this book, here the deflecting mass is manifestly three-dimensional; we therefore need to generalize the theory of geometrically-thin mass distributions and consider the propagation of light in an inhomogeneous Universe. As will be shown, to leading order this situation can again be described in terms of an 'equivalent' surface mass density. The theoretical aspects of this large-scale structure lensing, or cosmic shear, are contained in Sect. 6. Although the theory of cosmic shear was well in place for quite some time, it took until the year 2000 before it was observationally discovered, independently and simultaneously by four groups. These early results, as well as the much more extensive studies carried out in the past few years, are presented and discussed in Sect. 7. In Sect. 8, we consider the weak lensing effects of galaxies, which can be used to investigate the mass profile of galaxies. As we shall see, this galaxy-galaxy lensing, first detected by Brainerd et al. (1996), is directly related to the connection between the galaxy distribution in the Universe and the underlying (dark) matter distribution; this lensing effect is therefore ideally suited to study the biasing of galaxies; we shall also describe alternative lensing effects for investigating the relation between luminous and dark matter. In the final Sect. 9 we discuss higher-order cosmic shear statistics and how lensing by the large-scale structure affects the lens properties of localized mass concentrations. Some final remarks are given in Sect. 10.

Until very recently, weak lensing has been considered by a considerable fraction of the community as 'black magic' (or to quote one member of a PhD examination committee: "You have a mass distribution about which you don't know anything, and then you observe sources which you don't know either, and then you claim to learn something about the mass distribution ?"). Most likely the reason for this is that weak lensing is indeed weak. One cannot 'see' the effect, nor can it be graphically displayed easily. Only by investigating many faint galaxy images can a signal be extracted from the data, and the human eye is not sufficient to perform this analysis. This is different even from the analysis of CMB anisotropies which, similarly, need to be analyzed by statistical means, but at least one can display a temperature map of the sky. However, in recent years weak lensing has gained a lot of credibility, not only because it has contributed substantially to our knowledge about the mass distribution in the Universe, but also because different teams, with different data set and different data analysis tools, agree on their results.

Weak lensing has been reviewed before; we shall mention only five extensive reviews. Mellier (1999) provides a detailed compilation of the weak lensing results before 1999, whereas Bartelmann and Schneider (2001; hereafter BS01) present a detailed account of the theory and technical aspects of weak lensing.[1]

[1] We follow here the notation of BS01, except that we denote the angular diameter distance explicitly by $D^{\rm ang}$, whereas D is the comoving angular diameter distance,

More recent summaries of results can also be found in Wittman (2002) and Refregier (2003a), as well as the cosmic shear review by van Waerbeke and Mellier (2003).

The coverage of topics in this review has been a subject of choice; no claim is made about completeness of subjects or references. In particular, due to the lack of time during the lectures, the topic of weak lensing of the CMB temperature fluctuations has not been covered at all, and is also not included in this written version. Apart from this increasingly important subject, I hope that most of the currently actively debated aspects of weak lensing are mentioned, and the interested reader can find her/his way to more details through the references provided.

2 The Principles of Weak Gravitational Lensing

2.1 Distortion of Faint Galaxy Images

Images of distant sources are distorted in shape and size, owing to the tidal gravitational field through which light bundles from these sources travel to us. Provided the angular size of a lensed image of a source is much smaller than the characteristic angular scale on which the tidal field varies, the distortion can be described by the linearized lens mapping, i.e., the Jacobi matrix $\mathcal{A}$. The invariance of the surface brightness by gravitational light deflection, $I(\boldsymbol{\theta}) = I^{(\mathrm{s})}[\boldsymbol{\beta}(\boldsymbol{\theta})]$, together with the locally linearized lens equation,

$$\boldsymbol{\beta} - \boldsymbol{\beta}_0 = \mathcal{A}(\boldsymbol{\theta}_0) \cdot (\boldsymbol{\theta} - \boldsymbol{\theta}_0) \; , \tag{1}$$

where $\boldsymbol{\beta}_0 = \boldsymbol{\beta}(\boldsymbol{\theta}_0)$, then describes the distortion of small lensed images as

$$I(\boldsymbol{\theta}) = I^{(\mathrm{s})}[\boldsymbol{\beta}_0 + \mathcal{A}(\boldsymbol{\theta}_0) \cdot (\boldsymbol{\theta} - \boldsymbol{\theta}_0)] \; . \tag{2}$$

We recall (see IN) that the Jacobi matrix can be written as

$$\mathcal{A}(\boldsymbol{\theta}) = (1-\kappa) \begin{pmatrix} 1-g_1 & -g_2 \\ -g_2 & 1+g_1 \end{pmatrix} \; , \text{ where } \; g(\boldsymbol{\theta}) = \frac{\gamma(\boldsymbol{\theta})}{[1-\kappa(\boldsymbol{\theta})]} \tag{3}$$

is the reduced shear, and the g_α, $\alpha = 1, 2$, are its Cartesian components. The reduced shear describes the shape distortion of images through gravitational light deflection. The (reduced) shear is a 2-component quantity, most conveniently written as a complex number,

$$\gamma = \gamma_1 + \mathrm{i}\gamma_2 = |\gamma| \, \mathrm{e}^{2\mathrm{i}\varphi} \; ; \quad g = g_1 + \mathrm{i}g_2 = |g| \, \mathrm{e}^{2\mathrm{i}\varphi} \; ; \tag{4}$$

---

which we also write as f_K, depending on the context; see Sect. 4.3 of IN for more details. In most cases, the distance ratio $D_{\mathrm{ds}}/D_{\mathrm{s}}$ is used, which is the same for both distance definitions.

its amplitude describes the degree of distortion, whereas its phase φ yields the direction of distortion. The reason for the factor '2' in the phase is the fact that an ellipse transforms into itself after a rotation by 180°. Consider a circular source with radius R (see Fig. 1); mapped by the local Jacobi matrix, its image is an ellipse, with semi-axes

$$\frac{R}{1-\kappa-|\gamma|} = \frac{R}{(1-\kappa)(1-|g|)} \quad ; \quad \frac{R}{1-\kappa+|\gamma|} = \frac{R}{(1-\kappa)(1+|g|)}$$

and the major axis encloses an angle φ with the positive θ_1-axis. Hence, if sources with circular isophotes could be identified, the measured image ellipticities would immediately yield the value of the reduced shear, through the axis ratio

$$|g| = \frac{1-b/a}{1+b/a} \quad \Leftrightarrow \quad \frac{b}{a} = \frac{1-|g|}{1+|g|}$$

and the orientation of the major axis φ. In these relations it was assumed that $b \leq a$, and $|g| < 1$. We shall discuss the case $|g| > 1$ later.

However, faint galaxies are not intrinsically round, so that the observed image ellipticity is a combination of intrinsic ellipticity and shear. The strategy to nevertheless obtain an estimate of the (reduced) shear consists in locally averaging over many galaxy images, assuming that the intrinsic ellipticities are *randomly oriented*. In order to follow this strategy, one needs to clarify first how to define 'ellipticity' for a source with arbitrary isophotes (faint galaxies are not simply elliptical); in addition, seeing by the atmospheric turbulence will blur – and thus circularize – observed images, together with other effects related to the observation procedure. We will consider these issues in turn.

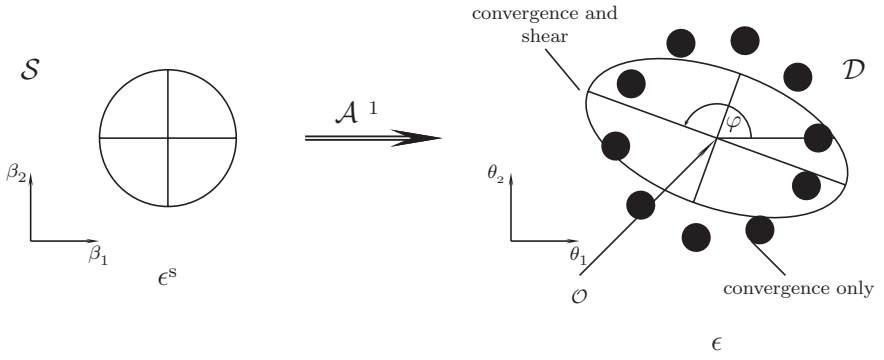

Fig. 1. A circular source, shown at the left, is mapped by the inverse Jacobian $\mathcal{A}^{-1}$ onto an ellipse. In the absence of shear, the resulting image is a circle with modified radius, depending on κ. Shear causes an axis ratio different from unity, and the orientation of the resulting ellipse depends on the phase of the shear (source: M. Bradac)

2.2 Measurements of Shapes and Shear

Definition of Image Ellipticities

Let $I(\boldsymbol{\theta})$ be the brightness distribution of an image, assumed to be isolated on the sky; the center of the image can be defined as

$$\bar{\boldsymbol{\theta}} \equiv \frac{\int \mathrm{d}^2\theta\; I(\boldsymbol{\theta})\, q_I[I(\boldsymbol{\theta})]\, \boldsymbol{\theta}}{\int \mathrm{d}^2\theta\; I(\boldsymbol{\theta})\, q_I[I(\boldsymbol{\theta})]}\;, \tag{5}$$

where $q_I(I)$ is a suitably chosen weight function; e.g., if $q_I(I) = \mathrm{H}(I - I_{\mathrm{th}})$, where $\mathrm{H}(x)$ is the Heaviside step function, $\bar{\boldsymbol{\theta}}$ would be the center of light within a limiting isophote of the image. We next define the tensor of second brightness moments,

$$Q_{ij} = \frac{\int \mathrm{d}^2\theta\; I(\boldsymbol{\theta})\, q_I[I(\boldsymbol{\theta})]\, (\theta_i - \bar{\theta}_i)\, (\theta_j - \bar{\theta}_j)}{\int \mathrm{d}^2\theta\; I(\boldsymbol{\theta})\, q_I[I(\boldsymbol{\theta})]}\;, \quad i,j \in \{1,2\}\;. \tag{6}$$

Note that for an image with circular isophotes, $Q_{11} = Q_{22}$, and $Q_{12} = 0$. The trace of Q describes the size of the image, whereas the traceless part of Q_{ij} contains the ellipticity information. From Q_{ij}, one defines two complex ellipticities,

$$\chi \equiv \frac{Q_{11} - Q_{22} + 2\mathrm{i}Q_{12}}{Q_{11} + Q_{22}} \quad \text{and} \quad \epsilon \equiv \frac{Q_{11} - Q_{22} + 2\mathrm{i}Q_{12}}{Q_{11} + Q_{22} + 2(Q_{11}Q_{22} - Q_{12}^2)^{1/2}}\;. \tag{7}$$

Both of them have the same phase (because of the same numerator), but a different absolute value. Figure 2 illustrates the shape of images as a function of their complex ellipticity χ. For an image with elliptical isophotes of axis ratio $r \le 1$, one obtains

$$|\chi| = \frac{1 - r^2}{1 + r^2} \quad ; \quad |\epsilon| = \frac{1 - r}{1 + r}\;. \tag{8}$$

Which of these two definitions is more convenient depends on the context; one can easily transform one into the other,

$$\epsilon = \frac{\chi}{1 + (1 - |\chi|^2)^{1/2}}\;, \quad \chi = \frac{2\epsilon}{1 + |\epsilon|^2}\;. \tag{9}$$

In fact, other (but equivalent) ellipticity definitions have been used in the literature (e.g., Kochanek 1990; Miralda-Escudé 1991; Bonnet and Mellier 1995), but the two given above appear to be most convenient.

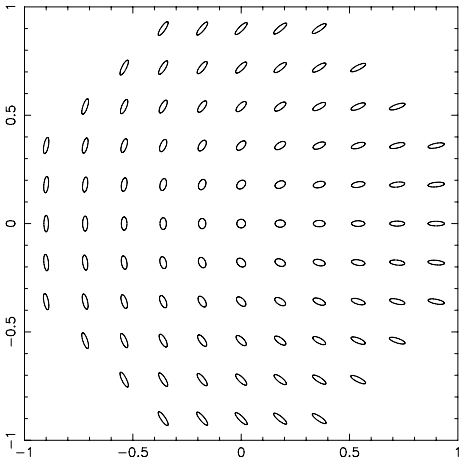

Fig. 2. The shape of image ellipses for a circular source, in dependence on their two ellipticity components χ_1 and χ_2; a corresponding plot in term of the ellipticity components ϵ_i would look quite similar. Note that the ellipticities are rotated by 90° when $\chi \to -\chi$ (source: D. Clowe)

From Source to Image Ellipticities

In total analogy, one defines the second-moment brightness tensor $Q_{ij}^{(\mathrm{s})}$, and the complex ellipticities $\chi^{(\mathrm{s})}$ and $\epsilon^{(\mathrm{s})}$ for the unlensed source. From

$$Q_{ij}^{(\mathrm{s})} = \frac{\displaystyle\int \mathrm{d}^2\beta\; I^{(\mathrm{s})}(\boldsymbol{\theta})\, q_I[I^{(\mathrm{s})}(\boldsymbol{\beta})]\,(\beta_i - \bar{\beta}_i)\,(\beta_j - \bar{\beta}_j)}{\displaystyle\int \mathrm{d}^2\beta\; I^{(\mathrm{s})}(\boldsymbol{\theta})\, q_I[I^{(\mathrm{s})}(\boldsymbol{\beta})]}\;, \quad i,j \in \{1,2\}\;, \tag{10}$$

one finds with $\mathrm{d}^2\beta = \det \mathcal{A}\, \mathrm{d}^2\theta$, $\boldsymbol{\beta} - \bar{\boldsymbol{\beta}} = \mathcal{A}\left(\boldsymbol{\theta} - \bar{\boldsymbol{\theta}}\right)$, that

$$Q^{(\mathrm{s})} = \mathcal{A}\, Q\, \mathcal{A}^T = \mathcal{A}\, Q\, \mathcal{A}\;, \tag{11}$$

where $\mathcal{A} \equiv \mathcal{A}(\bar{\boldsymbol{\theta}})$. Using the definitions of the complex ellipticities, one finds the transformations (e.g., Schneider and Seitz 1995; Seitz and Schneider 1997)

$$\chi^{(\mathrm{s})} = \frac{\chi - 2g + g^2\chi^*}{1 + |g|^2 - 2\mathcal{R}\mathrm{e}(g\chi^*)}\;; \quad \epsilon^{(\mathrm{s})} = \begin{cases} \dfrac{\epsilon - g}{1 - g^*\epsilon} & \text{if } |g| \le 1\;; \\[2ex] \dfrac{1 - g\epsilon^*}{\epsilon^* - g^*} & \text{if } |g| > 1\;. \end{cases} \tag{12}$$

The inverse transformations are obtained by interchanging source and image ellipticities, and $g \to -g$ in the foregoing equations.

Estimating the (Reduced) Shear

In the following we make the assumption that the intrinsic orientation of galaxies is random,

$$\mathrm{E}\left(\chi^{(\mathrm{s})}\right) = 0 = \mathrm{E}\left(\epsilon^{(\mathrm{s})}\right) \ , \tag{13}$$

which is expected to be valid since there should be no direction singled out in the Universe. This then implies that the expectation value of ϵ is [as obtained by averaging the transformation law (12) over the intrinsic source orientation]

$$\mathrm{E}(\epsilon) = \begin{cases} g & \text{if } |g| \le 1 \\ \\ 1/g^* & \text{if } |g| > 1 \ . \end{cases} \tag{14}$$

This is a remarkable result (Schramm and Kayser 1995; Seitz and Schneider 1997), since it shows that each image ellipticity provides an unbiased estimate of the local shear, though a very noisy one. The noise is determined by the intrinsic ellipticity dispersion

$$\sigma_\epsilon = \sqrt{\left\langle \epsilon^{(\mathrm{s})} \epsilon^{(\mathrm{s})*} \right\rangle} \ ,$$

in the sense that, when averaging over N galaxy images all subject to the same reduced shear, the 1-σ deviation of their mean ellipticity from the true shear is $\sigma_\epsilon/\sqrt{N}$. A more accurate estimate of this error is

$$\sigma = \sigma_\epsilon \left[1 - \min\left(|g|^2, |g|^{-2}\right)\right] / \sqrt{N} \tag{15}$$

(Schneider et al. 2000). Hence, the noise can be beaten down by averaging over many galaxy images; however, the region over which the shear can be considered roughly constant is limited, so that averaging over galaxy images is always related to a smoothing of the shear. Fortunately, we live in a Universe where the sky is 'full of faint galaxies', as was impressively demonstrated by the Hubble Deep Field images (Williams et al. 1996) and previously from ultra-deep ground-based observations (Tyson 1988). Therefore, the accuracy of a shear estimate depends on the local number density of galaxies for which a shape can be measured. In order to obtain a high density, one requires deep imaging observations. As a rough guide, on a 3 hour exposure with a 4-meter class telescope, about 30 galaxies per arcmin^2 can be used for a shape measurement.

In fact, considering (14) we conclude that the expectation value of the observed ellipticity is the same for a reduced shear g and for $g' = 1/g^*$. Schneider and Seitz (1995) have shown that one cannot distinguish between these two values of the reduced shear from a purely local measurement, and term this fact the 'local degeneracy'; this also explains the symmetry between $|g|$ and $|g|^{-1}$ in (15). Hence, from a local weak lensing observation one cannot tell the case $|g| < 1$ (equivalent to $\det \mathcal{A} > 0$) from the one of $|g| > 1$ or $\det \mathcal{A} < 0$.

This local degeneracy is, however, broken in large-field observations, as the region of negative parity of any lens is small (the Einstein radius inside of which $|g| > 1$ of massive lensing clusters is typically $\lesssim 30''$, compared to data fields of several arcminutes used for weak lensing studies of clusters), and the reduced shear must be a smooth function of position on the sky.

Whereas the transformation between source and image ellipticity appears simpler in the case of χ than ϵ – see (12), the expectation value of χ cannot be easily calculated and depends explicitly on the intrinsic ellipticity distribution of the sources. In particular, the expectation value of χ is not simply related to the reduced shear (Schneider and Seitz 1995). However, in the weak lensing regime, $\kappa \ll 1$, $|\gamma| \ll 1$, one finds

$$\gamma \approx g \approx \langle \epsilon \rangle \approx \frac{\langle \chi \rangle}{2} \,. \tag{16}$$

2.3 Tangential and Cross Component of Shear

Components of the Shear

The shear components γ_1 and γ_2 are defined relative to a reference Cartesian coordinate frame. Note that the shear is *not* a vector (though it is often wrongly called that way in the literature), owing to its transformation properties under rotations: Whereas the components of a vector are multiplied by $\cos\varphi$ and $\sin\varphi$ when the coordinate frame is rotated by an angle φ, the shear components are multiplied by $\cos(2\varphi)$ and $\sin(2\varphi)$, or simply, the complex shear gets multiplied by $\mathrm{e}^{-2\mathrm{i}\varphi}$. The reason for this transformation behavior of the shear traces back to its original definition as the traceless part of the Jacobi matrix $\mathcal{A}$. This transformation behavior is the same as that of the linear polarization; the shear is therefore a *polar*. In analogy with vectors, it is often useful to consider the shear components in a rotated reference frame, that is, to measure them w.r.t. a different direction; for example, the arcs in clusters are tangentially aligned, and so their ellipticity is oriented tangent to the radius vector in the cluster.

If ϕ specifies a direction, one defines the *tangential* and *cross components* of the shear *relative to this direction* as

$$\gamma_\mathrm{t} = -\mathcal{R}\mathrm{e}\left[\gamma\,\mathrm{e}^{-2\mathrm{i}\phi}\right] \quad , \quad \gamma_\times = -\mathcal{I}\mathrm{m}\left[\gamma\,\mathrm{e}^{-2\mathrm{i}\phi}\right] \;; \tag{17}$$

For example, in case of a circularly-symmetric matter distribution, the shear at any point will be oriented tangent to the direction toward the center of symmetry. Thus in this case choose ϕ to be the polar angle of a point; then, $\gamma_\times = 0$. In full analogy to the shear, one defines the tangential and cross components of an image ellipticity, ϵ_t and $\epsilon_\times$. An illustration of these definitions is provided in Fig. 3.

The sign in (17) is easily explained (and memorized) as follows: consider a circular mass distribution and a point on the θ_1-axis outside the Einstein

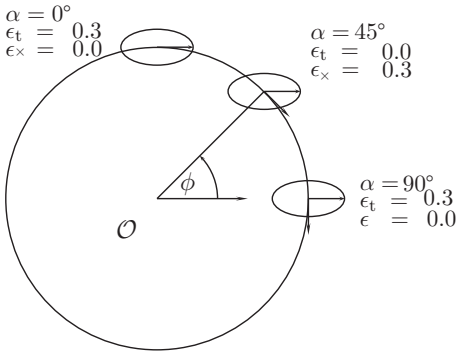

Fig. 3. Illustration of the tangential and cross-components of the shear, for an image with $\epsilon_1 = 0.3$, $\epsilon_2 = 0$, and three different directions ϕ with respect to a reference point (source: M. Bradac)

radius. The image of a circular source there will be stretched in the direction of the θ_2-axis. In this case, $\phi = 0$ in (17), the shear is real and negative, and in order to have the tangential shear positive, and thus to define tangential shear in accordance with the intuitive understanding of the word, a minus sign is introduced. Negative tangential ellipticity implies that the image is oriented in the radial direction. We warn the reader that sign conventions and notations have undergone several changes in the literature, and the current author had his share in this.

Minimum Lens Strength for its Weak Lensing Detection

As a first application of this decomposition, we consider how massive a lens needs to be in order that it produces a detectable weak lensing signal. For this purpose, consider a lens modeled as an SIS with one-dimensional velocity dispersion σ_v. In the annulus $\theta_{\rm in} \le \theta \le \theta_{\rm out}$, centered on the lens, let there be N galaxy images with positions $\boldsymbol{\theta}_i = \theta_i(\cos\phi_i, \sin\phi_i)$ and (complex) ellipticities ϵ_i. For each one of them, consider the tangential ellipticity

$$\epsilon_{ti} = -\mathcal{R}\mathrm{e}\left(\epsilon_i\, \mathrm{e}^{-2\mathrm{i}\phi_i}\right) \ . \tag{18}$$

The weak lensing signal-to-noise for the detection of the lens obtained by considering a weighted average over the tangential ellipticity is (see BS01, Sect. 4.5)

$$\begin{aligned} \frac{\mathrm{S}}{\mathrm{N}} &= \frac{\theta_{\rm E}}{\sigma_\epsilon}\sqrt{\pi n}\,\sqrt{\ln(\theta_{\rm out}/\theta_{\rm in})} \\ &= 8.4\left(\frac{n}{30\,\mathrm{arcmin}^{-2}}\right)^{1/2}\left(\frac{\sigma_\epsilon}{0.3}\right)^{-1}\left(\frac{\sigma_v}{600\,\mathrm{km\,s}^{-1}}\right)^2 \\ &\quad\times\left(\frac{\ln(\theta_{\rm out}/\theta_{\rm in})}{\ln 10}\right)^{1/2}\left\langle\frac{D_{\rm ds}}{D_{\rm s}}\right\rangle\ , \end{aligned} \tag{19}$$

where $\theta_{\rm E} = 4\pi(\sigma_v/c)^2(D_{\rm ds}/D_{\rm s})$ is the Einstein radius of an SIS, n the mean number density of galaxies, and the average of the distance ratio is taken over the source population from which the shear measurements are obtained. Hence, the S/N is proportional to the lens strength (as measured by $\theta_{\rm E}$), the square root of the number density, and inversely proportional to σ_ϵ, as expected. From this consideration we conclude that clusters of galaxies with $\sigma_v \gtrsim 600\,{\rm km/s}$ can be detected with sufficiently large S/N by weak lensing, but individual galaxies ($\sigma_v \lesssim 200\,{\rm km/s}$) are too weak as lenses to be detected individually. Furthermore, the final factor in (19) implies that, for a given source population, the cluster detection will be more difficult for increasing lens redshift.

Mean Tangential Shear on Circles

In the case of axi-symmetric mass distributions, the tangential shear is related to the surface mass density $\kappa(\theta)$ and the mean surface mass density $\bar\kappa(\theta)$ inside the radius θ by $\gamma_{\rm t} = \bar\kappa - \kappa$, as can be easily shown by the relation in Sect. 3.1 of IN. It is remarkable that a very similar expression holds for general matter distributions. To see this, we start from Gauss' theorem, which states that

$$\int_0^\theta {\rm d}^2\vartheta\; \nabla\cdot\nabla\psi = \theta \oint {\rm d}\varphi\; \nabla\psi\cdot\mathbf{n}\;,$$

where the integral on the left-hand side extends over the area of a circle of radius θ (with its center chosen as the origin of the coordinate system), ψ is an arbitrary scalar function, the integral on the right extends over the circle with radius θ, and $\mathbf{n}$ is the outward directed normal on this circle. Taking ψ to be the deflection potential and noting that $\nabla^2\psi = 2\kappa$, one obtains

$$m(\theta) \equiv \frac{1}{\pi}\int_0^\theta {\rm d}^2\vartheta\;\kappa(\boldsymbol{\vartheta}) = \frac{\theta}{2\pi}\oint {\rm d}\varphi\;\frac{\partial\psi}{\partial\theta}\;, \tag{20}$$

where we used that $\nabla\psi\cdot\mathbf{n} = \psi_{,\theta}$. Differentiating this equation with respect to θ yields

$$\frac{{\rm d}m}{{\rm d}\theta} = \frac{m}{\theta} + \frac{\theta}{2\pi}\oint {\rm d}\varphi\;\frac{\partial^2\psi}{\partial\theta^2}\;. \tag{21}$$

Consider a point on the θ_1-axis; there, $\psi_{,\theta\theta} = \psi_{11} = \kappa + \gamma_1 = \kappa - \gamma_{\rm t}$. This last expression is independent on the choice of coordinates and must therefore hold for all φ. Denoting by $\langle\kappa(\theta)\rangle$ and $\langle\gamma_{\rm t}(\theta)\rangle$ the mean surface mass density and mean tangential shear on the circle of radius θ, (21) becomes

$$\frac{{\rm d}m}{{\rm d}\theta} = \frac{m}{\theta} + \theta\left[\langle\kappa(\theta)\rangle - \langle\gamma_{\rm t}(\theta)\rangle\right]\;. \tag{22}$$

The dimensionless mass $m(\theta)$ in the circle is related to the mean surface mass density inside the circle $\bar{\kappa}(\theta)$ by

$$m(\theta) = \theta^2\,\bar{\kappa}(\theta) = 2\int_0^\theta \mathrm{d}\vartheta\;\vartheta\;\langle\kappa(\vartheta)\rangle\;. \tag{23}$$

Together with $\mathrm{d}m/\mathrm{d}\theta = 2\theta\,\langle\kappa(\theta)\rangle$, (22) becomes, after dividing through θ,

$$\langle\gamma_\mathrm{t}\rangle = \bar{\kappa} - \langle\kappa\rangle\;, \tag{24}$$

a relation which very closely matches the result mentioned above for axi-symmetric mass distributions (Bartelmann 1995). One important immediate implication of this result is that from a measurement of the tangential shear, averaged over concentric circles, one can determine the azimuthally-averaged mass profile of lenses, even if the density is not axi-symmetric.

2.4 Magnification Effects

Recall from IN that a magnification μ changes source counts according to

$$n(>S,\boldsymbol{\theta},z) = \frac{1}{\mu(\boldsymbol{\theta},z)}\,n_0\left(>\frac{S}{\mu(\boldsymbol{\theta},z)},z\right)\;, \tag{25}$$

where $n(>S,z)$ and $n_0(>S,z)$ are the lensed and unlensed cumulative number densities of sources, respectively. The first argument of n_0 accounts for the change of the flux (which implies that a magnification $\mu>1$ allows the detection of intrinsically fainter sources), whereas the prefactor in (25) stems from the change of apparent solid angle. In the case that $n_0(S)\propto S^{-\alpha}$, this yields

$$\frac{n(>S)}{n_0(>S)} = \mu^{\alpha-1}\;, \tag{26}$$

and therefore, if $\alpha>1$ ($<$1), source counts are enhanced (depleted); the steeper the counts, the stronger the effect. In the case of weak lensing, where $|\mu-1|\ll 1$, one probes the source counts only over a small range in flux, so that they can always be approximated (locally) by a power law. Provided that $\kappa\ll 1$, $|\gamma|\ll 1$, a further approximation applies,

$$\mu\approx 1+2\kappa\;;\quad\text{and}\quad \frac{n(>S)}{n_0(>S)}\approx 1+2(\alpha-1)\kappa\;. \tag{27}$$

Thus, from a measurement of the local number density $n(>S)$ of galaxies, κ can in principle be inferred directly. It should be noted that $\alpha\sim 1$ for galaxies in the B-band, but in redder bands, $\alpha<1$ (e.g., Ellis 1997); therefore, one expects a depletion of their counts in regions of magnification $\mu>1$. Broadhurst et al. 1995 have discussed in detail the effects of magnification in weak lensing. Not only are the number counts affected, but since this is a redshift-dependent effect (since both κ and γ depend, for a given physical surface mass density, on the source redshift), the redshift distribution of galaxies is locally changed by magnification.

Since magnification is merely a stretching of solid angle, Bartelmann and Narayan (1995) pointed out that magnified images at fixed surface brightness have a larger solid angle than unlensed ones; in addition, the surface brightness of a galaxy is expected to be a strong function of redshift [$I \propto (1+z)^{-4}$], owing to the Tolman effect. Hence, if this effect could be harnessed, a (redshift-dependent) magnification could be measured statistically. Unfortunately, this method is hampered by observational difficulties; it seems that estimating a reliable estimate for the surface brightness from seeing-convolved images (see Sect. 3.5) is even more difficult than determining image shapes.

3 Observational Issues and Challenges

Weak lensing, employing the shear method, relies on the shape measurements of faint galaxy images. Since the noise due to intrinsic ellipticity dispersion is $\propto \sigma_\epsilon/\sqrt{n}$, one needs a high number density n to beat this noise component down. However, the only way to increase the number density of galaxies is to observe to fainter magnitudes. As it turns out, galaxies at faint magnitudes are small, in fact typically smaller than the size of the point-spread function (PSF), or the seeing disk (see Fig. 4). Hence, for them one needs usually large correction factors between the true ellipticity and that of the

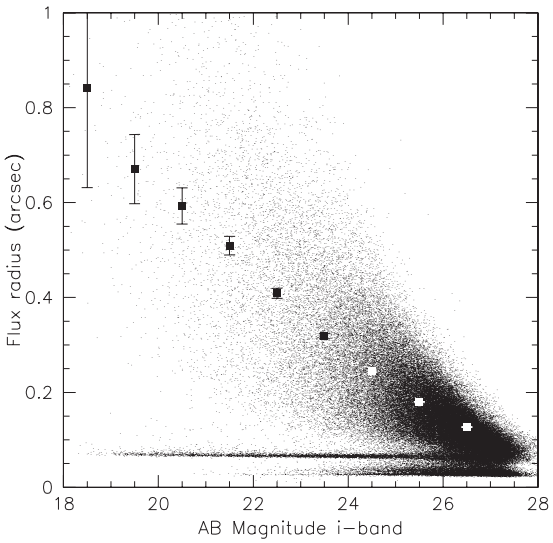

Fig. 4. The size of galaxies observed with the ACS camera on-board HST. Small dots denote the half-light radius of individual galaxies, bigger points with error bars show the mean size in a magnitude bin. The horizontal line of point at $r_\mathrm{h} \approx 0\farcs08$ correspond to stellar images in the ACS fields, as they have all the same size but vary in magnitude, and points at even smaller size are noise artefacts which are not used for any lensing analysis (source: T. Schrabback)

seeing-convolved image. On the other hand, fainter galaxies tend to probe higher-redshift galaxies, which increases the lensing signal due to $D_{\rm ds}/D_{\rm s}$-dependence of the 'lensing efficiency'.

3.1 Strategy

In the present observational situation, only the optical sky is densely populated with sources; therefore, weak lensing observations are performed with optical (or near-IR) CCD-cameras (photographic plates are not linear enough to measure these subtle effects). In order to substantiate this comment, note that the Hubble Deep Field North contains about 3000 galaxies, but only seven radio sources are detected in a very deep integration with the VLA (Richards et al. 1998).[2] In order to obtain a high number density of sources, long exposures are needed: as an illustrative example, to get a number density of useful galaxies (i.e., those for which a shape can be measured reliably) of $n \sim 20\,{\rm arcmin}^{-2}$, one needs $\sim$2 hours integration on a 4-m class telescope in good seeing $\sigma \lesssim 1''$.

Furthermore, large solid angles are desired, either to get large areas around clusters for their mass reconstruction, or to get good statistics of lenses on blank field surveys, such as they are needed for galaxy–galaxy lensing and cosmic shear studies. It is now possible to cover large area in reasonable amounts of observing time, since large format CCD cameras have recently become available; for example, the Wide-Field Imager (WFI) at the ESO/MPG 2.2-m telescope at La Silla has $(8{\rm K})^2$ pixels and covers an area of $\sim(0.5\,{\rm deg})^2$. Until recently, the CFH12K camera with $8{\rm K}\times 12{\rm K}$ pixels and field $\sim 30'\times 45'$ was mounted at the Canada-French-Hawaii Telescope (CFHT) on Mauna Kea and was arguably the most efficient wide-field imaging instrument hitherto. In 2003, MegaCam has been put into operation on the CFHT which has $(18{\rm K})^2$ pixels and covers $\sim 1\,{\rm deg}^2$. Several additional cameras of comparable size will become operational in the near future, including the 1 deg^2 instrument OmegaCAM on the newly built VLT Survey Telescope on Paranal. The largest field camera on a 10-m class telescope is Suprime-Cam, a $34'\times 27'$ multi-chip camera on the Subaru 8.2-meter telescope. Unfortunately, many optical astronomers (and decision making panels of large facilities) consider the prime use of large telescopes to be spectroscopy; for example, although the four ESO VLT unit telescopes are equipped with a total of ten instruments, the largest imagers on the VLT are the two FORS instruments, with a $\sim 6\farcm7$ field-of-view.[3]

[2] The source density on the radio sky will become at least comparable to that currently on the optical sky with the future Square Kilometer Array (SKA).

[3] Nominally, the VIMOS instrument has a four times larger f.o.v., but our analysis of early VIMOS imaging data indicates that it is totally useless for weak lensing observations, owing to its highly anisotropic PSF, which even seems to show discontinuities on chips, and its large variation of the seeing size across chips. It

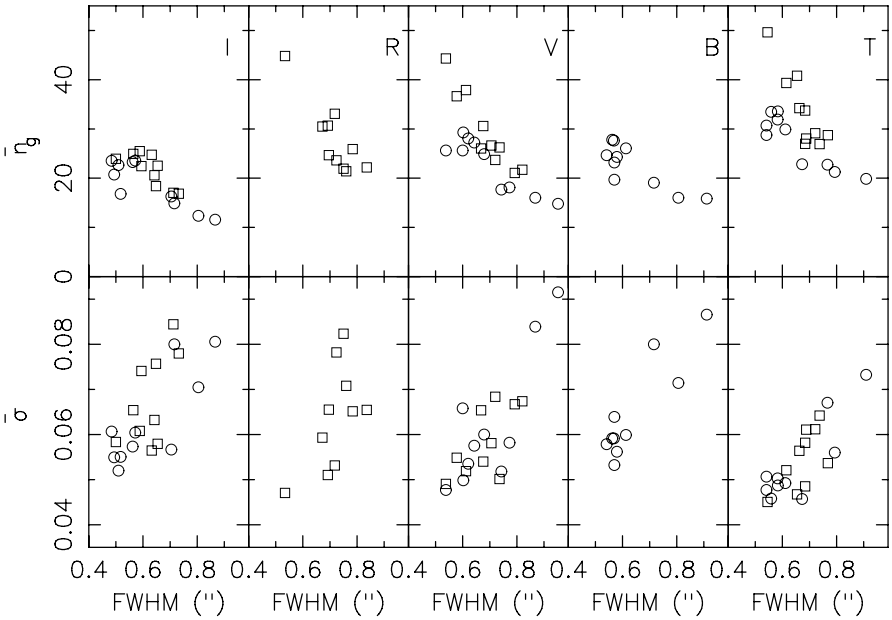

Fig. 5. Mean number density of galaxy images for which a shape can be measured (*upper row*) and the r.m.s. noise of a shear measurement in an area of 1 arcmin^2 as a function of the full width at half maximum (FWHM) of the point-spread function (PSF) – i.e., the seeing. The data were taken on 20 different fields with the FORS2 instrument at the VLT, with different filters (I, R, V and R). Squares show data taken with about 2 hours integration time, circles those with ∼45 min exposure. The right-most panels show the coadded data of I,R,V for the long exposures, and I,V,B for the 45 min fields. The useful number of galaxy images is seen to be a strong function of the seeing, except for the I-band (which is related to the higher sky brightness and the way objects are detected). But even more dramatically, the noise due to intrinsic source ellipticity decreases strongly for better seeing conditions, which is due to (1) higher number density of galaxies for which a shape can be measured, and (2) smaller corrections for PSF blurring, reducing the associated noise of this correction. In fact, this figure shows that seeing is a more important quantity than the total exposure time (from Clowe et al. 2004b)

The typical pixel size of these cameras is ∼0.″2, which is needed to sample the seeing disk in times of good seeing. From Fig. 4 one concludes immediately that the seeing conditions are absolutely critical for weak lensing: an image with 0.″6 is substantially more useful than one taken under the more typical condition of 0.″8 (see Fig. 5). There are two separate reasons why the seeing is such an important factor. First, seeing blurs the images and make

may be hoped that some of these image defects are improved after a complete overhaul of the instrument which occurred recently.

them rounder; accordingly, to correct for the seeing effect, a larger correction factor is needed in the worse seeing conditions. In addition, since the galaxy images from which the shear is to be determined are faint, a larger seeing smears the light from these galaxies over a larger area on the sky, reducing its contrast relative to the sky noise, and therefore leads to noisier estimates of the ellipticities even before the correction.

Deep observations of a field require multiple exposures. As a characteristic number, the exposure time for an R-band image on a 4-m class telescope is not longer than $\sim$10 min to avoid the non-linear part of the CCD sensitivity curve (exposures in shorter wavelength bands can be longer, since the night sky is fainter in these filters). Therefore, these large-format cameras imply a high data rate; e.g., one night of observing with the WFI yields $\sim$30 GB of science and calibration data. This number will increase by a factor $\sim$6 for MegaCam. Correspondingly, handling this data requires large disk space for efficient data reduction.

3.2 Data Reduction: Individual Frames

We shall now consider a number of issues concerning the reduction of imaging data, starting here with the steps needed to treat individual chips on individual frames, and later consider aspects of combining them into a coadded image.

Flatfielding

The pixels of a CCD have different sensitivity, i.e., they yield different counts for a given amount of light falling onto them (Fig. 6). In order to calibrate the pixel sensitivity, one needs flatfielding. Three standard methods for this are in use:

1. Dome-flats: a uniformly illuminated screen in the telescope dome is exposed; the counts in the pixels are then proportional to their sensitivity. The problem here is that the screen is not really of uniform brightness.
2. Twilight-flats: in the period of twilight after sunset, or before sunrise, the cloudless sky is nearly uniformly bright. Short exposures of regions of the sky without bright stars are then used to calibrate the pixel sensitivity.
3. Superflats: if many exposures with different pointings are taken with a camera during a night, then any given pixel is not covered by a source for most of the exposures (because the fraction of the sky at high galactic latitudes which is covered by objects is fairly small, as demonstrated by the deep fields taken by the HST). Hence, the (exposure-time normalized) counts of any pixel will show, in addition to a little tail due to those exposures when a source has covered it, a distribution around its sensitivity to the uniform night-sky brightness; from that distribution, the flat-field can be constructed, by taking its mode or its median.

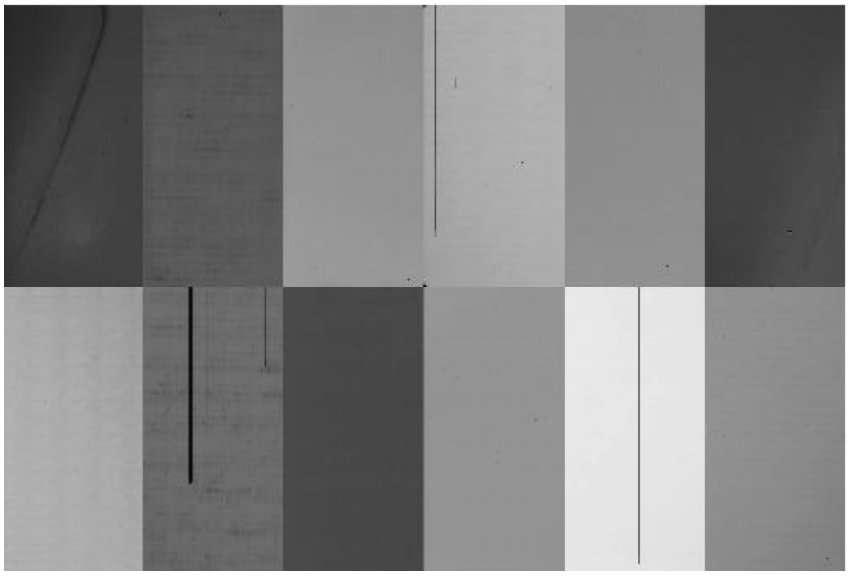

Fig. 6. A flat field for the CFH12K camera, showing the sensitivity variations between pixels and in particular between chips. Also, bad columns are clearly seen

Bad Pixels

Each CCD has defects, in that some pixels are dead or show a signal unrelated to their illumination. This can occur as individual pixels, or whole pixel columns (Fig. 6). No information of the sky image is available at these pixel positions. One therefore employs dithering: several exposures of the same field, but with slightly different pointings (dither positions) are taken. Then, any position of the field falls on bad pixels only in a small fraction of exposures, so that the full two-dimensional brightness distribution can be recovered.

Cosmic Rays

Those mimic groups of bad pixels; they can be removed owing to the fact that a given point of the image will most likely be hit by a cosmic only once, so that by comparison between the different exposures, cosmic rays can be removed (or more precisely, masked). Another signature of a cosmic ray is that the width of its track is typically much smaller than the seeing disk, the minimum size of any real source.

Bright Stars

Those cause large diffraction spikes, and depending on the optics and the design of the camera, reflection rings, ghost images and other unwanted features.

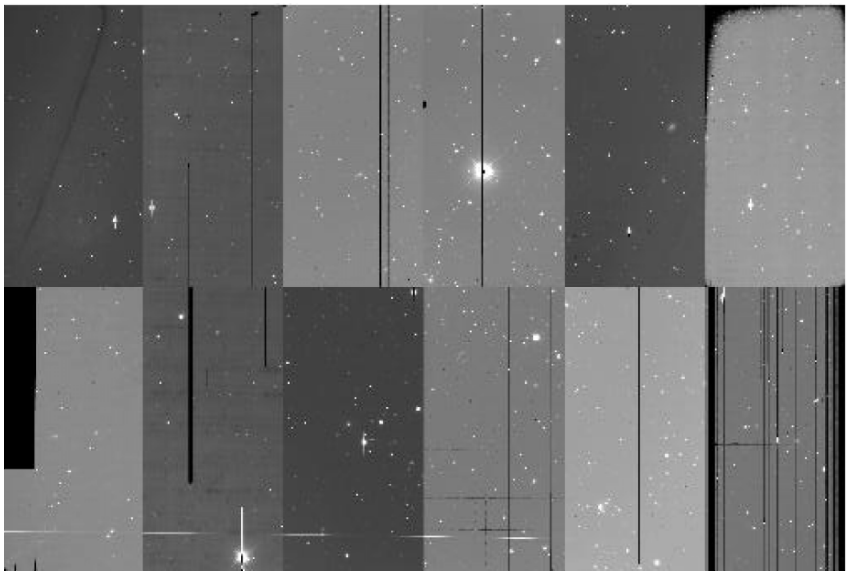

Fig. 7. A raw frame from the CFH12K camera, showing quite a number of effects mentioned in the text: bad column, saturation of bright stars, bleeding, and sensitivity variations across the field and in particular between chips

It is therefore best to choose fields where no or very few bright stars are present. The diffraction spikes of stars need to be masked, as well as the other features just mentioned (Fig. 7).

Fringes

Owing to light reflection within the CCD, patterns of illumination across the field can be generated (see Fig. 8); this is particularly true for thin chips when rather long wavelength filters are used. In clear nights, the fringe pattern is stable, i.e., essentially the same for all images taken during the night; in that case, it can be deduced from the images and subtracted off the individual exposures. However, if the nights are not clear, this procedure no longer works well; it is then safer to observe at shorter wavelength. For example, for the WFI, fringing is a problem for I-band images, but for the R-band filter, the amplitude of fringing is small. For the FORS instruments at the VLT, essentially no fringing occurs even in the I band (Maoli et al. 2001).

Gaps

The individual CCDs in multi-chip cameras cannot be brought together arbitrarily close; hence, there are gaps between the CCDs (see Fig. 9 for an

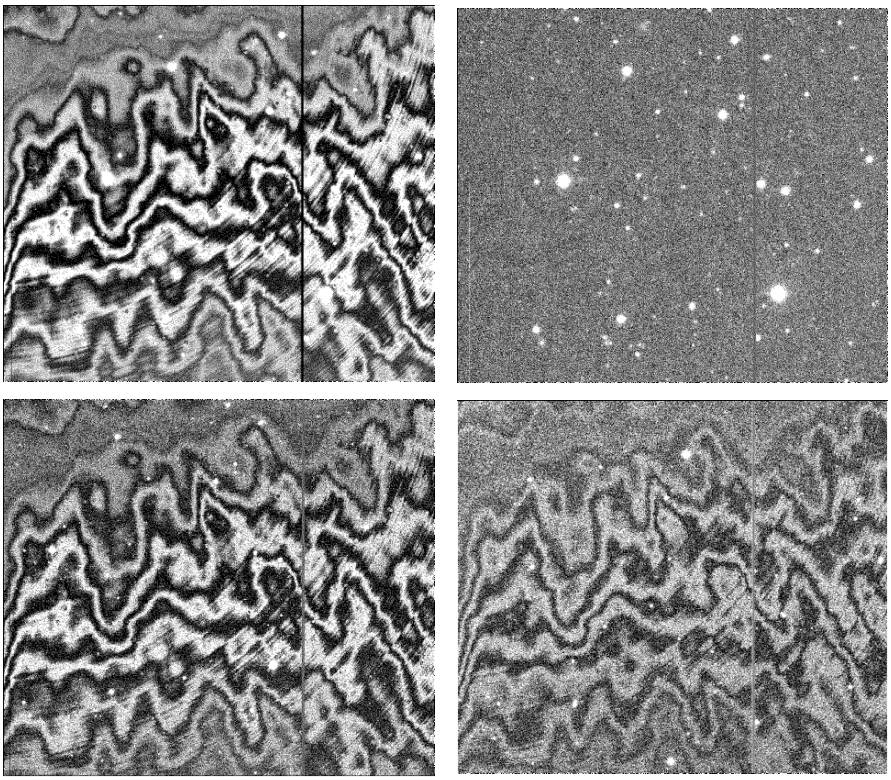

Fig. 8. The two left panels show the fringe patterns of images taken with the WFI in the I-band; the upper one was taken during photometric conditions, the lower one under non-photometric conditions. Since the fringe pattern is spatially stable, it can be corrected for (*right panels*), but the result is satisfactory only in the former case (source: M. Schirmer and T. Erben)

example). In order to cover the gaps, the dither pattern can be chosen such as to cover the gaps, so that they fall on different parts of the sky in different exposures. As we shall see, such relatively large dither patterns also provide additional advantages.

Satellite Trails, Asteroid Trails

Those have to be identified, either by visual inspection (currently the default) or by image recognition software which can detect these linear features which occur either only once, or at different positions on different exposures. These are then masked, in the same way as some of the other features mentioned above.

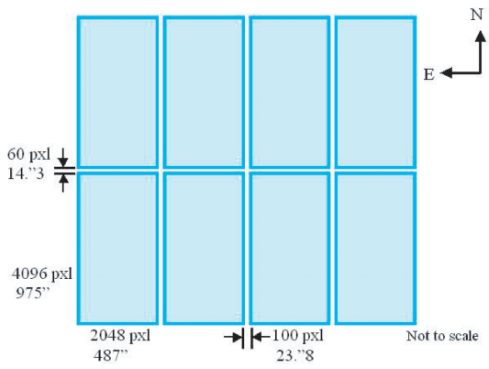

Fig. 9. Layout of the Wide Field Imager (WFI) at the ESO/MPG 2.2m telescope at La Silla. The eight chips each have $\sim 2048 \times 4096$ pixels and cover $\sim 7'.5 \times 15'$

3.3 Data Reduction: Coaddition

After taking several exposures with slightly different pointing positions (for the reasons given above), frames shall be coadded to a sum-frame; some of the major steps in this coaddition procedure are:

Astrometric Solution

One needs to coadd data from the same true (or sky) position, not the same pixel position. Therefore, one needs a very precise mapping from sky coordinates to pixel coordinates. Field distortions, which occur in every camera (and especially so in wide-field cameras), make this mapping non-linear (see Fig. 10). Whereas the distortion map of the telescope/camera system is to a large degree constant and therefore one of the known features, it is not stable to the sub-pixel accuracy needed for weak lensing work, owing to its dependence on the zenith angle (geometrical distortions of the telescope due to gravity), temperature etc. Therefore, the pixel-to-sky mapping has to be obtained from the data itself. Two methods are used to achieve this: one of them makes use of an external reference catalog, such as the US Naval Observatory catalogue for point sources; it contains about 2 point sources per arcmin^2 (at high Galactic latitudes) with ~ 0.3 arcsec positional accuracy. Matching point sources on the exposures with those in the USNO catalog therefore yields the mapping with sub-arcsecond accuracy. Far higher accuracy of the relative astrometry is achieved (and needed) from internal astrometry, which is obtained by matching objects which appear at different pixel coordinates, and in particular, on different CCDs for the various dithering positions. Whereas the sky coordinates are constant, the pixel coordinates change between dithering positions. Since the distortion map can be described by a low-order polynomial, the comparison of many objects appearing at (substantially) different

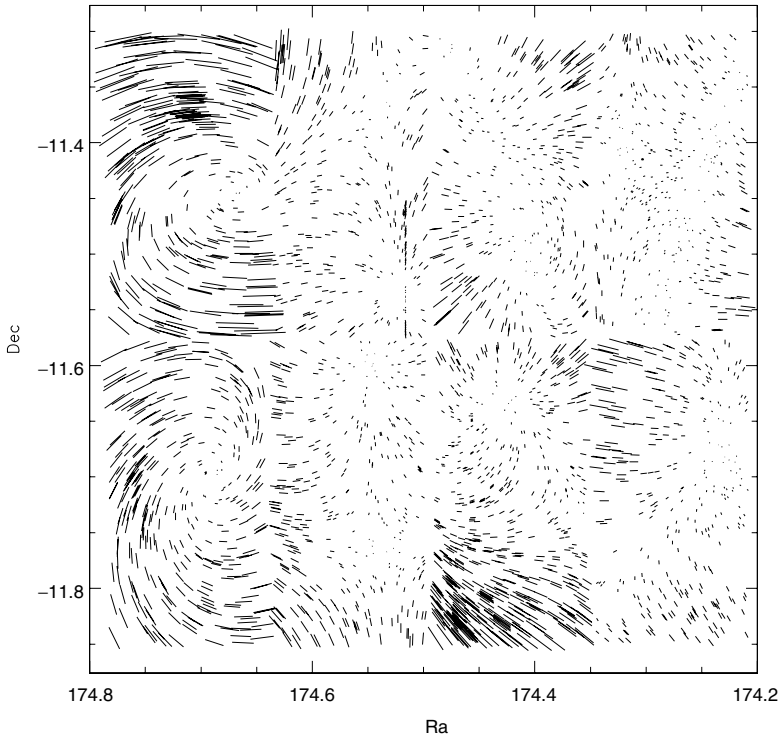

Fig. 10. This figure shows the geometric distortion of the WFI. Plotted is the difference of the positions of stars as obtained from a simple translation, and a third-order astrometric correction obtained in the process of image reduction. The patterns in the two left chips is due to their rotation relative to the other six chips. Whereas this effect looks dramatic at first sight, the maximum length of the sticks corresponds to about 6 pixels, or $1\farcs2$. Given that the WFI covers a field of $\sim 33'$, the geometrical distortions are remarkably small – however, they are sufficiently large that they have to be taken into account in the coaddition process (source: T. Erben and M. Schirmer)

pixel positions yield many more constraints than the free parameters in the distortion map and thus yields the distortion map with much higher relative accuracy than external data. The corresponding astrometric solution can routinely achieve an accuracy of 0.1 pixel, or typically $0\farcs02$ – compared with a typical field size of $\sim 30'$.

Photometric Solution

Flatfielding corrects for the different sensitivities of the pixels and therefore yields accurate relative photometry across individual exposures. The different exposures are tied together by matching the brightness of joint objects, in

particular across chip boundaries. To achieve an absolute photometric calibration, one needs external data (e.g., standard star observations).

The Coaddition Process

Coaddition has to happen with sub-pixel accuracy; hence, one cannot just shift pixels from different exposures on top of each other, although this procedure is still used by some groups. The by-now standard method is drizzling (Fruchter and Hook 2002), in which a new pixel frame is defined which usually has smaller pixel size than the original image pixels (typically by a factor of two) and which is linearly related to the sky coordinates. The astrometrically and photometrically calibrated individual frames are now remapped onto this new pixel grid, and the pixel values are summed up into the sub-pixel grid, according to the overlap area between exposure pixel and drizzle pixel (see Fig. 11). By that, drizzling automatically is flux conserving. In the coaddition process, weights are assigned, accounting for the noise properties of the individual exposures (including the masks, of course).

The result of the coaddition procedure is then a science frame, plus a weight map which contains information about the pixel noise, which is of course spatially varying, owing to the masks, CCD gaps, removed cosmic rays and bad pixels. Figure 12 shows a typical example of a coadded image and its corresponding weight map.

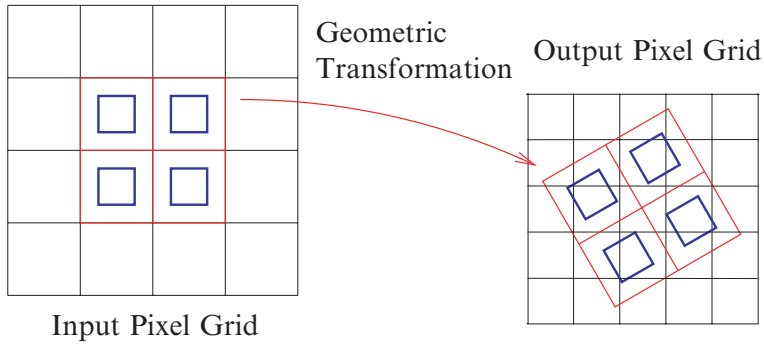

Fig. 11. The principle of drizzling in the process of coaddition is shown. The pixel grid of each individual exposure is mapped onto an output grid, where the shifts and geometric distortions obtained during the astrometric solutions are applied. The counts of the input pixel, multiplied by the relative weight of this pixel, are then dropped onto the output pixels, according to the relative overlap area, where the output pixels can be chosen smaller than the input pixels. The same procedure is applied to the weight maps of the individual exposures. If many exposures are coadded, the input pixel can also be shrunk before dropping onto the output pixel. After processing all individual exposures in this way, a coadded image and a coadded weight map is obtained (source: T. Schrabback)

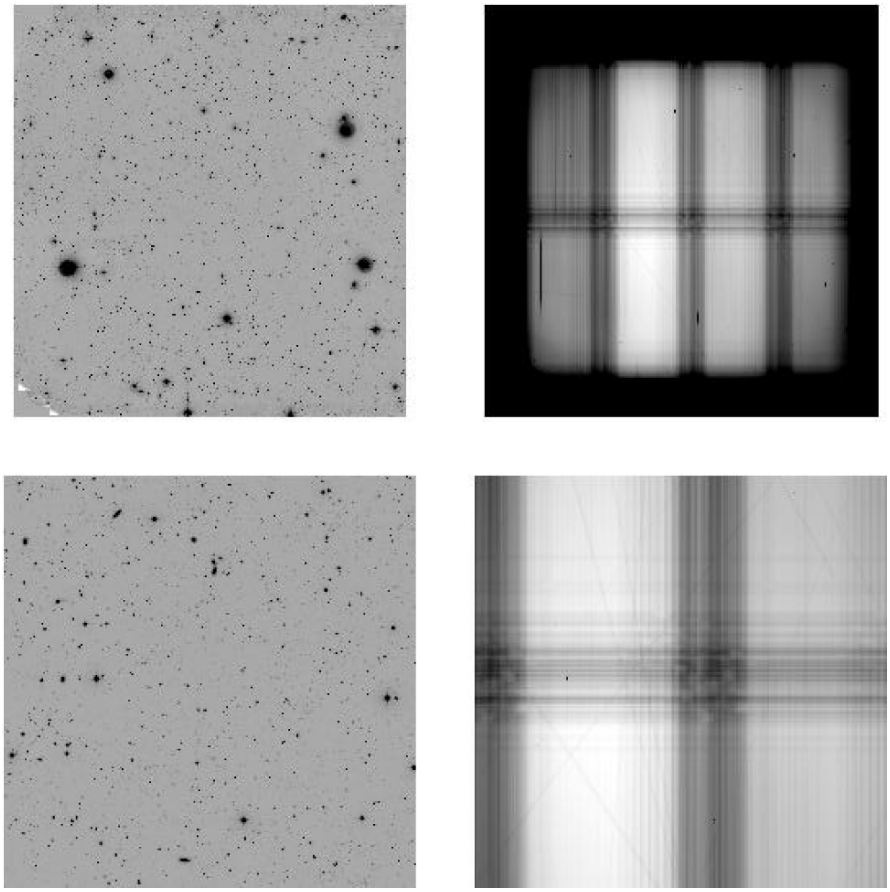

Fig. 12. A final coadded frame from a large number of individual exposures with the WFI is shown in the upper left panel, with the corresponding weight map at the upper right. The latter clearly shows the large-scale inhomogeneity of the chip sensitivity and the illumination, together with the different number of exposures contributing to various regions in the output image due to dithering and the gaps between CCDs. The two lower panels show a blow-up of the central part. Despite the highly inhomogeneous weight, the coadded image apparently shows no tracer of the gaps, which indicates that a highly accurate relative photometric solution was obtained (source: T. Erben and M. Schirmer)

The quality of the coadded image can be checked in a number of ways. Coaddition should not erase information contained in the original exposures (except, of course, the variability of sources). This means that the PSF of the coadded image should not be larger than the weighted mean of the PSFs of the individual frames. Insufficient relative astrometry would lead to a blurring of images in the coaddition. Furthermore, the anisotropy of the PSF should be

similar to the weighted mean of the PSF anisotropies of the individual frames; again, insufficient astrometry could induce an artificial anisotropy of the PSF in the coaddition (which can be easily visualized, by adding two round images with a slight center offset, where a finite ellipticity would be induced).

Probably, there does not exist the 'best' coadded image from a given set of individual exposures. This can be seen by considering a set of exposures with fairly different individual seeing. If one is mainly interested in photometric properties of rather large galaxies, one would prefer a coaddition which puts all the individual exposures together, in order to maximize the total exposure time and therefore to minimize the photometric noise of the coadded sources. For weak lensing purposes, such a coaddition is certainly not optimal, as adding exposures with bad seeing together with those of good seeing creates a coadded image with a seeing intermediate between the good and the bad. Since seeing is a much more important quantity than depth for the shape determination of faint and small galaxy images, it would be better to coadd only the images with the good seeing. In this respect, the fact that large imaging instruments are operated predominantly in service observing more employing queue scheduling is a very valuable asset: data for weak lensing studies are then taken only if the seeing is better than a specified limit; in this way one has a good chance to get images of homogeneously good seeing conditions.

As a specific example, we show in Fig. 13 the 'deepest wide-field image in the Southern sky', targeted toward the Chandra Deep Field South, one of regions in the sky in which all major observatories have agreed to obtain, and make publically available, very deep images for a detailed multi-band study. For example, the Hubble Ultra Deep Field (Beckwith et al. 2003) is located in the CDFS, the deepest Chandra X-ray exposures are taken in this field, as well as two ACS@HST mosaic images, one called the GOODS field (Great Observatories Origins Deep Survey; cf. Giavalisco and Mobasher 2004), the other the GEMS survey (Rix et al. 2004).

3.4 Image Analysis

The final outcome of the data reduction steps described above is an image of the sky, together with a weight map providing the noise properties of the image. The next step is the scientific exploitation of this image, which in the case of weak lensing includes the identification of sources, and to measure their magnitude, size and shape.

As a first step, individual sources on the image need to be identified, to obtain a catalog of sources for which the ellipticities, sizes and magnitudes are to be determined later. This can done with by-now standard software, like SExtractor (Bertin and Arnouts 1996), or may be part of specialized software packages developed specifically for weak lensing, such as IMCAT, developed by Nick Kaiser (see below). Although this first step seems straightforward at first glance, it is not: images of sources can be overlapping, the brightness

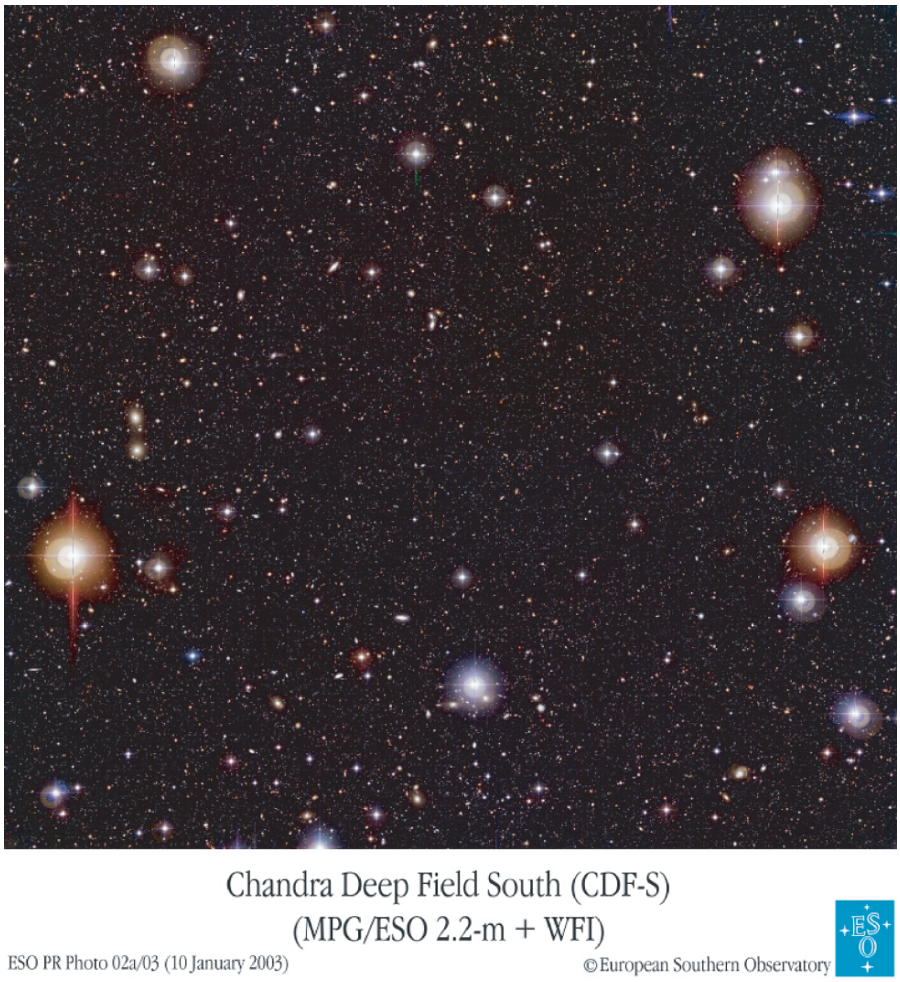

Fig. 13. A multi-color WFI image of the CDFS; the field is slightly larger than one-half degree on the side. To obtain this image, about 450 different WFI exposures were combined, resulting in a total exposure time of 15.8 hours in B, 15.6 hours in V, and 17.8 hours in R. The data were obtained in the frame of three different projects – the GOODS project, the public ESO Imaging Survey, and the COMBO-17 survey. These data were reduced and coadded by Mischa Schirmer and Thomas Erben; more than 2 TB of disk space were needed for the reduction

distribution of many galaxies (in particular those with active star formation) tends to be highly structured, with a collection of bright spots, and therefore the software must be taught whether or not these are to be split into different sources, or be taken as one (composite) source. This is not only a software problem; in many cases, even visual inspection cannot decide whether a given

light distribution corresponds to one or several sources. The shape and size of the images are affected by the point-spread function (PSF), which results from the telescope optics, but for ground-based images, is dominated by the blurring caused by the atmospheric turbulence; furthermore, the PSF may be affected by telescope guiding and the coaddition process described earlier.

The Point-Spread Function

Atmospheric turbulence and the other effects mentioned above smear the image of the sky, according to

$$I^{\rm obs}(\boldsymbol{\theta}) = \int \mathrm{d}^2\vartheta\; I(\boldsymbol{\vartheta})\, P(\boldsymbol{\theta} - \boldsymbol{\vartheta})\;, \tag{28}$$

where $I(\boldsymbol{\vartheta})$ is the brightness profile outside the atmosphere, $I^{\rm obs}(\boldsymbol{\vartheta})$ the observed brightness profile, and P is the PSF; it describes how point sources would appear on the image. To first approximation, the PSF is a bell-shaped function; its full width at half maximum (FWHM) is called the 'seeing' of the image. At excellent sites, and excellent telescopes, the seeing has a median of $\sim 0\farcs7$–$\sim 0\farcs8$; exceptionally, images with a seeing of $\sim 0\farcs5$ can be obtained. Recall that typical faint galaxies are considerably smaller than this seeing size, hence their appearance is dominated by the PSF.

The main effect of seeing on image shapes is that it makes an elliptical source rounder: a small source with a large ellipticity will nevertheless appear as a fairly round image if its size is considerably smaller than the PSF. If not properly corrected for, this smearing effect would lead to a serious underestimate of ellipticities, and thus of the shear estimates. Furthermore, the PSF is not fully isotropic; small anisotropies can be introduced by guiding errors, the coaddition, the telescope optics, bad focusing etc. An anisotropic PSF makes round sources elliptical, and therefore mimics a shear. Also here, the effect of the PSF anisotropy depends on the image size and is strongest for the smallest sources. PSF anisotropies of several percent are typical; hence, if not corrected for, its effect can be larger than the shear to be measured.

The PSF can be measured at the position of stars (point sources) on the field; if it is a smooth function of position, it can be fitted by a low-order polynomial, which then yields a model for the PSF at all points, in particular at every image position, and one can correct for the effects of the PSF. A potential problem occurs if the PSF jumps between chips boundaries in multi-chip cameras, since then the coaddition produces PSF jumps on the coadded frame; this happens in cameras where the chips are not sufficiently planar, and thus not in focus simultaneously. For the WFI@ESO/MPG 2.2-m, this however is not a problem, but for some other cameras this problem exists and is severe. There is an obvious way to deal with that problem, namely to coadd data only from the same CCD chip. In this case, the gaps between chips cannot be closed in the coadded image, but for most weak lensing purposes this is not a very serious issue. In order not to lose too much area in this

coaddition, the dither pattern, i.e., the pointing differences in the individual exposures, should be kept small; however, it should not be smaller than, say, $20''$, since otherwise some pixels may always fall onto a few larger galaxies in the field, which then causes problems in constructing a superflat. Furthermore, small shifts between exposures means that the number of objects falling onto different chips in different exposures is small, thus reducing the accuracy of the astrometric solution. In any case, the dither strategy shall be constructed for each camera individually, taken into account its detailed properties.

3.5 Shape Measurements

Specific software has been developed to deal with the issues mentioned above; the one that is most in use currently has been developed by Kaiser et al. (1995; hereafter KSB), with substantial additions by Luppino and Kaiser (1997), and later modifications by Hoekstra et al. (1998). The numerical implementation of this method is called IMCAT and is publically available. The basic features of this method shall be outlined next.

First one notes that the definition (6) of the second-order moments of the image brightness is not very practical for applying it to real data. As the effective range of integration depends on the surface brightness of the image (through the weight function q_I) the presence of noise enters the definition of the Q_{ij} in a non-linear fashion. Furthermore, neighboring images can lead to very irregularly shaped integration ranges. In addition, this definition is hampered by the discreteness of pixels. For these reasons, the definition is modified by introducing a weight function $q_\theta(\boldsymbol{\theta})$ which depends explicitly on the image coordinates,

$$Q_{ij} = \frac{\int \mathrm{d}^2\theta\, q_\theta(\boldsymbol{\theta})\, I(\boldsymbol{\theta})\, (\theta_i - \bar{\theta}_i)\, (\theta_j - \bar{\theta}_j)}{\int \mathrm{d}^2\theta\, q_\theta(\boldsymbol{\theta})\, I(\boldsymbol{\theta})} \;, \quad i,j \in \{1,2\} \;, \tag{29}$$

where the size of the weight function q_θ is adapted to the size of the galaxy image (for optimal S/N measurement). One typically chooses q_θ to be circular Gaussian. The image center $\bar{\boldsymbol{\theta}}$ is defined as before, but also with the new weight function $q_\theta(\boldsymbol{\theta})$, instead of $q_I(I)$. However, with this definition, the transformation between image and source brightness moments is no longer simple; in particular, the relation (11) between the second-order brightness moments of source and image no longer holds. The explicit spatial dependence of the weight, introduced for very good practical reasons, destroys the convenient relations that we derived earlier – welcome to reality.

In KSB, the anisotropy of the PSF is characterized by its (complex) ellipticity q, measured at the positions of the stars, and fitted by a low-order polynomial. Assume that the (reduced) shear g and the PSF anisotropy q are small; then they both will have a small effect on the measured ellipticity. Linearizing these two effects, one can write (employing the Einstein summation convention)

$$\hat{\chi}^{\mathrm{obs}}_\alpha = \chi^0_\alpha + P^{\mathrm{sm}}_{\alpha\beta} q_\beta + P^g_{\alpha\beta} g_\beta \;. \tag{30}$$

The interpretation of the various terms is found as follows: First consider an image in the absence of shear and the case of an isotropic PSF; then $\hat{\chi}^{\rm obs} = \chi^0$; thus, χ^0 is the image ellipticity one would obtain for $q = 0$ and $g = 0$; it is the source smeared by an isotropic PSF. It is important to note that $\mathrm{E}(\chi^0) = 0$, due to the random orientation of sources. The tensor P^{sm} describes how the image ellipticity responds to the presence of a PSF anisotropy; similarly, the tensor P^g describes the response of the image ellipticity to shear in the presence of smearing by the seeing disk. Both, $P^{\rm sm}$ and P^g have to be calculated for each image individually; they depend on higher-order moments of the brightness distribution and the size of the PSF. A full derivation of the explicit equations can be found in Sect. 4.6.2 of BS01.

Given that $\langle \chi^0 \rangle = 0$, an estimate of the (reduced) shear is provided by

$$\epsilon = (P^g)^{-1} \left(\hat{\chi}^{\rm obs} - P^{\rm sm} q \right) \ . \tag{31}$$

If the source size is much smaller than the PSF, the magnitude of P^g can be very small, i.e., the correction factor in (31) can be very large. Given that the measured ellipticity $\hat{\chi}^{\rm obs}$ is affected by noise, this noise then also gets multiplied by a large factor. Therefore, depending on the magnitude of P^g, the error of the shear estimates differ between images; this can be accounted for by specifically weighting these estimates when using them for statistical purposes (e.g., in the estimate of the mean shear in a given region). Different authors use different weighting schemes when applying KSB. Also, the tensors P^{sm} and P^g are expected to depend mainly on the size of the image and their signal-to-noise; therefore, it is advantageous to average these tensors over images having the same size and S/N, instead of using the individual tensor values which are of course also affected by noise. Erben et al. (2001) and Bacon et al. (2001) have tested the KSB scheme on simulated data and in particular investigated various schemes for weighting shear estimates and for determining the tensors in (30); they concluded that simulated shear values can be recovered with a systematic uncertainty of about 10%.

Maybe by now you are confused – what is 'real ellipticity' of an image, independent of weights etc. ? Well, this question has no answer, since only images with conformal elliptical isophotes have a 'real ellipticity'. By the way, not necessarily the one that is the outcome of the KSB procedure. The KSB process does not aim toward measuring 'the' ellipticity of any individual galaxy image; it tries to measure 'a' ellipticity which, when averaged over a random intrinsic orientation of the source, yields an unbiased estimate of the reduced shear.

Given that the shape measurements of faint galaxies and their correction for PSF effects is central for weak lensing, several different schemes for measuring shear have been developed (e.g., Valdes et al. 1983; Bonnet and Mellier 1995; Kuijken 1999; Kaiser 2000; Refregier 2003b; Bernstein and Jarvis 2002). In the shapelet method of Refregier (2003b; see also Refregier and Bacon 2003), the brightness distribution of galaxy images is expanded in a set of basis functions ('shapelets') whose mathematical properties are particularly

convenient. With a corresponding decomposition of the PSF (the shape of stars) into these shapelets and their low-order polynomial fit across the image, a partial deconvolution of the measured images becomes possible, using linear algebraic relations between the shapelet coefficients. The effect of a shear on the shapelet coefficients can be calculated, yielding then an estimate of the reduced shear. In contrast to the KSB scheme, higher-order brightness moments, and not just the quadrupoles, of the images are used for the shear estimate.

These alternative methods for measuring image ellipticities (in the sense mentioned above, namely to provide an unbiased estimate of the local reduced shear) have not been tested yet to the same extent as is true for the KSB method. Before they become a standard in the field of weak lensing, several groups need to independently apply these techniques to real and synthetic data sets to evaluate their strengths and weaknesses. In this regard, one needs to note that weak lensing has, until recently, been regarded by many researchers as a field where the observational results are difficult to 'believe' (and sure, not all colleagues have given up this view, yet). The difficulty to display the directly measured quantities graphically so that they can be directly 'seen' makes it difficult to convince others about the reliability of the measurements. The fact that the way from the coadded imaging data to the final result is, except for the researchers who actually do the analysis, close to a black box with hardly any opportunity to display intermediate results (which would provide others with a quality check) implies that the methods employed should be standardized and well checked.

Surprisingly enough, there are very few (published) attempts where the same data set is analyzed by several groups independently, and intermediate and final results being compared. Kleinheinrich (2003) in her dissertation has taken several subsets of the data that led to the deep image shown in Fig. 13 and compared the individual image ellipticities between the various subsets. If the subsets had comparable seeing, the measured ellipticities could be fairly well reproduced, with an rms difference of about 0.15, which is small compared to the dispersion of the image ellipticities $\sigma_\epsilon \sim 0.35$. Hence, these differences, which presumably are due to the different noise realizations on the different images, are small compared to the 'shape noise' coming from the finite intrinsic ellipticities of galaxies. If the subsets had fairly different seeing, the smearing correction turns out to lead to a systematic bias in the measured ellipticities. From the size of this bias, the conclusions obtained from the simulations are confirmed – measuring a shear with better than $\sim$10% accuracy will be difficult with the KSB method, where the main problem lies in the smearing correction.

Shear Observations from Space

We conclude this section with a few comments on weak lensing observations from space. Since the PSF is the largest problem in shear measurements, one might be tempted to use observations from space which are not affected by

the atmosphere. At present, the Hubble Space Telescope (HST) is the only spacecraft that can be considered for this purpose. Weak lensing observations have been carried out using two of its instruments, WFPC2 and STIS. The former has a field-of-view of about 5 arcmin^2, whereas STIS has a field of $51''$. These small fields imply that the number of stars that can be found on any given exposure at high galactic latitude is very small, in fact typically zero for STIS. Therefore, the PSF cannot be measured from these exposures themselves. Given that an instrument in space is expected to be much more stable than one on the ground, one might expect that the PSF is stable in time; then, it can be investigated by analyzing exposures which contain many stars (e.g., from a star cluster). In fact, Hoekstra et al. (1998) and Hämmerle et al. (2002) have shown that the PSFs of WFPC2 and STIS are approximately constant in time. The situation is improved with the new camera ACS onboard HST, where the field size of $\sim 3'.4$ is large enough to contain about a dozen stars even for high galactic latitude, and where some control over the PSF behavior on individual images is obtained. We shall discuss the PSF stability of the ACS in Sect. 7.3 below.

The PSF of a diffraction-limited telescope is much more complex than that of the seeing-dominated one for ground-based observations. The assumption underlying the KSB method, namely that the PSF can be described by a axi-symmetric function convolved with a small anisotropic kernel, is strongly violated for the HST PSF; it is therefore less obvious how well the shear measurements with the KSB method work in space. In addition, the HST PSF in not well sampled with the current imaging instruments, even though STIS and ACS have a pixel scale of $0''.05$. The number density of cosmic rays is much larger in space, so their removal can be more cumbersome than for ground-based observations. The intense particle bombardment also leads to aging of the CCD, which lose their sensitivity and attain charge-transfer efficiency problems. Despite these potential problems, a number of highly interesting weak lensing results obtained with the HST have been reported, in particular on clusters, and we shall discuss some of them in later sections. The new Advanced Camera for Surveys (ACS) on-board HST has a considerably larger field-of-view than previous instruments and will most likely become a highly valuable tool for weak lensing studies.

4 Clusters of Galaxies: Introduction, and Strong Lensing

4.1 Introduction

Galaxies are not distributed randomly, but they cluster together, forming groups and clusters of galaxies. Those can be identified as overdensities of galaxies projected onto the sky, and this has of course been the original method for the detection of clusters, e.g., leading to the famous and still heavily used Abell (1958) catalog and its later Southern extension (Abell et al. 1989; ACO).

Only later – with the exception of Zwicky's early insight in 1933 that the Coma cluster must contain a lot of missing mass – it was realized that the visible galaxies are but a minor contribution to the clusters since they are dominated by dark matter. From X-ray observations we know that clusters contain a very hot intracluster gas which emits via free-free and atomic line radiation. Many galaxies are members of a cluster or a group; indeed, the Milky Way is one of them, being one of two luminous galaxies of the Local Group (the other one is M31, the Andromeda galaxy), of which ∼35 member galaxies are known, most of them dwarfs.

In the first part of this section we shall describe general properties of galaxy clusters, in particular methods to determine their masses, before turning to their strong lensing properties, such as show up in the spectacular giant luminous arcs. Very useful reviews on clusters of galaxies are from Sarazin (1986) and in a recent proceedings volume (Mulchaey et al. 2004).

4.2 General Properties of Clusters

Clusters of galaxies contain tens to hundreds of bright galaxies; their galaxy population is dominated by early-type galaxies (E's and S0's), i.e. galaxies without active star formation. Often a very massive cD galaxy is located at their center; these galaxies differ from normal ellipticals in that they have a much more extended brightness profile – they are the largest galaxies. The morphology of clusters as seen in their distribution of galaxies can vary a lot, from regular, compact clusters (often dominated by a central cD galaxy) to a bimodal distribution, or highly irregular morphologies with strong substructure. Since clusters are at the top of the mass scale of virialized objects, the hierarchical merging scenario of structure growth predicts that many of them have formed only recently through the merging of two or more lower-mass sub-clusters, and so the irregular morphology just indicates that this happened.

X-ray observations reveal the presence of a hot (several keV) intracluster medium (ICM) which is highly enriched in heavy elements; hence, this gas has been processed through star-formation cycles in galaxies. The mass of the ICM surpasses that of the baryons in the cluster galaxies; the mass balance in clusters is approximately as follows: stars in cluster galaxies contribute ∼3% of the total mass, the ICM another ∼15%, and the rest (≳80%) is dark matter. Hence, clusters are dominated by dark matter; as discussed below (Sect. 4.3), the mass of clusters can be determined with three vastly different methods which overall yield consistent results, leading to the aforementioned mass ratio.

We shall now quote a few characteristic values which apply to rich, massive clusters. Their virial radius, i.e., the radius inside of which the mass distribution is in approximate virial equilibrium (or the radius inside of which the mean mass density of clusters is ∼200 times the critical density of the Universe – cf. Sect. 4.5 of IN) is $r_{\rm vir} \sim 1.5\,h^{-1}\,{\rm Mpc}$. A typical value for the

one-dimensional velocity dispersion of the member galaxies is $\sigma_v \sim 1000\,\mathrm{km/s}$. In equilibrium, this equals the thermal velocity of the ICM, corresponding to a temperature of $T \sim 10^{7.5}\,\mathrm{K} \sim 3\,\mathrm{keV}$. The mass of massive clusters within the virial radius (i.e., the *virial mass*) is $\sim 10^{15} M_\odot$. The mass-to-light ratio of clusters (as measured from the B-band luminosity) is typically of order $(M/L) \sim 300 h^{-1}\,(M_\odot/L_\odot)$. Of course, the much more numerous typical clusters have smaller masses (and temperatures).

Cosmological Interest for Clusters

Clusters are the most massive bound and virialized structures in the Universe; this, together with the (related) fact that their dynamical time scale (e.g., the crossing time $\sim r_{\rm vir}/\sigma_v$) is not much smaller than the Hubble time H_0^{-1} – so that they retain a 'memory' of their formation – render them of particular interest for cosmologists. The evolution of their abundance, i.e., their comoving number density as a function of mass and redshift, is an important probe for cosmological models and traces the growth of structure; massive clusters are expected to be much rarer at high redshift than today. Their present-day abundance provides one of the measures for the normalization of the power spectrum of cosmological density fluctuations. Furthermore, they form (highly biased) signposts of the dark matter distribution in the Universe, so their spatial distribution traces the large-scale mass distribution in the Universe. Clusters act as laboratories for studying the evolution of galaxies and baryons in the Universe. Since the galaxy number density is highest in clusters, mergers of their member galaxies and, more importantly, other interactions between them occur frequently. Therefore, the evolution of galaxies with redshift is most easily studied in clusters. For example, the Butcher–Oemler effect (the fact that the fraction of blue galaxies in clusters is larger at higher redshifts than today) is a clear sign of galaxy evolution which indicates that star formation in galaxies is suppressed once they have become cluster members. More generally, there exists a density-morphology relation for galaxies, with an increasing fraction of early-types with increasing spatial number density, with clusters being on the extreme for the latter. Finally, clusters were (arguably) the first objects for which the presence of dark matter has been concluded (by Zwicky 1933). Since they are so large, and present the gravitational collapse of a region in space with initial comoving radius of $\sim 8h^{-1}\,\mathrm{Mpc}$, one expects that their mixture of baryonic and dark matter is characteristic for the mean mass fraction in the Universe (White et al. 1993). With the baryon fraction of $\sim 15\%$ mentioned above, and the density parameter in baryons determined from big-bang nucleosynthesis in connection to the determination of the deuterium abundance in Lyα QSO absorption systems, $\Omega_{\rm b} \approx 0.02 h^{-2}$, one obtains a density parameter for matter of $\Omega_{\rm m} \sim 0.3$, in agreement with results from other methods, most noticeably from the recent WMAP CMB measurements (e.g., Spergel et al. 2003).

4.3 The Mass of Galaxy Clusters

Cosmologists can predict the abundance of clusters as a function of their mass (e.g., using numerical simulations); however, the mass of a cluster is not directly observable, but only its luminosity, or the temperature of the X-ray emitting intra-cluster medium. Therefore, in order to compare observed clusters with the cosmological predictions, one needs a way to determine their masses. Three principal methods for determining the mass of galaxy clusters are in use:

- Assuming virial equilibrium, the observed velocity distribution of galaxies in clusters can be converted into a mass estimate, employing the virial theorem; this method typically requires assumptions about the statistical distribution of the anisotropy of the galaxy orbits.
- The hot intra-cluster gas, as visible through its Bremsstrahlung in X-rays, traces the gravitational potential of the cluster. Under certain assumptions (see below), the mass profile can be constructed from the X-ray emission.
- Weak and strong gravitational lensing probes the projected mass profile of clusters, with strong lensing confined to the central regions of clusters, whereas weak lensing can yield mass measurements for larger radii.

All three methods are complementary; lensing yields the line-of-sight projected density of clusters, in contrast to the other two methods which probe the mass inside spheres. On the other hand, those rely on equilibrium (and symmetry) conditions; e.g., the virial method assumes virial equilibrium (that the cluster is dynamically relaxed) and the degree of anisotropy of the galaxy orbit distribution.

Dynamical Mass Estimates

Estimating the mass of clusters based on the virial theorem,

$$2E_{\rm kin} + E_{\rm pot} = 0\,, \tag{32}$$

has been the traditional method, employed by Zwicky (1933) to find strong hints for the presence of dark matter in the Coma cluster. The specific kinetic energy of a galaxy is $v^2/2$, whereas the potential energy is determined by the cluster mass profile, which can thus be determined using (32). One should note that only the line-of-sight component of the galaxy velocities can be measured; hence, in order to derive the specific kinetic energy of galaxies, one needs to make an assumption on the distribution of orbit anisotropies in the cluster potential. Assuming an isotropic distribution of orbits, the l.o.s. velocity distribution can then be related to the 3-D velocity dispersion, which in turn can be transformed into a mass estimate if spherical symmetry is assumed. This method requires many redshifts for an accurate mass estimate, which are available only for a few clusters. However, a revival of this method is expected and already seen by now, owing to the new high-multiplex optical spectrographs.

X-ray Mass Determination of Clusters

The intracluster gas emits via Bremsstrahlung; the emissivity depends on the gas density and temperature, and, at lower T, also on its chemical composition, since at $T \lesssim 1\,\mathrm{keV}$ the line radiation from highly ionized atomic species starts to dominate the total emissivity of a hot gas. Investigating the properties of the ICM with X-ray observations have revealed a wealth of information on the properties of clusters (see Sarazin 1986). Assuming that the gas is in hydrostatic equilibrium in the potential well of the cluster, the gas pressure P must balance gravity, or

$$\nabla P = -\rho_\mathrm{g}\,\nabla\Phi\;,$$

where ρ_g is the gas density. In the case of spherical symmetry, this becomes

$$\frac{1}{\rho_\mathrm{g}}\frac{\mathrm{d}P}{\mathrm{d}r} = -\frac{\mathrm{d}\Phi}{\mathrm{d}r} = -\frac{G\,M(r)}{r^2}\;.$$

From the X-ray brightness profile and temperature measurement, $M(r)$, the mass inside r, both dark and luminous, can then be determined,

$$M(r) = -\frac{k_\mathrm{B}Tr^2}{G\mu m_\mathrm{p}}\left(\frac{\mathrm{d}\ln\rho_\mathrm{g}}{\mathrm{d}r} + \frac{\mathrm{d}\ln T}{\mathrm{d}r}\right)\;, \tag{33}$$

where μm_p is the mean particle mass in the gas. Only for relatively few clusters are detailed X-ray brightness and temperature profile measurements available. In the absence of a temperature profile measurement, one often assumes that T does not vary with distance form the cluster center. In this case, assuming that the dark matter particles also have an isothermal distribution (with velocity traced by the galaxy velocities), one can show that

$$\rho_\mathrm{g}(r) \propto [\rho_\mathrm{tot}(r)]^\beta\;; \quad \text{with} \quad \beta = \frac{\mu m_\mathrm{p}\sigma_v^2}{k_\mathrm{B}T_\mathrm{g}}\;. \tag{34}$$

Hence, β is the ratio between kinetic and thermal energy. The mass profile corresponding to the isothermality assumption follows from the Lame–Emden equation which, however, has no closed-form solution. In the King approximation, the density and X-ray brightness profile (which is obtained by a line-of-sight integral at projected distance R from the cluster center over the emissivity, which in turn is proportional to the square of the electron density, or $\propto \rho_\mathrm{g}^2$, for an isothermal gas) become

$$\rho_\mathrm{g}(r) = \rho_\mathrm{g0}\left[1+\left(\frac{r}{r_\mathrm{c}}\right)^2\right]^{-3\beta/2} \quad;\quad I(R) \propto \left[1+\left(\frac{R}{r_\mathrm{c}}\right)^2\right]^{-3\beta/2+1/2}\;,$$

where r_c is the core radius. The observed brightness profile can now be fitted with these β-models, yielding estimates of β and r_c from which the cluster

mass follows. Typical values for r_c range from 0.1 to $0.3h^{-1}\,\mathrm{Mpc}$; and $\beta = \beta_{\mathrm{fit}} \sim 0.65$. On the other hand, one can determine β from the temperature T and the galaxy velocity dispersion using (34), which yields $\beta_{\mathrm{spec}} \approx 1$. The discrepancy between these two estimates of β is not well understood and probably indicates that one of assumptions underlying this 'β-models' fails in many clusters, which is not too surprising (see below).

The hot ICM loses energy through its thermal radiation; the cooling time t_{cool} of the gas, i.e., the ratio between the thermal energy density and the X-ray emissivity, is larger than the Hubble time $\sim H_0^{-1}$ for all but the innermost regions. In the center of clusters, the gas density can be high enough to have $t_{\mathrm{cool}} < H_0^{-1}$, so that there the gas can no longer be in hydrostatic equilibrium. One expects that the gas flows toward the cluster center, thereby being compressed and therefore maintain approximate pressure balance. Such 'cooling flows' (see, e.g., Fabian 1994) are observed indirectly, through highly peaked X-ray emission in cluster centers which indicates a strong increase of the gas density; furthermore, these cooling-flow clusters show a decrease of T toward the center. The mass-flow rate in these clusters can be as high as $100 M_\odot\,\mathrm{yr}^{-1}$ or even more, so that the total cooled mass can be larger than the baryonic mass of a massive galaxy. However, the fate of the cooled gas is unknown.

New Results from Chandra and XMM

The two X-ray satellites Chandra and XMM, launched in 1999, have greatly increased our view of the X-ray Universe, and have led to a number of surprising results about clusters. X-ray spectroscopy verified the presence of cool gas near the center of cooling-flow clusters, but no indication for gas with temperature below $\sim$1 keV has been seen, whereas the cooling is expected to rapidly proceed to very low temperatures, as the cooling function increases for lower T where atomic transitions become increasingly important. Furthermore, the new observations have revealed that at least the inner regions of clusters often show a considerably more complicated structure than implied by hydrostatic equilibrium. In some cases, the intracluster medium is obviously affected by a central AGN, which produces additional energy and entropy input, which might explain why no sub-keV gas has been detected. As the AGN activity of a galaxy may be switched on and off, depending on the fueling of the central black hole, even in clusters without a currently active AGN such heating might have occurred in the recent past, as indicated in some cases by radio relics. Cold fronts with very sharp edges (discontinuities in density and temperature, but such that $P \propto \rho T$ is approximately constant across the front), and shocks have been discovered, most likely showing ongoing or recent merger events. In many clusters, the temperature and metallicity appears to be strongly varying functions of position which invalidates the assumption of isothermality underlying the β-model. Therefore, mass estimates of central parts of clusters from X-ray observations require special care, and one needs to revise the

simplified models used in the pre-Chandra era. In fact, has there ever been the believe that the β-model provides an adequate description of the gas in a cluster, the results from Chandra and XMM show that this is unjustified. The physics of the intracluster gas appears to be considerably more complicated than that.

4.4 Luminous Arcs and Multiple Images

Strong lensing effects in cluster show up in the form of giant luminous arcs, strongly distorted arclets, and multiple images of background galaxies. Since strong lensing only occurs in the central part of clusters, it can be used only to probe their inner mass structure. However, strong lensing yields by far the most accurate central mass determinations in those cases where several strong lensing features can be identified. For a detailed account of strong lensing in clusters, the reader is referred to the review by Fort and Mellier (1994).

Furthermore, clusters thus act as a 'natural telescope'; many of the most distant galaxies have been found by searching behind clusters, employing the lensing magnification. For example, the recently discovered very high redshift galaxies at $z \approx 7$ (Kneib et al. 2004) and $z = 10$ (Pelló et al. 2004) were found through a search in the direction of the high-magnification region in the clusters A 2218 and A1835, respectively. In the first of these two cases, the multiple imaging of the background galaxy provides not only the magnification, but also an estimate of the redshift of the source (which is not determined by any spectral line), whereas in the latter case, only the implied high magnification makes the source visible on deep HST images and allows its spectroscopy, yielding a spectral line which most likely is due to Lyα. The magnification is indeed a very important asset, as can be seen from a simple example: a value of $\mu = 5$ reduces the observing time for obtaining a spectrum by a factor 25 (in the case where the noise is sky background dominated) – which is the difference of being doable or not. Recognizing the power of natural telescopes, the deepest SCUBA surveys for faint sub-millimeter sources have been conducted (e.g., Blain et al. 1999) around clusters with well-constrained (from lensing) mass distribution to reach further down the (unlensed) flux scale.

First go: $M(\leq \boldsymbol{\theta}_{\mathbf{E}})$

Giant arcs occur where the distortion (and magnification) is very large, that is near critical curves. To a first approximation, assuming a spherical mass distribution, the location of the arc from the cluster center (which usually is assumed to coincide with the brightest cluster galaxy) yields the Einstein radius of the cluster, so that the mass estimate (see IN, Eq. 43) can be applied:

$$M(\theta_{\rm arc}) \approx \pi\,(D_{\rm d}^{\rm ang}\,\theta_{\rm arc})^2\,\Sigma_{\rm cr}\;. \tag{35}$$

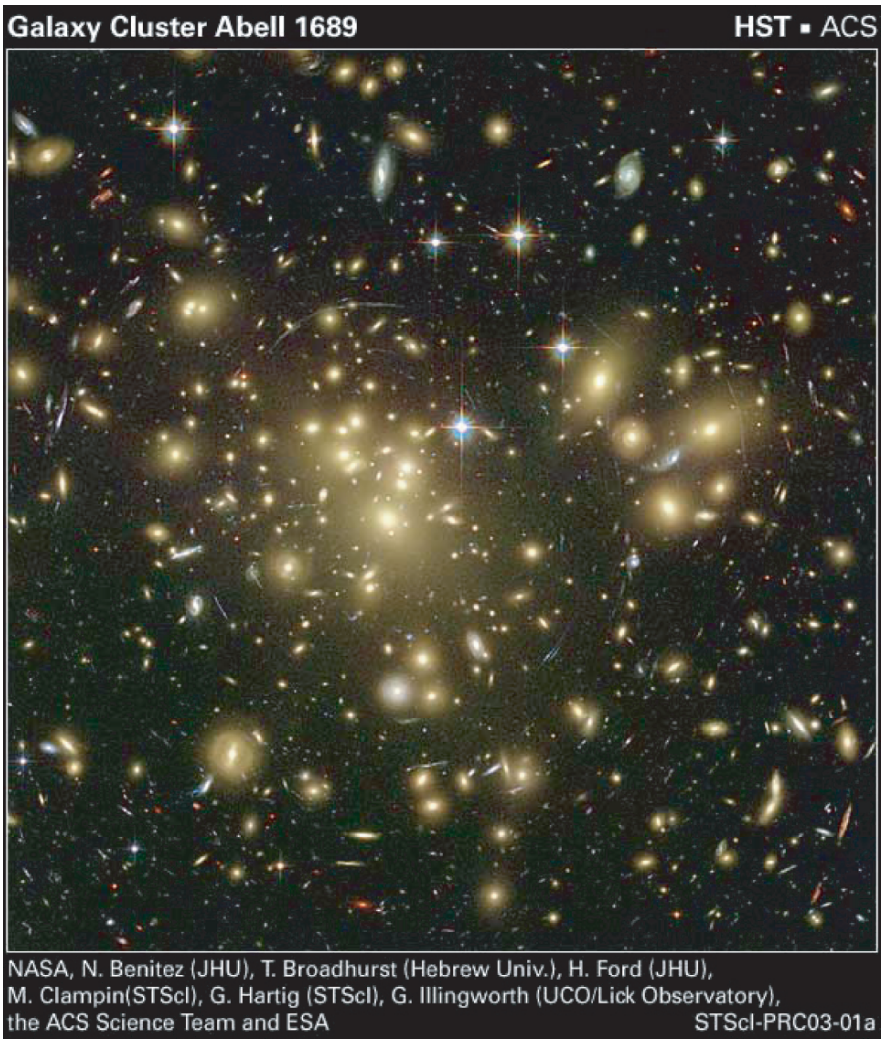

Fig. 14. The galaxy cluster Abell 1689 is the most impressive lensing cluster yet found. This image has been taken with the new Advanced Camera for Surveys (ACS) onboard HST. Numerous arcs are seen. A simple estimate for the mass of the center of the cluster, obtained by identifying the arcs radius with the Einstein radius, yields an extremely large equivalent velocity dispersion. The distribution of the arcs shown here indicates that such a simple assumption is misleading, and more detailed modeling required

Therefore, this simple estimate yields the mass inside the arc radius. However, this estimate is not very accurate, perhaps good to within ∼30% (Bartelmann and Steinmetz 1996). Its reliability depends on the level of asymmetry and substructure in the cluster mass distribution. Furthermore, it is likely

to overestimate the mass in the mean, since arcs preferentially occur along the major axis of clusters. Of course, the method is very difficult to apply if the center of the cluster is not readily identified or if the cluster is obviously bimodal. For these reasons, this simple method for mass estimates is not regarded as particularly accurate.

Detailed Modeling

The mass determination in cluster centers becomes much more accurate if several arcs and/or multiple images are present, since in this case, detailed modeling can be done. This typically proceeds in an interactive way: First, multiple images have to be identified (based on their colors and/or detailed morphology, as available with HST imaging). Simple (plausible) mass models are then assumed, with parameters fixed by matching the multiple images, and requiring the distortion at the arc location(s) to be strong and to have the correct orientation. This model then predicts the presence of possible further multiple images; they can be checked for through morphology, surface brightness (in particular if HST images of the cluster are available) and color. If confirmed, a new, refined model is constructed including these new additional strong lensing constraints, which yields further strong lensing predictions etc. As is the case for galaxy lensing (see SL), the components of the mass models are not arbitrary, but chosen to be physically motivated. Typically, as major component an ellipsoidal isothermal or NWF distribution is used to describe the overall mass distribution of the cluster. Refinements of the mass distribution are introduced as mass components centered on bright cluster member galaxies or on subgroups of such galaxies, describing massive subhalos which survived a previous merger. Such models have predictive power and can be trusted in quite some detail; the accuracy of mass estimates in some favorable cases can be as high as a few percent.

In fact, these models can be used to predict the redshift of arcs and arclets. As an example, we mention the strong lensing analysis of the cluster Abell 2390 based on HST imaging (Pelló et al. 1999). Two pairs of multiple images were identified (see Fig. 15) which then implies that the critical curve has to pass between the individual components. The location of the critical curves depends, however, on the source redshift. As shown in the figure, the sources have to be at a high redshift in order for the corresponding critical curves to have the correct location. In fact, spectroscopy placed the two sources at $z_\mathrm{s} = 4.04$ and $z_\mathrm{s} = 4.05$, as predicted by the lens model.

Since the distortion of a lens also depends on the source redshift, once a detailed mass model is available from arcs with known redshifts for at least some of them, one can estimate the value of the lens strength $\propto D_\mathrm{ds}/D_\mathrm{s}$ and thus infer the redshift of arclets. This method has been successfully applied to HST observations of clusters (Ebbels et al. 1998). Of course, having spectroscopic redshifts of the arcs available increases the calibration of the mass models; they are therefore very useful.

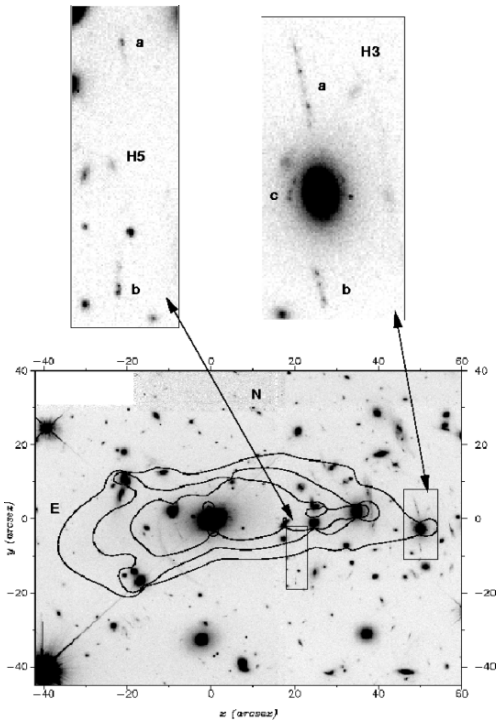

Fig. 15. The lower panel shows the critical curves of the cluster A 2390 (cluster redshift $z_\mathrm{d} = 0.231$), for three different source redshifts of $z_\mathrm{s} = 1$, 2.5 and 4 (from inner to outer). The lens model is based on the detailed HST image shown here. Identified are two sets of multiple images, shown in the upper two panels, which obviously need to be at very high redshift. Indeed, spectroscopy shows that they have $z_\mathrm{s} = 4.04$ and $z_\mathrm{s} = 4.05$ (from Pelló et al. 1999)

Lens Properties from Fourier Transforms

Before discussing results from these detailed models, a brief technical section shall be placed here, related to calculating lens properties of general mass distributions. A general method to obtain the lensing quantities of a mass distribution is through Fourier transformation. We assume that we have a mass distribution of finite mass; this is not a serious restriction even for models with formally infinite total mass, because we can truncate them on large scales, thus making the total mass finite, without affecting any lensing properties at smaller scales. We define the Fourier transform $\hat{\kappa}(\boldsymbol{\ell})$ of the surface mass density as[4]

$$\hat{\kappa}(\boldsymbol{\ell}) = \int_{\mathbb{R}^2} \mathrm{d}^2\theta \; \kappa(\boldsymbol{\theta}) \; \exp\left(\mathrm{i}\boldsymbol{\ell}\cdot\boldsymbol{\theta}\right) \; , \tag{36}$$

[4] We denote the Fourier variable of three-dimensional space as $\mathbf{k}$, that of angular position by $\boldsymbol{\ell}$.

and its inverse by

$$\kappa(\boldsymbol{\theta}) = \frac{1}{(2\pi)^2} \int_{\mathbb{R}^2} \mathrm{d}^2\ell\ \hat{\kappa}(\boldsymbol{\ell}) \exp\left(-\mathrm{i}\boldsymbol{\ell}\cdot\boldsymbol{\theta}\right)\ . \tag{37}$$

Similarly, we define the Fourier transforms of the deflection potential, $\hat{\psi}(\boldsymbol{\ell})$, of the deflection angle, $\hat{\boldsymbol{\alpha}}(\boldsymbol{\ell})$, and of the complex shear, $\hat{\gamma}(\boldsymbol{\ell})$. Differentiation by θ_i in real space is replaced by multiplication by $-\mathrm{i}\ell_i$ in Fourier space. Therefore, the Fourier transform of $\partial\psi/\partial\theta_j$ is $-\mathrm{i}\ell_j\hat{\psi}(\boldsymbol{\ell})$. Hence, the Poisson equation as given in Sect. 2.2 of IN becomes in Fourier space

$$-|\boldsymbol{\ell}|^2\hat{\psi}(\ell) = 2\hat{\kappa}(\boldsymbol{\ell})\ . \tag{38}$$

Thus, for $\boldsymbol{\ell} \neq \mathbf{0}$, the Fourier transform of the potential which satisfies the Poisson equation can be readily determined. The $\boldsymbol{\ell} = \mathbf{0}$ mode remains undetermined; however, since this mode corresponds to a constant in ψ, it is unimportant and can be set to zero. Once $\hat{\psi}$ is determined, the Fourier transform of the deflection angle and the shear follows from their definitions in terms of the deflection potential, given in Sect. 2.2 of IN,

$$\hat{\boldsymbol{\alpha}}(\boldsymbol{\ell}) = -\mathrm{i}\boldsymbol{\ell}\hat{\psi}(\boldsymbol{\ell})\ , \tag{39}$$

$$\hat{\gamma}(\boldsymbol{\ell}) = -\left(\frac{\ell_1^2 - \ell_2^2}{2} + \mathrm{i}\ell_1\ell_2\right)\hat{\psi}(\boldsymbol{\ell})\ . \tag{40}$$

Thus, in principle, one determines the relevant quantities by Fourier transforming κ, then calculating the Fourier transforms of the potential, deflection, and shear, whose real-space counterparts are then obtained from an inverse Fourier transform, like in (37).

Up to now we have not gained anything; the Fourier transforms as defined above are two-dimensional integrals, as are the real-space relations between deflection angle and shear, and the surface-mass density. However, provided κ becomes 'small enough' for large values of $|\boldsymbol{\theta}|$, the integral in (36) may be approximated by one over a finite region in $\boldsymbol{\theta}$-space. This finite integral is further approximated as a sum over gridpoints, with a regular grid covering the lens plane. Consider a square in the lens plane of side L, and let N be the number of gridpoints per dimension, so that $\Delta\theta = L/N$ is the size of a gridcell. The inverse grid, i.e., the $\boldsymbol{\ell}$-grid, has a gridcell of size $\Delta\ell = 2\pi/L$. The discrete Fourier transform then uses the values of κ on the $\boldsymbol{\theta}$-grid to calculate $\hat{\kappa}$ on the $\boldsymbol{\ell}$-grid. The latter, in fact, is then the Fourier transform of the periodic continuation of the mass distribution in $\boldsymbol{\theta}$-space. Because of this periodic continuation, the deflection angle as calculated from the discrete Fourier transform, which is performed by the Fast Fourier Transform (FFT) method, is the sum of the input mass distribution, plus all of its periodic continuation. Here, finally, is why we have considered the Fourier method: the FFT is a very efficient and quick procedure (see, e.g., Press et al. 1986), and arguably the best one in cases of mass distributions for which no analytical

progress can be made. The lensing properties are calculated on a grid; if needed, they can be obtained for other points by interpolation.

Because of the periodic continuation, the mass distribution has to decrease sufficiently quickly for large $|\boldsymbol{\theta}|$, or be truncated at large radii. In any case, L should be taken sufficiently large to minimize these periodicity effects.

Another point to mention is that a periodic mass distribution, each element of which has positive total mass, has an infinite mass, so that the deflection potential has to diverge; on the other hand, the deflection potential is enforced to be periodic. This apparent contradiction can be resolved by noting that the $\boldsymbol{\ell} = \mathbf{0}$ mode of $\hat{\kappa}$ is not used in the calculation of $\hat{\boldsymbol{\alpha}}$ and $\hat{\gamma}$. Indeed, if $\hat{\psi}$ and ψ are calculated from the above equations, then the resulting ψ *does not satisfy the Poisson equation*; the ψ resulting from this procedure is the one corresponding to $\kappa - \bar{\kappa}$, where $\bar{\kappa}$ is the average of κ on the $\boldsymbol{\theta}$-grid. A similar remark is true for the deflection angle. Thus, at the end, one has to add a term $\bar{\kappa}\,|\boldsymbol{\theta}|^2/2$ to ψ, and a term $\bar{\kappa}\boldsymbol{\theta}$ to $\boldsymbol{\alpha}$.

Since the FFT is very fast, one can choose N and L large, and then consider only the central part of the $\boldsymbol{\theta}$-grid needed for the actual lens modeling.

4.5 Results from Strong Lensing in Clusters

The main results of the strong lensing investigations of clusters can be summarized as follows:

- The mass in cluster centers is much more concentrated than predicted by (simple) models based on X-ray observations. The latter usually predict a relatively large core of the mass distribution. These large cores would render clusters sub-critical to lensing, i.e., they would be unable to produce giant arcs or multiple images. In fact, when arcs were first discovered they came as a big surprise because of these expectations. By now we know that the intracluster medium is much more complicated than assumed in these 'β-model' fits for the X-ray emission.
- The mass distribution in the inner region of clusters often shows strong substructure, or multiple mass peaks. These are also seen in the galaxy distribution of clusters, but with the arcs can be verified to also correspond to mass peaks (examples of this include the cluster Abell 2218 where arcs also curve around a secondary concentration of bright galaxies, clearly indicating the presence of a mass concentration, or the obviously bimodal cluster Abell 370). These are easily understood in the frame of hierarchical mergers in a CDM model; the merged clusters retain their multiple peaks for a dynamical time or even longer, and are therefore not in virial equilibrium.
- The orientation of the (dark) matter appears to follow closely the orientation of the light in the cD galaxy; this supports the idea that the growth of the cD galaxy is related to the cluster as a whole, through repeated accretion of lower-mass member galaxies. In that case, the cD galaxy 'knows' the orientation of the cluster.

- There is in general good agreement between lensing and X-ray mass estimates (e.g., Ettori and Lombardi 2003; Donahue et al. 2003) for those clusters where a 'cooling flow' indicates that they are in dynamical equilibrium, provided the X-ray analysis takes the presence of the cooling flow into account (Allen 1998).

Probably our 'favorite' clusters in which strong lensing effects are investigated in detail are biased in favor of having strong substructure, as this increases the lensing cross section for the occurrence of giant arcs (see below). Hence, it may be that the most detailed results obtained from strong lensing in clusters apply to a class of clusters which are especially selected because of their ability to produce spectacular arcs, and thus of their asymmetric mass distribution. Therefore, one must be careful in generalizing conclusions drawn from the 'arc clusters' to the cluster population as a whole.

Discrepancies

There are a few clusters where the lensing results and those obtained from analyzing the X-ray observations or cluster dynamics are in stong apparent conflict. Two of the most prominent ones shall be mentioned here. The cluster A 1689 (see Fig. 14) has arcs more than $\sim 40''$ away from the cluster center, which would imply a huge mass in this cluster center. This high mass is apparently confirmed by the high velocity dispersion of its member galaxies, although their distribution in redshift makes it likely that the cluster consists of several subcomponents (see Clowe and Schneider 2001 for a summary of these results). Several weak lensing results of this cluster have been published, and they are not all in agreement: whereas Tyson and Fischer (1995) from weak shear, and Taylor et al. (1998) and Dye et al. (2001) from the magnification method (that will be discussed in the next section) find also a very high mass for this cluster, the weak lensing analysis of Clowe and Schneider (2001; see also King et al. 2002b), based on deep wide-field imaging data of this cluster, finds a more moderate mass (or equivalent velocity dispersion) for this cluster. A new XMM-Newton X-ray observation of this cluster (Andersson and Madejski 2004) lends support for the smaller mass; in fact, their estimate of the virial mass of the cluster agrees with that obtained by Clowe and Schneider (2001). However, the disrepancy with the strong lensing mass in the cluster center remains at present; a quantitative analysis of the ACS data shown in Fig. 14 will hopefully shed light on this issue.

A second clear example for discrepant results in the cluster Cl 0024+17. It has a prominent arc system, indicating an Einstein radius of $\sim 30''$, and thus a high mass. The X-ray properties of this cluster, however, indicate a much smaller mass (Soucail et al. 2000), roughly by a factor of three. This discrepancy has been reaffirmed by recent Chandra observations, which confirmed this factor-of-three problem (Ota et al. 2004). The resolution of this discrepancy has probably been found by Czoske et al. (2001, 2002), who performed an extensive spectroscopic survey of cluster galaxies. Their result is

best interpreted such that Cl 0024+17 presents a merger of two clusters along our line-of-sight, which implies that the measured velocity dispersion cannot be easily turned into a mass, as this system is not in virial equailibrium, and that the X-ray data cannot be converted to a mass either, due to the likely strong deviation from spherical symmetry and equilibrium. A wide field sparsely sampled HST observation of this cluster (Kneib et al. 2003) also indicates the presence of a second mass concentration about $3'$ away from the main peak. As will be mentioned below, clusters undergoing mergers have particularly high cross sections for producing arcs (Torri et al. 2004); hence, our 'favorites' are most likely selected for these non-equilibrium clusters.

Arc Statistics

The abundance of arcs is expected to be a strong function of the cosmological parameters: they not only determine the abundance of massive clusters (through the mass function discussed in Sect. 4.5 of IN), but also the degree of relaxation of clusters, which in turn affects their strong lensing cross section (Bartelmann et al. 1998). It is therefore interesting to consider the expected abundance of arcs as a function of cosmological parameters and compare this to the observed abundance. In a series of papers, M. Bartelmann and his colleagues have studied the expected giant arc abundance, using analytical as well as numerical techniques (e.g., Bartelmann and Weiss 1994; Bartelmann et al. 1995, 1998, 2002; Meneghetti et al. 2005; see also Dalal et al. 2003; Oguri et al. 2003; Wambsganss et al. 2004). Some of the findings of these studies can be summarized as follows:

- The formation of arcs depends very sensitively on the deviation from spherical symmetry and the detailed substructure of the mass distribution in the cluster. For this reason, analytical models which cannot describe this substructure with sufficient realism (see Bergmann and Petrosian 1993) do not provide realiable predictions for the arc statistics (in particular, axisymmetric mass models are essentially useless for estimating arc statistics), and one needs to refer to numerical simulations of structure formation. Since the substructure and triaxiality plays such an important role, these simulations have to be of high spatial and mass resolution.
- The frequency of arcs depends of course on the abundance of clusters, which in turn depends on the cosmological model and the fluctuation spectrum of the matter, in particular its normalization σ_8. Furthermore, clusters at a given redshift have different mean ages in different cosmological models, as the history of structure growth, and thus the merging history, depends on Ω_m and Ω_Λ. Since the age of a cluster is one of the determining parameters for its level of substructure – younger clusters do not have had enough time to fully relax – this affects the lensing cross section of the clusters for arc formation. In fact, during epochs of mergers, the arc cross-section can have temporary excursions by large factors. Even the same cluster at the same epoch can have arc forming cross sections that vary by

more than an order-of-magnitude between different projection directions of the cluster. For fixed cluster abundance today, low-density models form clusters earlier than high-density models.

- Since the largest contribution of the total cross section for arc formation comes from clusters at intermediate redshift ($z \sim 0.4$), also the equation-of-state of the dark energy matters; as shown in Meneghetti et al. (2005), what matters is the dark energy density at the epoch of cluster formation. In addition, the earlier clusters form, the higher their characteristic density, which then makes them more efficient lenses for arc formation.

Taking these effects together, a low-density open model produces a larger number of arcs than a flat low-density model, which in turn has more arcs than a high-density model, for a given cluster abundance today. Whereas the differences between these models obtained by Meneghetti et al. (2005) are smaller than claimed in Bartelmann et al. (1998), they in principle allow constraining the cosmological parameters, provided they can be compared with the observed number of arcs.

Unfortunately, there are only a few systematic studies of clusters with regards to their strong lensing contents. Luppino et al. (1999) report on 8 giant arcs in their sample of the 38 most massive clusters found in the Einstein Medium Sensitivity Survey. Zaritsky and Gonzalez (2003) surveyed clusters in the redshift range $0.5 \lesssim z \lesssim 0.7$ over $69\,\mathrm{deg}^2$ and found two giant arcs with $R < 21.5$ and a length $\theta_1 > 10''$. Gladders at al. (2003) found 5 arc candidates in their Red Cluster Sequence survey of $90\,\mathrm{deg}^2$, all of them being associated with high-redshift clusters. In contrast to the claim by Bartelmann et al. (1998), these observered arc frequencies can be accounted for in a standard ΛCDM Universe, as shown by Dalal et al. (2003). There are several differences between these two studies, which are based on different assumptions about the number density of clusters and the source redshift distribution, which Dalal et al. (2003) took from the Hubble Deep Field, whereas Bartelmann et al. (1998) assumed all sources having $z_\mathrm{s} = 1$.

The strong dependence on the source redshift distribution has been pointed out by Wambsganss et al. (2004). In contrast to the other studies, they investigated the arc statistics using ray tracing through a three-dimensional mass distribution obtained from cosmological simulations, where- as the other studies mentioned considered the lensing effect of individual clusters found in these simulations. Although the former approach is more realistic, the assumption of Wambsganss et al. (2004) that the magnification of a light ray is a good measure for the length-to-width ratio of a corresponding arc is certainly not justified in detail, as shown in Dalal et al. (2003). The agreement of the lensing probability between Wambsganss et al. (2004) and Bartelmann et al. (1998) for all $z_\mathrm{s} = 1$ is therefore most likely a coincidence.

There are further difficulties in obtaining realistic predictions for the occurrence of giant arcs that can be compared with observations. First, the question of whether an image counts as an arc depends on a combination of source size, lens magnification, and seeing. Seeing makes arcs rounder and

therefore reduces their length-to-width ratio. An impressive demonstration of this effect is provided by the magnificent system of arcs in the cluster A 1689 observed with the ACS onboard the HST, as shown in Fig. 14, compared to earlier ground-based images of this cluster. Second, several of the above-mentioned papers assume the source size to be $\theta = 1''$, whereas many arcs observed with HST are essentially unresolved in width, implying much smaller source sizes (and accordingly, a much higher sensitivity to seeing effects). Third, magnification bias is usually not taken into account in these theoretical studies. In fact, accounting properly for the magnification bias is quite difficult, as the surveys reporting on arc statistics are not really flux-limited. One might argue that they are surface brightness-limited, but even if this were true, the surface brightness of an arc coming from a small source depends very much on the seeing.

Therefore at present, the abundance of arcs seem to be not in conflict with a ΛCDM model, but more realistic simulations which take the aforementioned effects into account are certainly needed for a definite conclusion on this issue. On the observational side, increasing the number of clusters for which high-quality imaging is performed is of great importance, and the survey of luminous X-ray clusters imaged either with the ACS@HST or with ground-based telescopes during periods of excellent seeing would improve the observational situation dramatically. Blank-field surveys, such as they are conducted for cosmic shear research (see Sect. 7), could be used for blind searches of arcs (that is, not restricted to regions around known clusters). It may turn out, however, that the number of 'false positives' is unacceptably high, e.g., by misidentification of edge-on spirals, or blends of sources that yield apparent images with a high length-to-width ratio.

Constraints on Collisional Dark Matter

Spergel and Steinhardt (2000) suggested the possibility that dark matter particles are not only weakly interacting, but may have a larger elastic scattering cross-section. If this cross-section of such self-interacting dark matter is sufficiently large, it may help to explain two of the remaining apparent discrepancies between the predictions of the Cold Dark Matter model and observations: The slowly rising rotation curves of dwarf galaxies (e.g., de Blok et al. 2001) and the substructure of galaxy-scale dark matter halos (see Sect. 8 of SL). Self-interacting may soften the strength of the central density concentration as compared to the NFW profile, and could destroy most of the subclumps. However, there are other consequence of such an interaction, in that the shapes of the inner parts of dark matter halos tend to be more spherical. Meneghetti et al. (2001) have investigated the influence of self interaction of dark matter particles on clusters of galaxies, in particular their ability to form giant arcs. From their numerical simulations of clusters with varying cross-sections of particles, they showed that even a relatively small cross-section is sufficient to reduce the ability of clusters to produce giant arcs by an order of magnitude.

This is mainly due to two effects, the reduced asymmetry of the resulting mass distribution and the shallower central density profile. Furthermore, self-interactions destroy the ability of clusters to form radial arcs. Therefore, the 'desired' effect of self-interaction – to smooth the mass distribution of galaxies – has the same consequence for clusters, and can therefore probably be ruled out as a possible mechanism to cure the aforementioned apparent problems of the CDM model. From combining X-ray and lensing data of the cluster 0657−56, Markevitch et al. (2004) obtained upper limits on the self-interaction cross section of dark matter.

Do Clusters Follow the Universal NFW Profile ?

The CDM paradigm of structure formation predict a universal density profile of dark matter halos. One might therefore investigate whether the strong lensing properties of clusters are compatible with this mass profile. Of particular value for such an investigation are clusters which contain several strong lensing features, and in particular a radial arc, as it probes the inner critical curve of the cluster. Sand et al. (2004; see also Sand et al. 2002) claim from a sample of three clusters with radial arcs, that the slope of the inner mass profile must be considerably flatter than predicted by the NFW model. However, this conclusion is derived under the assumption of an axially-symmetric lens model. As is true for strong lensing by galaxies (see SL), axisymmetric mass model are not generic, and therefore conclusions derived from them are prone to the systematic of the symmetry assumption. That was demonstrated by Bartelmann and Meneghetti (2004) who showed that, as expected, the conclusion about the inner slope changes radically once a finite ellipticity of the mass distribution is allowed for, removing the apparent discrepancy with the predictions from CDM models.

Cosmological Parameters from Strong Lensing Systems

The lens strength, at given physical surface mass density Σ, depends on the redshifts of lens and source, as well as on the geometry of the Universe which enters the distance-redshift relation. Therefore, it has been suggested that a cluster which contains a large number of strong lensing features can be used to constrain cosmological parameters, provided the sources of the arcs and multiple image systems cover a large range of redshifts (Link and Pierce 1998). Simulations of this effect, using realistic cluster models, confirmed that such purely geometrical constraints can in principle be derived (Golse et al. 2002). One of the best studied strong-lensing cluster up to now is A 2218, for which four multiple-image systems with measured (spectroscopic) redshift have been identified which allows very tight constraints on the mass distribution in this cluster. Soucail et al. (2004) applied the aforementioned method to this cluster and obtained first constraints on the density parameter $\Omega_{\rm m}$, assuming a flat cosmological model. This work can be viewed as a proof of concept; the new

ACS camera onboard HST will allow the identification of even richer strong lensing systems in clusters, of which the one in A 1689 (see Fig. 14) is a particularly impressive example.

5 Mass Reconstructions from Weak Lensing

Whereas strong lensing probes the mass distribution in the inner part of clusters, weak lensing can be used to study the mass distribution at much larger angular separations from the cluster center. In fact, as we shall see, weak lensing can provide a parameter-free reconstruction of the projected two-dimensional mass distribution in clusters – and hence offers the prospect of mapping the dark matter distribution of clusters directly. This discovery (Kaiser and Squires 1993) can be viewed to mark the beginning of quantitative weak lensing research. But even before this discovery, weak lensing by clusters has been observed in a number of cases. Fort et al. (1988) found that in addition to the giant arc in Abell 370, there are a number of images stretched in the direction tangent to the center of the cluster, but with much less spectacular axis ratios than the giant arc in this cluster; they termed these new features 'arclets'. Tyson et al. (1990) found a statistically significant tangential alignment of faint galaxy images relative to the center of the clusters Abell 1689 and Cl 1409+52, and obtained a mass profile from these lens distortion maps. Comparison with numerical simulations yielded an estimate of the cluster velocity dispersion, assuming an isothermal sphere profile.

In this section we consider the parameter-free mass reconstruction technique, first the original Kaiser and Squires method, and then a number of improvements of this method. We then turn to the magnification effects; the change of the number density of background sources, as predicted from (26), can be turned into a local estimate of the surface mass density, and this method has been employed in a number of clusters. Next we shall consider inverse methods for the reconstruction of the mass distribution, which on the one hand are more difficult to apply than the 'direct' methods, but on the other hand are expected to yield more satisfactory results. Whereas the two-dimensional maps yield a good visual impression on the mass distribution in clusters, it is hard to extract quantitative information from them. In order to get quantities that describe the mass and that can be compared between clusters, often parameterized mass models are more useful, which are considered next. Finally, we consider aperture mass measures, which have been introduced originally to obtain a mass quantity that is unaffected by the mass-sheet degeneracy, but as will be shown, has a number of other useful features. In particular, employing the aperture mass, one can device a method to systematically search for mass concentrations on cluster-mass scales, using their shear properties only, i.e. without referring to their luminous properties.

5.1 The Kaiser–Squires Inversion

Weak lensing yields an estimate of the local (reduced) shear, as discussed in Sect. 2.2. Here we shall discuss how to derive the surface mass density from a measurement of the (reduced) shear. Recalling (IN-26), the relation between shear and surface mass density is

$$\gamma(\boldsymbol{\theta}) = \frac{1}{\pi}\int_{\mathbb{R}^2} \mathrm{d}^2\theta'\, \mathcal{D}(\boldsymbol{\theta}-\boldsymbol{\theta}')\,\kappa(\boldsymbol{\theta}')\;, \quad \text{with}$$

$$\mathcal{D}(\boldsymbol{\theta}) \equiv -\frac{\theta_1^2-\theta_2^2+2\mathrm{i}\theta_1\theta_2}{|\boldsymbol{\theta}|^4} = \frac{-1}{(\theta_1-\mathrm{i}\theta_2)^2}\;. \tag{41}$$

Hence, the complex shear γ is a convolution of κ with the kernel $\mathcal{D}$, or, in other words, $\mathcal{D}$ describes the shear generated by a point mass. This relation can be inverted: in Fourier space this convolution becomes a multiplication,

$$\hat{\gamma}(\boldsymbol{\ell}) = \pi^{-1}\hat{\mathcal{D}}(\boldsymbol{\ell})\,\hat{\kappa}(\boldsymbol{\ell}) \quad \text{for} \quad \boldsymbol{\ell}\neq\mathbf{0}\;,$$

which can be inverted to yield

$$\hat{\kappa}(\boldsymbol{\ell}) = \pi^{-1}\hat{\gamma}(\boldsymbol{\ell})\,\hat{\mathcal{D}}^*(\boldsymbol{\ell}) \quad \text{for} \quad \boldsymbol{\ell}\neq\mathbf{0}\;, \tag{42}$$

where the Fourier transform of $\mathcal{D}$ is[5]

$$\hat{\mathcal{D}}(\boldsymbol{\ell}) = \pi\frac{\left(\ell_1^2-\ell_2^2+2\mathrm{i}\ell_1\ell_2\right)}{|\boldsymbol{\ell}|^2}\;; \tag{43}$$

note that this implies that $\hat{\mathcal{D}}(\boldsymbol{\ell})\hat{\mathcal{D}}^*(\boldsymbol{\ell}) = \pi^2$, which has been used in obtaining (42). It is obvious that $\hat{\mathcal{D}}$ is undefined for $\boldsymbol{\ell}=\mathbf{0}$, which has been indicated in the foregoing equations. Fourier back-transformation of (42) then yields

$$\kappa(\boldsymbol{\theta})-\kappa_0 = \frac{1}{\pi}\int_{\mathbb{R}^2}\mathrm{d}^2\theta'\,\mathcal{D}^*(\boldsymbol{\theta}-\boldsymbol{\theta}')\,\gamma(\boldsymbol{\theta}')$$

$$= \frac{1}{\pi}\int_{\mathbb{R}^2}\mathrm{d}^2\theta'\,\mathcal{R}\mathrm{e}\left[\mathcal{D}^*(\boldsymbol{\theta}-\boldsymbol{\theta}')\,\gamma(\boldsymbol{\theta}')\right]\;. \tag{44}$$

Note that the constant κ_0 occurs since the $\boldsymbol{\ell}=\mathbf{0}$-mode is undetermined. Physically, this is related to the fact that a uniform surface mass density yields no shear. Furthermore, it is obvious (physically, though not so easily seen mathematically) that κ must be real; for this reason, the imaginary part

[5] The form of $\hat{\mathcal{D}}$ can be obtained most easily by using the relations between the surface mass density and the shear components in terms of the deflection potential ψ, given in (IN-18). Fourier transforming those immediately yields $\hat{\kappa} = -|\boldsymbol{\ell}|^2\hat{\psi}/2$, $\hat{\gamma}_1 = -(\ell_1^2-\ell_2^2)\hat{\psi}/2$, $\hat{\gamma}_2 = -\ell_1\ell_2\hat{\psi}$. Eliminating $\hat{\psi}$ from the foregoing relations, the expression for $\hat{\mathcal{D}}$ is obtained.

of the integral should be zero, and taking the real-part only [as in the second line of (44)] makes no difference. However, in practice this is different, since noisy data, when inserted into the inversion formula, will produce a non-zero imaginary part. What (44) shows is that if γ can be measured, κ can be determined.

Before looking at this in more detail, we briefly mention some difficulties with the inversion formula as given above:

- Since γ can at best be estimated at discrete points (galaxy images), smoothing is required. One might be tempted to replace the integral in (44) by a discrete sum over galaxy positions, but as shown by Kaiser and Squires (1993), the resulting mass density estimator has infinite noise (due to the θ^{-2}-behavior of the kernel $\mathcal{D}$).
- It is not the shear γ, but the reduced shear g that can be determined from the galaxy ellipticities; hence, one needs to obtain a mass density estimator in terms of g. In the case of 'weak' weak lensing, i.e., where $\kappa \ll 1$ and $|\gamma| \ll 1$, then $\gamma \approx g$.
- The integral in (44) extends over $\mathbb{R}^2$, whereas data are available only on a finite field; therefore, it needs to be seen whether modifications allow the construction of an estimator for the surface mass density from finite-field shear data.
- To get absolute values for the surface mass density, the additive constant κ_0 is of course a nuisance. As will be explained soon, this indeed is the largest problem in mass reconstructions, and is the *mass-sheet degeneracy* discussed in Sect. 2.5 of IN.

5.2 Improvements and Generalizations

Smoothing

Smoothing of data is needed to get a shear field from discrete data points. Consider first the case that we transform (44) into a sum over galaxy images (ignoring the constant κ_0 for a moment, and also assuming the weak lensing case, $\kappa \ll 1$, so that the expectation value of ϵ is the shear γ),

$$\kappa_{\rm disc}(\boldsymbol{\theta}) = \frac{1}{n\,\pi} \sum_i \mathcal{R}{\rm e}\left[\mathcal{D}(\boldsymbol{\theta} - \boldsymbol{\theta}_i)\,\epsilon_i\right] \ , \tag{45}$$

where the sum extends over all galaxy images at positions $\boldsymbol{\theta}_i$ and complex ellipticity ϵ_i, and n is the number density of background galaxies. As shown by Kaiser and Squires (1993), the variance of this estimator for κ diverges. However, one can smooth this estimator, using a weight function $W(\Delta\theta)$ (assumed to be normalized to unity), to obtain

$$\kappa_{\rm smooth}(\boldsymbol{\theta}) = \int {\rm d}^2\theta'\ W(|\boldsymbol{\theta} - \boldsymbol{\theta}'|)\,\kappa_{\rm disc}(\boldsymbol{\theta}') \ , \tag{46}$$

which now has a finite variance. One might expect that, since (i) smoothing can be represented by a convolution, (ii) the relation between κ and γ is a convolution, and (iii) convolution operations are transitive, it does not matter whether the shear field is smoothed first and inserted into (44), or one uses (46) directly. This statement is true if the smoothing of the shear is performed as

$$\gamma_{\rm smooth;1}(\boldsymbol{\theta}) = \frac{1}{n}\sum_i W(|\boldsymbol{\theta}-\boldsymbol{\theta}_i|)\,\epsilon_i\ . \tag{47}$$

If this expression is inserted into (44), one indeed recovers the estimate (46). However, this is not a particularly good method for smoothing, as can be seen as follows: the background galaxy positions will at least have Poisson noise; in fact, since the angular correlation function even of faint galaxies is non-zero, local number density fluctuations will be larger than predicted from a Poisson distribution. However, in the estimator (45) and in the smoothing procedure (47), these local variations of the number density are not taken into account. A much better way (Seitz and Schneider 1995a,b) to smooth the shear is given by

$$\gamma_{\rm smooth;2}(\boldsymbol{\theta}) = \left[\sum_i W(|\boldsymbol{\theta}-\boldsymbol{\theta}_i|)\right]^{-1} \sum_i W(|\boldsymbol{\theta}-\boldsymbol{\theta}_i|)\,\epsilon_i\ , \tag{48}$$

which takes these local number density fluctuations into account. Lombardi and Schneider (2001) have shown that the expectation value of the smoothed shear estimate (48) is not exactly the shear smoothed by the kernel W, but the deviation (i.e., the bias) is very small provided the effective number of galaxy images inside the smoothing function W is substantially larger than unity, which will always be the case for realistic applications. Lombardi and Schneider (2002) then have demonstrated that the variance of (48) is indeed substantially reduced compared to that of (47), in agreement with the finding of Seitz and Schneider (1995a,b).

When smoothed with a Gaussian kernel of angular scale $\theta_{\rm s}$, the covariance of the resulting mass map is finite, and given by (Lombardi and Bertin 1998; van Waerbeke 2000)

$$\mathrm{Cov}\left(\kappa(\boldsymbol{\theta}),\kappa(\boldsymbol{\theta}')\right) = \frac{\sigma_\epsilon^2}{4\pi\theta_{\rm s}^2 n}\exp\left(-\frac{|\boldsymbol{\theta}-\boldsymbol{\theta}'|^2}{2\theta_{\rm s}^2}\right)\ . \tag{49}$$

Thus, the larger the smoothing scale, the less noisy is the corresponding mass map; on the other hand, the more are features washed out. Choosing the appropriate smoothing scale is not easy; we shall come back to this issue in Sect. 5.3 below.

The Non-linear Case, $g \neq \gamma$

Noting that the reduced shear $g = \gamma/(1-\kappa)$ can be estimated from the ellipticity of images (assuming that we avoid the potentially critical inner

region of the cluster, where $|g| > 1$; indeed, this case can also be taken into account, at the price of somewhat increased complexity), one can write:

$$\kappa(\boldsymbol{\theta}) - \kappa_0 = \frac{1}{\pi} \int_{\mathbb{R}^2} \mathrm{d}^2\theta' \, \left[1 - \kappa(\boldsymbol{\theta}')\right] \, \mathcal{R}\mathrm{e}\left[\mathcal{D}^*(\boldsymbol{\theta} - \boldsymbol{\theta}') \, g(\boldsymbol{\theta}')\right] \; ; \tag{50}$$

this integral equation for κ can be solved by iteration, and it converges quickly (Seitz and Schneider 1995a,b). Note that in this case, the undetermined constant κ_0 no longer corresponds to adding a uniform mass sheet. What the arbitrary value of κ_0 corresponds to can be seen as follows: The transformation

$$\begin{aligned} \kappa(\boldsymbol{\theta}) \rightarrow \kappa'(\boldsymbol{\theta}) = \lambda\kappa(\boldsymbol{\theta}) + (1 - \lambda) \quad \text{or} \\ [1 - \kappa'(\boldsymbol{\theta})] = \lambda[1 - \kappa(\boldsymbol{\theta})] \end{aligned} \tag{51}$$

changes the shear $\gamma \rightarrow \gamma' = \lambda\gamma$, and thus leaves g invariant; this is the mass-sheet degeneracy ! It can be broken if magnification information can be obtained, since $\mathcal{A} \rightarrow \mathcal{A}' = \lambda\mathcal{A}$, so that

$$\mu \rightarrow \mu' = \lambda^{-2}\mu \; .$$

Magnification information can be obtained from the number counts of images (Broadhurst et al. 1995), owing to the magnification bias, provided the unlensed number density is sufficiently well known. In principle, the mass sheet degeneracy can also be broken if redshift information of the source galaxies is available and if the sources are widely distributed in redshift; this can be seen as follows: let

$$Z(z_\mathrm{s}) = \frac{D_\mathrm{ds}/D_\mathrm{s}}{\lim_{z_\mathrm{s}\rightarrow\infty} D_\mathrm{ds}/D_\mathrm{s}} \, \mathrm{H}(z_\mathrm{s} - z_\mathrm{d}) \tag{52}$$

(H being the Heaviside step function) be the ratio of the lens strength of a source at z_s to that of a fiducial source at infinite redshift (see Fig. 16); then, if κ_∞ and γ_∞ denote the surface mass density and shear for such a fiducial source, the reduced shear for a source at z_s is

$$g = \frac{Z\gamma_\infty}{1 - Z\kappa_\infty} \; , \tag{53}$$

and there is no global transformation of κ_∞ that leaves g invariant for sources at all redshifts, showing the validity of the above statement. However, even in this case the mass-sheet degeneracy is only mildly broken (see Bradac et al. 2004). In particular, only those regions in the cluster where the non-linearity (i.e., the difference between γ and g) is noticeable can contribute to the degeneracy breaking, that is, the region near the critical curves where $|g| \sim 1$.

In the non-linear case ($\gamma \neq g$) the reduced shear needs to be obtained from smoothing the galaxy ellipticities in the first place. Since the relation between

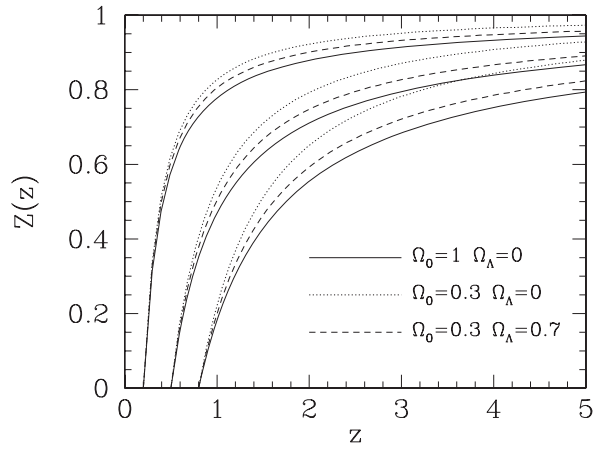

Fig. 16. The redshift weight function $Z(z_\mathrm{s})$, defined in (52), for three different values of the lens redshift $z_\mathrm{d} = 0.2$, 0.5, and 0.8, and three different geometries of the Universe, as indicated in the labels (here, Ω_m is denoted as Ω_0). Asymptotically for $z_\mathrm{s} \to \infty$, all curves tend to $Z = 1$ (from Bartelmann and Schneider 2001)

g and κ is non-linear, the 'transitivity of convolutions' no longer applies; one thus cannot start from a discretization of an integral over image ellipticities and smooth the resulting mass map later. We also note that the accuracy with which the (reduced) shear is estimated can be improved provided redshift estimates of individual source galaxies are available (see Fig. 17). In particular for high-redshift clusters, redshift information on individual source galaxies becomes highly valuable. This can be understood by considering a high-redshift lens, where an appreciable fraction of faint 'source' galaxies are located in front of the lens, and thus do not contribute to the lensing signal. However, they do contribute to the noise of the measurement. Redshift information allows the elimination of these foreground galaxies in the shear estimate and thus the reduction of noise.

Finite-Field Mass Reconstruction

In order to obtain a mass map from a finite data field, one starts from the relation (Kaiser 1995)

$$\nabla\kappa = \begin{pmatrix} \gamma_{1,1} + \gamma_{2,2} \\ \gamma_{2,1} - \gamma_{1,2} \end{pmatrix} \equiv \mathbf{u}_\gamma(\boldsymbol{\theta}) \;, \tag{54}$$

which is a *local* relation between shear and surface mass density; it can easily be derived from the definitions of κ and γ in terms of $\psi_{,ij}$. A similar relation can be obtained in terms of reduced shear,

$$\nabla K(\boldsymbol{\theta}) = \frac{-1}{1 - g_1^2 - g_2^2} \begin{pmatrix} 1 - g_1 & -g_2 \\ -g_2 & 1 + g_1 \end{pmatrix} \begin{pmatrix} g_{1,1} + g_{2,2} \\ g_{2,1} - g_{1,2} \end{pmatrix} \equiv \mathbf{u}_g(\boldsymbol{\theta}) \;, \tag{55}$$

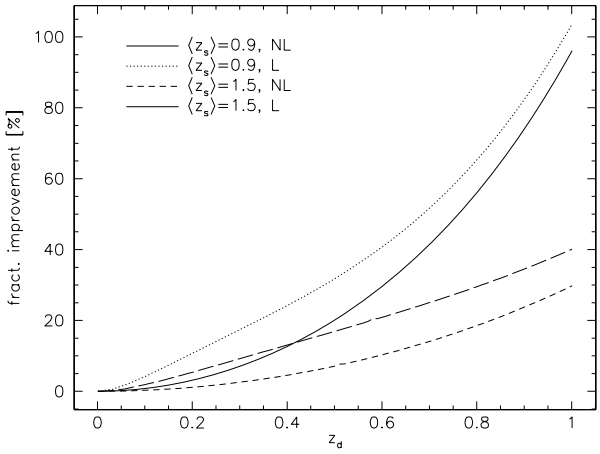

Fig. 17. The fractional gain in accuracy of the shear estimate when using redshift information of individual source galaxies, relative to the case where only the redshift distribution of the population is known, plotted as a function of the lens redshift. It is assumed that the sources have a broad redshift distribution, with a mean of $\langle z_{\rm s}\rangle = 0.9$ (*solid and dotted curves*) or $\langle z_{\rm s}\rangle = 1.5$ (*short-dashed and long-dashed curves*). The gain of accuracy also depends on the lens strength; the dotted and long-dashed curves assume local lens parameters of $\gamma_\infty = 0.3 = \kappa_\infty$, whereas the solid and short-dashed curves assume only very weak lensing, here approximated by $\gamma_\infty = 0 = \kappa_\infty$. One sees that the gain is dramatic once the lens redshift becomes comparable to the mean redshift of the source galaxies and is therefore of great importance for high-redshift clusters (from Bartelmann and Schneider 2001)

where

$$K(\boldsymbol{\theta}) \equiv \ln[1-\kappa(\boldsymbol{\theta})] \tag{56}$$

is a non-linear function of κ. Based on these local relations, finite-field inversion relations can be derived, and several of them appeared in the literature right after the foregoing equations have been published. For example, it is possible to obtain finite-field mass maps from line integrations (Schneider 1995; for other methods, see Squires and Kaiser 1996). Of all these finite-field methods, one can be identified as optimal, by the following reasoning: in the case of noise-free data, the imaginary part of (44) should vanish. Since one is always dealing with noisy data (at least coming from the finite intrinsic ellipticity distribution of the sources), in real life the imaginary part of (44) will not be zero. But being solely a noise component, one can choose that finite-field inversion which yields a zero imaginary component when averaged over the data field (Seitz and Schneider 1996). One way of deriving this mass map is obtained by a further differentiation of (54); this then yields a von Neumann boundary-value problem on the data field $\mathcal{U}$ (Seitz and Schneider 2001),

$$\nabla^2\kappa = \nabla\cdot\mathbf{u}_\gamma \quad \text{with} \quad \mathbf{n}\cdot\nabla\kappa = \mathbf{n}\cdot\mathbf{u}_\gamma \quad \text{on} \quad \partial\mathcal{U}\,, \tag{57}$$

where $\mathbf{n}$ is the outward-directed normal on the boundary $\partial\mathcal{U}$ of $\mathcal{U}$. The analogous equation holds for K in terms of g and $\mathbf{u}_g$,

$$\nabla^2 K = \nabla\cdot\mathbf{u}_g \quad \text{with} \quad \mathbf{n}\cdot\nabla K = \mathbf{n}\cdot\mathbf{u}_g \quad \text{on} \quad \partial\mathcal{U}\,. \tag{58}$$

Note that (57) determines the solution κ only up to an additive constant, and (58) determines K only up to an additive constant, i.e., $(1-\kappa)$ up to a multiplicative factor. Hence, in both cases we recover the mass-sheet degeneracies for the linear and non-linear case, respectively. The numerical solution of these equations is fast, using overrelaxation (see Press et al. 1992). In fact, the foregoing formulation of the problem is equivalent (Lombardi and Bertin 1998) to the minimization of the action

$$A = \int_{\mathcal{U}} \mathrm{d}^2\theta\, |\nabla\kappa(\boldsymbol{\theta}) - \mathbf{u}_\gamma(\boldsymbol{\theta})|^2\,, \tag{59}$$

from which the von Neumann problem can be derived as the Euler equation of the variational principle $\delta A = 0$. Furthermore, Lombardi and Bertin (1998) have shown that the solution of (57) is 'optimal', in that for this estimator the variance of κ is minimized.

Since (57) provides a linear relation between the shear and the surface mass density, one expects that it can also be written in the form

$$\kappa(\boldsymbol{\theta}) = \int_{\mathcal{U}} \mathrm{d}^2\theta'\, \mathbf{H}(\boldsymbol{\theta};\boldsymbol{\theta}')\cdot\mathbf{u}_\gamma(\boldsymbol{\theta}')\,, \tag{60}$$

where the vector field $\mathbf{H}(\boldsymbol{\theta};\boldsymbol{\theta}')$ is the Green's function of the von Neumann problem (57). Accordingly,

$$K(\boldsymbol{\theta}) = \int_{\mathcal{U}} \mathrm{d}^2\theta'\, \mathbf{H}(\boldsymbol{\theta};\boldsymbol{\theta}')\cdot\mathbf{u}_g(\boldsymbol{\theta}')\,. \tag{61}$$

Seitz and Schneider (1996) gave explicit expression for $\mathbf{H}$ in the case of a circular and rectangular data field.

One might ask how important the changes in the resulting mass maps are compared to the Kaiser–Squires formula applied to a finite data field. For that we note that applying (44) or (50) to a finite data field is equivalent to setting the shear outside the data field to zero. Hence, the resulting mass distribution will be such as to yield a zero shear outside the data field, despite the fact that we have no indication from data that the shear indeed is zero there. This induces features in the mass map, in form of a pillow-like overall mass distribution. The amplitude of this feature depends on the strength of the lens, its location inside the data field, and in particular the size of the data field. Whereas for large data fields this amplitude is small compared to the noise amplitude of the mass map, it is nevertheless a systematic that can easily be avoided, and should be avoided, by using the finite-field inversions, which cause hardly any additional technical problems.

Various tests have been conducted in the literature as to the accuracy of the various inversions. For those, one generates artificial shear data from a known mass distribution, and compares the mass maps reconstructed with the various methods with the original (e.g., Seitz and Schneider 1996, 2001; Squires and Kaiser 1996). One of the surprising results of such comparisons is that in some cases, the Kaiser and Squires original reconstruction faired better than the explicit finite-field inversions, although it is known to yield systematics. The explanation for this apparent paradox is, however, easy: the mass models used in these test consisted of one or more localized mass peaks well inside the data field, so the shear outside the data field is very small. Noting that the KS formula applied to a finite data field is equivalent to setting $\gamma = 0$ outside the data field, this methods provides 'information' to the reconstruction process which is not really there, but for the mass models used in the numerical tests is in fact close to the truth. Of course, by adding this nearly correct 'information' to the mass reconstruction, the noise can be lowered relative to the finite-field reconstructions where no assumptions about the shear field outside the data field is made.

Constraints on the Geometry of the Universe from Weak Lensing Mass Reconstructions

The strength of the lensing signal depends, for a given lens redshift, on the redshift of the sources, through the function $Z(z_\mathrm{s})$ (52). Suppose that the surface mass density of a cluster was well known, and that the redshifts of background sources can be determined. Then, by comparing the measured shear signal from sources at a given redshift z_s with the one expected from the mass distribution, the value of $Z(z_\mathrm{s})$ can be determined. Since $Z(z)$ depends on the geometry of the Universe, parameterized through Ω_m and Ω_Λ, these cosmological parameters can in principle be determined. A similar strategy for strong lensing clusters was described at the end of Sect. 4.

Of course, the surface mass density of the cluster cannot be assumed to be known, but needs to be reconstructed from the weak lensing data itself. Consider for a moment only the amplitude of the surface mass density, assuming that its shape is obtained from the reconstruction. Changing the function $Z(z)$ by a multiplicative factor would be equivalent to changing the surface mass density Σ of the cluster by the inverse of this factor, and hence such a constant factor in Z is unobservable due to the mass-sheet degeneracy. Hence, not the amplitude of the function $Z(z)$ shown in Fig. 16 is important here, but its shape.

Lombardi and Bertin (1999) have suggested a method to perform cluster mass reconstructions and at the same time determine the cosmological parameters by minimizing the difference between the shear predicted from the reconstructed mass profile and the observed image ellipticities, where the former depends on the functional form of $Z(z)$. A nice and simple way to illustrate such a method was given in Gautret et al. (2000), called the 'triplet

method'. Consider three background galaxies which have a small separation on the sky, and assume to know the three source redshifts. Because of their closeness, one might assume that they all experience the same tidal field and surface mass density from the cluster. In that case, the shear of the three galaxies is described by five parameters, the two components of γ_∞, κ, and Ω_m and Ω_Λ. From the six observables (two components of three galaxy ellipticities), one can minimize the difference between the predicted shear and the observed ellipticities with respect to these five parameters, and in particular obtain an estimate for the cosmological parameters. Repeating this process for a large number of triplets of background galaxies, the accuracy on the Ω's can be improved, and results from a large number of clusters can be combined.

This procedure is probably too simple to be applied in practice; in particular, it treats κ_∞ and γ_∞ for each triplet as independent numbers, whereas the mass profile of the cluster is described by a single scalar function. However, it nicely illustrates the principle. Lombardi and Bertin (1999) have used a single density profile $\kappa_\infty(\boldsymbol{\theta})$ of the cluster, but assumed that the mass-sheet degeneracy is broken by some other means. Jain and Taylor (2003) suggested a similar technique for employing the lensing strength as a function of redshifts and cosmological parameters to infer constraints on the latter. Clearly, more work is needed in order to turn these useful ideas into a practically applicable method.

5.3 Inverse Methods

In addition to these 'direct' methods for determining κ, inverse methods have been developed, such as a maximum-likelihood fit (Bartelmann et al. 1996; Squires and Kaiser 1996) to the data. There are a number of reasons why these are in principle preferable to the direct method discussed above. First, in the direct methods, the smoothing scale is set arbitrarily, and in general kept constant. It would be useful to obtain an objective way how this scale should be chosen, and perhaps, that the smoothing scale be a function of position: e.g., in regions with larger number densities of sources, the smoothing scale could be reduced. Second, the direct methods do not allow additional input coming from complementary observations; for example, if both shear and magnification information are available, the latter could not be incorporated into the mass reconstruction. The same is true for clusters where strong lensing constraints are known.

The Shear Likelihood Function

In the inverse methods, one tries to fit a (very general) lens model to the observational data, such that the data agree within the estimated errors with the model. In the maximum-likelihood methods, one parameterizes the lens by the deflection potential ψ on a grid and then minimizes the regularized log-likelihood

$$-\ln\mathcal{L} = \sum_{i=1}^{N_\mathrm{g}} \frac{|\epsilon_i - g\,(\boldsymbol{\theta}_i, \{\psi_n\})\,|^2}{\sigma_i^2\,(\boldsymbol{\theta}_i, \{\psi_n\})} + 2\ln\sigma_i(\boldsymbol{\theta}_i, \{\psi_n\}) + \lambda_\mathrm{e} S(\{\psi_n\})\;, \qquad (62)$$

where $\sigma_i \approx \sigma_\epsilon \left(1 - |g(\boldsymbol{\theta}_i, \{\psi_n\})|^2\right)$ [see (15) for the case $|g| < 1$ that was assumed here], with respect to these gridded ψ-values; this specific form of the likelihood assumes that the intrinsic ellipticity distribution follows a Gaussian with width σ_ϵ.[6] In order to avoid overfitting, one needs a regularization term S; entropy regularization (Seitz et al. 1998) seems very well suited (see Bridle et al. 1998; Marshall et al. 2002 for alternative regularizations). The entropy term S gets large if the mass distribution has a lot of structure; hence, in minimizing (62) one tries to match the data as closely as permitted by the entropic term (Narayan and Nityananda 1986). As a result, one obtains a model as smooth as compatible with the data, but where structure shows up where the data require it. The parameter λ_e is a Langrangean multiplier which sets the relative weight of the likelihood function and the regularization; it should be chosen such that the χ^2 per galaxy image is about unity, i.e.,

$$\sum_{i=1}^{N_\mathrm{g}} \frac{|\epsilon_i - g\,(\boldsymbol{\theta}_i, \{\psi_n\})\,|^2}{\sigma_i^2\,(\boldsymbol{\theta}_i, \{\psi_n\})} \approx N_\mathrm{g}\;,$$

since then the deviation of the observed galaxy ellipticities from their expectation value g is as large as expected from the ellipticity dispersion. This choice of the regularization parameter λ_e then fixes the effective smoothing used for the reconstruction.

Strong lensing constraints can be incorporated into the inverse method by adding a term to the log-likelihood function which forces the minimum to satisfy these strong constraints nearly precisely. E.g., if a pair of multiple images at $\boldsymbol{\theta}_1$ and $\boldsymbol{\theta}_2$ is identified, one could add the term

$$\lambda_\mathrm{s}\,|\boldsymbol{\beta}(\boldsymbol{\theta}_1) - \boldsymbol{\beta}(\boldsymbol{\theta}_2)|^2 = \lambda_\mathrm{s}\,|[\boldsymbol{\theta}_1 - \boldsymbol{\alpha}(\boldsymbol{\theta}_1)] - [\boldsymbol{\theta}_2 - \boldsymbol{\alpha}(\boldsymbol{\theta}_2)]|^2$$

to the log-likelihood; by turning up the parameter λ_s, its minimum is guaranteed to correspond to a solution where the multiple image constraint is satisfied. Note that the form of this 'source-plane minimization' is simplified – see Sect. 4.6 of SL – but in the current context this approach suffices.

[6] This specific form (62) of the likelihood function assumes that the sheared ellipticity probability distribution follows a two-dimensional Gaussian with mean g and dispersion σ; note that this assumption is not valid in general, not even when the intrinsic ellipticity distribution is Gaussian (see Geiger and Schneider 1999 for an illustration of this fact). The exact form of the lensed ellipticity distribution follows from the intrinsic distribution $p_\mathrm{s}(\epsilon^{(\mathrm{s})})$ and the transformation law (12) between intrinsic and lensed ellipticity, $p(\epsilon) = p_\mathrm{s}\left(\epsilon^{(\mathrm{s})}(\epsilon; g)\right) \det\left(\partial\epsilon^{(\mathrm{s})}/\partial\epsilon\right)$. However, in many cases the Gaussian approximation underlying (62) is sufficient and convenient for analytical considerations.

Magnification Likelihood

Similarly, when accurate number counts of faint background galaxies are available, the magnification information can be incorporated into the log-likelihood function. If the number counts behave (locally) as a power law, $n_0(>S) \propto S^{-\alpha}$, the expected number of galaxies on the data field $\mathcal{U}$ then is

$$\langle N\rangle = n_0 \int_{\mathcal{U}} \mathrm{d}^2\theta\, |\mu(\boldsymbol{\theta})|^{\alpha-1}\;; \tag{63}$$

see (26). The likelihood of observing N galaxies at the positions $\boldsymbol{\theta}_i$ can then be factorized into a term that yields the probability of observing N galaxies when the expected number is $\langle N\rangle$, and one that the N galaxies are at their observed locations. Since the probability for a galaxy to be at $\boldsymbol{\theta}_i$ is proportional to the expected number density there, $n = n_0\,\mu^{\alpha-1}$, the likelihood function becomes (Seitz et al. 1998)

$$\mathcal{L}_\mu = P_N\left(\langle N\rangle\right) \prod_{i=1}^{N} |\mu(\boldsymbol{\theta}_i)|^{\alpha-1}\;, \tag{64}$$

with the first factor yielding the Poisson probability. Note that this expression assumes that the background galaxies are unclustered on the sky; in reality, where (even faint) galaxies cluster, this factorization does not strictly apply.

It should be pointed out that the deflection potential ψ, and not the surface mass density κ, should be used as variable on the grid, for two reasons: first, shear and κ depend locally on ψ, and are thus readily calculated by finite differencing from ψ, whereas the relation between γ and κ is non-local and requires summation over all gridpoints, which is of course more time consuming. Second, and more important, the surface mass density on a finite field *does not* determine γ on this field, since mass outside the field contributes to γ as well. In fact, one can show (Schneider and Bartelmann 1997) that the shear inside a circle is fully determined by the mass distribution inside the circle and the multipole moments of the mass distribution outside the circle; in principle, the latter can thus be determined from the shear measurement.

Despite these reasons, some authors prefer to construct inverse methods in which the surface mass density on a grid serves as variables (e.g., Bridle et al. 1998; Marshall et al. 2002). The fact that the mass density on a finite field does not describe the shear in this field is accounted for in these methods by choosing a reconstruction grid that is larger than the data field and by allowing the surface mass density in this outer region to vary as well. Whereas the larger numerical grid requires a larger numerical effort, in addition to the non-local relation between κ and γ, this is of lesser importance, provided the numerical resources are available. Worse, however, is the view that the mass distribution outside the data field obtained by this method has any physical significance ! It has not. This mass distribution is solely one of infinitely many that can approximately generate the shear in the data field from mass outside the data field. The fact that numerical tests show that one can indeed recover

some of the mass distribution outside the data field is again a fluke, since these models are usually chosen such that all mass distribution outside the field in contained in a boundary region around the data field which is part of the numerical grid – and hence, the necessary 'external' shear must be generated by a mass distribution in this boundary zone which by construction is where it is. In real life, however, there is no constraint on where the 'external' shear contribution comes from.

5.4 Parameterized Mass Models

Whereas the parameter-free mass maps obtained through one of the methods discussed above provide a direct view of the mass distribution of a cluster, their quantitative interpretation is not straightforward. Peaks in the surface mass density can indicate the presence of a mass concentration, or else be a peak caused by the ellipticity noise of the galaxies. Since the estimated values for κ at different locations $\boldsymbol{\theta}$ are correlated [see (49)], it is hard to imagine 'error bars' attached to each point. Therefore, it is often preferable to use parameterized mass models to fit the observed data; for example, fitting shear (and/or magnification) data to an NFW mass profile (see IN, Sect. 6.2) yields the virial mass M_{200} of the cluster and its concentration index c. There are basically two methods which have been used to obtain such parameterized models. The first one, assuming a spherical mass model, orders the tangential component of the observed image ellipticities into radial bins and fits a parameterized shear profile through these bins, by minimizing a corresponding χ^2-function. One of the disadvantages of this method is that the result of the fitting process can depend on the selected binning, but this can be largely avoided by choosing the bins fine enough. This then essentially corresponds to minimizing the first term in (62).

Alternatively, a likelihood method can be used, in which the log-likelihood function (62) – without the regularization term – is minimized, with the values of the potential on the grid $\{\psi_n\}$ replaced by a set of parameters which describe the mass profile. Schneider et al. (2000) have used this likelihood method to investigate with which accuracy the model parameters of a mass profile can be obtained, using both the shear information as well as magnification information from number counts depletion. One of the surprising findings of this study was that the slope of the fitted mass profile is highly degenerate if only shear information is used; indeed, the mass-sheet degeneracy strikes again and causes even fairly different mass profiles to have very similar reduced shear profiles, as is illustrated for a simple example in Fig. 18. In Fig. 19, the resulting degeneracy of the profile slope is seen. This degeneracy can be broken if number count information is used in addition. As seen in the middle panel of Fig. 18, the magnification profiles of the four models displayed are quite different and thus the number counts sensitive to the profile slope. Indeed, the confidence regions in the parameter fits, shown in Fig. 19, obtained from the magnification information are highly inclined relative to

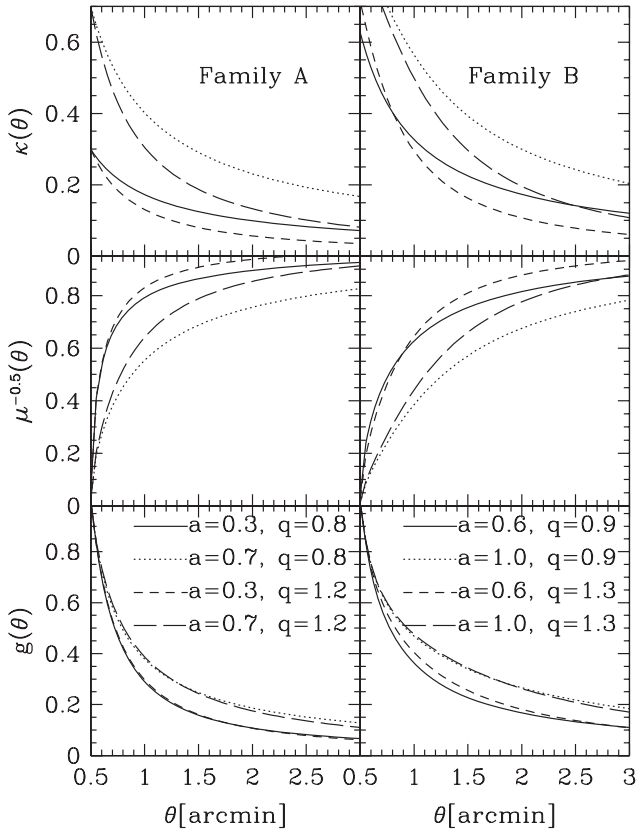

Fig. 18. The Einstein radius of a spherical mass distribution was assumed to be $\theta_{\rm E} = 0'.5$, and the density profile outside the Einstein radius was assumed to follow a power law, $\kappa(\theta) = a(\theta/\theta_{\rm E})^{-q}$; an SIS would have $a = 1/2$ and $q = 1$. The figure displays for four combinations of model parameters the surface mass density $\kappa(\theta)$, the function $\mu^{-1/2}$, which would be the depletion factor for source counts of slope $\beta = 1/2$, and the reduced shear $g(\theta)$. As can be seen, whereas the density profiles of the four models are quite different, the reduced shear profiles are pairwise almost fully degenerate. This is due to the mass-sheet degeneracy; it implies that it will be difficult to determine the slope q of the profiles from shear measurements alone, unless much larger fields around the cluster are used (from Schneider et al. 2000)

those from the shear measurements, implying that the combination of both methods yields much better constraints on the model parameters. Of course, as mentioned before, the mass-sheet degeneracy can also be broken if redshift information of individual background galaxies is available.

However, in order for the magnification information to yield significant constraints on the mass parameters, one needs to know the unlensed number density n_0 of sources quite accurately. In fact, even an uncertainty of less than

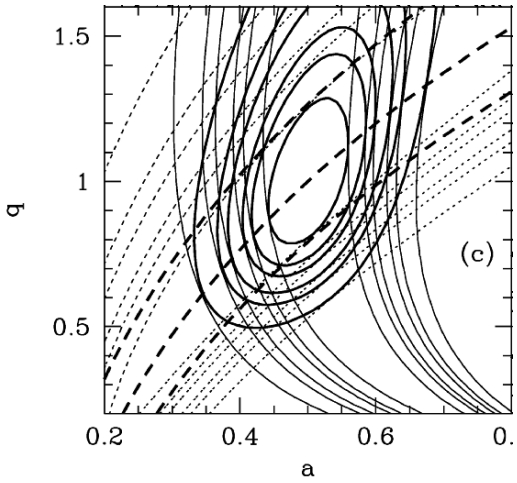

Fig. 19. For the power-law models of Fig. 18, confidence regions in the slope q and amplitude a are drawn, as derived from the shear (*thin solid contours*), the magnification (*dotted*) and their combination (*thick solid*). A number density of 30/arcmin^2 for shear measurements and 120/arcmin^2 for number counts was assumed. Thick dashed curves show models with constant total number of galaxies in the field, demonstrating that most of the constraint from magnification is due to the total counts, with little information about the detailed profile. It was assumed here that the unlensed number density of background galaxies is perfectly known; the fact that most of the magnification information comes from the total number of galaxies in the field implies that any uncertainty in the unlensed number density will quickly remove most of the magnification information (from Schneider et al. 2000)

$\sim$10% in the value of n_0 renders the magnification information in relation to the shear information essentially useless (in the frame of parameterized models). Note that an accurate determination of n_0 is difficult to achieve: since n_0 corresponds to the unlensed number density of faint galaxies at the same flux limit as used for the actual data field, one requires an accurate photometric calibration. A flux calibration uncertainty of 0.1 mag corresponds to an uncertainty in n_0 of about $\sim$5% for a slope of $\alpha = 0.5$, and such uncertainties are likely at the very faint flux limits needed to achieve a high number density of sources. In addition, the presence of bright cluster galaxies renders the detection and accurate brightness measurement of background galaxies difficult and requires masking of regions around them. Nevertheless, in cases where only magnification information is available, it can provide information on the mass profile by itself. Such a situation can occur for observing conditions with seeing above $\sim 1''$, when the shear method is challenged by the smallness of faint galaxies.

The result shown in Fig. 19 implies that the shape of the mass profile cannot be very well determined from the shear method, owing to the mass sheet

degeneracy. This result extends to more general mass profiles than power-law models; e.g., King and Schneider 2001 considered NFW models with their two parameters c and r_{200}. A fairly strong degeneracy between these two parameters was found. Furthermore, the mass-sheet degeneracy renders it surprisingly difficult to distinguish an isothermal mass model from an NFW profile. The ability to distinguish these two families of models increases with a larger field-of-view of the observations. This expectation was indeed verified in King et al. 2002b where the wide-field imaging data of the cluster A 1689 were analyzed with the likelihood method. Although the field size is larger than $30'$, so that the shear profile up to $\sim 15'$ from the cluster center can be measured, an NFW profile is preferred with less than 90% confidence over a power-law mass model. The determination of the mass profiles is likely to improve when strong lensing constraints are taken into account as well.

The likelihood method for obtaining the parameters of a mass model is robust in the sense that the result is only slightly affected by substructure, as has been shown by King et al. (2001) using numerically generated cluster models. However, if a 'wrong' parameterization of the mass distribution is chosen, the interpretation of the resulting best-fit model must proceed carefully, and the resulting physical parameters, such as the total mass, may be biased. The principal problems with parameterized models are the same as for lens galaxies in strong lensing: unless the parameters have a well-defined physical meaning, one does not learn much, even if they are determined with good accuracy (see Sect. 4.7 of SL).

5.5 Problems of Weak Lensing Cluster Mass Reconstruction and Mass Determination

In this section, some of the major problems of determining the mass profile of clusters from weak lensing techniques are summarized. The finite ellipticity dispersion of galaxies generates a noise which provides a fundamental limit to the accuracy of all shear measurements. We will mention a number of additional issues here.

Number 1: The Mass-Sheet Degeneracy

As mentioned several times, the major problem is the mass-sheet degeneracy, which implies that there is always one arbitrary constant that is undetermined from the shear data. Number count depletion can in principle lift this degeneracy, but this magnification effect has been observed in only a few clusters yet, and as mentioned above, this method has its own problems. Employing redshift information of individual source galaxies can also break this degeneracy (Bradac et al. 2004). Note that the mass-sheet degeneracy causes quite different mass profiles to have very similar reduced shear profiles.

Source Redshift Distribution

Since the critical surface mass density $\Sigma_{\rm cr}$ depends on the source redshift, a quantitative interpretation of the weak lensing mass reconstruction requires the knowledge of the redshift distribution of the galaxy sample used for the shear measurements. Those are typically so faint (and numerous) that it is infeasible to obtain individual spectroscopic redshifts for them. There are several ways to deal with this issue: probably the best is to obtain multi-color photometry of the fields and employ photometric redshift techniques (e.g. Connolly et al. 1995; Benítez 2000; Bolzonella et al. 2000). In order for them to be accurate, the number of bands needs to be fairly large; in addition, since much of the background galaxy population is situated at redshifts above unity, one requires near-IR images, as optical photometry alone cannot be used for photometric redshifts above $z \gtrsim 1.3$ (where the 4000 Å-break is redshifted out of the optical window). The problem with near-IR photometry is, however, that currently near-IR cameras have a substantially smaller field-of-view than optical cameras; in addition, due to the much higher sky brightness for ground-based near-IR observations, they extend to brighter flux limits (or smaller galaxy number densities) than optical images, for the same observing time. Nevertheless, upcoming wide-field near-IR cameras, such as theVISTA project on Paranal or WIRCAM at the CFHT, will bring great progress in this direction.

The alternative to individual redshift estimates of background galaxies is to use the redshift distribution obtained through spectroscopic (or detailed photometric redshift) surveys in other fields, and identify this with the faint background galaxy population at the same magnitude. In this way, the redshift distribution of the galaxies can be estimated. The issues that need to be considered here is that neither the targets for a spectroscopic survey, nor the galaxy population from which the shear is estimated, are strictly magnitude selected. Very small galaxies, for example, cannot be used for a shear estimate (or are heavily downweighted) owing to their large smearing corrections from the PSF. Similarly, for low-surface brightness galaxies it is much harder to determine a spectroscopic redshift. Hence, in these redshift identifications, care needs to be excersized.

For cluster mass reconstructions, the physical mass scale is obtained from the average $\beta := \langle D_{\rm ds}/D_{\rm s}\rangle$ over all source galaxies. This average is fairly insensitive to the detailed redshift distribution, as long as the mean source redshift is substantially larger than the lens redshift. This is typically the case for low-redshift ($z \lesssim 0.3$) clusters. However, for higher-redshift lenses, determining β requires a good knowledge of the galaxy redshift distribution.

Contamination of the Source Sample

Next on the list is the contamination of the galaxy sample from which the shear is measured by cluster galaxies; a fraction of the faint galaxies will be

foreground objects or faint cluster members. Whereas the foreground population is automatically taken into account in the normal lensing analysis (i.e., in determining β), the cluster members constitute an additional population of galaxies which is not included in the statistical redshift distribution. The galaxy sample used for the shear measurement is usually chosen as to be substantially fainter than the brighter cluster member galaxies; however, the abundance of dwarf galaxies in clusters (or equivalently, the shape of the cluster galaxy luminosity function) is not well known, and may vary substantially from cluster to cluster (e.g., Trentham and Tully 2002, and references therein). Including cluster members in the population from which the shear is measured weakens the lensing signal, since they are not sheared. As a consequence, a smaller shear is measured, and a lower cluster mass is derived. In addition, the dwarf contamination varies as a function of distance from the cluster center, so that the shape of the mass distribution will be affected. Color selection of faint galaxies can help in the selection of background galaxies, i.e., to obtain a cleaner set of true background galaxies. Of course, cluster dwarfs, if not properly accounted for, will also affect the magnification method. One method to deal with this problem is to use only galaxies redder than the Red Cluster Sequence of the cluster galaxies in the color-magnitude diagram, as this sequence indicates the reddest galaxies at the corresponding redshift.

Accuracy of Mass Determination via Weak Lensing

Comparing the 'true' mass of a cluster with that measured by weak lensing is not trivial, as one has to define what the true mass of a cluster is. Using clusters from numerical simulations, the mass is defined as the mass inside a sphere of radius r_{200} around the cluster center within which the overdensity is 200 times the critical density of the universe at the redshift considered. When comparing this mass with the projected mass inside a circle of radius $R = r_{200}$, one should not be surprised that the latter is larger (Metzler et al. 2001), since one compares apples (the mass inside a sphere) with oranges (the mass within a cylinder). Metzler et al. ascribed this to the mass in dark matter filaments at the intersection of which massive clusters are located, but it is most likely mainly an effect of the mass definitions.

The mass-sheet degeneracy tell us there is little hope to measure the 'total' mass of a cluster without further assumptions. Therefore, one natural strategy is to assume a parameterized mass profile and see how accurately one can determine these parameters. The effect of ellipticity noise has already been described in Sect. 5.4. Using simulated clusters, Clowe et al. (2004a) have studied the effect of asphericity and substructure of clusters on these mass parameters, by analyzing the shear field obtained from independent projection of the clusters. They find that the non-spherical mass distribution and substructure induce uncertainties in the two parameters (r_{200} and the concentration c) of an NWF profile which are larger than those from the ellipticity noise under very good observing conditions. Among different projections of

the same cluster, the value of r_{200} has a spread of 10–15%, corresponding to a spread in virial mass of ∼40 %. Averaging over the different projections, they find that there is little bias in the mass determination, except for clusters with very large ellipticity.

Lensing by the Large-Scale Structure

Lensing by foreground and background density inhomogeneities (i.e., the LSS), yields a fundamental limit to the accuracy of cluster mass estimates. Since lensing probes the projected density, these foreground and background inhomogeneities are present in the lensing signal. Hoekstra (2003) has investigated this effect in the determination of the parameters of an NFW mass profile; we shall return to this issue in Sect. 9.2 below when we consider lensing by the large-scale structure. In principle, the foreground and background contributions can be eliminated if the individual redshifts of the source galaxies are known, since in this case a three-dimensional mass reconstruction becomes possible (see Sect. 7.6); however, the resulting cluster mass map will be very noisy.

5.6 Results

After the first detection of a coherent alignment of galaxy images in two clusters by Tyson et al. (1990) and the development of the Kaiser and Squires (1993) mass reconstruction method, the cluster MS 1224+20 was the first for which a mass map was obtained (Fahlman et al. 1994). This investigation of the X-ray selected cluster yielded a mass map centered on the X-ray centroid of the cluster, but also a surprisingly high M/L-ratio of $\sim 800\,h$ (here and in following we quote mass-to-light ratios always in Solar units). This high M/L ratio has later been confirmed in an independent analysis by Fischer (1999). This mass estimate is in strong conflict with that obtained from a virial analysis (Carlberg et al. 1994); however, it is known that this cluster has a very complex structure, is not relaxed, and most likely a superposition of galaxy concentrations in redshift.

Since this pioneering work,mass reconstructions of many clusters have been performed; see Mellier (1999) and Sect. 5.4 of BS. Here, only a few recent results shall be mentioned, followed by a summary.

Wide-Field Mass Reconstructions

The advent of large mosaic CCD cameras provides an opportunity to map large regions around clusters to be used for a mass reconstruction, and thus to measure the shear profile out to the virial radius of clusters. These large-scale observations offer the best promise to investigate the outer slope of the mass profile, and in particular distinguish between isothermal distributions

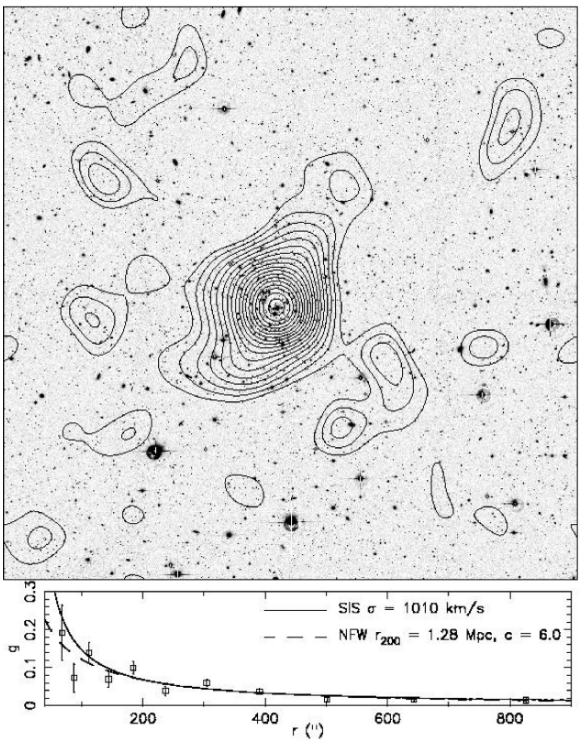

Fig. 20. Contours show the mass reconstruction of the cluster A 1689, obtained from data taken with the WFI at the ESO/MPG 2.2m telescope. The image is $\sim 33'$ on a side, corresponding to $\sim 4.3\,h^{-1}$ Mpc at the cluster redshift of $z_{\rm d} = 0.18$. In the lower panel, the reduced shear profile is shown, together with the best fitting SIS and NFW models. The mass reconstruction has been smoothed by a $1'.15$ Gaussian, and contour spacing is $\Delta\kappa = 0.01$. No corrections have been applied to account for contamination of the lensing signal by cluster dwarf galaxies – that would increase the mass of the best fit models by ~ 25 % (taken from Clowe and Schneider 2001)

and those following the NWF profile. Figure 20 shows an example of such a mass reconstruction, that of the cluster Abell 1689 with $z_{\rm d} = 0.182$. A significant shear is observed out to the virial radius. The mass peak is centered on the brightest cluster galaxy, and the overall lens signal is significant at the 13.4-σ level. The shear signal is fit with two models, as shown in the lower panel of Fig. 20; the NWF profile yields a better fit than an SIS profile. Two more clusters observed with the WFI by Clowe and Schneider (2002) yield similar results, i.e., a detection of the lensing signal out to the virial radius, and a preference for an NWF mass profile, although in one of the two cases this preference is marginal. The lensing signal of such rich clusters could be contaminated by faint cluster member galaxies; correcting for this effect would

increase the estimate of the lensing strength, but requires multi-color imaging for source selection.

The cluster A 1689 is (one of) the strongest lensing clusters known (see Fig. 14); in fact, it is strong enough so that a weak lensing signal can be significantly detected from near-IR images (King et al. 2002a) despite the fact that the usable number density of (background) galaxies is only $\sim 3\,\mathrm{arcmin}^{-2}$. The estimate of its velocity dispersion from weak lensing yields an Einstein radius well below the distance of the giant arcs from the cluster center. Hence, in this cluster we see a discrepancy between the strong and weak lensing results, which cannot be easily explained by redshift differences between the arc sources and the mean redshift of the faint galaxies used for the weak lensing analysis. On the other hand, A 1689 is known to be not a relaxed cluster, due to the redshift distribution of its member galaxies. This may explain the fact that the weak lensing mass estimates is also lower than that obtained from X-ray studies.

Filaments Between Clusters

One of the predictions of CDM models for structure formation is that clusters of galaxies are located at the intersection points of filaments formed by the dark matter distribution. In particular, this implies that a physical pair of clusters should be connected by a bridge or filament of (dark) matter, and weak lensing mass reconstructions can in principle be used to search for them. In the investigation of the $z = 0.42$ supercluster MS 0302+17, Kaiser et al. (1998) found an indication of a possible filament connecting two of the three clusters, with the caveat (as pointed out by the authors) that the filament lies just along the boundary of two CCD chips; in fact, an indepedent analysis of this supercluster (Gavazzi et al. 2004) failed to confirm this filament. Gray et al. (2002) saw evidence for a filament connecting the two clusters A 901A/901B in their mass reconstruction of the A 901/902 supercluster field. Another potential filament has been found in the wide-field mass reconstruction of the field containing the pair of clusters A 222/223 (Fig. 21, Dietrich et al. 2004). Spectroscopy shows that there are also galaxies at the same redshift as the two clusters present in the 'filament' (Dietrich et al. 2002).

One of the problems related to the unambiguous detection of filaments is the difficulty to define what a 'filament' is, i.e. to device a statistics to quantify the presence of a mass bridge. The eye easily picks up a pattern and identifies it as a 'filament', but quantifying such a pattern turns out to be very difficult, as shown by Dietrich et al. (2004). Because of that, it is difficult to distinguish between noise in the mass maps, the 'elliptical' extension of two clusters pointing toward each other, and a true filament. However, this problem is not specific to the weak investigation: even if the true projected mass distribution of a pair of clusters were known (e.g., from a cluster pair in numerical simulations), it is not straightforward to define what a filament would be.

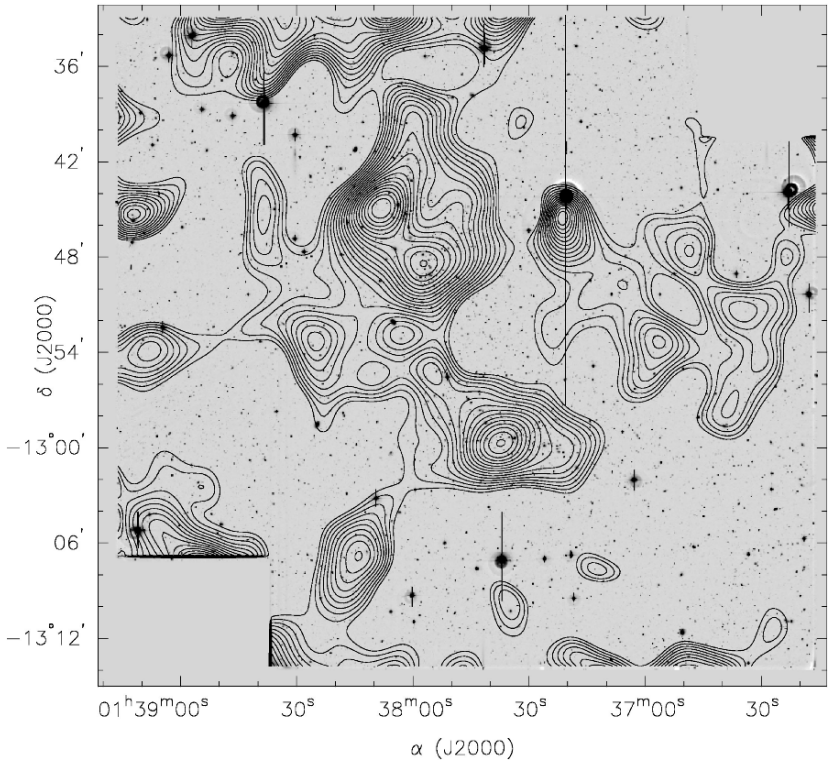

Fig. 21. A deep R-band image of the cluster pair Abell 222/223, obtained from two different pointings with the WFI@ESO/MPG 2.2m, with contours showing the reconstructed κ-map. The two clusters are in the region where the pointings overlap and thus deep imaging is available there. Both clusters are obviously detected in the mass map, with A223 (the Northern one) clearly split up into two subclusters. The mass reconstruction shows a connection between the two clusters which can be interpreted as a filament; galaxies at the clusters' redshift are present in this intercluster region. A further mass concentration is seen about $13'$ to the South-East of A222, which is significant at the 3.5σ level and where a clear concentration of galaxies is visible. A possible red cluster sequence indicates a substantially higher redshift for this cluster, compared to $z \approx 0.21$ of the double cluster (from Dietrich et al. 2004)

Correlation Between Mass and Light

Mass reconstructions on wide-fields, particularly those covering supercluster regions, are ideally suited to investigate the relation between mass and galaxy light. For example, a smoothed light map of the color-selected early-type galaxies can be correlated with the reconstructed κ-map; alternatively, assuming that light traces mass, the expected shear map can be predicted from the early-type galaxies and compared to the observed shear, with the

mass-to-light ratio being the essential fit parameter. Such studies have been carried out on the aforementioned supercluster fields, as well as on blank fields (Wilson et al. 2001). These studies yield very consistent results, in that the mass of clusters is very well traced by the distribution of early-type galaxies, but the mass-to-light ratio seems to vary between different fields, with $\sim 400h$ (in solar units) for the 0302 supercluster (Gavazzi et al. 2004), $\sim 200h$ for the A 901/902 supercluster (Gray et al. 2002), and $\sim 300h$ for empty fields (Wilson et al. 2001) in the rest-frame B-band. When one looks in more detail at these supercluster fields, interesting additional complications appear. The three clusters in the 0302 field, as well as the three clusters in the A 901/902 field (A 901 is indeed a pair of clusters) have quite different properties. In terms of number density of color-selected galaxies, A 901a and A 902 dominate the field, whereas only A 901b seems to be detected inX-rays. Considering early-type galaxies' luminosity, A 901a is the most prominent of the three clusters. In contrast to this, A 902 seems to be most massive as judged from the weak lensing reconstruction. Similar differences between the three clusters in the 0302 field are also seen. It therefore appears that the mass-to-light properties of clusters cover quite a range.

Cluster Mass Reconstructions from Space

The exquisite image quality that can be achieved with the HST – imaging without the blurring effects of atmospheric seeing – suggests that such data would be ideal for weak lensing studies. This is indeed partly true: from space, the shape of smaller galaxy images can be measured than from the ground where the size of the seeing disk limits the image size of galaxies that can be used for ellipticity measurements in practice. Figure 22 shows an HST image of the cluster A 851 ($z_\mathrm{d} = 0.41$), together with a mass reconstruction. The agreement between the mass distribution and the angular distribution of bright cluster galaxies is striking. A detailed X-ray observation of this cluster with XMM-Newton (De Filippis et al. 2003) finds two extended X-ray components coinciding with the two maxima of the bright galaxy distribution, and thus of the mass map shown in Fig. 22, in addition to several compact X-ray sources inside the HST field. Clearly, this cluster is a dynamically young system, as also seen by the inhomogeneities of the X-ray temperature and metallicity of the intracluster gas.

The drawback of cluster weak lensing studies with the HST is the small field-of-view of its WFPC2 camera, which precludes imaging of large regions around the cluster center. To compensate for this, one can use multiple pointings to tile a cluster. For example, Hoekstra and collaborators have observed three X-ray selected clusters with HST mosaics; the results from this survey are summarized in Hoekstra et al. (2002d). One example is shown in Fig. 23, the high-redshift cluster MS 1054−03 at $z_\mathrm{d} = 0.83$. Also in this cluster one detects clear substructure, here consisting of three mass peaks, which is matched by the distribution of bright cluster galaxies. The shape of the

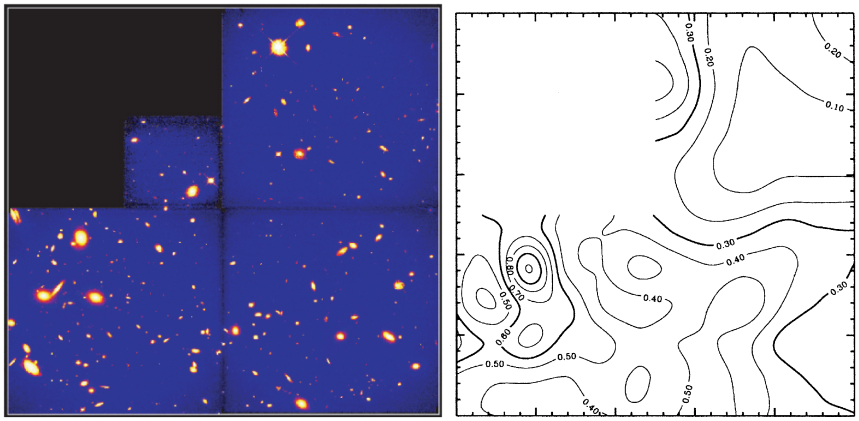

Fig. 22. The left panel shows an WFPC2@HST image of the cluster Cl0939+4713 (=Abell 851; taken from Seitz et al. 1996; the field is about 2.′5 on a side), whereas the right panel shows a mass reconstruction obtained by Geiger and Schneider (1999); this was obtained using the entropy-regularized maximum likelihood method of Seitz et al. (1998). One notices the increased spatial resolution of the resulting mass map near the center of the cluster, which this method yields 'automatically' in those regions where the shear signal is large. Indeed, this mass map predicts that the cluster is critical in the central part, in agreement with the finding of Trager et al. (1997) that strong lensing features (multiple images plus an arc) of sources with $z \sim 4$ are seen there. The strong correlation between the distribution of mass and that of the bright cluster galaxies is obvious: Not only does the peak of the mass distribution coincide with the light center of the cluster, but also a secondary maximum in the surface mass density corresponds to a galaxy concentration (seen in the lower middle), as well as a pronounced minimum on the left where hardly any bright galaxies are visible

mass maps indicates that this cluster is not relaxed, but perhaps in a later stage of merging, a view also supported by its hot X-ray temperature. In fact, new observations with Chandra and XMM-Newton of MS 1054 have shown that this cluster has a much lower temperature than measured earlier with ASCA (Gioia et al. 2004). Only two of the three components seen in the galaxy distribution and the mass reconstruction are seen in X-rays, with the central weak lensing component being the dominant X-ray source. The newly determined X-ray temperature is consistent with the velocity dispersion of cluster galaxies.

Magnification Effects

As mentioned in Sect. 2.4, the magnification of a lens can also be used to reconstruct its surface mass density (Broadhurst et al. 1995). Provided a population of background source galaxies is identified whose number count slope α – see (26) - differs significantly from unity, local counts of these sources

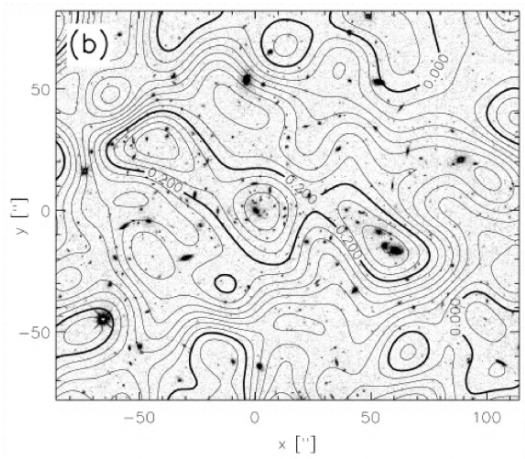

Fig. 23. Mass reconstruction (contours) of the inner part of the high-redshift ($z_{\rm d} = 0.83$) cluster MS 1054−03, based on a mosaic of six pointings obtained with the WFPC2@HST (from Hoekstra et al. 2000). The splitting of the cluster core into three subcomponents, also previously seen from ground-based images by Clowe et al. (2000), shows that this cluster is not yet relaxed

can be turned into an estimator of the local magnification. If the lens is weak, (27) provides a relation between the local number counts and the local surface mass density. If the lens is not weak, this relation no longer suffices, but one needs to use the full expression

$$|\mu|^{-1} = \left|(1-\kappa)^2 - |\gamma|^2\right| \ , \tag{65}$$

where we have written absolute values to account for the fact that the sign of the magnification cannot be observed. There are two obvious difficulties with (65): the first comes from the sign ambiguities, namely whether μ is positive or negative, and whether $\kappa < 1$ or >1. Assuming that we are in the region of the cluster where $\mu > 0$ and $\kappa < 1$ (that is, outside the outer critical curve), then (65) can be rewritten as

$$\kappa = 1 - \sqrt{\mu^{-1} + |\gamma|^2} \ , \tag{66}$$

which shows the second difficulty: in order to estimate κ from μ, one needs to know the shear magnitude $|\gamma|$.

There are various ways to deal with this second problem. Consider first the case that the (reduced) shear is also observed, in which case one better writes

$$\kappa = 1 - \left[\mu\left(1 - |g|^2\right)\right]^{-1/2} \ ; \tag{67}$$

but of course, if shear measurements are available, they should be combined with magnification observations in a more optimized way. A second method,

using magnification only, is based on the fact that γ depends linearly on κ (ignoring finite-field problems here), and so (66) can be turned into a quadratic equation for the κ field (Dye and Taylor 1998). From numerical models of clusters, van Kampen (1998) claimed that the shear in these clusters approximately follows on average a relation of the form $|\gamma| = (1-c)\sqrt{\kappa/c}$, with $c \sim 0.7$; however, there is (as expected) large scatter around this mean relation which by itself has little theoretical justification. Figure 24 shows the mass reconstruction of the cluster Cl 0024+17 using galaxy number counts and the two reconstruction methods just mentioned.

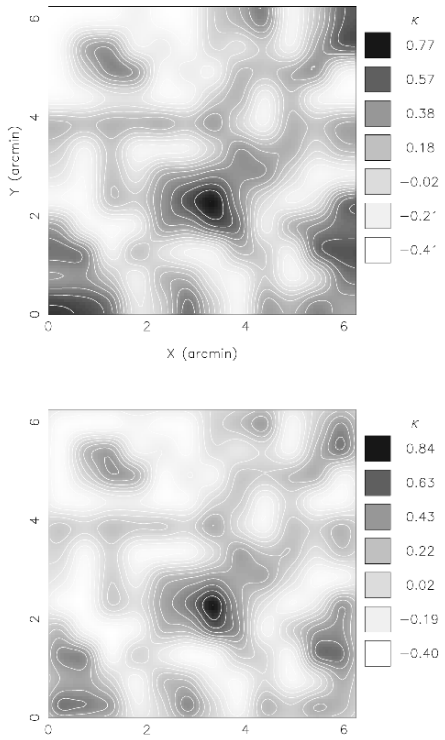

Fig. 24. Mass reconstruction of the cluster Cl 0024+17 from the magnification method. The two different reconstructions are based on two different ways to turn the magnification signal – number count depletions – into a surface mass density mass, as described in the text: in the upper panel, a local relation between surface mass density and shear magnitude has been used, whereas in the lower panel, the magnification was transformed into a κ map using the (non-local) quadratic dependence of the inverse magnification on the surface mass density field. Overall, these two reconstructions agree very well. To account for the presence of bright foreground galaxies, the data field had to be masked before local number densities of background galaxies were estimated – the mask is shown in Fig. 25 (from Dye et al. 2002)

Magnification effects have been observed for a few clusters, most noticeably Cl 0024+17 (Fort et al. 1997; Rögnvaldsson et al. 2001; Dye et al. 2002) and A 1689 (Taylor et al. 1998; Dye et al. 2001). We shall describe some of the results obtained for Cl 0024+17 as an example (Dye et al. 2002). Since the cluster galaxies generate a local overdensity of galaxy counts, they need to be removed first, which can be done based on a color and magnitude criterion. Comparison with extensive spectroscopy of this cluster (Czoske et al. 2001) shows that this selection is very effective for the brighter objects. For the fainter galaxies – those from which the lensing signal is actually measured – a statistical subtraction of foreground and cluster galaxies needs to be performed, which is done by subtracting galaxies according to the field luminosity function with $z < z_{\rm d}$ and cluster galaxies according to the cluster luminosity function. The latter is based on the assumption that the luminosity distribution of cluster galaxies is independent from the distance to the cluster center. Next, the field of the cluster needs to be masked for bright objects, near which the photometry of fainter galaxies becomes inaccurate or impossible; Fig. 25 shows the masked data field. The number density of sources is then determined from the unmasked area. The resulting mass reconstruction is shown in Fig. 24. The results confirm the earlier finding from strong lensing (see Sect. 4.4) that the mass in the inner part of this cluster is larger by a factor ∼3 than estimated from its X-ray emission (Soucail et al. 2000).

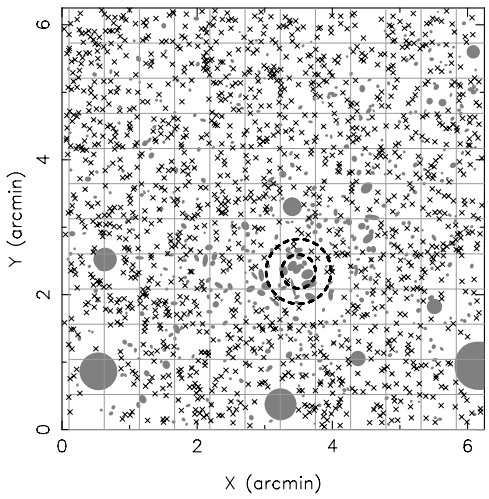

Fig. 25. The mask of the data field of the cluster Cl 0024+17 (*grey circles*) and the location of putative background objects (*crosses*). The inner dashed circle shows the critical curve of the cluster as derived from the multiply imaged arc system (from Dye et al. 2002)

Magnification and Shear Method Compared

It is interesting to consider the relative merits of shear and magnification methods for weak lensing studies. The number of clusters that have been investigated with either method are quite different, with less than a handful for which the magnification effect has been seen. The reason for this is multi-fold. First, the shear method does not need external calibration, as it is based on the assumption of random source ellipticity; in contrast to this, the magnification method requires the number counts of unlensed sources. Whereas this can be obtained from the same dataset, provided it covers a sufficiently large area, this self-calibration removes one of the strongest appeals of the magnification effect, namely its potential to break the mass-sheet degeneracy. Second, the magnification method is affected by the angular correlation of galaxies, as clearly demonstrated by Athreya et al. (2002) in their study of the clusterMS 1008−1224, where the background number counts revealed the presence of a background cluster which, if not cut out of the data, would contaminate the resulting mass profile substantially. Third, the removal of foreground galaxies, and more seriously, of faint cluster members introduces an uncertainty in the results which is difficult to control. Finally, the number count method yields a lower lensing signal-to-noise than the shear method: If we consider N_γ and N_μ galaxies in a given patch of the sky, such that for the former ones the ellipticities have been measured, and for the latter ones accurate photometry is available and the galaxies are above the photometric completeness brightness, the signal-to-noise ratio from the shear – see (15) – and number count methods are

$$\left(\frac{\mathrm{S}}{\mathrm{N}}\right)_\gamma = \frac{|\gamma|}{\sigma_\epsilon}\sqrt{N_\gamma}\;;\;\left(\frac{\mathrm{S}}{\mathrm{N}}\right)_\mu = 2\kappa|\alpha-1|\sqrt{N_\mu}\;, \tag{68}$$

where we employed (27) in the latter case and assumed that the source galaxy positions are uncorrelated. The ratio of these two S/N values is

$$\frac{(\mathrm{S/N})_\gamma}{(\mathrm{S/N})_\mu} = \frac{|\gamma|}{\kappa}\;\frac{1}{2\sigma_\epsilon|1-\alpha|}\sqrt{\frac{N_\gamma}{N_\mu}}\;. \tag{69}$$

For an isothermal mass profile, the first of these factors is unity. With $\sigma_\epsilon \approx 0.4$ and $\alpha \approx 0.75$ for R-band counts, the second factor is $\sim$5. The final factor depends on the quality of the data: in good seeing conditions, this ratio is of order unity. However, when the seeing is bad, the photometric completeness level can be considerably fainter than the magnitude for which the shape of galaxies can be measured reliably. Therefore, for data with relatively bad seeing, the magnification effect may provide a competitive means to extract weak lensing information. Having said all of this, the magnification method will keep its position as an alternative to shear measurements, in particular for future multi-color datasets where the separation of foreground and cluster galaxies from the background population can be made more cleanly.

Summary

The mass reconstruction of clusters using weak lensing has by now become routine; quite a few cameras at excellent sites yield data with sub-arcsecond image quality to enable this kind of work. Overall, the reconstructions have shown that the projected mass distribution is quite similar to that of the projected galaxy distribution and the shape of the X-ray emission, at least for clusters that appear relaxed. There is no strong evidence for a discrepancy between the mass obtained from weak lensing and that from X-rays, again with exceptions like for Cl0024+16 mentioned above (which most likely is not a single cluster). The weak lensing mass profiles are considered more reliable than the ones obtained from X-ray studies, since they do not rely on symmetry or equilibrium assumptions. On the other hand, they contain contributions from foreground and background mass inhomogeneities, and are affected by the mass-sheet degeneracy. What is still lacking is a combined analysis of clusters, making use of weak lensing, X-ray, Sunyaev–Zeldovich, and galaxy dynamics measurements, although promising first attempts have been published (e.g., Zaroubi et al. 1998, 2001; Reblinsky 2000; Doré et al. 2001; Marshall et al. 2003).

5.7 Aperture Mass and Other Aperture Measures

In the weak lensing regime, $\kappa \ll 1$, the mass-sheet degeneracy corresponds to adding a uniform surface mass density κ_0. However, one can define quantities in terms of the surface mass density which are invariant under this transformation. In addition, several of these quantities can be determined directly in terms of the locally measured shear. In this section we shall present the basic properties of the aperture measures, whereas in the following section we shall demonstrate how the aperture mass can be used to find mass concentrations based solely on their weak lensing properties.

Aperture Mass

Let $U\,(|\boldsymbol{\theta}|)$ be a compensated weight (or filter) function, meaning $\int \mathrm{d}\theta\, \theta\, U(\theta) = 0$, then the *aperture mass*

$$M_{\mathrm{ap}}(\boldsymbol{\theta}_0) = \int \mathrm{d}^2\theta\, \kappa(\boldsymbol{\theta})\, U(|\boldsymbol{\theta} - \boldsymbol{\theta}_0|) \tag{70}$$

is independent of κ_0, as can be easily seen. For example, if U has the shape of a Mexican hat, M_{ap} will have a maximum if the filter center is centered on a mass concentration. The important point to notice is that M_{ap} can be written directly in terms of the shear (Kaiser et al. 1994; Schneider 1996)

$$M_{\mathrm{ap}}(\boldsymbol{\theta}_0) = \int \mathrm{d}^2\theta\, Q(|\boldsymbol{\theta}|)\, \gamma_{\mathrm{t}}(\boldsymbol{\theta}; \boldsymbol{\theta}_0)\ , \tag{71}$$

where we have defined the *tangential component* γ_t of the shear relative to the point $\boldsymbol{\theta}_0$ [cf. 17], and

$$Q(\theta) = \frac{2}{\theta^2}\int_0^\theta \mathrm{d}\theta'\;\theta'\,U(\theta') - U(\theta)\;. \tag{72}$$

These relations can be derived from (54), by rewriting the partial derivatives in polar coordinates and subsequent integration by parts (see Schneider and Bartelmann 1997); it can also be derived directly from the Kaiser and Squires inversion formula (44), as shown in Schneider (1996). Perhaps easiest is the following derivation (Squires and Kaiser 1996): We first rewrite (70) as

$$\begin{aligned} M_\mathrm{ap} &= 2\pi\int_0^{\theta_\mathrm{u}} \mathrm{d}\vartheta\;\vartheta\,U(\vartheta)\;\langle\kappa(\vartheta)\rangle \\ &= 2\pi\left[X(\vartheta)\;\langle\kappa(\vartheta)\rangle\right]_0^{\theta_\mathrm{u}} - 2\pi\int_0^{\theta_\mathrm{u}}\mathrm{d}\vartheta\;X(\vartheta)\,\frac{\mathrm{d}\,\langle\kappa\rangle}{\mathrm{d}\vartheta}\;, \end{aligned} \tag{73}$$

where θ_u is the radius of the aperture, and we have defined

$$X(\theta) = \int_0^\theta \mathrm{d}\vartheta\;\vartheta\,U(\vartheta)\;.$$

This definition and the compensated nature of U implies that the boundary terms in (73) vanish. Making use of (24), one finds that

$$\frac{\mathrm{d}\,\langle\kappa\rangle}{\mathrm{d}\vartheta} = \frac{\mathrm{d}\bar\kappa}{\mathrm{d}\vartheta} - \frac{\mathrm{d}\,\langle\gamma_\mathrm{t}\rangle}{\mathrm{d}\vartheta} = -\frac{2}{\vartheta}\,\langle\gamma_\mathrm{t}\rangle - \frac{\mathrm{d}\,\langle\gamma_\mathrm{t}\rangle}{\mathrm{d}\vartheta}\;,$$

where we used (23) and (24) to obtain $\mathrm{d}\bar\kappa/\mathrm{d}\vartheta = -2\,\langle\gamma_\mathrm{t}\rangle/\vartheta$. Inserting the foregoing equation into (73), one obtains

$$\begin{aligned} M_\mathrm{ap} &= 2\pi\int_0^{\theta_\mathrm{u}}\mathrm{d}\vartheta\;\vartheta\,\frac{2X(\vartheta)}{\vartheta^2}\,\langle\gamma_\mathrm{t}(\vartheta)\rangle \\ &\quad + 2\pi\left[X(\vartheta)\;\langle\gamma_\mathrm{t}(\vartheta)\rangle\right]_0^{\theta_\mathrm{u}} - 2\pi\int_0^{\theta_\mathrm{u}}\mathrm{d}\vartheta\,\frac{\mathrm{d}X}{\mathrm{d}\vartheta}\;\langle\gamma_\mathrm{t}(\vartheta)\rangle\;. \end{aligned} \tag{74}$$

The boundary term again vanishes, and one sees that the last equation has the form of (71), with the weight function $Q = 2X/\vartheta^2 - U$, reproducing (72).

We shall now consider a few properties of the aperture mass, which follow directly from (72).

- If U has finite support, then Q has finite support, which is due to the compensated nature of U. This implies that the aperture mass can be calculated on a finite data field, i.e., from the shear in the same circle where $U \neq 0$.
- If $U(\theta) = \text{const.}$ for $0 \le \theta \le \theta_\mathrm{in}$, then $Q(\theta) = 0$ for the same interval, as is seen directly from (72). Therefore, the strong lensing regime (where γ deviates appreciably from g) can be avoided by properly choosing U (and Q).

- If $U(\theta) = (\pi\theta_{\rm in}^2)^{-1}$ for $0 \le \theta \le \theta_{\rm in}$, $U(\theta) = -[\pi(\theta_{\rm out}^2 - \theta_{\rm in}^2)]^{-1}$ for $\theta_{\rm in} < \theta \le \theta_{\rm out}$, and $U = 0$ for $\theta > \theta_{\rm out}$, then $Q(\theta) = \theta_{\rm out}^2\,\theta^{-2}\left[\pi(\theta_{\rm out}^2 - \vartheta_{\rm in}^2)\right]^{-1}$ for $\theta_{\rm in} \le \theta \le \theta_{\rm out}$, and $Q(\theta) = 0$ otherwise. For this special choice of U,

$$M_{\rm ap} = \bar\kappa(\theta_{\rm in}) - \bar\kappa(\theta_{\rm in}, \theta_{\rm out})\;, \tag{75}$$

  the mean mass density inside $\theta_{\rm in}$ minus the mean density in the annulus $\theta_{\rm in} \le \theta \le \theta_{\rm out}$ (Kaiser 1995). Since the latter is non-negative, this yields a lower limit to $\bar\kappa(\theta_{\rm in})$, and thus to $M(\theta_{\rm in})$.

The aperture mass can be generalized to the case where the weight function U is constant on curves other than circles, e.g., on ellipses, in the sense that the corresponding expressions can be rewritten directly in terms of the shear on a finite region (see Squires and Kaiser 1996 for the case where U is constant on a set of self-similar curves, and Schneider and Bartelmann 1997 for a general set of nested curves). In general, $M_{\rm ap}$ is not a particularly good measure for the total mass of a cluster – since it employs a compensated filter – but it has been specifically designed that way to be immune against the mass-sheet degeneracy. However, $M_{\rm ap}$ is a very convenient measure for mass concentrations (see Sect. 5.8) and, as shown above, yields a robust lower limit on cluster masses.

Aperture Multipoles

The aperture method can also be used to calculate multipoles of the mass distribution: define the multipoles

$$Q^{(n)} := \int {\rm d}^2\theta\;\; |\boldsymbol{\theta}|^n\; U(|\boldsymbol{\theta}|)\, {\rm e}^{{\rm i}n\varphi}\, \kappa(\boldsymbol{\theta})\;, \tag{76}$$

then the $Q^{(n)}$ can again be expressed as an integral over the shear. Here, U is a radial weight function for which certain restrictions apply (see Schneider and Bartelmann 1997 for details), but is not required to be compensated for $n > 0$. A few cases of interest are: a weight function U which is non-zero only within an annulus $\theta_{\rm in} \le \theta \le \theta_{\rm out}$ and which continuously goes to zero as $\theta \to \theta_{\rm in,out}$; in this case, the shear is required only within the same annulus. Likewise, if U is constant for $0 \le \theta \le \theta_{\rm in}$ and then decreases smoothly to zero at $\theta_{\rm out}$, only the shear within the annulus is required to calculate the multipoles. Aperture multipoles can be used to calculate the multipole moments of mass concentrations like clusters directly from the shear, i.e., without obtaining first a mass map, which allows a more direct quantification of signal-to-noise properties.

The Cross Aperture

We have seen that the Kaiser and Squires inversion, given by the first expression in (44), must yield a real result; the imaginary part of the integral

in (44) vanishes in the absence of noise. Suppose one would multiply the complex shear by $\mathrm{i} = \mathrm{e}^{2\mathrm{i}\pi/4}$; this would transform the real part of the integral into the imaginary part and the imaginary part into the negative of the real part. Geometrically, multiplication by this phase factor corresponds to rotating the shear at every point by 45°. Hence, if all shears are rotated by $\pi/4$, the real part of the Kaiser and Squires inversion formula (44) yields zero. This 45-degree test has been suggested by A. Stebbins; it can be used on real data to test whether typical features in the mass map are significant, as those should have larger amplitude than spurious features obtained from the mass reconstruction in which the shear has been rotated by $\pi/4$ (the corresponding 'mass map' then yields a good indication of the typical noise present in the real mass map).

One can define in analogy to (71) the cross aperture by replacing the tangential component of the shear by its cross component. According to the 45-degree test, the resulting cross aperture should be exactly zero. Hence, if we define for $\boldsymbol{\theta}_0 = \mathbf{0}$

$$M := M_{\rm ap} + \mathrm{i}M_\perp = \int \mathrm{d}^2\theta\, Q(|\boldsymbol{\theta}|)\,[\gamma_{\rm t}(\boldsymbol{\theta}) + \mathrm{i}\gamma_\times(\boldsymbol{\theta})]$$

$$= -\int \mathrm{d}^2\theta\, Q(|\boldsymbol{\theta}|)\,\gamma(\boldsymbol{\theta})\,\mathrm{e}^{-2\mathrm{i}\phi}\,, \tag{77}$$

where ϕ is the polar angle of $\boldsymbol{\theta}$ as in (17), then M is expected to be purely real. We shall make use of this definition and the interpretation of M in later sections.

5.8 Mass Detection of Clusters

Motivation

If a weak lensing mass reconstruction of a cluster has been performed and a mass peak is seen, it can also be quantified by applying the aperture mass statistics to it: placing the center of the aperture on the mass peak, and choosing the radius of the aperture to match the extent of the mass peak will give a significant positive value of $M_{\rm ap}$. Now consider to observe a random field in the sky, and to determine the shear in this field. Then, one can place apertures on this field and determine $M_{\rm ap}$ at each point. If $M_{\rm ap}$ attains a significant positive value at some point, it then corresponds to a point around which the shear is tangentially oriented. Such shear patterns are generated by mass peaks according to (70) – hence, a significant peak in the $M_{\rm ap}$-map corresponds to a mass concentration (which can, in principle at least, be a mass concentration just in two-dimensional projection, not necessarily in 3D). Hence, the aperture mass statistics allows us to search for mass concentrations on blank fields, using weak lensing methods (Schneider 1996). From the estimate (19), we see that the detectable mass concentrations have to have typical cluster masses.

The reason why this method is interesting is obvious: As discussed in Sect. 6 of IN, the abundance of clusters as a function of mass and redshift is an important cosmological probe. Cosmological simulations are able to predict the abundance of massive halos for a given choice of cosmological parameters. To compare these predictions with observations, cluster samples are analyzed. However, clusters are usually detected either as an overdensity in the galaxy number counts (possibly in connection with color information, to employ the red cluster sequence – see Gladders and Yee 2000), or from extended X-ray sources. In both cases, one makes use of the luminous properties of the clusters, and cosmologists find it much more difficult to predict those, as the physics of the baryonic component of the matter is much harder to handle than the dark matter. Hence, a method for cluster detection that is independent of their luminosity would provide a clean probe of cosmology. From what was said above, the aperture mass provides such method (Schneider 1996).

To illustrate this point, we show in Fig. 26 the projected mass and the corresponding shear field as it results from studying the propagation of light rays through a numerically generated cosmological matter distribution (Jain et al. 2000; we shall return to such simulations in Sect. 6.6). From the comparison of these two panels, one sees that for each large mass concentration there is a tangential shear pattern centered on the mass peak. Thus, a systematic search for such shear patterns can reveal the presence and abundance of peaks in the mass map.

The Method

The search for mass concentrations can thus be carried out by calculating the aperture mass on a grid over the data field and to identify significant peaks. A practical estimator for $M_{\rm ap}$ is obtained by replacing the integral in (71) by a finite sum over image ellipticities:

$$\hat{M}_{\rm ap}(\boldsymbol{\theta}_0) = \frac{1}{n} \sum_i \epsilon_{{\rm t}i}(\boldsymbol{\theta}_0)\, Q(|\boldsymbol{\theta}_i - \boldsymbol{\theta}_0|)\;, \tag{78}$$

where n is the mean number density of galaxy images, and $\epsilon_{{\rm t}i}(\boldsymbol{\theta}_0)$ is the ellipticity component of a galaxy at $\boldsymbol{\theta}_i$ tangent to the center $\boldsymbol{\theta}_0$ of the aperture. This estimator has easy-to-quantify signal-to-noise properties. In the absence of a lensing signal, $\left\langle \hat{M}_{\rm ap} \right\rangle \equiv 0$, and the dispersion of $\hat{M}_{\rm ap}(\boldsymbol{\theta}_0)$ is

$$\sigma^2(\boldsymbol{\theta}_0) = \frac{\sigma_\epsilon^2}{2n^2} \sum_i Q^2(|\boldsymbol{\theta}_i - \boldsymbol{\theta}_0|)\;; \tag{79}$$

hence, the signal-to-noise of $\hat{M}_{\rm ap}(\boldsymbol{\theta}_0)$ is

$$\frac{\rm S}{N} = \frac{\sqrt{2}}{\sigma_\epsilon} \frac{\sum_i \epsilon_{{\rm t}i}(\boldsymbol{\theta}_0)\, Q(|\boldsymbol{\theta}_i - \boldsymbol{\theta}_0|)}{\sqrt{\sum_i Q^2(|\boldsymbol{\theta}_i - \boldsymbol{\theta}_0|)}}\;. \tag{80}$$

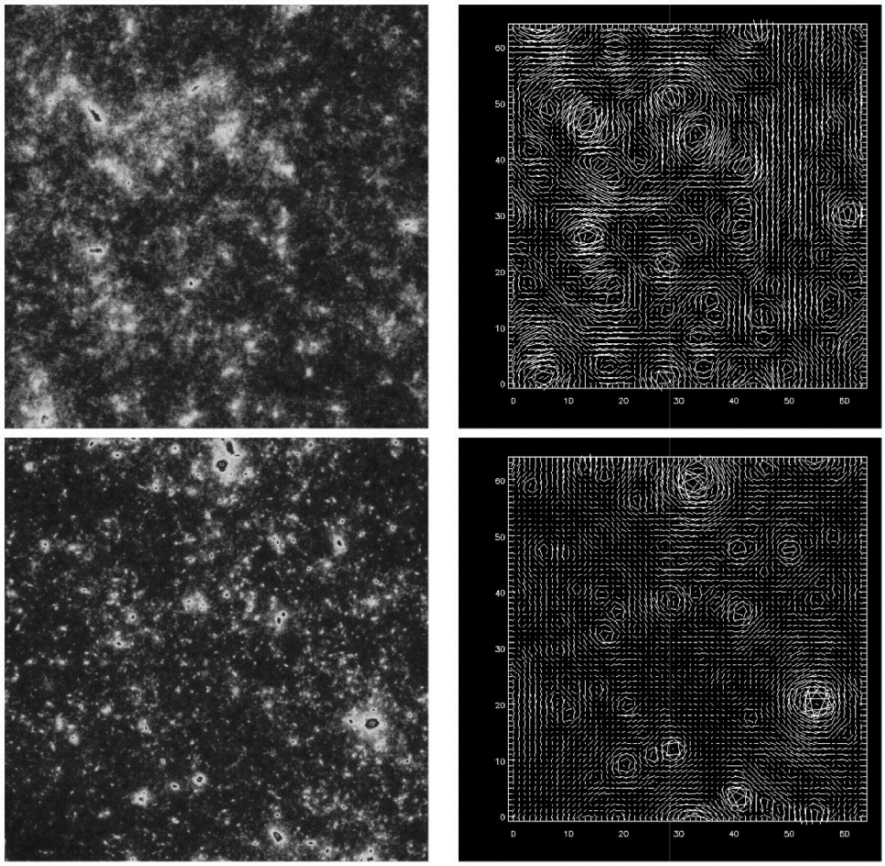

Fig. 26. Projected mass distribution of the large-scale structure (*left*), and the corresponding shear field (*right*), where the length and orientation of the sticks indicate the magnitude and direction of the local shear. The top panels correspond to an Einstein–de Sitter model of the Universe, whereas the bottom panels are for a low density open model. The size of the field is one degree on the side, and the background galaxies are assumed to all lie at the redshift $z_{\rm s} = 1$. Note that each mass concentration seen in the left-hand panels generates a circular shear pattern at this position; this forms the basic picture of the detection of mass concentrations from a weak lensing observation (from Jain et al. 2000)

The noise depends on $\boldsymbol{\theta}_0$, as the image number density can vary of data field. The size (or radius) of the aperture shall be adapted to the mass concentrations excepted: too small aperture radii miss most of the lensing signal of real mass concentrations, but is more susceptible to noise peaks, whereas too large aperture radii include regions of very low signal which may be swamped again by noise. In addition, the shape of the filter function Q can be adapted to the expected mass profiles of mass concentrations; e.g., one can design filters

which are particularly sensitive to NFW-like density profiles. In order not to prejudice the findings of a survey, it may be advantageous to use a 'generic' filter function, e.g., of the form

$$U(\vartheta) = \frac{9}{\pi\theta^2}\left(1-\frac{\vartheta^2}{\theta^2}\right)\left(\frac{1}{3}-\frac{\vartheta^2}{\theta^2}\right)\ ;\ \ Q(\vartheta) = \frac{6}{\pi\theta^2}\,\frac{\vartheta^2}{\theta^2}\left(1-\frac{\vartheta^2}{\theta^2}\right)\ . \qquad (81)$$

The relation between the two expressions for $M_{\rm ap}$ given by (70) and (71) is only valid if the aperture lies fully inside the data field. If it does not, i.e., if the aperture crosses the boundary of the data field, these two expressions are no longer equivalent; nevertheless, the estimator (78) still measures a tangential shear alignment around the aperture center and thus signifies the presence of a mass concentration.

There are superior estimates of the significance of a detected mass peak than using the signal-to-noise ratio (80). One consists in bootstrapping; there one calculates $M_{\rm ap}$ at a given point (where N galaxies are in the aperture) many times by randomly drawing – with replacement – N galaxies and tests how often is signal negative. The fraction of cases with negative values corresponds to the error level of having a positive detection of $M_{\rm ap}$. Alternatively, one can conduct another Monte-Carlo experiment, by randomizing all galaxy image orientations and calculating $M_{\rm ap}$ from these randomized samples, and ask in which fraction of realizations is the value of $M_{\rm ap}$ larger than the measured value ? As the randomized galaxies should show no lensing signal, this fraction is again the probability of getting a value as large as that measured from random galaxy orientations. In fact, from the central limit theorem one expects that the probability distribution of $M_{\rm ap}$ from randomizing the image orientations will be a Gaussian of zero mean, and its dispersion can be calculated directly from (78) to be

$$\sigma^2(\boldsymbol{\theta}_0) = \frac{1}{2n^2}\sum_i |\epsilon_i|^2\, Q^2(|\boldsymbol{\theta}_i-\boldsymbol{\theta}_0|)\ , \qquad (82)$$

which is similar to (79), but accounts for the moduli of the ellipticity of the individual galaxy images.

Both of the aforementioned methods take the true ellipticity distribution of galaxy images into account, and should yield very similar results for the significance. Highly significant peaks signify the presence of a mass concentration, detected solely on the basis of its mass, and therefore, it is a very promising search method for clusters.

There is nothing special about the weight function (81), except mathematical simplicity. It is therefore not clear whether these filter functions are most efficient to detect cluster-mass matter concentrations. In fact, as shown in Schneider (1996), the largest S/N is obtained if the filter function U follows the true mass profile of the lens or, equivalently, if Q follows its radial shear profile. Hennawi and Spergel (2005) and Schirmer (2004) tested a large range of filter functions, including (81), Gaussians, and those approximating

an NFW profile. Based on numerical ray-tracing simulations, Hennawi and Spergel conclude that the 'truncated' NFW filter is most efficient for cluster detections; the same conclusion has been achieved by Schirmer (2004) based on wide-field imaging data.

Furthermore, Hennawi and Spergel have complemented their cluster search by a 'tomographic' component, assuming that the source galaxies have (photometric) redshift estimates available. Since the lens strength is a function of source redshift, the expected behavior of the aperture mass signal as a function of estimated source redshift can be used as an additional search criteria. They shown that this additional information increases the sensitivity of weak lensing to find mass concentrations, in particular for higher-redshift ones; in fact, the cluster search by Wittman et al. (described below) has made use of redshift information. As an additional bonus, this method also provides an estimate of the lens redshift.

Results

In the past few years, a number of clusters and/or cluster candidates have been detected by the weak lensing method, and a few of them shall be discussed here. The right-hand panel of Fig. 27 shows the mass reconstruction

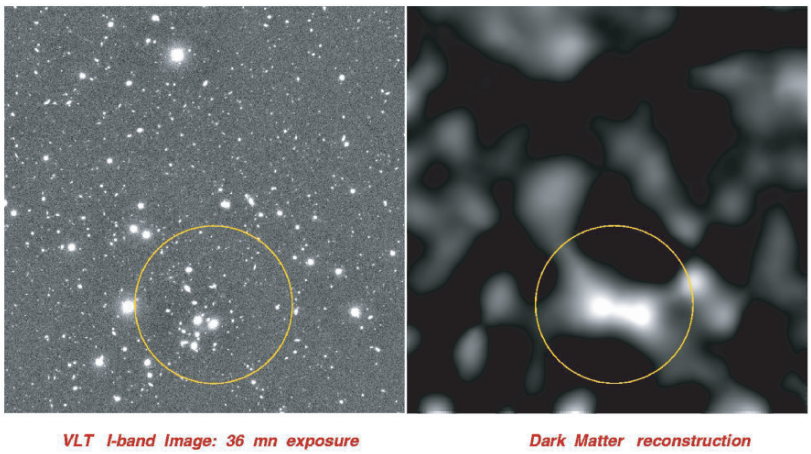

Fig. 27. A cosmic shear survey was carried out with the FORS1 instrument on the VLT (see Maoli et al. 2001 and Sect. 7.1 below). The left panel shows one of the 50 fields observed in the course of this survey, whereas the right panel shows a weak-lensing mass reconstruction of this field. Obviously, a strong mass peak is detected in this reconstruction, indicated by the circle. At the same position, one finds a strong overdensity of relatively bright galaxies on the VLT image; therefore, this mass peak corresponds to a cluster of galaxies. A reanalysis of all 50 VLT fields (Hetterscheidt 2003) yielded no further significant cluster candidate; however, with a field size of only $\sim 6'.5$, detecting clusters in them is difficult unless these are positioned close to the field centers

of one of the 50 FORS1@VLT fields observed in the course of a cosmic shear survey (see Sect. 7.1). This reconstruction shows an obvious mass peak, indicated by a circle. The left panel shows the optical image, and it is obvious that the location of the mass peak coincides with a concentration of bright galaxies – this certainly is a cluster, detected by its weak lensing signal. However, no follow-up observations have been conducted yet to measure its redshift.

Wittman et al. (2001, 2003) reported on the discovery of two clusters from their wide-field weak lensing survey; one of them is shown in Fig. 28 and discussed here. First, a peak in their mass reconstruction was identified which has a significance of 4.5σ. The location of the mass peak is identified with a concentration of red elliptical galaxies, with the two centers separated by about $1'$ (which is about the accuracy with which the centers of mass concentrations are expected to be determined from mass reconstructions). Follow-up spectroscopy confirmed the galaxy concentration to be a cluster at redshift $z_\mathrm{d} = 0.28$, with a velocity dispersion of $\sigma_v \sim 600\,\mathrm{km/s}$. Since multicolor photometry data are available, photometric redshift estimates of the faint galaxy population have been obtained, and the tangential shear around the mass peak has been investigated as a function of this estimated redshift. The lens signal rises as the redshift increases, as expected due to the lensing efficiency factor $D_\mathrm{ds}/D_\mathrm{s}$. In fact, from the source redshift dependence of the lens signal, the lens redshift can be estimated, and yields a result within $\sim$0.03 of the spectroscopically measured z_d. Hence, in this case not only can the presence of a cluster be inferred from weak lensing, but at the same time a cluster redshift has been obtained from lensing observations alone. This is one example of using source redshift information to investigate the redshift structure of the lensing matter distribution; we shall return to a more general discussion of this issue in Sect. 7.6.

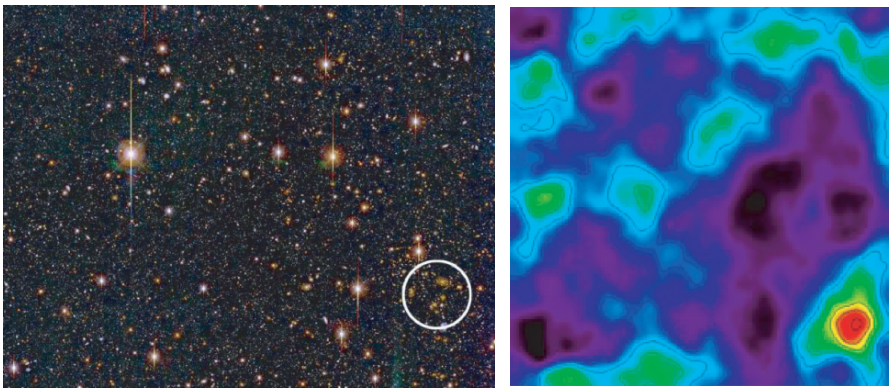

Fig. 28. Left: BTC image of a blank field, right: mass reconstruction, showing the presence of a (mass-selected) cluster near the lower right corner – spectroscopically verified to be at $z = 0.276$ (from Wittman et al. 2001)

In a wide-field imaging weak lensing survey of galaxy clusters, Dahle et al. (2003) detected three significant mass peaks away from the clusters that were targeted. One of these cases is illustrated in Fig. 29, showing the mass reconstruction in the field of the cluster Abell 1705. The mass peak South-West of the cluster coincides with a galaxy concentration at $z \sim 0.55$, as estimated from their color, and an arc is seen near the brightest galaxy of this cluster. A further cluster was detected in the wide-field image of the A222/223 double cluster field (Dietrich et al. 2004) which coincides with an overdensity of galaxies. Hence, by now of order ten cluster-mass matter concentrations have been discovered by weak lensing techniques and verified as genuine clusters from optical photometry and, for some of them, spectroscopy.

Miyazaki et al. (2002) used a $2.1\,\mathrm{deg}^2$ deep image taken with the Suprime-Cam wide-field imager on Subaru to search for mass peaks. They compared their peak statistics with both, the expected peak statistics from a noise field created by intrinsic galaxy ellipticities (Jain and van Waerbeke 2000) as well as from N-body simulations, and found a broader distribution in the actual data. They interpret this as statistical evidence for the presence of mass peaks; however, their interpretation of the significant dips in the mass map as evidence for voids cannot hold, as the density contrast of voids is too small (since the fractional density contrast $\delta > -1$) to be detectable with weak

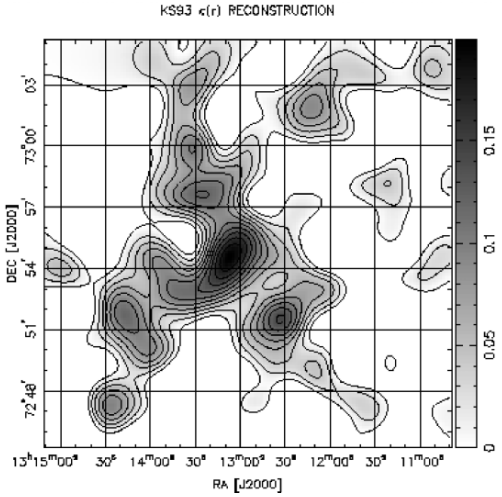

Fig. 29. Shown is the mass reconstruction of the field containing the cluster A 1705, located near the center of this field. The peak $\sim 4'$ to the North-East of A 1705 appears to be associated with galaxies at the same redshift as A 1705. However, the peak $\sim 4'$ South-West of A 1705 seems to be associated with galaxies at considerably larger redshift, at $z \sim 0.55 \pm 0.05$, as determined from the $V - I$ colors of the corresponding galaxy concentration. Indeed, an arc curving around the central galaxy of this newly detected cluster candidate is observed (from Dahle et al. 2003)

lensing. They find a number density of $> 5\sigma$ peaks of about $5\,\mathrm{deg}^{-2}$, well in agreement with predictions from Kruse and Schneider (1999) and Reblinsky et al. (1999). Schirmer (2004) investigated about $16\,\mathrm{deg}^2$ of images taken with the WFI@ESO/MPG 2.2m, and detected $100 > 4\sigma$-peaks, again in good agreement with theoretical expectations.

Dark Clusters?

In addition, however, this method has the potential to discover mass concentrations with very large mass-to-light ratio, i.e., clusters which are very faint optically and which would be missed in more conventional surveys for clusters. Two potential 'dark clusters' have been reported in the literature.[7] Umetsu and Futamase (2000), using the WFPC2 onboard HST detected a highly significant (4.5σ) mass concentration $1\farcm7$ away from the cluster Cl 1604+4304, also without an apparent overdensity of associated galaxies.

In the course of a wide-field weak lensing analysis of the cluster A 1942, Erben et al. (2000) detected a mass peak which, using the aperture mass statistics introduced previously, has been shown to be highly significant ($\sim 4.7\sigma$ on the V-band image), with the significance being obtained from the randomization and bootstrapping techniques described above. An additional I-band image confirmed the presence of a mass peak at the same location as on the V-band image, though with somewhat lower significance. No concentration of galaxies is seen near the location of the mass peak, which indicates that it either is a very dark mass concentration, or a cluster at a fairly high redshift (which, however, would imply an enormous mass for it), or, after all, a statistical fluke. It is important to note that the signal in M_{ap} comes from a range of radii (see Fig. 30); it is not dominated by a few highly flattened galaxies which happen to have a fortuitous orientation. Gray et al. (2000) have used near-IR images to search for a galaxy concentration in this direction, without finding an obvious candidate. Therefore, at present it is unclear whether the 'dark clump' is indeed a very unusual cluster. A low-significance X-ray source near its position, as obtained in a ROSAT observation of Abell 1942, certainly needs confirmation by the more sensitive X-ray observatory XMM.[8] Of course, if there are really dark clusters, their confirmation by methods other than weak lensing would be extremely difficult; but even if we are dealing with a statistical fluke, it would be very important to find the cause for it. An HST mosaic observation of this field has been conducted; a first analysis of these data was able to confirm the findings of Erben et al., in the sense that the shear signal from galaxies seen in both, the HST images and the

[7] A third case reported in Miralles et al. (2002) has in the meantime been considerably weakened (Erben et al. 2003).

[8] Judging from the results of several proposal submissions, people on X-ray TACs seem not to care too much about dark cluster candidates.

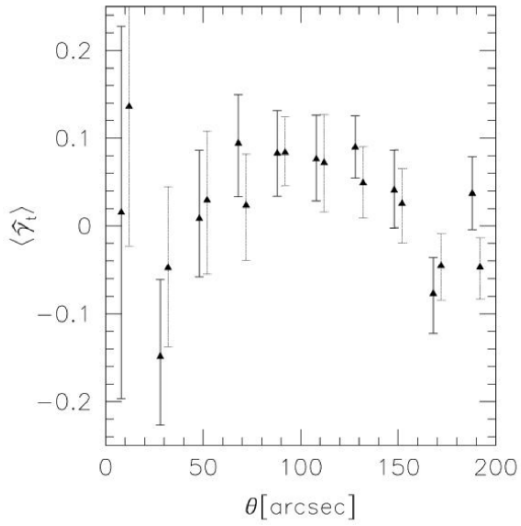

Fig. 30. Tangential shear profile from both (V- and I-band) images around the 'dark cluster' candidate near the cluster A1942. For each angular scales, two points (and corresponding error bars) are plotted, which are derived from two different images of the field in the V- and I-band. It can be seen that the tangential shear signal extends over quite a range in radius (from Erben et al. 2000)

ground-based data, have a significant tangential alignment (von der Linden 2004). However, contrary to expectations if this was truly a lensing mass signal, there is hardly any tangential alignment from fainter galaxies, although they are expected to be located at higher redshift and thus should show a stronger shear signal. However, as a word of caution, the PSF anisotropy of WFPC2 cannot be controlled from stars on the image, owing to the small field-of-view, and no stellar cluster has been observed with the filter with which the dark clump observations were conducted, so that the PSF anisotropy cannot be accurately inferred from such calibration images. The existence of dark clusters would be highly unexpected in view of our current understanding of structure formation and galaxy evolution, and would require revisions of these models.

The search for clusters by weak lensing will certainly continue, due to the novel properties of the cluster samples obtained that way. The observational data required are the same as those used for cosmic shear studies, and several very wide-field surveys are currently conducted, as will be described in Sect. 7. Hence, we can expect to have a sizable sample of shear-selected clusters in the near future. The search for mass concentrations by weak lensing techniques is affected by foreground and background inhomogeneities, which impose fundamental limits on the reliability and completeness of such searches; we shall return to this issue in Sect. 9.2.

Expectations

Kruse and Schneider (1999) have calculated the expected number density of lensing-detected clusters, using the aperture-mass method, for different cosmological parameters; these have been verified in numerical simulations of the large-scale structure by Reblinsky et al. (1999). Depending on the cosmological model, a few clusters per deg^2 should be detected at about the 5σ level. The dependence of the expected number density of detectable mass peaks on the cosmological parameters can be used as a cosmological probe; in particular, Bartelmann et al. (2002) and Weinberg and Kamionkowski (2003) demonstrate that the observed abundance of weak lensing clusters can probe the equation-of-state of the dark energy. Bartelmann et al. (2001) argued that the abundance of weak lensing detected clusters strongly depends on their mass profile, with an order-of-magnitude difference between NFW profiles and isothermal spheres. Weinberg and Kamionkowski (2002) argued, based on the spherical collapse model of cluster formation, that a considerable fraction of such detections are expected to be due to non-virialized mass concentrations, which would then be considerably weaker X-ray emitters and may be candidates for the 'dark clusters'.

6 Cosmic Shear – Lensing by the LSS

Up to now we have considered the lensing effect of localized mass concentrations, like galaxies and clusters. In addition to that, light bundles propagating through the Universe are continuously deflected and distorted by the gravitational field of the inhomogeneous mass distribution, the large-scale structure (LSS) of the cosmic matter field. This distortion of light bundles causes shape and size distortions of images of distant galaxies, and therefore, the statistics of the distortions reflect the statistical properties of the LSS (Gunn 1967; Blandford et al. 1991; Miralda-Escudé 1991; Kaiser 1992).

Cosmic shear deals with the investigation of this connection, from the measurement of the correlated image distortions to the inference of cosmological information from this distortion statistics. As we shall see, cosmic shear has become a very important tool in observational cosmology. From a technical point-of-view, it is quite challenging, first because the distortions are indeed very weak and therefore difficult to measure, and second, in contrast to 'ordinary' lensing, here the light deflection does not occur in a 'lens plane' but by a 3-D matter distribution, implying the need for a different description of the lensing optics. We start by looking at the description of light propagating through the Universe, and then consider the second-order statistical properties of the cosmic shear which reflect the second-order statistical properties of the cosmic matter field, i.e., the power spectrum. Observational results from cosmic shear surveys are presented in Sect. 7, whereas higher-order statistical properties of the shear field will be treated in Sect. 9.

6.1 Light Propagation in an Inhomogeneous Universe

In this brief, but rather technical section, we outline the derivation of the lensing effects of the three-dimensional mass distribution between the faint background galaxy population and us; the reader is referred to Bartelmann and Schneider (2001) for a more detailed discussion. The final result of this consideration has a very simple interpretation: in the lowest-order approximation, the 3-D cosmological mass distribution can be considered, for sources at a single redshift $z_{\rm s}$, as an effective surface mass density κ, just like in ordinary lensing. The resulting κ is obtained as a line-of-sight integral of the density contrast $\Delta\rho$, weighted by the usual geometrical factor entering the lens equations.

The laws of light propagation follow from Einstein's General Relativity; according to it, light propagates along the null-geodesics of the space-time metric. As shown in Schneider et al. (1992, hereafter SEF; see also Seitz et al. 1994), one can derive from General Relativity that the governing equation for the propagation of thin light bundles through an arbitrary space-time is the equation of geodesic deviation,

$$\frac{{\rm d}^2\boldsymbol{\xi}}{{\rm d}\lambda^2} = \mathcal{T}\,\boldsymbol{\xi}\;, \tag{83}$$

where $\boldsymbol{\xi}$ is the separation vector of two neighboring light rays, λ the affine parameter along the central ray of the bundle, and $\mathcal{T}$ is the *optical tidal matrix* which describes the influence of space-time curvature on the propagation of light. $\mathcal{T}$ can be expressed directly in terms of the Riemann curvature tensor (Fig. 31).

For the case of a weakly inhomogeneous Universe, the tidal matrix can be explicitly calculated in terms of the peculiar Newtonian potential. For that, we write the slightly perturbed metric of the Universe in the form

$${\rm d}s^2 = a^2(\tau)\left[\left(1+\frac{2\Phi}{c^2}\right)c^2{\rm d}\tau^2 - \left(1-\frac{2\Phi}{c^2}\right)\left({\rm d}w^2 + f_K^2(w){\rm d}\omega^2\right)\right]\;, \tag{84}$$

where w is the comoving radial distance, $a = (1+z)^{-1}$ the scale factor, normalized to unity today, τ is the conformal time, related to the cosmic time

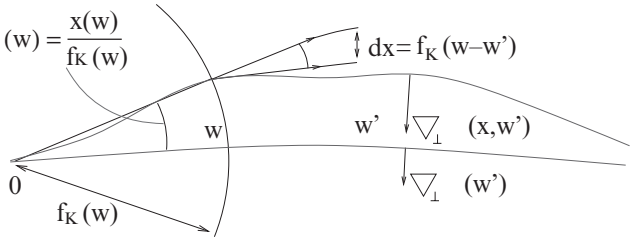

Fig. 31. Illustration of the evolution of the separation between two light rays in a curved space-time (source: T. Schrabback)

t through $\mathrm{d}t = a\,\mathrm{d}\tau$, $f_K(w)$ is the comoving angular diameter distance, which equals w in a spatially flat model, and $\Phi(\mathbf{x}, w)$ denotes the Newtonian peculiar gravitational potential which depends on the comoving position vector $\mathbf{x}$ and cosmic time, here expressed in terms of the comoving distance w (see Sect. 4 of IN for a more detailed description of the various cosmological terms). In this metric, the tidal matrix $\mathcal{T}$ can be calculated in terms of the Newtonian potential Φ, and correspondingly, the equation of geodesic deviation (83) yields the evolution equation for the comoving separation vector $\mathbf{x}(\boldsymbol{\theta}, w)$ between a ray separated by an angle $\boldsymbol{\theta}$ at the observer from a fiducial ray (Fig. 31)

$$\frac{\mathrm{d}^2\mathbf{x}}{\mathrm{d}w^2} + K\,\mathbf{x} = -\frac{2}{c^2}\left[\nabla_\perp\Phi\left(\mathbf{x}(\boldsymbol{\theta}, w), w\right) - \nabla_\perp\Phi^{(0)}\left(w\right)\right] , \tag{85}$$

where $K = (H_0/c)^2\,(\Omega_\mathrm{m} + \Omega_\Lambda - 1)$ is the spatial curvature of the Universe, $\nabla_\perp = (\partial/\partial x_1, \partial/\partial x_2)$ is the transverse *comoving* gradient operator, and $\Phi^{(0)}(w)$ is the potential along the fiducial ray.[9] The formal solution of this transport equation is obtained by the method of Green's function, to yield

$$\mathbf{x}(\boldsymbol{\theta}, w) = f_K(w)\boldsymbol{\theta} - \frac{2}{c^2}\int_0^w \mathrm{d}w'\, f_K(w-w')\left[\nabla_\perp\Phi\left(\mathbf{x}(\boldsymbol{\theta}, w'), w'\right) - \nabla_\perp\Phi^{(0)}\left(w'\right)\right] . \tag{86}$$

A source at comoving distance w with comoving separation $\mathbf{x}$ from the fiducial light ray would be seen, in the absence of lensing, at the angular separation $\boldsymbol{\beta} = \mathbf{x}/f_K(w)$ from the fiducial ray (this statement is nothing but the definition of the comoving angular diameter distance). Hence, $\boldsymbol{\beta}$ is the unlensed angular position in the 'comoving source plane' at distance w, where the origin of this source plane is given by the intersection point with the fiducial ray. Therefore, in analogy with standard lens theory, we define the Jacobian matrix

$$\mathcal{A}(\boldsymbol{\theta}, w) = \frac{\partial\boldsymbol{\beta}}{\partial\boldsymbol{\theta}} = \frac{1}{f_K(w)}\frac{\partial\mathbf{x}}{\partial\boldsymbol{\theta}} , \tag{87}$$

and obtain from (86)

$$\mathcal{A}_{ij}(\boldsymbol{\theta}, w) = \delta_{ij} - \frac{2}{c^2}\int_0^w \mathrm{d}w'\,\frac{f_K(w-w')f_K(w')}{f_K(w)}\,\Phi_{,ik}\left(\mathbf{x}(\boldsymbol{\theta}, w'), w'\right)\,\mathcal{A}_{kj}(\boldsymbol{\theta}, w') , \tag{88}$$

which describes the locally linearized mapping introduced by LSS lensing. To derive (88), we noted that $\nabla_\perp\Phi^{(0)}$ does not depend on $\boldsymbol{\theta}$, and used the chain

[9] In some of the literature, this transport equation is written without the term accounting for the potential along the fiducial ray. The idea behind this is to compare a light ray in the inhomogeneous universe with one in the homogeneous, unperturbed universe. Apart from the conceptual difficulty, this 'first-order expansion' is not justified, as the light rays in an inhomogeneous universe can deviate quite significantly from straight rays in the homogeneous reference universe – much more than the length scale of typical density fluctuations. These difficulties are all avoided if one starts from the exact equation of geodesic deviation, as done here.

rule in the derivative of Φ. This equation still is exact in the limit of validity of the weak-field metric. Next, we expand $\mathcal{A}$ in powers of Φ, and truncate the series after the linear term:

$$\mathcal{A}_{ij}(\boldsymbol{\theta}, w) = \delta_{ij} - \frac{2}{c^2}\int_0^w \mathrm{d}w' \, \frac{f_K(w-w')f_K(w')}{f_K(w)}\, \Phi_{,ij}\left(f_K(w')\boldsymbol{\theta}, w'\right) \ . \quad (89)$$

Hence, to linear order, the distortion can be obtained by integrating along the unperturbed ray $\mathbf{x} = f_K(w)\,\boldsymbol{\theta}$; this is also called the Born approximation. Corrections to the Born approximation are necessarily of order Φ^2. Throughout this article, we will employ the Born approximation; later, we will comment on its accuracy. If we now define the deflection potential

$$\psi(\boldsymbol{\theta}, w) := \frac{2}{c2}\int_0^w \mathrm{d}w' \, \frac{f_K(w-w')}{f_K(w)\, f_K(w')}\, \Phi\left(f_K(w')\boldsymbol{\theta}, w'\right) \ , \quad (90)$$

then $\mathcal{A}_{ij} = \delta_{ij} - \psi_{,ij}$, just as in ordinary lens theory. *In this approximation, lensing by the 3-D matter distribution can be treated as an equivalent lens plane with deflection potential ψ, mass density $\kappa = \nabla^2\psi/2$, and shear $\gamma = (\psi_{,11} - \psi_{,22})/2 + \mathrm{i}\psi_{,12}$.*

6.2 Cosmic Shear: The Principle

The Effective Surface Mass Density

Next, we relate κ to fractional density contrast δ of matter fluctuations in the Universe; this is done in a number of steps:

1. To obtain $\kappa = \nabla^2\psi/2$, take the 2-D Laplacian of ψ, and add the term $\Phi_{,33}$ in the resulting integrand; this latter term vanishes in the line-of-sight integration, as can be seen by integration by parts.
2. We make use of the 3-D Poisson equation in comoving coordinates

$$\nabla^2\Phi = \frac{3H_0^2\Omega_\mathrm{m}}{2a}\delta \quad (91)$$

to obtain

$$\kappa(\boldsymbol{\theta}, w) = \frac{3H_0^2\Omega_\mathrm{m}}{2c^2}\int_0^w \mathrm{d}w' \, \frac{f_K(w')f_K(w-w')}{f_K(w)}\, \frac{\delta\left(f_K(w')\boldsymbol{\theta}, w'\right)}{a(w')} \ . \quad (92)$$

Note that κ is proportional to Ω_m, since lensing is sensitive to $\Delta\rho \propto \Omega_\mathrm{m}\,\delta$, not just to the density contrast $\delta = \Delta\rho/\bar{\rho}$ itself.
3. For a redshift distribution of sources with $p_z(z)\,\mathrm{d}z = p_w(w)\,\mathrm{d}w$, the effective surface mass density becomes

$$\begin{aligned}\kappa(\boldsymbol{\theta}) &= \int \mathrm{d}w \; p_w(w)\,\kappa(\boldsymbol{\theta}, w) \\ &= \frac{3H_0^2\Omega_\mathrm{m}}{2c^2}\int_0^{w_\mathrm{h}} \mathrm{d}w \; g(w)\, f_K(w)\, \frac{\delta\left(f_K(w)\boldsymbol{\theta}, w\right)}{a(w)} \ , \end{aligned} \quad (93)$$

with

$$g(w) = \int_w^{w_\mathrm{h}} \mathrm{d}w' \; p_w(w') \frac{f_K(w'-w)}{f_K(w')} \; , \tag{94}$$

which is the source-redshift weighted lens efficiency factor $D_\mathrm{ds}/D_\mathrm{s}$ for a density fluctuation at distance w, and w_h is the comoving horizon distance, obtained from $w(a)$ by letting $a \to 0$.

The expression (92) for the effective surface mass density can be interpreted in a very simple way. Consider a redshift interval of width $\mathrm{d}z$ around z, corresponding to the proper radial distance interval $\mathrm{d}D_\mathrm{prop} = |c\,\mathrm{d}t| = H^{-1}(z)(1+z)^{-1}\,c\,\mathrm{d}z$. The surface mass density in this interval is $\Delta\rho\,\mathrm{d}D_\mathrm{prop}$, where only the density contrast $\Delta\rho = \rho - \bar{\rho}$ acts as a lens (the 'lensing effect' of the mean matter density of the Universe is accounted for by the relations between angular diameter distance and redshift; see Schneider and Weiss 1988a). Dividing this surface mass density by the corresponding critical surface mass density, and integrating along the line-of-sight to the sources, one finds

$$\kappa = \int_0^{z_\mathrm{s}} \mathrm{d}z \; \frac{4\pi G}{c^2} \, \frac{D_\mathrm{d}^\mathrm{ang} D_\mathrm{ds}^\mathrm{ang}}{D_\mathrm{s}^\mathrm{ang}} \, \frac{\mathrm{d}D_\mathrm{prop}}{\mathrm{d}z} \, \Delta\rho \; . \tag{95}$$

This expression is equivalent to (92), as can be easily shown (by the way, this is a good exercise for practicing the use of cosmological quantities like redshift, distances etc.).

Limber's Equation

The density field δ is assumed to be a realization of a random field. It is the properties of the random field that cosmologists can hope to predict, and not a specific realization of it. In particular, the second-order statistical properties of the density field are described in terms of the power spectrum (see IN, Sect. 6.1). We shall therefore look at the relation between the quantities relevant for lensing and the power spectrum $P_\delta(k)$ of the matter distribution in the Universe. The basis of this relation is formed by Limber's equation. If δ is a homogeneous and isotropic 3-D random field, then the projections

$$g_i(\boldsymbol{\theta}) = \int \mathrm{d}w \; q_i(w) \, \delta\left(f_K(w)\boldsymbol{\theta}, w\right) \tag{96}$$

also are (2-D) homogeneous and isotropic random fields, where the q_i are weight functions. In particular, the correlation function

$$C_{12} = \langle g_1(\boldsymbol{\varphi}_1) \, g_2(\boldsymbol{\varphi}_2) \rangle \equiv C_{12}(|\boldsymbol{\varphi}_1 - \boldsymbol{\varphi}_2|) \tag{97}$$

depends only on the modulus of the separation vector. The original form of the Limber (1953) equation relates C_{12} to the correlation function of δ which is a line-of-sight projection. Alternatively, one can consider the Fourier-space

analogy of this relation: The power spectrum $P_{12}(\ell)$ – the Fourier transform of $C_{12}(\theta)$ – depends linearly on $P_\delta(k)$ (Kaiser 1992, 1998),

$$P_{12}(\ell) = \int \mathrm{d}w \, \frac{q_1(w)\, q_2(w)}{f_K^2(w)} \, P_\delta \left(\frac{\ell}{f_K(w)}, w \right) \, , \tag{98}$$

if the largest-scale structures in δ are much smaller than the effective range Δw of the projection. Hence, we obtain the (very reasonable) result that the 2-D power at angular scale $1/\ell$ is obtained from the 3-D power at length scale $f_K(w)\,(1/\ell)$, integrated over w.

Comparing (93) with (98), one sees that $\kappa(\boldsymbol{\theta})$ is such a projection of δ with the weights $q_1(w) = q_2(w) = (3/2)(H_0/c)^2 \Omega_\mathrm{m} g(w) f_K(w)/a(w)$, so that

$$P_\kappa(\ell) = \frac{9 H_0^4 \Omega_\mathrm{m}^2}{4c^4} \int_0^{w_\mathrm{h}} \mathrm{d}w \, \frac{g^2(w)}{a^2(w)} \, P_\delta \left(\frac{\ell}{f_K(w)}, w \right) \, . \tag{99}$$

The power spectrum P_κ, if observable, can therefore be used to constrain the 3-D power spectrum P_δ. For a number of cosmological models, the power spectrum $P_\kappa(\ell)$ is plotted in Fig. 32. Predictions of P_κ are plotted both for assuming linear growth of the density structure (see Sect. 6.1 of IN), as well as the prescription of the fully nonlinear power spectrum as given by the fitting formulae of Peacock and Dodds (1996). From this figure one infers that the nonlinear evolution of the density fluctuations becomes dominant for values of $\ell \gtrsim 200$, corresponding to an angular scale of about $30'$; the precise values depend on the cosmological model and the redshift distribution of the sources. Furthermore, the dimensionless power spectrum $\ell^2 P_\kappa(\ell)$, that is, the power per logarithmic bin, peaks at around $\ell \sim 10^4$, corresponding to an angular scale of $\sim 1'$, again somewhat depending on the source redshift distribution. Third, one notices that the shape and amplitude of P_κ depends on the values of the cosmological parameters; therefore, by measuring the power spectrum, or quantities directly related to it, one can constrain the values of the cosmological parameters. We consider next appropriate statistical measures of the cosmic shear which are directly and simply related to the power spectrum P_κ.

6.3 Second-Order Cosmic Shear Measures

We will now turn to statistical quantities of the cosmic shear field which are quadratic in the shear, i.e., to second-order shear statistics. Higher-order statistical properties, which already have been detected in cosmic shear surveys, will be considered in Sect. 9. As we shall see, all second-order statistics of the cosmic shear yield (filtered) information about, and are fully described in terms of P_κ. The most-often used second-order statistics are:

- The two-point correlation function(s) of the shear, $\xi_\pm(\theta)$,
- the shear dispersion in a (circular) aperture, $\left\langle |\bar{\gamma}|^2 \right\rangle(\theta)$, and
- the aperture mass dispersion, $\left\langle M_\mathrm{ap}^2 \right\rangle(\theta)$.

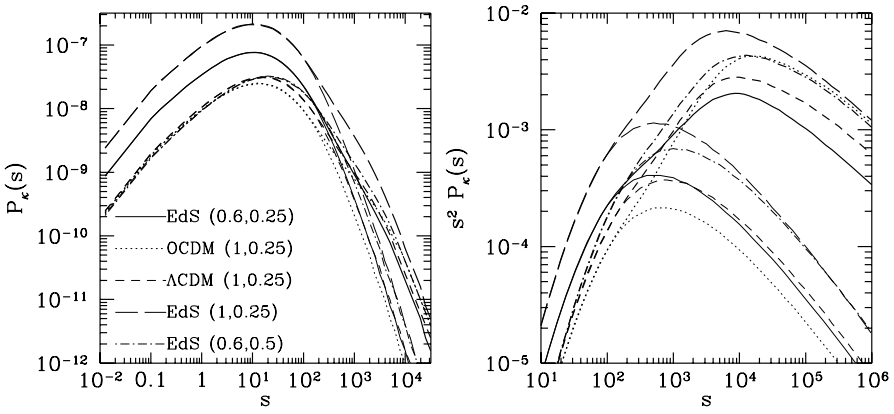

Fig. 32. The power spectrum $P_\kappa(\ell)$ (*left panel*) and its dimensionless form $\ell^2\,P_\kappa(\ell)$ (*right panel*) for several cosmological models (where here, ℓ is denoted by s). Specifically, EdS denotes an $\Omega_\mathrm{m} = 1$, $\Omega_\Lambda = 0$ Einstein-de Sitter model, OCDM an open $\Omega_\mathrm{m} = 0.3$, $\Omega_\Lambda = 0$ Universe, and ΛCDM a flat, low-density $\Omega_\mathrm{m} = 0.3$, $\Omega_\Lambda = 0.7$ model. Numbers in parenthesis indicate $(\Gamma_\mathrm{spect}, \sigma_8)$, where Γ_spect is the shape parameter of the power spectrum (see IN, Sect. 6.1) and σ_8 is the power-spectrum normalization. For these power spectra, the mean redshift of the galaxy distribution was assumed to be $\langle z_\mathrm{s}\rangle = 1.5$. Thin curves show the power spectra assuming linear evolution of the density fluctuations in the Universe, and thick curves use the fully non-linear evolution, according to the prescription of Peacock and Dodds (1996). For angular scales below $\sim 30'$, corresponding to $\ell \geq 200$, the non-linear evolution of the power spectrum becomes very important (from Schneider et al. 1998a)

Those will be discussed next, and their relation to $P_\kappa(\ell)$ shown. As a preparation, consider the Fourier transform of κ,

$$\hat\kappa(\boldsymbol{\ell}) = \int \mathrm{d}^2\theta\, \mathrm{e}^{\mathrm{i}\boldsymbol{\ell}\cdot\boldsymbol{\theta}}\,\kappa(\boldsymbol{\theta})\;; \tag{100}$$

then,

$$\left\langle \hat\kappa(\boldsymbol{\ell})\hat\kappa^*(\boldsymbol{\ell}')\right\rangle = (2\pi)^2\,\delta_\mathrm{D}(\boldsymbol{\ell}-\boldsymbol{\ell}')\,P_\kappa(\ell)\;, \tag{101}$$

which provides another definition of the power spectrum P_κ [compare with (123) of IN]. The Fourier transform of the shear is

$$\hat\gamma(\boldsymbol{\ell}) = \left(\frac{\ell_1^2-\ell_2^2+2\mathrm{i}\ell_1\ell_2}{|\boldsymbol{\ell}|^2}\right)\hat\kappa(\boldsymbol{\ell}) = \mathrm{e}^{2\mathrm{i}\beta}\,\hat\kappa(\boldsymbol{\ell})\;, \tag{102}$$

where β is the polar angle of the vector $\boldsymbol{\ell}$; this follows directly from (42) and (43). Equation (102) implies that

$$\left\langle \hat\gamma(\boldsymbol{\ell})\hat\gamma^*(\boldsymbol{\ell}')\right\rangle = (2\pi)^2\,\delta_\mathrm{D}(\boldsymbol{\ell}-\boldsymbol{\ell}')\,P_\kappa(\ell). \tag{103}$$

Hence, the power spectrum of the shear is the same as that of the surface mass density.

Shear Correlation Functions

Consider a pair of points (i.e., galaxy images); their separation direction φ (i.e. the polar angle of the separation vector $\boldsymbol{\theta}$) is used to define the tangential and cross-component of the shear at these positions *for this pair*, $\gamma_\mathrm{t} = -\mathcal{R}\mathrm{e}\left(\gamma\,\mathrm{e}^{-2\mathrm{i}\varphi}\right)$, $\gamma_\times = -\mathcal{I}\mathrm{m}\left(\gamma\,\mathrm{e}^{-2\mathrm{i}\varphi}\right)$, as in (17). Using these two shear components, one can then define the correlation functions $\langle\gamma_\mathrm{t}\gamma_\mathrm{t}\rangle(\theta)$ and $\langle\gamma_\times\gamma_\times\rangle(\theta)$, as well as the mixed correlator. However, it turns out to be more convenient to define the following combinations,

$$\xi_\pm(\theta) = \langle\gamma_\mathrm{t}\gamma_\mathrm{t}\rangle(\theta) \pm \langle\gamma_\times\gamma_\times\rangle(\theta)\;,\quad \xi_\times(\theta) = \langle\gamma_\mathrm{t}\gamma_\times\rangle(\theta)\;. \tag{104}$$

Due to parity symmetry, $\xi_\times(\theta)$ is expected to vanish, since under such a transformation, $\gamma_\mathrm{t} \to \gamma_\mathrm{t}$, but $\gamma_\times \to -\gamma_\times$. Next we relate the shear correlation functions to the power spectrum P_κ: Using the definition of $\xi_\pm$, replacing γ in terms of $\hat\gamma$, and making use of relation between $\hat\gamma$ and $\hat\kappa$, one finds (e.g., Kaiser 1992)

$$\xi_+(\theta) = \int_0^\infty \frac{\mathrm{d}\ell\,\ell}{2\pi}\,\mathrm{J}_0(\ell\theta)\,P_\kappa(\ell)\;;\quad \xi_-(\theta) = \int_0^\infty \frac{\mathrm{d}\ell\,\ell}{2\pi}\,\mathrm{J}_4(\ell\theta)\,P_\kappa(\ell)\;, \tag{105}$$

where $\mathrm{J}_n(x)$ is the n-th order Bessel function of first kind. $\xi_\pm$ can be measured as follows: on a data field, select all pairs of faint galaxies with separation within $\varDelta\theta$ of θ and then take the average $\langle\epsilon_{\mathrm{t}i}\,\epsilon_{\mathrm{t}j}\rangle$ over all these pairs; since $\epsilon_i = \epsilon_i^{(\mathrm{s})} + \gamma(\boldsymbol{\theta}_i)$, the expectation value of $\langle\epsilon_{\mathrm{t}i}\,\epsilon_{\mathrm{t}j}\rangle$ is $\langle\gamma_\mathrm{t}\gamma_\mathrm{t}\rangle(\theta)$, provided source ellipticities are uncorrelated. Similarly, the correlation for the cross-components is obtained. It is obvious how to generalize this estimator in the presence of a weight factor for the individual galaxies, as it results from the image analysis described in Sect. 3.5.

The Shear Dispersion

Consider a circular aperture of radius θ; the mean shear in this aperture is $\bar\gamma$. Averaging over many such apertures, one defines the shear dispersion $\left\langle|\bar\gamma|^2\right\rangle(\theta)$. It is related to the power spectrum through

$$\left\langle|\bar\gamma|^2\right\rangle(\theta) = \frac{1}{2\pi}\int \mathrm{d}\ell\,\ell\,P_\kappa(\ell)\,W_\mathrm{TH}(\ell\theta)\;,\quad \text{where}\;\; W_\mathrm{TH}(\eta) = \frac{4\mathrm{J}_1^2(\eta)}{\eta^2} \tag{106}$$

is the top-hat filter function (see, e.g., Kaiser 1992). A practical unbiased estimator of the mean shear in the aperture is $\hat{\bar\gamma} = N^{-1}\sum_{i=1}^N \epsilon_i$, where N is the number of galaxies in the aperture. However, the square of this expression is *not* an unbiased estimator of $\left\langle|\bar\gamma|^2\right\rangle$, since the diagonal terms of the resulting double sum yield additional terms, since $\mathrm{E}\left(\epsilon_i\epsilon_i^*\right) = |\gamma(\boldsymbol{\theta}_i)|^2 + \sigma_\epsilon^2$.

An unbiased estimate for the shear dispersion is obtained by omitting the diagonal terms,

$$\widehat{\left\langle|\bar{\gamma}|^2\right\rangle} = \frac{1}{N(N-1)}\sum_{i\neq j}^{N}\epsilon_i\,\epsilon_j^* \,. \tag{107}$$

This expression is then averaged over many aperture placed on the data field. Again, the generalization to allow for weighting of galaxy images is obvious. Note in particular that this estimator is not positive semi-definite.

The Aperture Mass

Consider a circular aperture of radius θ; for a point inside the aperture, define the tangential and cross-components of the shear relative to the center of the aperture (as before); then define

$$M_{\rm ap}(\theta) = \int \mathrm{d}^2\vartheta\; Q(|\boldsymbol{\vartheta}|)\,\gamma_{\rm t}(\boldsymbol{\vartheta}) \,, \tag{108}$$

where Q is a weight function with support $\vartheta \in [0,\theta]$. If we use the function Q given in (81), the dispersion of $M_{\rm ap}(\theta)$ is related to power spectrum by (Schneider et al. 1998a)

$$\left\langle M_{\rm ap}^2\right\rangle(\theta) = \frac{1}{2\pi}\int_0^\infty \mathrm{d}\ell\;\ell\,P_\kappa(\ell)\,W_{\rm ap}(\theta\ell) \,, \quad \text{with} \quad W_{\rm ap,1}(\eta) := \frac{576\mathrm{J}_4^2(\eta)}{\eta^4} \,. \tag{109}$$

Crittenden et al. (2002) suggested a different pair U and Q of filter functions,

$$U(\vartheta) = \frac{1}{2\pi\,\theta^2}\left[1-\left(\frac{\vartheta^2}{2\theta^2}\right)\right]\exp\left(-\frac{\vartheta^2}{2\theta^2}\right) \;;\; Q(\vartheta) = \frac{\vartheta^2}{4\pi\theta^4}\exp\left(-\frac{\vartheta^2}{2\theta^2}\right) \,. \tag{110}$$

These function have the disadvantage of not having finite support; however, due to the very strong fall-off for $\vartheta \gg \theta$, for many practical purposes the support can be considered effectively as finite. This little drawback is compensated by the convenient analytic properties of these filter functions, as we shall see later. For example, the relation of the corresponding aperture mass dispersion is again given by the first of (109), but the filter function simplifies to

$$W_{\rm ap,2}(\eta) = \frac{\eta^4}{4}\,\mathrm{e}^{-\eta^2} \,. \tag{111}$$

Whereas the filter functions which relate the power spectrum to the shear correlation functions, i.e., the Bessel function appearing in (105), and to the shear dispersion, given by $W_{\rm TH}$, are quite broad filters, implying that these statistics at a given angular scale depend on the power spectrum over a wide range of ℓ, the two filter functions $W_{\rm ap,1,2}$ are very localized and thus the aperture mass dispersion yields highly localized information about the power spectrum

(see Bartelmann and Schneider 1999, who showed that replacing the filter function W by a delta-'function' causes an error of only $\sim$10%). Hence, the shape of $\langle M_{\rm ap}^2\rangle(\theta)$ directly reflects the shape of the power spectrum as can also be seen in Fig. 35 below.

Interrelations

These various 2-point statistics all depend linearly on the power spectrum P_κ; therefore, one should not be too surprised that they are all related to each other (Crittenden et al. 2002). The surprise perhaps is that these interrelations are quite simple. First, the relations between $\xi_\pm$ and P_κ can be inverted, making use of the orthonormality relation of Bessel functions:

$$P_\kappa(\ell) = 2\pi\int_0^\infty {\rm d}\theta\,\theta\,\xi_+(\theta)\,{\rm J}_0(\ell\theta) = 2\pi\int_0^\infty {\rm d}\theta\,\theta\,\xi_-(\theta)\,{\rm J}_4(\ell\theta)\;. \tag{112}$$

Next, we take one of these and plug them into the relation (105) between the other correlation function and P_κ, to find:

$$\xi_+(\theta) = \xi_-(\theta) + \int_\theta^\infty \frac{{\rm d}\vartheta}{\vartheta}\xi_-(\vartheta)\left(4 - 12\frac{\theta^2}{\vartheta^2}\right)\;; \tag{113}$$

$$\xi_-(\theta) = \xi_+(\theta) + \int_0^\theta \frac{{\rm d}\vartheta\,\vartheta}{\theta^2}\xi_+(\vartheta)\left(4 - 12\frac{\vartheta^2}{\theta^2}\right)\;. \tag{114}$$

These equations show that the two shear correlation functions are not independent of each other, the reason for that being that the shear (which itself is a two-component quantity) is derived from a single scalar field, namely the deflection potential ψ. We shall return to this issue further below. Using (112) in the equation for the shear dispersion, one finds

$$\left\langle|\bar\gamma|^2\right\rangle(\theta) = \int_0^{2\theta}\frac{{\rm d}\vartheta\,\vartheta}{\theta^2}\,\xi_+(\vartheta)\,S_+\left(\frac{\vartheta}{\theta}\right) = \int_0^\infty\frac{{\rm d}\vartheta\,\vartheta}{\theta^2}\,\xi_-(\vartheta)\,S_-\left(\frac{\vartheta}{\theta}\right)\;,$$

where the $S_\pm$ are simple functions, given explicitly in Schneider et al. (2002a) and plotted in Fig. 33. Finally, the same procedure for the aperture mass dispersion lets us write

$$\langle M_{\rm ap}^2\rangle(\theta) = \int_0^{2\theta}\frac{{\rm d}\vartheta\,\vartheta}{\theta^2}\,\xi_+(\vartheta)\,T_+\left(\frac{\vartheta}{\theta}\right) = \int_0^{2\theta}\frac{{\rm d}\vartheta\,\vartheta}{\theta^2}\,\xi_-(\vartheta)\,T_-\left(\frac{\vartheta}{\theta}\right)\;, \tag{115}$$

again with analytically known functions $T_\pm$, given for the filter function (81) in Schneider et al. (2002a), and for the filter function (110) in Jarvis et al. (2003). Hence, all these 2-point statistics can be evaluated from the correlation

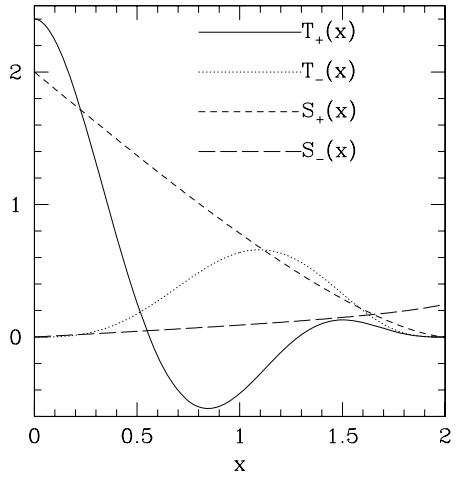

Fig. 33. The function $S_\pm(x)$ and $T_\pm(x)$ which relate the shear and aperture mass dispersion to the correlation functions. Note that S_- does not vanish for $x > 2$, as is the case for the other three functions (from Schneider et al. 2002a)

functions $\xi_\pm(\theta)$, which is of particular interest, since they can be measured best: Real data fields contain holes and gaps (like CCD defects; brights stars; nearby galaxies, etc.) which makes the placing of apertures difficult; however, the evaluation of the correlation functions is not affected by gaps, as one uses all pairs of galaxy images with a given angular separation. Furthermore, it should be noted that the aperture mass dispersion at angular scale θ can be calculated from $\xi_\pm(\vartheta)$ in the finite range $\vartheta \in [0, 2\theta]$, and the shear dispersion can be calculated from ξ_+ on $\vartheta \in [0, 2\theta]$, but not from ξ_- on a finite interval; this is due to the fact that ξ_- on small scales does not contain the information of the power spectrum on large scales, because of the filter function J_4 in (105).

We also note that from a cosmic shear survey, the power spectrum P_κ can be determined directly, as has been investigated by Kaiser (1998), Seljak (1998) and Hu and White (2001). This is *not* done by applying (112), as these relations would require the determination of the correlation function for all separation, but by more sophisticated methods. A simple example (though not optimal) is to consider the measured shear field on the square; Fourier transforming it and binning modes in $|\boldsymbol{\ell}|$ then yields an estimate of the power spectrum, once the power from the intrinsic ellipticity dispersion is subtracted. Better methods aim at minimizing the variance of the reconstructed power spectrum (Seljak 1998; Hu and White 2001). As mentioned before, the aperture mass dispersion is a filtered version of the power spectrum with such a narrow filter, that it contains essentially the same information as P_κ over the corresponding angular scale and at $\ell \sim 5/\theta$, provided P_κ has no sharp features.

6.4 Cosmic Shear and Cosmology

Why Cosmology From Cosmic Shear ?

Before continuing, it is worth to pause for a second and ask the question why one tries to investigate cosmological questions by using cosmic shear – since it is widely assumed that the CMB will measure 'all' cosmological quantities with high accuracy. Partial answers to this question are:

- Cosmic shear measures the mass distribution at much lower redshifts ($z \lesssim 1$) and at smaller physical scales [$R \sim 0.3\,h^{-1}\,(\theta/1')\,\mathrm{Mpc}$] than the CMB; indeed, it is the only way to map out the dark matter distribution directly without any assumptions about the relation between dark and baryonic matter.
- Cosmic shear measures the non-linearly evolved mass distribution and its associated power spectrum $P_\delta(k)$; hence, in combination with the CMB it allows us to study the evolution of the power spectrum and in particular, provide a very powerful test of the gravitational instability paradigm for structure growth.
- As was demonstrated by the recent results from the WMAP satellite (Bennett et al. 2003), the strongest constraints are derived when combining CMB measurements (constraining the power spectrum on large spatial scales) with measurements on substantially smaller scales, to break parameter degeneracies remaining from the CMB results alone (see Spergel et al. 2003). Hu and Tegmark (1999) have explicitly demonstrated how much the accuracy of estimates of cosmological parameters is improved when the CMB results from missions like WMAP and later Planck is complemented by cosmic shear measurements (see Fig. 34). In fact, as we shall see later, combinations of CMB anisotropy measurements have already been combined with cosmic shear measurements (see Fig. 47) and lead to substantially improved constraints on the cosmological parameters.
- It provides a fully independent way to probe the cosmological model; given the revolutionary claims coming from the CMB, SN Ia, and the LSS of the galaxy distribution, namely that more than 95% of the contents in the Universe is in a form that we have not the slightest idea about what it is (the names 'dark matter' and 'dark energy' reflect our ignorance about their physical nature), an additional independent verification of these claims is certainly welcome.
- For a foreseeable future, astronomical observations will provide the only possibility to probe the dark energy empirically. The equation of state of the dark energy can be probed best at relatively low redshifts, that is with SN Ia and cosmic shear observations, whereas CMB anisotropy measurements are relatively insensitive to the properties of the dark energy, as the latter was subdominant at the epoch of recombination.
- As we have seen in Sect. 5.8, cosmic shear studies provide a new and highly valuable search method for cluster-scale matter concentrations.

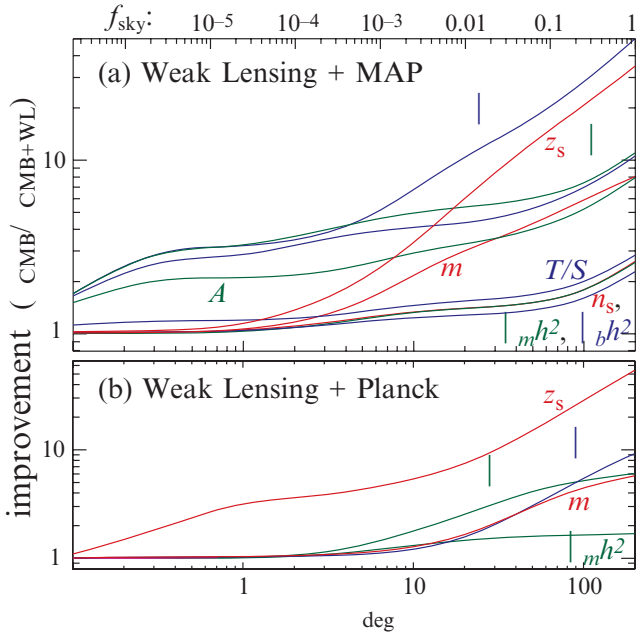

Fig. 34. The improvement of the accuracy of cosmological parameters when supplementing CMB data from WMAP (*upper panel*) and the Planck satellite (*lower panel*) by a cosmic shear survey of solid angle $\theta^2\pi$. The accuracies are significantly improved, certainly when combined with WMAP, but even in combination with Planck, the accuracies of the density parameters can be increased, when using next-generation cosmic shear surveys with hundreds of square degrees (from Hu and Tegmark 1999)

Expectations

The cosmic shear signal depends on the cosmological model, parameterized by $\Omega_{\rm m}$, Ω_Λ, and the shape parameter $\Gamma_{\rm spect}$ of the power spectrum, the normalization of the power spectrum, usually expressed in terms of σ_8, and the redshift distribution of the sources. By measuring $\xi_\pm$ over a significant range of angular scales one can derive constraints on these parameters. To first order, the amplitude of the cosmic shear signal depends on the combination $\sim\sigma_8\,\Omega_{\rm m}^{0.5}$, very similar to the cluster abundance. Furthermore, the cosmic shear signal shows a strong dependence on the source redshift distribution. These dependencies are easily understood qualitatively: A higher normalization σ_8 increases P_δ on all scales, thus increasing P_κ. The increase with $\Omega_{\rm m}$ is mainly due to the prefactor in (99), i.e. due to the fact that the light deflection depends on $\Delta\rho$, not just merely on $\delta = \Delta\rho/\bar\rho$, as most other cosmological probes. Finally, increasing the redshift of sources has two effects: first, the lens

efficiency $D_{\rm ds}/D_{\rm s} = f_K(w_{\rm s} - w)/f_K(w_{\rm s})$ at given distance w increases as the sources are moved further away, and second, a larger source redshift implies a longer ray path through the inhomogeneous matter distribution.

In Fig. 35 the predictions of the shear dispersion and the aperture mass dispersion are shown as a function of angular scale, for several cosmological models. The dependencies of the power spectrum P_κ on cosmological parameters and ℓ is reflected in these cosmic shear measures. In particular, the narrow filter function which relates the aperture mass dispersion to the power spectrum implies that the peak in $\ell^2 P_\kappa(\ell)$ at around $\ell \sim 10^4$ (see Fig. 32) translates into a peak of $\left\langle M_{\rm ap}^2 \right\rangle$ at around $\theta \sim 1'$. The non-linear evolution of the power spectrum is dominating the cosmic shear result for scales below

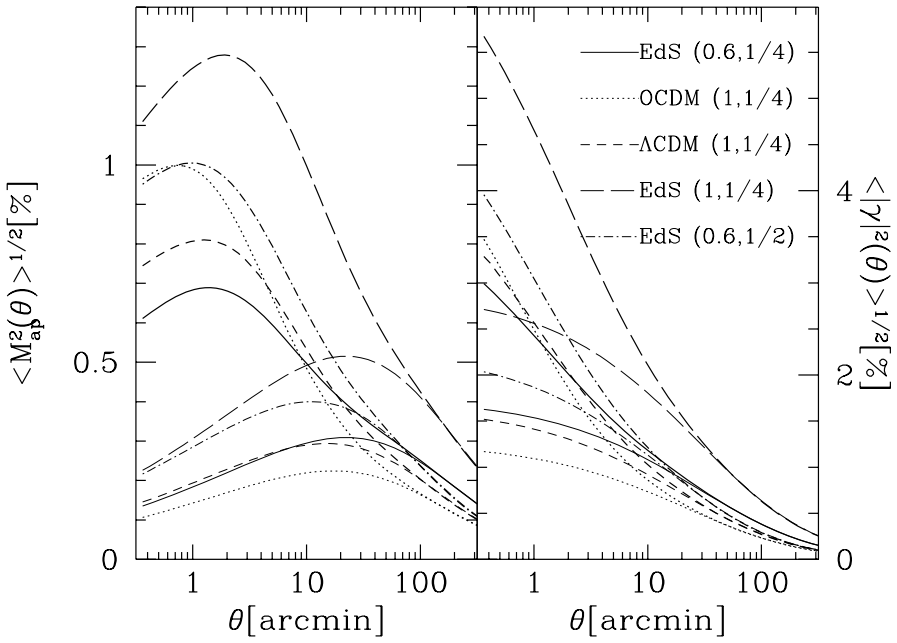

Fig. 35. The square root of the aperture mass dispersion (*left*) and of the shear dispersion (*right*), for the same cosmological models as were used for Fig. 32, again with results from assuming linear growth of structure in the Universe shown as thin curves, whereas the fully non-linear evolution was taken into account for the thick curves. One sees that the aperture mass signal is considerably smaller than that of the shear dispersion; this is due to the fact that the filter function $W_{\rm ap}$ is much narrower than $W_{\rm TH}$; hence, at a given angular scale, $\left\langle M_{\rm ap}^2 \right\rangle$ samples less power than $\left\langle |\bar\gamma|^2 \right\rangle$. However, this also implies that the aperture mass dispersion provides much more localized information about the power spectrum than the shear dispersion and is therefore a more useful statistics to consider. Other advantages of $\left\langle M_{\rm ap}^2 \right\rangle$ will be described further below. For scales below $\sim 30'$, the non-linear evolution of the power spectrum becomes very important (from Schneider et al. 1998a)

$\sim 30'$; the fact that the non-linear prediction approach the linear ones at somewhat smaller scales for the shear dispersion $\langle|\bar{\gamma}|^2\rangle$ is due to the fact that this statistics corresponds to a broad-band filter $W_{\rm TH}$ (106) of P_κ which includes the whole range of small ℓ values, which are less affected by non-linear evolution.

Deriving Constraints

From the measured correlation functions $\xi_\pm(\theta)$ (or any other measure of the cosmic shear, but we will concentrate on the statistics which is most easily obtained from real data), obtaining constraints on cosmological parameters can proceed through maximizing the likelihood $\mathcal{L}(p|\xi^{\rm obs})$, which yields the probability for the set of cosmological parameters being p, given the observed correlation function $\xi^{\rm obs}$. This likelihood is given by the probability $P(\xi^{\rm obs}|p)$ that the observed correlation function is $\xi^{\rm obs}$, given the parameters p. For a given set of parameters p, the correlation function $\xi(p)$ is predicted. If one assumes that the observed correlations $\xi^{\rm obs}$ are drawn from a (multi-variate) Gaussian probability distribution, then

$$P(\xi^{\rm obs}|p) = \frac{1}{(2\pi)^{n/2}\sqrt{\det {\rm Cov}}} \exp\left(\frac{-\chi^2(p,\xi^{\rm obs})}{2}\right) ,$$

with

$$\chi^2(p,\xi^{\rm obs}) = \sum_{ij} \left(\xi_i(p) - \xi_i^{\rm obs}\right) {\rm Cov}_{ij}^{-1} \left(\xi_j(p) - \xi_j^{\rm obs}\right) . \qquad (116)$$

Here, the $\xi_i = \xi(\theta_i)$ are the values of the correlation function(s) (i.e., either $\xi_\pm$, or using both) in angular bins, n is the number of angular bins in case either one of the $\xi_\pm$ is used, or if both are combined, twice the number of angular bins, and ${\rm Cov}_{ij}^{-1}$ is the inverse of the covariance matrix, which is defined as

$${\rm Cov}_{ij} = \left\langle \left[\xi_i(p) - \xi_i^{\rm obs}\right] \left[\xi_j(p) - \xi_j^{\rm obs}\right] \right\rangle , \qquad (117)$$

where the average is over multiple realizations of the cosmic shear survey under consideration. ${\rm Cov}_{ij}$ can be determined either from the $\xi_\pm$ itself, from simulations, or estimated from the data in terms of the $\xi_\pm^{\rm obs}$ (see Schneider et al. 2002b; Kilbinger and Schneider 2004, Simon et al. 2004). Nevertheless, the calculation of the covariance is fairly cumbersome, and most authors have used approximate methods to derive it, such as the field-to-field variations of the measured correlation. In fact, this latter approach may be more accurate than using the analytic expressions of the covariance in terms of the correlation function, which are obtained by assuming that the shear field is Gaussian, so that the four-point correlation function can be factorized as products of two-point correlators. As it turns out, $\xi_+(\theta)$ is strongly correlated across angular bins, much less so for $\xi_-(\theta)$; this is due to the fact that the filter function that describes ξ in terms of the power spectrum P_κ is much broader for ξ_+ (namely J_0) than J_4 which applies for ξ_-.

The accuracy with which $\xi_\pm$ can be measured, and thus the covariance matrix, depends on the number density of galaxies (that is, depth and quality of the images), the total solid angle covered by the survey, and its geometrical arrangement (compact survey vs. widely separated pointings). The accuracy is determined by a combination of the intrinsic ellipticity dispersion and the cosmic (or sampling) variance. The likelihood function then becomes

$$\mathcal{L}(p|\xi^{\rm obs}) = \frac{1}{(2\pi)^{n/2}\sqrt{\det {\rm Cov}}}\,\exp\left(\frac{-\chi^2(p,\xi^{\rm obs})}{2}\right)\,P_{\rm prior}(p)\;, \qquad (118)$$

where $P_{\rm prior}(p)$ contains prior information (or prejudice) about the parameters to be determined. For example, the redshift distribution of the sources (at given apparent magnitude) is fairly well known from spectroscopic redshift surveys, and so the prior probability for $z_{\rm s}$ would be chosen to be a fairly narrow function which describes this prior knowledge on the redshifts. One often assumes that all but a few parameters are known precisely, and thus considers a restricted space of parameters; this is equivalent to replacing the prior for those parameters which are fixed by a delta-'function'. If m parameters are assumed to be undetermined, but one is mainly interested in the confidence contours of $m' < m$ parameters, then the likelihood function is integrated over the remaining $m - m'$ parameters; this is called marginalization and yields the likelihood function for these m' parameters.

There are two principal contributions to the 'noise' of cosmic shear measurements. One is the contribution coming from the finite intrinsic ellipticity dispersion of the source galaxies, the other due to the finite data fields of any survey. This latter effect implies that only a *typical* part of the sky is mapped, whose properties will in general deviate from the *average* properties of such a region in the sky for a given cosmology. This effect is called cosmic variance, or sample variance. Whereas the noise from intrinsic ellipticity dispersions dominates at small angular scales, at scales beyond a few arcminutes the cosmic variance is always the dominating effect (e.g., Kaiser 1998; White and Hu 2000).

Of course, all of what was said above can be carried over to the other second-order shear statistics, with their respective covariance matrices. The first cosmic shear measurements were made in terms of the shear dispersion and compared to theoretical prediction from a range of cosmological models. As is true for the correlation functions, the shear dispersion is strongly correlated between different angular scales. This is much less the case for the aperture mass dispersion, where the correlation quickly falls off once the angular scales differ by more than a factor $\sim$1.5 (see Schneider et al. 2002b). Even less correlated is the power spectrum itself. These properties are of large interest if the results from a cosmic shear survey are displayed as a curve with error bars; for the aperture mass dispersion and the power spectrum estimates, these errors are largely uncorrelated. However, for deriving cosmological constraints, the correlation function $\xi_\pm$ are most useful since they contain all second-order information in the data, in addition of being the primary observable.

6.5 E-Modes, B-Modes

In the derivation of the lensing properties of the LSS, we ended up with an equivalent surface mass density. In particular, this implied that $\mathcal{A}$ is a symmetric matrix, and that the shear can be obtained in terms of κ or ψ. Now, the shear is a 2-component quantity, whereas both κ and ψ are scalar fields. This then obviously implies that the two shear components are not independent of each other !

Recall that (54) yields a relation between the gradient of κ and the first derivatives of the shear components; in particular, (54) implies that $\nabla \times \mathbf{u}_\gamma \equiv 0$, yielding a local constraint relation between the second derivatives of the shear components. The validity of this constraint equation guarantees that the imaginary part of (44) vanishes. This constraint is also present at the level of 2-point statistics, since one expects from (112) that

$$\int_0^\infty \mathrm{d}\theta\, \theta\, \xi_+(\theta) \mathrm{J}_0(\theta\ell) = \int_0^\infty \mathrm{d}\theta\, \theta\, \xi_-(\theta) \mathrm{J}_4(\theta\ell) \ .$$

Hence, the two correlation functions $\xi_\pm$ are not independent. The observed shear field is not guaranteed to satisfy these relations, due to noise, remaining systematics, or other effects. Therefore, searching for deviations from this relation allows a check for these effects. However, there might also be a 'shear' component present that is not due to lensing (by a single equivalent thin matter sheet κ). Shear components which satisfy the foregoing relations are called E-modes; those which don't are B-modes – these names are exported from the polarization of the CMB, which has the same mathematical properties as the shear field, namely that of a polar.

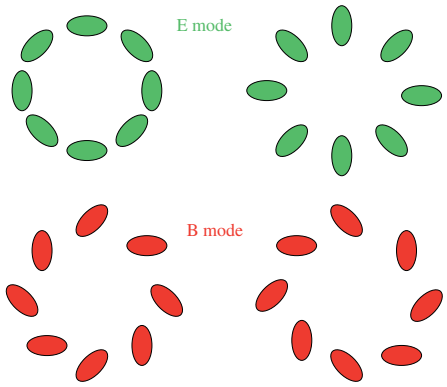

Fig. 36. Sketch of the distinction between E- and B-modes of the shear. The upper row shows a typical E-mode shear pattern coming from a mass overdensity (*left*) or underdensity (*right*), yielding tangential and radial alignment of the shear, respectively. The lower row shows a B-mode pattern, which is obtained from the E-mode pattern by rotating all shears by 45°. Those cannot be produced from gravitational lensing (from van Waerbeke and Mellier 2003)

The best way to separate these modes locally is provided by the aperture measures: $\langle M_{\rm ap}^2(\theta)\rangle$ is sensitive *only* to E-modes. If one defines in analogy – recall (77)

$$M_\perp(\theta) = \int \mathrm{d}^2\vartheta\, Q(|\boldsymbol{\vartheta}|)\,\gamma_\times(\boldsymbol{\vartheta})\;, \tag{119}$$

then $\langle M_\perp^2(\theta)\rangle$ is sensitive *only* to B-modes. In fact, one can show that for a pure E-mode shear field, $M_\perp \equiv 0$, and for a pure B-mode field, $M_{\rm ap} \equiv 0$. Furthermore, in general (that is, even if a B-mode is present), $\langle M_{\rm ap}\rangle = 0$, since $\langle\kappa\rangle = 0$, and $\langle M_\perp\rangle = 0$, owing to parity invariance: a non-zero mean value of $M_\perp$ would introduce a net orientation into the shear field. Using the same argument, one finds that $\langle M_{\rm ap}^m M_\perp^n\rangle = 0$ for n odd (Schneider 2003).

E/B-mode Decomposition of a Shear Field

There are a number of (equivalent) ways to decompose a shear field into its two modes. One is provided by the Kaiser and Squires mass reconstruction (44), which yields, for a general shear field, a complex surface mass density $\kappa = \kappa^{\rm E} + \mathrm{i}\kappa^{\rm B}$. Another separation is obtained by considering the vector field $\mathbf{u}_\gamma(\boldsymbol{\theta})$ (54) obtained from the first derivatives of the shear components. This vector will in general not be a gradient field; its gradient component corresponds to the E-mode field, the remaining one to the B-mode. Hence one defines

$$\nabla^2\kappa^{\rm E} = \nabla\cdot\mathbf{u}_\gamma \quad ; \quad \nabla^2\kappa^{\rm B} = \nabla\times\mathbf{u}_\gamma\;. \tag{120}$$

In full analogy with the 'lensing-only' case (i.e., a pure E-mode), one defines the (complex) potential $\psi(\boldsymbol{\theta}) = \psi^{\rm E}(\boldsymbol{\theta}) + \mathrm{i}\psi^{\rm B}(\theta)$ by the Poisson equation $\nabla^2\psi = 2\kappa$, and the shear is obtained in terms of the complex ψ in the usual way,

$$\begin{aligned}\gamma = \gamma_1 + \mathrm{i}\gamma_2 &= \left(\psi_{,11} - \psi_{,22}\right)/2 + \mathrm{i}\psi_{,12} \\ &= \left[\frac{1}{2}\left(\psi^{\rm E}_{,11} - \psi^{\rm E}_{,22}\right) - \psi^{\rm B}_{,12}\right] + \mathrm{i}\left[\psi^{\rm E}_{,12} + \frac{1}{2}\left(\psi^{\rm B}_{,11} - \psi^{\rm B}_{,22}\right)\right]\;.\end{aligned} \tag{121}$$

On the level of second-order statistics, one considers the Fourier transforms of the E- and B-mode convergence, and defines the two power spectra $P_{\rm E}$, $P_{\rm B}$, and the cross-power spectrum $P_{\rm EB}$ by

$$\begin{aligned}\left\langle\hat\kappa^{\rm E}(\boldsymbol{\ell})\hat\kappa^{\rm E*}(\boldsymbol{\ell}')\right\rangle &= (2\pi)^2\,\delta_{\rm D}(\boldsymbol{\ell}-\boldsymbol{\ell}')\,P_{\rm E}(\ell)\;,\\ \left\langle\hat\kappa^{\rm B}(\boldsymbol{\ell})\hat\kappa^{\rm B*}(\boldsymbol{\ell}')\right\rangle &= (2\pi)^2\,\delta_{\rm D}(\boldsymbol{\ell}-\boldsymbol{\ell}')\,P_{\rm B}(\ell)\;,\\ \left\langle\hat\kappa^{\rm E}(\boldsymbol{\ell})\hat\kappa^{\rm B*}(\boldsymbol{\ell}')\right\rangle &= (2\pi)^2\,\delta_{\rm D}(\boldsymbol{\ell}-\boldsymbol{\ell}')\,P_{\rm EB}(\ell)\;.\end{aligned} \tag{122}$$

From what was said above, the cross power $P_{\rm EB}$ vanishes for parity-symmetric shear fields, and we shall henceforth ignore it. The shear correlation functions

now depend on the power spectra of both modes, and are given as (Crittenden et al. 2002; Schneider et al. 2002a)

$$\xi_+(\theta) = \int_0^\infty \frac{\mathrm{d}\ell\,\ell}{2\pi}\,\mathrm{J}_0(\ell\theta)\,[P_\mathrm{E}(\ell) + P_\mathrm{B}(\ell)]\ ,$$

$$\xi_-(\theta) = \int_0^\infty \frac{\mathrm{d}\ell\,\ell}{2\pi}\,\mathrm{J}_4(\ell\theta)\,[P_\mathrm{E}(\ell) - P_\mathrm{B}(\ell)]\ .$$

Hence, in the presence of B-modes, the ξ_- correlation function cannot be obtained from ξ_+, as was the case for a pure E-mode shear field. The inverse relation (112) now gets modified to

$$P_\mathrm{E}(\ell) = \pi \int_0^\infty \mathrm{d}\theta\,\theta\ [\xi_+(\theta)\mathrm{J}_0(\ell\theta) + \xi_-(\theta)\mathrm{J}_4(\ell\theta)]\ ,$$

$$P_\mathrm{B}(\ell) = \pi \int_0^\infty \mathrm{d}\theta\,\theta\ [\xi_+(\theta)\mathrm{J}_0(\ell\theta) - \xi_-(\theta)\mathrm{J}_4(\ell\theta)]\ . \tag{123}$$

Hence, the two power spectra can be obtained from the shear correlation functions. However, due to the infinite range of integration, one would need to measure the correlation functions over all angular scales to apply the previous equations for calculating the power spectra. Much more convenient for the E/B-mode decomposition is the use of the aperture measures, since one can show that

$$\left\langle M_\mathrm{ap}^2 \right\rangle(\theta) = \frac{1}{2\pi} \int_0^\infty \mathrm{d}\ell\,\ell\,P_\mathrm{E}(\ell)\,W_\mathrm{ap}(\theta\ell)\ ,$$

$$\left\langle M_\perp^2 \right\rangle(\theta) = \frac{1}{2\pi} \int_0^\infty \mathrm{d}\ell\,\ell\,P_\mathrm{B}(\ell)\,W_\mathrm{ap}(\theta\ell)\ , \tag{124}$$

so that these two-point statistics clearly separate E- and B-modes. In addition, as mentioned before, they provide a highly localized measure of the corresponding power spectra, since the filter function $W_\mathrm{ap}(\eta)$ involved is very narrow. As was true for the E-mode only case, the aperture measures can be expressed as finite integrals over the correlation functions,

$$\left\langle M_\mathrm{ap}^2 \right\rangle(\theta) = \frac{1}{2} \int \frac{\mathrm{d}\vartheta\,\vartheta}{\theta^2} \left[\xi_+(\vartheta)\,T_+\!\left(\frac{\vartheta}{\theta}\right) + \xi_-(\vartheta)\,T_-\!\left(\frac{\vartheta}{\theta}\right)\right]\ ,$$

$$\left\langle M_\perp^2 \right\rangle(\theta) = \frac{1}{2} \int \frac{\mathrm{d}\vartheta\,\vartheta}{\theta^2} \left[\xi_+(\vartheta)\,T_+\!\left(\frac{\vartheta}{\theta}\right) - \xi_-(\vartheta)\,T_-\!\left(\frac{\vartheta}{\theta}\right)\right]\ , \tag{125}$$

where the two functions $T_\pm$ are the same as in (115) and have been given explicitly in Schneider et al. (2002a) for the weight function Q given in (81), and in Jarvis et al. (2003) for the weight function (110). Hence, the relations (125) remove the necessity to calculate the aperture measures by placing apertures

on the data field which, owing to gaps and holes, would make this an inaccurate and biased determination. Instead, obtaining the correlation functions from the data is all that is needed.

The relations given above have been applied to recent cosmic shear surveys, and significant B-modes have been discovered (see Sect. 7); the question now is what are they due to ? As mentioned before, the noise, which contributes to both E- and B-modes in similar strengths, could be underestimated, the cosmic variance which also determines the error bars on the aperture measures and which depends on fourth-order statistical properties of the shear field could also be underestimated, there could be remaining systematic effects, or B-modes could indeed be present. There are two possibilities known to generate a B-mode through lensing: The first-order in Φ (or 'Born') approximation may not be strictly valid, but as shown by ray-tracing simulations through cosmic matter fields (e.g., Jain et al. 2000), the resulting B-modes are expected to be very small. Clustering of sources also yields a finite B-mode (Schneider et al. 2002a), but again, this effect is much smaller than the observed amplitude of the B-modes (see Fig. 37).

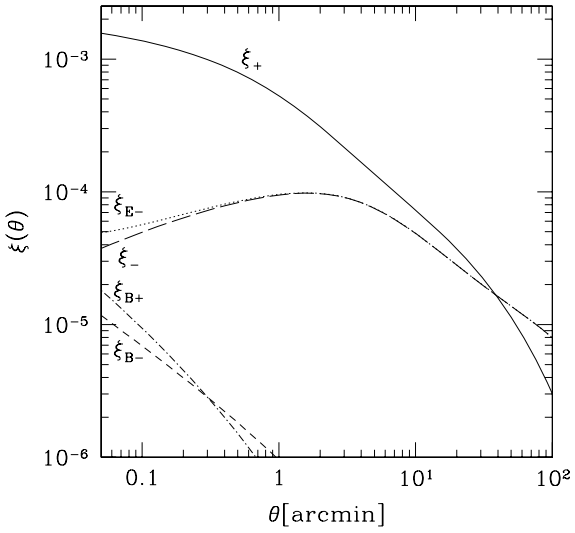

Fig. 37. The correlation functions $\xi_\pm(\theta)$ for a ΛCDM model with $\Gamma_{\rm spect} = 0.21$ and $\sigma_8 = 1$, and a source population with mean redshift of $\langle z_{\rm s}\rangle = 1.5$. Also plotted are the corresponding correlation functions that arise separately from the E- and B-modes, with the $\xi_{\rm E+}$ mode curve coinciding within the line thickness with ξ_+. In this calculation, the clustering of the faint galaxy population was taken into account, and they give rise to a very small B-mode contribution, as can be seen from the $\xi_{\rm B\pm}$ curves. The smallness of the B-mode due to intrinsic source clustering renders this effect not viable to explain the B-modes observed in some of the cosmic shear surveys (from Schneider et al. 2002a)

Intrinsic Alignment of Source Galaxies

Currently the best guess for the generation of a finite B-mode are intrinsic correlations of galaxy ellipticities. Such intrinsic alignments of galaxy ellipticities can be caused by tidal gravitational fields during galaxy formation, owing to tidal interactions between galaxies, or between galaxies and clusters. Predictions of the alignment of the projected ellipticity of the galaxy mass can be made analytically (e.g. in the frame of tidal torque theory) or from numerical simulations; however, the predictions from various groups differ by large factors (e.g., Croft and Metzler 2001; Crittenden et al. 2001; Heavens et al. 2000; Jing 2002) which means that the process is not well understood at present. For example, the results of these studies depend on whether one assumes that the light of a galaxy is aligned with the dark matter distribution, or aligned with the angular momentum vector of the dark halo. This is related to the question of whether the orientation of the galaxy light (which is the issue of relevance here) is the same as that of the mass.

If intrinsic alignments play a role, then

$$\xi_+ = \left\langle \epsilon_i \, \epsilon_j^* \right\rangle = \left\langle \epsilon_i^{(\mathrm{s})} \, \epsilon_j^{(\mathrm{s})*} \right\rangle + \xi_+^{\mathrm{lens}} \, , \tag{126}$$

and measured correlations $\xi_\pm$ contain both components, the intrinsic correlation and the shear. Of course, there is no reason why intrinsic correlations should have only a B-mode. If a B-mode contribution is generated through this process, then the measured E-mode is most likely also contaminated by intrinsic alignments. Given that intrinsic alignments yield ellipticity correlations only for spatially close sources (i.e., close in 3-D, not merely in projection), it is clear that the deeper a cosmic shear survey is, and thus the broader the redshift distribution of source galaxies, the smaller is the relative amplitude of an intrinsic signal. Most of the theoretical investigations on the strength of intrinsic alignments predict that the deep cosmic shear surveys (say, with mean source redshifts of $\langle z_{\mathrm{s}} \rangle \sim 1$) are affected at a $\sim$10% level, but that shallower cosmic shear surveys are more strongly affected; for them, the intrinsic alignment can be of same order or even larger than the lensing signal.

However, the intrinsic signal can be separated from the lensing signal if redshift information of the sources is available, owing to the fact that $\left\langle \epsilon_i^{(\mathrm{s})} \, \epsilon_j^{(\mathrm{s})*} \right\rangle$ will be non-zero only if the two galaxies are at essentially the same redshift. Hence, if z-information is available (e.g., photometric redshifts), then galaxy pairs which are likely to have similar redshifts are to be avoided in estimating the cosmic shear signal (King and Schneider 2002, Heymans and Heavens 2003, Takada and White 2004). This will change the expectation value of the shear correlation function, but in a controllable way, as the redshifts are assumed to be known. Indeed, using (photometric) redshifts, one can simultaneously determine the intrinsic and the lensing signal, essentially providing a cosmic shear tomography (King and Schneider 2003). This again is accomplished by

employing the fact that the intrinsic correlation can only come from galaxies very close in redshift. Hence, in the presence of intrinsic alignments, the redshift dependent correlation functions $\xi_\pm(z_1, z_2; \theta)$ between galaxies with estimated redshifts z_i are expected to show a strong peak over the range $|z_1 - z_2| \lesssim \Delta z$, where Δz is the typical uncertainty in photometric redshifts. It is this peak that allows one to identify and subtract the intrinsic signal from the correlation functions. An efficient method to calculate the covariance of the redshift-dependent correlation functions has been developed by Simon et al. (2004), where the improvement in the constraints on cosmological parameters from redshift information has been studied, confirming the earlier results by Hu (1999) which were based on considerations of the power spectrum.

Brown et al. (2003) obtained a measurement of the intrinsic ellipticity correlation from the Super-COSMOS photographic plate data, where the galaxies are at too low a redshift for cosmic shear playing any role. Heymans et al. (2004) used the COMBO-17 data set (that will be described in Sect. 7.3 below) for which accurate photometric redshifts are available to measure the intrinsic alignment. The results from both studies is that the models predicting a large intrinsic amplitude can safely be ruled out. Nevertheless, intrinsic alignment affects cosmic shear measurements, at about the 2% level for a survey with the depth of the VIRMOS-DESCART survey, and somewhat more for the slightly shallower COMBO-17 survey. Hence, to obtain precision measurements of cosmic shear, very important for constraining the equation of state of dark energy, these physically close pairs of galaxies need to be identified in the survey, making accurate photometric redshifts mandatory.

Correlation Between Intrinsic Ellipticity and Shear

The relation (126) above implicitly assumes that the shear is uncorrelated with the intrinsic shape of a neighboring galaxy. However, as pointed out by Hirata and Seljak (2004), this is not necessarily the case. Hence consider galaxies at two significantly different redshifts $z_i < z_j$. For them, the first term in (126) vanishes. However, making use of $\epsilon = \epsilon^{(\mathrm{s})} + \gamma$, one finds

$$\left\langle \epsilon_i \epsilon_j^* \right\rangle = \left\langle \epsilon_i^{(\mathrm{s})} \gamma_j^* \right\rangle + \xi_+^{\mathrm{lens}} \,, \tag{127}$$

where the first term on the right-hand side describes the correlation between the intrinsic ellipticity of the lower-redshift galaxy with the shear along the l.o.s. to the higher-redshift one. The correlation can in principle be non-zero: if the intrinsic alignment of the light of a galaxy is determined by the large-scale tidal gravitational field, then this tidal field at the redshift z_i causes both, an alignment of the nearer galaxy and a contribution to the shear of the more distant one (see Fig. 38). This alignment effect can therefore not be removed by considering only pairs at different redshifts.

The importance of this effect depends on the nature of the alignment of galaxies relative to an external tidal field. If the alignment is linear in the tidal

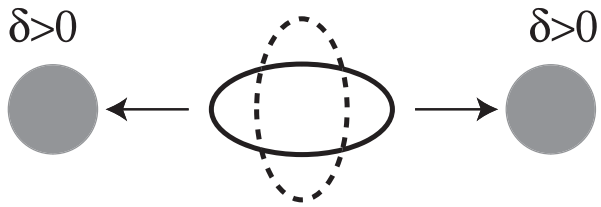

Fig. 38. A tidal gravitational field, for example caused by two matter concentrations, can produce an alignment of a galaxy situated at the same redshift (indicated by the *solid ellipse*), as well as contributing to the shear toward a more distant galaxy (as indicated by the *dashed ellipse*) (from Hirata and Seljak 2004)

field strength, then this effect can be a serious contaminant of the cosmic shear signal, in particular for relatively shallow surveys (where the mean source redshift is small); in particular, this effect can yield much larger contaminations than the intrinsic alignment given by the first term in (126). As can be seen from Fig. 38, the resulting contribution is negative, hence decreases the lensing signal. If, however, the intrinsic alignment depends quadratically on the tidal field, as is suggested by tidal torque theory, than this effect is negligible. Whether or not this effect is relevant needs to be checked from observations. Assuming that the matter density field is represented approximately by the galaxy distribution, the latter can be used to estimate the tidal gravitational field, in particular its direction. Alternatively, since the correlation between the intrinsic alignment and the shear toward more distant galaxies has a different redshift dependence than the lensing shear signal, these two contributions can be disentangled from the z-dependence of the signal.

It should be noted that the use of photometric redshifts also permits to study the cosmic shear measures as a function of source redshift; hence, one can probe various redshift projections $P_\kappa(\ell)$ of the underlying power spectrum $P_\delta(k;z)$ separately. This is due to the fact that the cosmic shear signal from different populations of galaxies (i.e., with different redshift distributions) lead to different weight functions $g(w)$ [see (94)], and thus to different weighting in the projection (99) of the power spectrum. Not surprisingly, uncertainties of cosmological parameters are thereby reduced (Hu 1999; Simon et al. 2004). Also, as shown by Taylor (2001), Hu and Keeton (2002) and Bacon and Taylor (2003), in principle the three-dimensional mass distribution $\delta(\boldsymbol{x})$ can be reconstructed if the redshifts of the source galaxies are known (see Sect. 7.6).

6.6 Predictions; Ray-Tracing Simulations

The power spectrum of the convergence P_κ can be calculated from the power spectrum of the cosmological matter distribution P_δ, using (99); the latter in turn is determined by the cosmological model. However, since the non-linear

evolution of the power spectrum is essential for making accurate quantitative predictions for the shear properties, there is no analytic method known how to calculate the necessary non-linear P_δ. As was mentioned in Sect. 6.1 of IN, fairly accurate fitting formulae exist which yield a closed-form expression for P_δ and which can be used to obtain P_κ (see, e.g., Jain and Seljak 1997). Nevertheless, there are a number of reasons why this purely analytic approach should at least be supplemented by numerical simulations.

- First, the fitting formulae for P_δ (Peacock and Dodds 1996; Smith et al. 2003) have of course only a finite accuracy, and are likely to be insufficient for comparison with results from the ongoing cosmic shear surveys which are expected to yield very accurate measurements, owing to their large solid angle.
- A second reason why simulations are needed is to test whether the various approximations that enter the foregoing analytical treatment are in fact accurate enough. To recall them, we employed the Born approximation, i.e., neglected terms of higher order than linear in the Newtonian potential when deriving the convergence, and we assumed that the shear everywhere is small, so that the difference between shear and reduced shear can be neglected, at least on average. This, however, is not guaranteed: regions in the sky with large shear are most likely also those regions where the convergence is particularly large, and therefore, there one expects a correlation between γ and κ, which can affect the dispersion of $g = \gamma/(1-\kappa)$.
- Third, whereas fairly accurate fitting formulae exist for the power spectrum, this is not the case for higher-order statistical properties of the matter distribution; hence, when considering higher-order shear statistics (Sect. 9), numerical simulations will most likely be the only way to obtain accurate predictions.
- The covariance of the shear correlations (and all other second-order shear measures) depends on fourth-order statistics of the shear field, for which hardly any useful analytical approximations are available. The analytical covariance estimates are all based on the Gaussian assumption for the fourth-order correlators. Therefore, simulations are invaluable for the calculation of these covariances, which can be derived for arbitrary survey geometries.

Ray-Tracing Simulations: The Principle

The simulations proceed by following light rays through the inhomogeneous matter distribution in the Universe. The latter is generated by cosmological simulations of structure evolution. Those start at an early epoch by generating a realization of a Gaussian random field with a power spectrum according to the cosmological model considered, and follow the evolution of the density and velocity field of the matter using Newtonian gravity in an expanding Universe.

The mass distribution is represented by discrete particles whose evolution in time is followed. A finite volume of the Universe is simulated this way, typically a box of comoving side-length L, for which periodic boundary conditions are applied. This allows one to use Fast Fourier Transforms (FFT) to evaluate the gravitational potential and forces from the density distribution. The box size L should be chosen such that the box contains a representative part of the real Universe, and must therefore be larger than the largest scales on which structure is expected, according to the power spectrum; a reasonable choice is $L \gtrsim 100h^{-1}\,\mathrm{Mpc}$. The number of grid points and the number of particles that can be distributed in this volume is limited by computer memory; modern simulations work typically with 256^3 points and the same number of particles, though larger simulations have also been carried out; this immediately yields the size of grid cells, of order $0.5h^{-1}\,\mathrm{Mpc}$. This comoving length, if located at a redshift of $z \sim 0.3$ (which is about the most relevant for cosmic shear), subtends an angle of roughly $2'$ on the sky. The finite number of particles yields the mass resolution of the simulations, which is typically $\sim 10^{10}h^{-1}M_\odot$, depending on cosmological parameters.

In order to obtain higher spatial resolution, force calculations are split up into near-field and far-field forces. The gravitational force due to the distant matter distribution is obtained by grid-based FFT methods, whereas the force from nearby masses is calculated from summing up the forces of individual particles; such simulations yield considerably higher resolution of the resulting mass distribution. Since the matter in these simulations is represented by massive particles, these can undergo strong interactions, leading to (unphysical) large orbital deflections. In order to avoid these unphysical strong collisions, the force between pairs of particles is modified at short distances, typically comparable to the mean separation of two particles in the simulation. This softening length defines the minimum length scale on which the results from numerical simulations can be considered reliable. Cosmological simulations consider either the dark matter only or, more recently, the hydrodynamics effects of baryons have been incorporated as well.

The outcome of such simulations, as far as they are relevant here, are the 3-dimensional positions of the matter particles at different (output) times or redshifts. In order to study the light propagation through this simulated mass distribution, one employs multiple lens-plane theory. First, the volume between us and sources at some redshift z_s is filled with boxes from the cosmological simulations. That is, the comoving distance $w_\mathrm{s} = w(z_\mathrm{s})$ is split up into n intervals of length L, and the mass distribution at an output time close to $t_i = t(w = (i - 1/2)L)$ is considered to be placed at this distance. In this way, one has a light cone covered by cubes containing representative matter distributions. Since the mass distributions at the different times t_i are not independent of each other, but one is an evolved version of the earlier one, the resulting mass distribution is highly correlated over distances much larger than L. This can be avoided by making use of the statistical homogeneity and isotropy of the mass distribution: each box can be

translated by an arbitrary two-dimensional vector, employing the periodicity of the mass distribution, and rotated by an arbitrary angle; furthermore, the three different projections of the box can be used for its orientation. In this way – a kind of recycling of numerical results – the worst correlations are removed.

Alternatively, one can combine the outputs from several simulations with different realizations of the initial conditions. In this case, one can use simulation boxes of different spatial extent, to match the comoving size of a big light cone as a function of redshift. That is, for a given light-cone size, only relatively small boxes are needed at low redshifts, and bigger ones at higher redshift (see White and Hu 2000).

Second, the mass in each of these boxes is projected along the line-of-sight, yielding a surface mass density at the appropriate comoving distance $w_i = (i - 1/2)L$. Each of these surface mass densities can now be considered a lens plane, and the propagation of light can be followed from one lens plane to the next; the corresponding theory was worked out in detail by Blandford and Narayan(1986; see also Chap. 9 of SEF), but applied as early as 1970 by Refsdal (1970) for a cosmological model consisting of point masses only (see also Schneider and Weiss 1988a,b). Important to note is that the surface mass density Σ in each lens plane is the projection of $\Delta\rho = \rho - \bar{\rho}$ of a box, so that for each lens plane, $\langle\Sigma\rangle = 0$. As has been shown in Seitz et al. (1994), this multiple lens-plane approach presents a well-defined discretization of the full 3-dimensional propagation equations. Light bundles are deflected and distorted in each lens plane and thus represented as piecewise straight rays. The resulting Jacobi matrix $\mathcal{A}$ is then obtained as a sum of products of the tidal matrices in the individual lens planes, yielding a discretized version of the form (88) for $\mathcal{A}$. The result of such simulations is then the matrix $\mathcal{A}(\boldsymbol{\theta})$ on a predefined angular grid, as well as the positions $\boldsymbol{\beta}(\boldsymbol{\theta})$ in the source plane. The latter will not be needed here, but have been used in studies of multiple images caused by the LSS (see Wambsganss et al. 1998).

One needs special care in applying the foregoing prescription; in particular, in the smoothing process to obtain a mass distribution from the discrete particles; Jain et al. (2000) contains a detailed discussion on these issues.[10] The finite spatial resolution in the simulations translates into a redshift-dependent angular resolution, which degrades for the low redshift lens planes; on the other hand, those have a small impact on the light propagation due to the large value of $\Sigma_{\rm cr}$ for them [see (10) of IN]. The discreteness of particles gives rise to a shot-noise term in the mass distribution, yielding increased power on small angular scales.

[10] For other recent ray-tracing simulations related to cosmic shear, see e.g. Barber et al. (2000); Hamana and Mellier (2001); Premadi et al. (2001); Taruya et al. (2002); Fluke et al. (2002); Barber (2002); Vale and White (2003).

Results From Ray-Tracing Simulations

We shall summarize here some of the results from ray-tracing simulation:

- Whereas the Jacobi matrix in this multi-deflection situation is no longer symmetric, the contribution from the asymmetry is very small. The power spectrum of the asymmetric part of $\mathcal{A}$ is at least three orders of magnitude smaller than the power spectrum P_κ, for sources at $z_\mathrm{s} = 1$ (Jain et al. 2000). This result is in accord with analytical expectations (e.g., Bernardeau et al. 1997; Schneider et al. 1998a), i.e., that terms quadratic in the Newtonian potential are considerably smaller than first-order terms, and supports the validity of the Born approximation. Furthermore, this result suggests that a simpler method for predicting cosmic shear distributions from numerical simulations may be legitimate, namely to project the mass distribution of all lens planes along the grid of angular positions, with the respective weighting factors, according to (92), i.e., employing the Born approximation. Of course this simplified method is computationally much faster than the full ray-tracing.
- The power spectra obtained reproduce the ones derived using (99), over the range of wavevectors which are only mildly affected by resolution and discreteness effects. This provides an additional check on the accuracy of the fitting formulae for the non-linear power spectrum.
- The simulation results give the full two-dimensional shear map, and thus can be used to study properties other than the second-order ones, e.g., higher-order statistics, or the occurrence of circular shear patters indicating the presence of strong mass concentrations. An example of such maps is shown in Fig. 26. These shear maps can be used to simulate real surveys, e.g, including the holes in the data field resulting from masking or complicated survey geometries, and thus to determine the accuracy with which the power spectra can be determined from such surveys. Note that in order to quantify the error (or covariance matrix) of any second-order statistics, one needs to know the fourth-order statistics, which in general cannot be obtained analytically when outside the linear (Gaussian) regime. Simulations are also used to obtain good survey strategies.

Higher-Order Correction Terms

Up to now we have considered the lowest-order approximation of the Jacobi matrix (88) and have argued that this provides a sufficiently accurate description. Higher-order terms in Φ were neglected since we argued that, because the Newtonian potential is very small, these should play no important role. However, this argument is not fully correct since, whereas the potential certainly is small, its derivatives are not necessarily so. Of course, proper ray-tracing simulation take these higher-order terms automatically into account.

We can consider the terms quadratic in Φ when expanding (88) to higher order. There are two such terms, one containing the product of second-order derivatives of Φ, the other a product of first derivatives of Φ and its third derivatives. The former is due to lens-lens coupling: The shear and surface mass densities from different redshifts (or lens planes, in the discretized approximation) do not simply add, but multi lens plane theory shows that the tidal matrices from different lens planes get multiplied. The latter term comes from dropping the Born approximation and couples the deflection of a light ray (first derivative of Φ) with the change of the tidal matrix with regards to the position (third derivatives of Φ). These terms are explicitly given in the appendix of Schneider et al. (1998a), in Bernardeau et al. (1997) and in Cooray and Hu (2002) and found to be indeed small, providing corrections of at most a few percent. Furthermore, Hamana (2001) has shown that the magnification bias caused by the foreground matter inhomogeneities on the selection of background galaxies has no practical effect on second-order cosmic shear statistics.

Another effect that affects the power spectrum P_κ is the difference between shear and reduced shear, the latter being the observable. Since the correlation function of the reduced shear is the correlation function of the shear plus a term containing a product of two shears and one surface mass density, this correction depends linearly on the third-order statistical properties of the projected mass κ. Also this correction turns out to be very small; moreover, it does not give rise to any B-mode contribution (Schneider et al. 2002a).

7 Large-Scale Structure Lensing: Results

After the theory of cosmic shear was considered in some detail in the previous section, we shall summarize here the observational results that have been obtained so far. In fact, as we will see, progress has been incredibly fast over the past ∼four years, with the first detections reported in 2000, and much larger surveys being available by now, with even larger ones ongoing or planned. Already by now, cosmic shear is one of the pillars on which our cosmological model rests.

The predictions discussed in the previous section have shown that the rms value of cosmic shear is of the order of ∼2 % on angular scales of ∼1′, and considerably smaller on larger scales. These small values make the measurements of cosmic shear particularly challenging, as the observational and instrumental effects described in Sect. 3 are expected to be larger than the cosmic shear signal, and thus have to be understood and removed with great precision. For example, the PSF anisotropy of nearly all wide-field cameras is considerably larger than a few percent and thus needs to be corrected for. But, as also discussed in Sect. 3, methods have been developed and thoroughly tested which are able to do so.

7.1 Early Detections of Cosmic Shear

Whereas the theory of cosmic shear was worked out in the early 1990's (Blandford et al. 1991; Miralda-Escudé 1991; Kaiser 1992), it took until the year 2000 before this effect was first discovered.[11] The reason for this evolution must be seen by a combination of instrumental developments, i.e. the wide-field CCD mosaic cameras, and the image analysis software, like IMCAT (the software package encoding the KSB method discussed in Sect. 3.5), with which shapes of galaxies can be accurately corrected for PSF effects. Then in March 2000, four groups independently announced their first discoveries of cosmic shear (Bacon et al. 2000; Kaiser et al. 2000; van Waerbeke et al. 2000, Wittman et al. 2000). In these surveys, of the order of 10^5 galaxy images have been analyzed, covering about 1 deg^2. Later that year, Maoli et al. (2001) reported a significant cosmic shear measurement from 50 widely separated FORS1@VLT images, each of size $\sim 6\farcm5 \times 6\farcm5$, which also agreed with the earlier results. The fact that the results from four independent teams agreed within the respective error bars immediately lend credit to this new window of observational cosmology. This is also due to the fact that 4 different telescopes, 5 different cameras (the UH8K and CFH12K at CFHT, the $8' \times 16'$-imager on WHT, the BTC at the 4m-CTIO telescope and FORS1 at the VLT), independent data reduction tools and at least two different image analysis methods have been used. These early results are displayed in Fig. 39, where the (equivalent) shear dispersion is plotted as a function of effective circular aperture radius, together with the predictions for several cosmological models. It is immediately clear that a high-normalization Einstein-de Sitter model can already be excluded from these early results, but the other three models displayed are equally valid approximations to the data.

Maoli et al. (2001) considered the constraints one obtains by combining the results from these five surveys, in terms of the normalization parameter σ_8 of the power spectrum. The confidence contours in the $\Omega_\mathrm{m} - \sigma_8$-plane are shown in Fig. 40. There is clearly a degeneracy between these two parameters from the data sets considered, roughly tracing $\sigma_8 \sim 0.59\Omega_\mathrm{m}^{-0.47}$; although the best fitting model is defined by $\Omega_\mathrm{m} = 0.26$, $\sigma_8 = 1.1$, it cannot be significantly distinguished from, e.g., a $\Omega_\mathrm{m} = 1$, $\sigma_8 = 0.62$ model since the error bars displayed in Fig. 39 are too large and the range of angular scales over which the shear was measured is too small. In Fig. 40, the solid curve displays the normalization as obtained from the abundance of massive clusters, which is seen to follow pretty much the valley of degeneracy from the cosmic shear analysis. This fact should not come as a surprise, since the cluster abundance probes the power spectrum on a comoving scale of about $8h^{-1}$ Mpc, which is

[11] An early heroic attempt by Mould et al. (1994) to detect cosmic shear on a single $\sim 9' \times 9'$ field only yielded an upper limit, and the putative detection of a shear signal by Schneider et al. (1998b; see also Fort et al. 1996) in three $2' \times 2'$ fields is, due to the very small sky area, of no cosmological relevance.

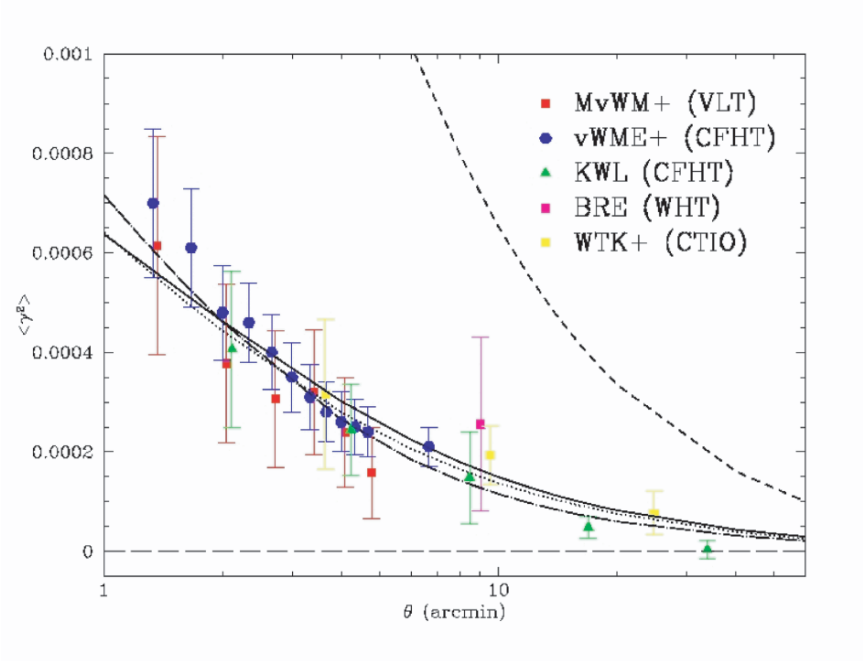

Fig. 39. Shear dispersion as a function of equivalent circular aperture radius as obtained from the first five measurements of cosmic shear (MvWM+: Maoli et al. 2001; vWME+: van Waerbeke et al. 2000; KWL: Kaiser, Wilson and Luppino 2000; BRE: Bacon, Refregier and Ellis 2000; WTK: Wittman et al. 2000). The data points within each team are not statistically independent, due to the fairly strong covariance of the shear dispersion on different angular scales, but points from different teams are independent (see text). The error bars contain the noise from the intrinsic ellipticity dispersion and, for some of the groups, also an estimate of cosmic variance. The four curves are predictions from four cosmological models; the upper-most one corresponds to an Einstein-de Sitter Universe with normalization $\sigma_8 = 1$, and can clearly be excluded by the data. The other three models are cluster normalized – see Sect. 4.4 of IN – and all provide equally good fits to these early data (courtesy: Y. Mellier)

comparable to the median scale probed by the cosmic shear measurements. However, the predictions of the cluster abundance rely on the assumption that the initial density field was Gaussian, whereas the cosmic shear prediction is independent of this assumption, which therefore can be tested by comparing the results from both methods.

7.2 Integrity of the Results

As mentioned before, the cosmic shear effects are smaller than many observational effects (like an anisotropic PSF) that could mimic a shear; it is therefore

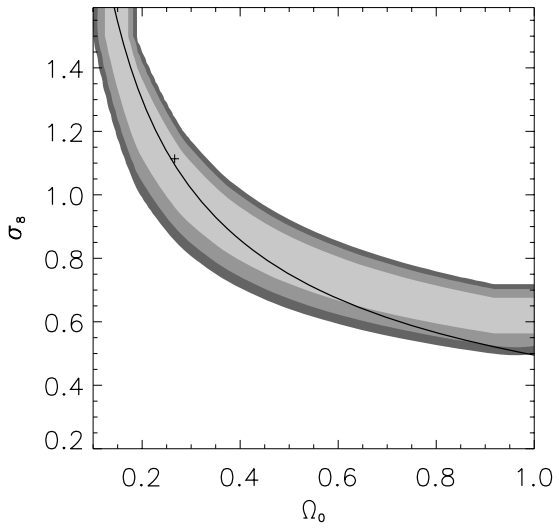

Fig. 40. Constraints on $\Omega_{\rm m}$ and σ_8 from the five surveys shown in Fig. 39; shown are 1, 2 and 3-σ confidence regions. The cross denotes the best-fitting model, but as can be seen, these two parameters are highly degenerate with the data used. The solid curve displays the constraint from cluster normalization (from Maoli et al. 2001)

necessary to exclude as much as possible such systematics from the data. The early results described above were therefore accompanied by quite a large number of tests; they should be applied to all cosmic shear surveys as a sanity check. A few of those shall be mentioned here.

Stellar Ellipticity Fits

The ellipticity of stellar objects should be well fitted by a low-order function, so one is able to predict the PSF anisotropy at galaxy locations. After subtracting this low-order fit from the measured stellar ellipticities, there should be no coherent spatial structure remaining, and the ellipticity dispersion of the corrected ellipticities should be considerably smaller that the original ones, essentially compatible with measurement noise.

Correlation of PSF Anisotropy with Corrected Galaxy Ellipticities

After correcting for the anisotropy of the PSF, there should remain no correlation between the corrected galaxy ellipticities and the ellipticity of the PSF. This correlation can be measured by considering $\langle \epsilon\, \epsilon^* \rangle$, where ϵ is the corrected galaxy ellipticity (31), and ϵ^* the uncorrected stellar ellipticity (i.e., the PSF anisotropy). Bacon et al. (2000) found that for fairly low signal-to-noise galaxy images, this correlation was significantly different from zero, but for galaxies with high S/N (only those entered their cosmic shear analysis), no

significant correlation remained. The same was found in van Waerbeke et al. (2000), except that the average $\langle\epsilon_1\rangle$ was slightly negative, but independent of ϵ_1^*. The level of $\langle\epsilon_1\rangle$ was much smaller than the estimated cosmic shear, and does not affect the latter by more than 10 %.

Spatial Dependence of Mean Galaxy Ellipticity

When a cosmic shear survey consist of many uncorrelated fields, the mean galaxy ellipticity at a given position on the CCD chips should be zero, due to the assumed statistical isotropy of the shear field. If, on the other hand, the shear averaged over many fields shows a dependence on the chip position, most likely optical distortions and/or PSF effects have not been properly accounted for.

Parity Invariance

The two-point correlation function $\xi_\times(\theta) = \langle\gamma_\mathrm{t}\gamma_\times\rangle\,(\theta)$ is expected to vanish for a density distribution that is parity symmetric. More generally, every astrophysical cause for a 'shear' signal (such as intrinsic galaxy alignments, or higher-order lensing effects) is expected to be invariant under parity transformation. A significant cross-correlation $\xi_\times$ would therefore indicate systematic effects in the observations and/or data analysis.

7.3 Recent Cosmic Shear Surveys

Relatively soon after the announcement of the first cosmic shear detections, additional results were published. These newer surveys can roughly be classified as follows: deep surveys, shallower, but much wider surveys, and special surveys, such as obtained with the Hubble Space Telescope. We shall mention examples of each of these classes here, without providing a complete list.

Deep Surveys

Currently the largest of the deep surveys from which cosmic shear results have been published is the VIRMOS-DESCART survey, carried out with the CFH12K camera at the CFHT; this camera covers about $45' \times 30'$ in one exposure. The exposure time of the images, taken in the I-band, is one hour. The survey covers four fields of $2^\circ \times 2^\circ$ each, of which roughly $8.5\,\mathrm{deg}^2$ have been used for a weak lensing analysis up to now (van Waerbeke et al. 2001, 2002). About 20% of the area is masked out, to account for diffraction spikes, image defects, bright and large foreground objects etc. The number density of galaxy images used for the cosmic shear analysis is about $17\,\mathrm{arcmin}^{-2}$. A small part of this survey was used for the early cosmic shear detection (van Waerbeke et al. 2000). Compared to the earlier results, the error bars on the shear

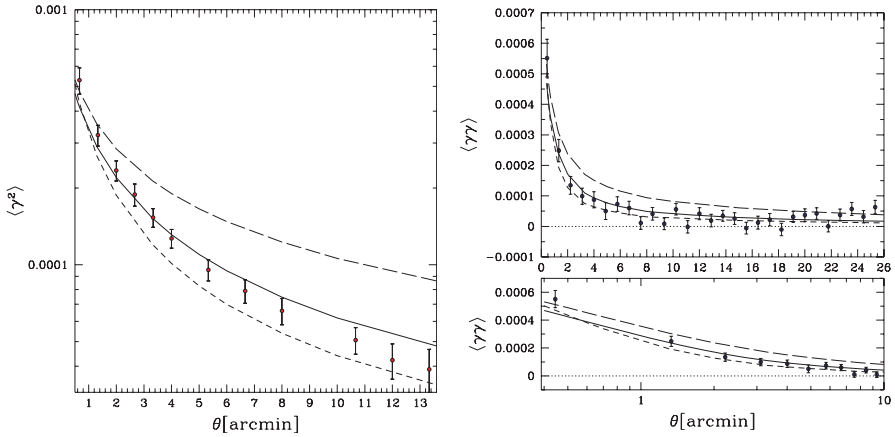

Fig. 41. The shear dispersion as a function of aperture radius (*left*) and the shear correlation function $\xi_+(\theta)$ (*right*) as measured from the VIRMOS-DESCART survey (van Waerbeke et al. 2001). The lower panel on the right shows an enlargement with logarithmic axis of the larger figure. The error bars were calculated from simulations in which the galaxy images have been randomized in orientation. The curves show predictions from three different cosmological models, corresponding to $(\Omega_\mathrm{m}, \Omega_\Lambda, \sigma_8) = (0.3, 0, 0.9)$ (open model, *short-dashed curves*), $(0.3, 0.7, 0.9)$ (low-density flat model, *solid curves*), and $(1, 0, 0.6)$ (Einstein-de Sitter Universe, long-dashed curves). In all cases, the shape parameter of the power spectrum was set to $\Gamma_\mathrm{spect} = 0.21$. The redshift distribution of the sources was assumed to follow the law (128), with $\alpha = 2$, $\beta = 1.5$ and $z_0 = 0.8$, corresponding to a mean redshift of $\bar{z} \approx 1.2$

measurements are greatly reduced, owing to the much better statistics. We show in Fig. 41 the shear dispersion and the correlation function as measured from this survey. Furthermore, this survey yielded the first detection of a significant $\langle M_\mathrm{ap}^2 \rangle$-signal; we shall come back to this later. In order to compare the measured shear signal with cosmological predictions, one needs to assume a redshift distribution for the galaxies; a frequently used parameterization for this is

$$p(z) = N \left(\frac{z}{z_0}\right)^\alpha \exp\left[-\left(\frac{z}{z_0}\right)^\beta\right] , \tag{128}$$

where α and β determine the shape of the redshift distribution, z_0 the characteristic redshift, and N is a normalization factor, chosen such as $\int \mathrm{d}z\, p(z) = 1$.

Another example of a deep survey is the Suprime-Cam survey (Hamana et al. 2003), a $2.1\,\mathrm{deg}^2$ survey taken with the wide-field camera Suprime-Cam (with a $34' \times 27'$ field-of-view) at the 8.2-m Subaru telescope. With an exposure time of 30 min, the data is considerably deeper than the VIRMOS-DESCART survey, due to the much larger aperture of the telescope. After cuts in the object catalog, the resulting number density of objects used for the weak lensing analysis is $\approx 30\,\mathrm{arcmin}^{-2}$. Figure 42 shows how small the

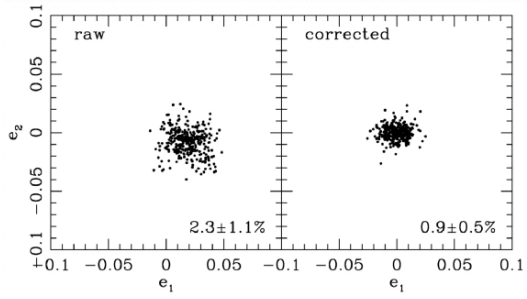

Fig. 42. Stellar ellipticities before and after correction for PSF anisotropies in the Suprime-Cam survey. Numbers give mean and dispersion of stellar ellipticities $|\chi|$ (from Hamana et al. 2003)

PSF anisotropy is, and that the correction with a fifth-order polynomial over the whole field-of-view in fact reduces the remaining stellar ellipticities considerably. This survey has detected a significant cosmic shear signal, as measured by the shear correlation functions and the aperture mass dispersion, over angular scales $2' \lesssim \theta \lesssim 40'$. The shear signal increases as fainter galaxies are used in the analysis, as expected, since fainter galaxies are expected to be at larger mean redshift and thus show a stronger shear signal.

Bacon et al. (2003) combine images taken at the Keck II telescope and the WHT. For the former, 173 fields were used, each having a f.o.v. of $2' \times 8'$; and the data from WHT were obtained from 20 different fields, covering about $1\,\mathrm{deg}^2$ in total. The large number of fields minimizes the sample variance of this particular survey, and the two instruments used allowed a cross-check of instrumental systematics.

Very Wide Surveys

Within a given observing time, instead of mapping a sky region to fairly deep magnitudes, one can also map larger regions with smaller exposure time; since most of the surveys have been carried out with goals in addition to cosmic shear, the survey strategy will depend on these other considerations. We shall mention two very wide surveys here.

Hoekstra et al. (2002a; also Hoekstra et al. 2002b) used the Red Cluster Sequence (RCS) survey, a survey designed to obtain a large sample of galaxy clusters using color selection techniques (Gladders and Yee 2000). The cosmic shear analysis is based on $53\,\mathrm{deg}^2$ of R_C-band data, spread over 13 patches on the sky and observed with two different instruments, the CFH12K@CFHT for Northern fields, and the Mosaic II camera at the CTIO 4m telescope in the South. The integration times are 900 s and 1200 s, respectively. The shear dispersion as measured with the two instruments are in satisfactory agreement and thus can be safely combined. Owing to the shallower magnitude, the detected shear is smaller than in the deeper surveys mentioned above: on a

scale of 2.5 arcmin, the shear dispersion is $\langle|\bar{\gamma}|^2\rangle \sim 4 \times 10^{-5}$ in the RCS survey, compared to $\sim 2 \times 10^{-4}$ in the deeper VIRMOS-DESCART survey (see Fig. 41), in accordance with expectations.

Jarvis et al. (2003) presented a cosmic shear survey of 75 deg^2, taken with the BTC camera and the Mosaic II camera on the CTIO 4m telescope, with about half the data taken with each instrument. The survey covers 12 fields, each with sidelength of $\sim 2.5^\circ$. For each pointing, three exposures of 5 min were taken, making the depth of this survey comparable to the RCS. A total of $\sim 2 \times 10^6$ galaxies with $R \leq 23$ were used for the shear analysis. Since this survey has some peculiar properties which are very educational, it will be discussed in somewhat more detail. The first point to notice is the large pixel size of the BTC, of $0\farcs43$ per pixel – for comparison, the CFH12K has $\sim 0\farcs20$ per pixel. With a median seeing of $1\farcs05$, the PSF is slightly undersampled with the BTC. Second, the PSF anisotropy on the BTC is very large, as shown in Fig. 43 – a large fraction of the exposures has stellar images with ellipticities higher than 10%. Obviously, this renders the image analysis and the correction for PSF effects challenging. As shown on the right-hand part of Fig. 43, this challenge is indeed met. This fact is very nicely illustrated in Fig. 44, where the corrected stellar ellipticities are shown as a function of the PSF anisotropy; in essence, the correction reduces the PSF anisotropy by nearly a factor of 300 !

The third point to notice is that the image analysis for this survey has not been carried out with IMCAT (as for most of the other surveys), but by a different image analysis method described in Bernstein and Jarvis (2002).

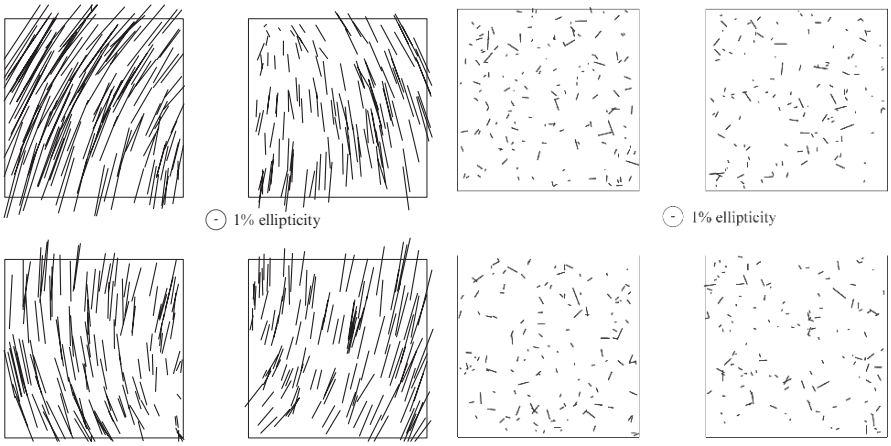

Fig. 43. On the left-hand side, the raw ellipticities of stars are shown for the four CCDs of the BTC instrument; for reference, a 1% ellipticity is indicated. After correcting for the PSF anisotropy, the remaining stellar ellipticities (shown on the right) are of order 1–2%, and essentially uncorrelated with position on the chip, i.e., they are compatible with measurement noise (from Jarvis et al. 2003)

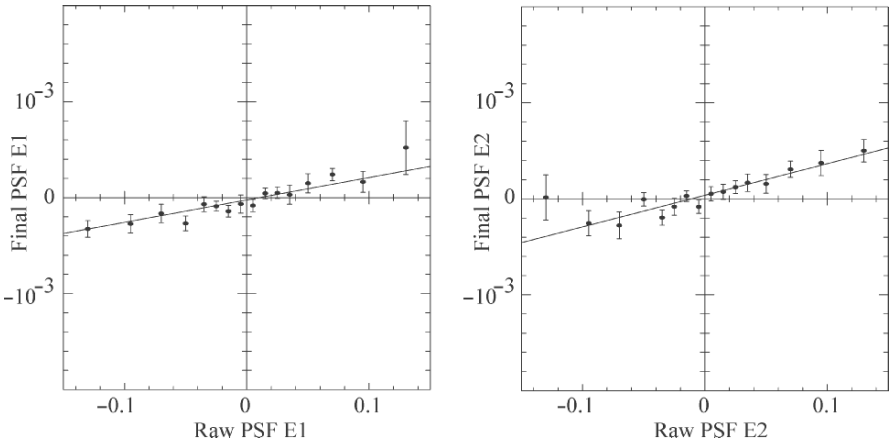

Fig. 44. These two plots show the two components of the stellar ellipticities as measured on the data (x-axis) and after correction, from the Jarvis et al. (2003) survey. The slope of the straight line is about 1/300, meaning that the strong PSF anisotropy can be corrected for up to this very small residual. The final PSF anisotropy is well below 5×10^{-4}. This figure, together with Fig. 43, demonstrates how well the procedures for PSF corrections work (from Jarvis et al. 2003)

In this respect, this survey is independent of all the others described in this section; it is important to have more than one image analysis tool to check potential systematics of either one.

One of the amazing results from the CTIO cosmic shear survey is that the shear dispersion can be measured with about a 3σ significance on each of the 12 fields. Hence, this provides a shear dispersion measurement on scales larger than 1 degree (the radius of a circle with area of the mean area of the 12 fields of $\sim 6.2\,\mathrm{deg}^2$); the shear dispersion on these scales is $\langle|\bar{\gamma}|^2\rangle = 0.0012 \pm 0.0003$.

Special Surveys

There are a number of cosmic shear surveys which cover a much smaller total area than the ones mentioned above, and are thus not competitive in terms of statistical accuracy, but which have some special properties which give them an important complementary role. One example are surveys carried out with the Hubble Space Telescope. Since for them the PSF is much smaller than for ground-based observations, PSF corrections in measuring galaxy ellipticities are expected to be correspondingly smaller. The drawback of HST observations is that its cameras, at least before the installment of the ACS, have a small field-of-view, less than $1\,\mathrm{arcmin}^2$ for the STIS CCD, and about $5\,\mathrm{arcmin}^2$ for WFPC2. This implies that the total area covered by HST surveys are smaller than those achievable from the ground, and that the number of stars per field are very small, so that PSF measurements are typically not

possible on those frames which are used for a cosmic shear analysis. Hence, the PSF needs to be measured on different frames, e.g., taken on star clusters, and one needs to assume (this assumption can be tested, of course) that the PSF is fairly stable in time. In fact, this is not really true, as the telescopes moves in and out the Earth's shadow every orbit, thereby changing its temperature and thus changing its length (an effect called breathing). A further potential problem of HST observations is that the WFPC2 has a pixel scale of $0\farcs1$ and thus substantially undersamples the PSF; this is likely to be a serious problem for very faint objects whose size is not much larger than the PSF size.

Cosmic shear surveys from two instruments onboard HST have been reported in the literature so far. One of the surveys uses archival data from the Medium Deep Survey, a mostly parallel survey carried out with the WFPC2. Refregier et al. (2002) used 271 WFPC2 pointings observed in the I-band, selected such that each of them is separated from the others by at least $10'$ to have statistically independent fields. They detected a shear dispersion on the scale of the WFC-chips (which is equivalent to a scale $\theta \sim 0\farcm72$) of $\left\langle|\bar{\gamma}|^2\right\rangle \sim 3.5 \times 10^{-4}$, which is a 3.8σ detection. The measurement accuracy is lower than that, owing to cosmic variance and uncertainties in the redshift distribution of the sources. Hämmerle et al. (2002) used archival parallel data taken with STIS; from the 121 fields which are deep enough, have multiple exposures, and are at sufficiently high galactic latitude, they obtained a shear dispersion of $\left\langle|\bar{\gamma}|^2\right\rangle \sim 15 \times 10^{-4}$ on an effective scale of $\sim 30''$, a mere 1.5σ detection. This low significance is due to the small total area covered by this survey. On the other hand, since the pixel scale of STIS is half of that of WFPC2, the undersampling problem is much less in this case. A larger set of STIS parallel observations were analyzed with respect to cosmic shear by Rhodes et al. (2004) and Miralles et al. (2005). Whereas Rhodes et al. obtained a significant ($\sim 5\sigma$) detection on an angular scale of $\sim 30''$, Miralles et al. concluded that the degradation of the STIS CCD in orbit regarding the charge transfer efficiency prevents a solid measurement of weak lensing. The discrepancies between these two works, which are based to a large degree on the same data set, is unclear at present. Personally I consider this discrepancy as a warning sign that weak lensing measurement based on small fields-of-view, and correspondingly too few stars to control the PSF on the science exposures, need to be regarded with extreme caution.

The new ACS onboard HST offers better prospects for cosmic shear measurements, since it has a substantially larger field-of-view. A first result was derived by Schrabback (2004), again based on parallel data. He found that the PSF is not stable in time, but that the anisotropy pattern changes among only a few characteristic patterns. He used those as templates, and the (typically a dozen) stars in the science frames to select a linear combination of these templates for the PSF correction of individual frames, thereby obtaining a solid detection of cosmic shear from the early ACS data.

A further survey that should be mentioned here is the one conducted on COMBO-17 fields (Brown et al. 2003). COMBO-17 is a one square degree

survey, split over four fields, taken with the WFI at the ESO/MPG 2.2m telescope on La Silla, in 5 broad-band and 12 medium-band filters. In essence, therefore, this multi-band survey produces low-resolution spectra of the objects and thus permits to determine very accurate photometric redshifts of the galaxies taken for the shear analysis. Therefore, for the analysis of Brown et al., the redshift distribution of the galaxies is assumed to be very well known and not a source of uncertainty in translating the cosmic shear measurement into a constraint on cosmological parameters. We shall return to this aspect in Sect. 7.6. The data set was reanalyzed by Heymans et al. (2004) where special care has been taken to identify and remove the signal coming from intrinsic alignment of galaxy shapes.

7.4 Detection of B-Modes

The recent cosmic shear surveys have measured the aperture mass dispersion $\langle M_{\rm ap}^2(\theta)\rangle$, as well as its counterpart $\langle M_\perp^2(\theta)\rangle$ for the B-modes (see Sect. 6.5). These aperture measures are obtained in terms of the directly measured shear correlation functions, using the relations (125). As an example, we show in Fig. 45 the aperture measures as obtained from the Red Cluster Sequence survey (Hoekstra et al. 2002a). A significant measurement of $\langle M_{\rm ap}^2(\theta)\rangle$ is obtained over quite a range of angular scales, with a peak around a few arcminutes, as predicted from CDM power spectra (see Fig. 35). In addition to that, however, a significant detection of $\langle M_\perp^2(\theta)\rangle$ signifies the presence of B-modes. As discussed in Sect. 6.5, those cannot be due to cosmic shear. The only plausible explanation for them, apart from systematics in the observations and data analysis, is an intrinsic alignment of galaxies. If this is the cause of the B-modes, then one would expect that the relative contribution of the B-mode signal decreases as higher-redshift galaxies are used for the shear measurement. In fact, this expectation is satisfied, as shown in Fig. 45, where the galaxy sample is split into a bright and faint part, and the relative amplitude of the B-mode signal is smaller for the fainter (and thus presumably more distant) sample.

Similar detections of a B-mode signal have been obtained by the other surveys. For example, van Waerbeke et al. (2001) reported a significant B-mode signal on angular scales of a few arcminutes. In the reanalysis of the VIRMOS-DESCART data, van Waerbeke et al. (2002) reported that the B-mode on these scales was caused by the polynomial PSF anisotropy fit: the third-order function (fitted for each chip individually) has its largest amplitude near the boundary of the chips and is least well constrained there, unless one finds stars close to these edges. If a second-order polynomial fit is used, the B-modes on a few arcminute scales disappear. van Waerbeke et al. (2002) calculate the aperture statistics from the uncorrected stellar ellipticities in their survey and found that the 'E- and B-modes' of the PSF anisotropy have very similar amplitude and shape (as a function of θ). This similarity is unlikely to change in the course of the PSF correction procedure. Thus,

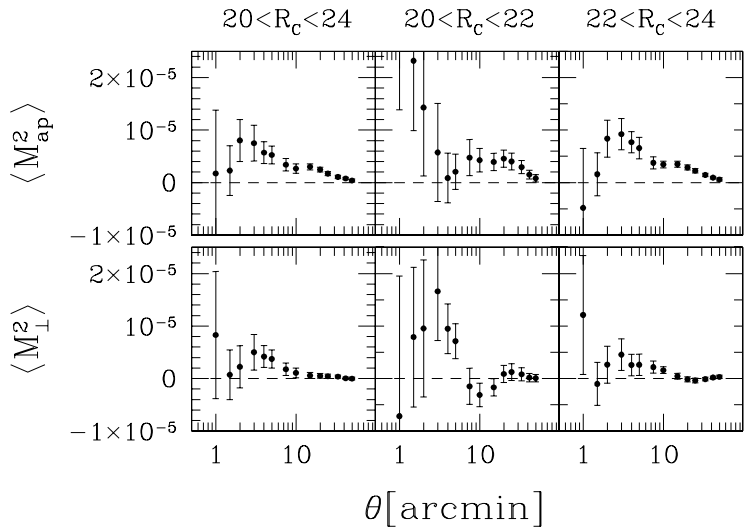

Fig. 45. The aperture mass dispersion $\left\langle M_{\rm ap}^2(\theta)\right\rangle$ (*top panels*) and the cross aperture dispersion $\left\langle M_\perp^2(\theta)\right\rangle$ (*bottom panels*) from the RCS survey (Hoekstra et al. 2002a). In the left panels, all galaxies with apparent magnitude $20 \le R_C \le 24$ are used, the middle and right panels show the same statistics for the brighter and fainter subsamples of background galaxies, respectively. Error bars in the former are larger, owing to the smaller number of bright galaxies

they argue, that if the B-mode is due to systematics in the data analysis, a systematic error of very similar amplitude will also affect the E-mode. Jarvis et al. (2003) found a significant B-mode signal on angular scales below $\sim 30'$; hence, despite their detection of an E-mode signal over a large range of angular scales $1' \lesssim \theta \lesssim 100'$, one suspects that part of this signal might be due to non-lensing effects.

Given our lack of understanding about the origin of the B-mode signal, and the associated likelihood that any effect causing a B-mode signal also contributes a non-lensing part to the E-mode signal, one needs a prescription on how to use the detected E-mode signal for a cosmological analysis. Depending on what one believes the B-modes are due to, this prescription varies. For example, if the B-mode is due to a residual systematic, one would add its signal in quadrature to the error bars of the E-mode signal, as done in van Waerbeke et al. (2002). On the other hand, if the B-mode signal is due to intrinsic alignments of galaxies, as is at least suggested for the RCS survey from Fig. 45 owing to its dependence on galaxy magnitudes, then it could be more reasonable to subtract the B-mode signal from the E-mode signal, if one assumes that intrinsic alignments produce similar amplitudes of both modes [which is far from clear, however; Mackey et al. (2002) find that the E-mode signal from intrinsic alignments is expected to be ~ 3.5 times higher than the corresponding B-mode signal].

Owing to the small size of the fields observed with the early HST instruments, no E/B-mode decomposition can be carried out from these surveys – the largest size of these fields is smaller than the angular scale at which the aperture mass dispersion is expected to peak (see Fig. 35). However, future cosmic shear studies carried out with ACS images will most likely be able to detect, or set upper bounds on the presence of B-modes.

In fact, it is most likely that (most of) the B-mode signal seen in the cosmic shear surveys is due to remaining systematics. Hoekstra (2004) investigated the PSF anisotropy of the CFH12k camera using fields with a high number density of stars. Randomly selecting about 100 stars per CCD, which is the typical number observed in high galactic latitute fields, he fitted a second-order polynomial to these stars representing the PSF anisotropy. Correcting with this model all the stars in the field, the remaining stellar ellipticities carry substantial E- and B-mode signals, essentially on all angular scales, but peaking at about the size of a CCD. A substantially smaller residual is obtained if the ellipticities of stars in one of the fields is corrected by a more detailed model of the PSF anisotropy as measured from a different field; this improvement indicates that the PSF anisotropy pattern in the data set used by Hoekstra is fairly stable between different exposures. This, however, is not necessarily the case in other datasets. Nevertheless, if one assumes that the PSF anisotropy is a superposition of two effects, one from the properties of the telescope and instrument itself, the other from the specific observation procedure (e.g., tracking, wind shake, etc.), and further assuming that the latter one affects mainly the large-scale properties of the anisotropy pattern, then a superposition of a PSF model (obtained from a dense stellar field and describing the small-scale properties of the anisotropy pattern) plus a low-order polynomial can be a better representation of the PSF anisotropy. This indeed was verified in the tests made by Hoekstra (2004). In their reanalysis of the VIRMOS-DESCART survey, van Waerbeke et al. (2005) have fitted the PSF anisotropy with a rational function, instead of a polynomial. This functional form was suggested by the study of Hoekstra (2004). When correcting the galaxy ellipticities with this new PSF model, essentially no more B-modes in the VIRMOS-DESCART survey are detected. Further studies on PSF anisotropy corrections need to be conducted; possibly the optimal way of dealing with them will be instrument-specific.

7.5 Cosmological Constraints

The measured cosmic shear signal can be translated into constraints on cosmological parameters, by comparing the measurements with theoretical predictions. In Sect. 6.4 we have outlined how such a comparison can be made; there, we have concentrated on the shear correlation functions as the primary observables. However, the detection of significant B-modes in the shear field makes the aperture measures the 'better' statistics to compare with predictions. They can be calculated from the shear correlation functions, as shown

in (125). Calculating a likelihood function from the aperture mass dispersion proceeds in the same way as outlined in Sect. 6.4 for the correlation functions.

We have argued in Sect. 6.3 that $\langle M_{\rm ap}^2(\theta)\rangle$ provides very localized information about the power spectrum $P_\kappa(\ell)$ and is thus a very useful statistic. One therefore might expect that the aperture mass dispersion as calculated from the shear correlation functions contains essentially all the second-order statistical information of the survey. This is not true, however; one needs to recall that the shear correlation function ξ_+ is a low-pass filter of the power spectrum, and thus contains information of P_κ on angular scales larger than the survey size. This information is no longer contained in the aperture mass dispersion, owing to its localized associated filter. Therefore, in order to keep this long-range information in the comparison with theoretical predictions, it is useful to complement the estimates of $\langle M_{\rm ap}^2(\theta)\rangle$ with either the shear dispersion, or the correlation function ξ_+, at a scale which is not much smaller than the largest scale at which $\langle M_{\rm ap}^2(\theta)\rangle$ is measured. Note, however, that this step implicitly assumes that on these large angular scales, the shear signal is essentially free of B-mode contributions. If this assumption is not true, and cannot be justified from the survey data, then this additional constraint should probably be dropped.

The various constraints on parameters that have been derived from the cosmic shear surveys differ in the amount of prior information that has been used. As an example, we consider the analysis of van Waerbeke et al. (2002). These authors have considered a model with four free parameters: $\Omega_{\rm m}$, the normalization σ_8, the shape parameter $\Gamma_{\rm spect}$ and the characteristic redshift $z_{\rm s}$ (or, equivalently, mean redshift $\bar{z}_{\rm s}$) of their galaxy sample, assuming a flat Universe, i.e., $\Omega_\Lambda = 1 - \Omega_{\rm m}$. They have used a flat prior for $\Gamma_{\rm spect}$ and $\bar{z}_{\rm s}$ in a fairly wide interval over which they marginalized the likelihood function (see Fig. 46). Depending on the width of these intervals, the confidence regions are more or less wide. It should be noted that the confidence contours close if $\Gamma_{\rm spect}$ and $\bar{z}_{\rm s}$ are assumed to be known (see van Waerbeke et al. 2001), but when these two parameters are kept free, $\Omega_{\rm m}$ and σ_8 are degenerate.

The right panel of Fig. 46 shows the corresponding constraints as obtained from the RCS survey. Since this survey is shallower and only extends to magnitudes where spectroscopic surveys provide information on their redshift distribution, the range of $\bar{z}_{\rm s}$ over which the likelihood is marginalized is smaller than for the VIRMOS-DESCART survey. Correspondingly, the confidence region is slightly smaller in this case. Even smaller confidence regions are obtained if external information is used: Hoekstra et al. (2002a) considered Gaussian priors with $\Omega_{\rm m} + \Omega_\Lambda = 1.02 \pm 0.06$, as follows from pre-WMAP CMB results, $\Gamma_{\rm spect} = 0.21 \pm 0.03$, as follows from the 2dF galaxy redshift survey, and $\bar{z}_{\rm s} = 0.59 \pm 0.02$, for which the width of the valley of maximum likelihood narrows considerably. Jarvis et al. (2003) used for their estimate of cosmological parameters the aperture mass dispersion at three angular scales plus the shear dispersion at $\theta = 100'$, and they considered alternatively the E-mode signal, and the E-mode signal $\pm$ the B-mode signal, to arrive at constraints

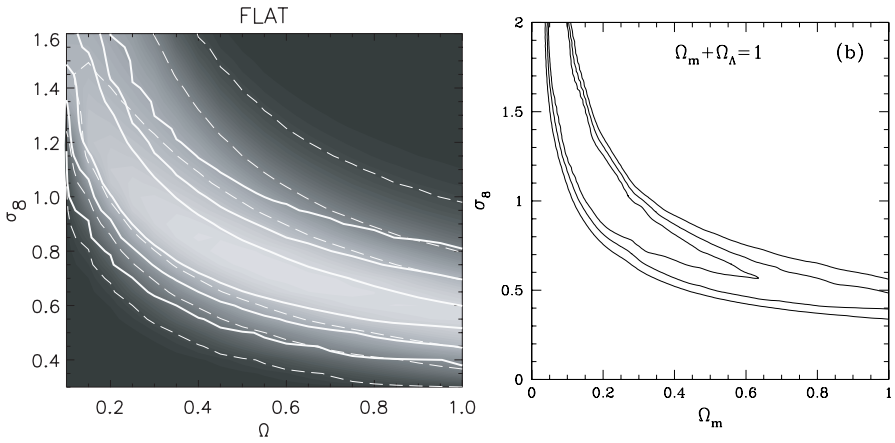

Fig. 46. Constraints on $\Omega_{\rm m}$ and σ_8 from two cosmic shear surveys. *Left*: The VIRMOS-DESCART survey (van Waerbeke et al. 2002). The grey-scale and dashed contours show the 68%, 95% and 99.9% confidence regions with a marginalization over the range $\Gamma_{\rm spect} \in [0.05, 0.7]$, and mean galaxy redshift in the range $\bar{z}_{\rm s} \in [0.50, 1.34]$, whereas the solid contours show the same confidence regions with the stronger priors $\Gamma_{\rm spect} \in [0.1, 0.4]$ and $\bar{z}_{\rm s} \in [0.8, 1.1]$. *Right*: The RCS survey (Hoekstra et al. 2002a,b,c,d), showing the 1, 2, and 3σ confidence regions for a prior $\Gamma_{\rm spect} \in [0.05, 0.5]$ and mean redshift $\bar{z}_{\rm s} \in [0.54, 0.66]$. In both cases, a flat Universe has been assumed

on the $\Omega_{\rm m}$–σ_8 parameter plane. Since the CTIO survey samples a larger angular scale than the other surveys (data at small angular scales are discarded owing to the large B-mode signal there), the results are much less sensitive to $\Gamma_{\rm spect}$; furthermore, for the same reason the Jarvis et al. results are much less sensitive to the fit of the non-linear power spectrum according to Peacock and Dodds (1996) which van Waerbeke et al. (2002) found to be not accurate enough for some cosmological models. In fact, if instead of the Peacock and Dodds fitting formula, the fit by Smith et al (2003) is used to describe the non-linear power spectrum, the resulting best estimate of σ_8 is decreased by 8% for the RCS survey (as quoted in Jarvis et al. 2003).

For the RCS and the CTIO surveys, the covariance matrix was obtained from field-to-field variations, i.e., $\mathrm{Cov}_{ij} = \langle (d_i - \mu_i)(d_j - \mu_j) \rangle$, where μ_i is the mean of the observable d_i (e.g., the aperture mass dispersion at a specific angular scale) over the independent patches of the survey, and angular brackets denote the average over all independent patches. The estimate of the covariance matrix for the VIRMOS-DESCART survey is slightly different, as it has only four independent patches.

To summarize the results from these surveys, each of them found that a combination of parameters of the form $\sigma_8 \Omega_{\rm m}^{\alpha}$ is determined best from the data, with $\alpha \sim 0.55$, where the exact value of α depends on the survey depth. If we consider the specific case of $\Omega_{\rm m} = 0.3$ which is close to the concordance

value that was recently confirmed by WMAP, then the VIRMOS-DESCART survey yields $\sigma_8 = 0.94 \pm 0.12$, the RCS survey has $\sigma_8 = 0.91^{+0.05}_{-0.12}$, which improves to $\sigma_8 = 0.86^{+0.04}_{-0.05}$ if the stronger (Gaussian) priors mentioned above are used, and the CTIO survey yields $\sigma_8 = 0.71^{+0.12}_{-0.16}$, here as 2σ limits. Whereas these results are marginally in mutual agreement, the CTIO value for σ_8 is lower than the other two. The higher values are also supported by results from the WFPC2 survey by Refregier et al. (2002), who find $\sigma_8 = 0.94 \pm 0.17$, Bacon et al. (2003) with $\sigma_8 = 0.97 \pm 0.13$, and the earlier surveys discussed in Sect. 7.1. The only survey supporting the low value of the CTIO survey is COMBO17 (Brown et al. 2003; see also the reanalysis of this dataset by Heymans et al. 2004). Most likely, these remaining discrepancies will be clarified in the near future; see discussion below. It should also be noted that at least for some of the surveys, a large part of the uncertainty comes from the unknown redshift distribution of the galaxies; this situation will most likely improve, as efficient spectrographs with large multiplex capability become available at 10m-class telescopes, which will in the near future deliver large galaxy redshift surveys at very faint magnitudes. Those can be used to much better constrain the redshift distribution of the source galaxies in cosmic shear surveys.

7.6 3-D Lensing

As mentioned several times before, using individual source redshift information, as will become available in future multi-color wide-field surveys, can improve the cosmological constraints obtained from weak lensing. In this section we shall therefore summarize some of the work that has been published on this so-called 3-D lensing.

Three-dimensional Matter Distribution

Provided the redshifts of individual source galaxies are known (or estimated from their multiple colors), one can derive the 3-D matter distribution, not only its projection. The principle of this method can be most easily illustrated in the case of a flat Universe, for which the surface mass density $\kappa(\boldsymbol{\theta}, w)$ for sources at comoving distance w becomes – see (93)

$$\kappa(\boldsymbol{\theta}, w) = \frac{3H_0^2\Omega_\mathrm{m}}{2c^2} \int_0^w \mathrm{d}w' \, \frac{w'(w-w')}{w} \, \frac{\delta(w'\boldsymbol{\theta}, w')}{a(w')} \, . \tag{129}$$

Multiplying this expression by w and differentiating twice yields

$$\frac{\mathrm{d}^2}{\mathrm{d}w^2} \left(w\,\kappa(\boldsymbol{\theta}, w)\right) = \frac{3H_0^2\Omega_\mathrm{m}}{2c^2} \, \frac{w}{a(w)} \, \delta(w\boldsymbol{\theta}, w) \, ,$$

which therefore allows one to obtain the three-dimensional density contrast δ in terms of the surface mass densities κ at different source redshifts. As we

have seen in Sect. 5, there are several methods how to obtain the surface mass density from the observed shear. To illustrate the 3-D method, we use the finite-field reconstruction in the form of (60), for which one finds

$$\delta(w\boldsymbol{\theta}, w) = \frac{2c^2}{3H_0^2\Omega_\mathrm{m}}\,\frac{a(w)}{w}\int \mathrm{d}^2\theta'\;\mathbf{H}(\boldsymbol{\theta};\boldsymbol{\theta}')\cdot\frac{d^2}{\mathrm{d}w^2}\left[w\,\mathbf{u}_\gamma(\boldsymbol{\theta}', w)\right]\;. \qquad (130)$$

Taylor (2001) derived the foregoing result, but concentrated on the 3-D gravitational potential instead of the mass distribution, and Bacon and Taylor (2003) and Hu and Keeton (2002) discussed practical implementations of this relation. First to note is the notorious mass-sheet degeneracy, which in the present context implies that one can add an arbitrary function of w to the reconstructed density contrast δ. This cannot be avoided, but if the data field is sufficiently large, so that averaged over it, the density contrast is expected to vanish, this becomes a lesser practical problem. For such large data fields, the above mass reconstruction can be substituted in favor of the simpler original Kaiser and Squires (1993) method. Still more freedom is present in the reconstruction of the gravitational potential. The second problem is one of smoothing: owing to the noisiness of the observed shear field, the w-differentiation (as well as the θ-differentiation present in the construction of the vector field $\mathbf{u}_\gamma$) needs to be carried out on the smoothed shear field. A discretization of the observed shear field, as also suggested by the finite accuracy of photometric redshifts, can be optimized with respect to this smoothing (Hu and Keeton 2002).

A first application of this methods was presented in Taylor et al. (2004) on one of the COMBO17 fields which contains the supercluster A 901/902. The clusters present clearly show up also in the 3-D mass map, as well as a massive structure behind the cluster A 902 at higher redshift. Already earlier, Wittman et al. (2001, 2003) estimated the redshifts of clusters found in their deep blank-field data by studying the dependence of the weak lensing signal on the estimated source redshifts, and subsequent spectroscopy showed that these estimates were fairly accurate.

Power Spectrum Estimates

A redshift-dependent shear field can also be used to improve on the cosmological constraints obtained from cosmic shear. Hu (1999) has pointed out that even crude information on the source redshifts can strongly reduce the uncertainties of cosmological parameters. In fact, the 3-D power spectrum can be constructed from redshift-dependent shear data (see, e.g., Heavens 2003, Hu 2002, and references therein). For illustration purposes, one can use the κ power spectrum for sources at fixed comoving distance w, which reads in a flat Universe – see (99)

$$P_\kappa(\ell, w) = \frac{9H_0^4\Omega_\mathrm{m}^2}{4c^4}\int_0^w \mathrm{d}w'\;\frac{(w-w')^2}{w^2\,a^2(w')}\,P_\delta\left(\frac{\ell}{w'}, w'\right)\;. \qquad (131)$$

Differentiating $w^2 P_\kappa$ three times w.r.t. w then yields (Bacon et al. 2004)

$$P_\delta(k,w) = \frac{2c^4}{9H_0^4\Omega_\mathrm{m}^2}\, a^2(w)\, \frac{\mathrm{d}^3}{\mathrm{d}w^3}\left[w^2\, P_\kappa(wk,w)\right] \ . \tag{132}$$

In this way, one could obtain the three-dimensional power spectrum of the matter. However, this method is essentially useless, since it is both very noisy (due to the third-order derivatives) and throws away most of the information contained in the shear field, as it makes use only of shear correlations of galaxies having the same redshift, and not of all the pairs at different distances. A much better approach to construct the three-dimensional power spectrum is given, e.g., by Pen et al. (2003a).

In my view, the best use of three-dimensional data is to construct the shear correlators $\xi_\pm(\theta; z_1, z_2)$, as they contain all second-order statistical information in the data and at the same time allow the identification and removal of a signal from intrinsic shape correlations of galaxies (King and Schneider 2003). From these correlation functions, one can calculate a χ^2 function as in (116) and minimize it w.r.t. the wanted parameters. One problem of this approach is the large size of the covariance matrix, which now has six arguments (two angular separations and four redshifts). However, as shown in Simon et al. (2004), it can be calculated fairly efficiently, provided one assumes that the fourth-order correlations factorize into products of two-point correlators, i.e., Gaussian fields (if this assumption is dropped, the covariance must be calculated from cosmological N-body simulations).

Bacon et al. (2004) used the COMBO17 data to derive the shape of the power spectrum, using the redshift dependent shear correlations. They parameterize the power spectrum in the form $P(k,z) \propto Ak^\alpha \mathrm{e}^{-sz}$, so that it is described by an amplitude A, a local slope α and a growth parameter s which describes how the amplitude of the power spectrum declines toward higher redshifts. In fact, the slope $\alpha = -1.2$ was fixed to the approximate value in ΛCDM models over the relevant range of spatial scales and redshifts probed by the COMBO17 data (since the data used cover only 1/2 deg^2, reducing the number of free parameters by fixing α is useful). The evolution of the power spectrum is found with high significance in the data. Furthermore, the authors show that the use of redshift information improves the accuracy in the determination of σ_8 by a factor of two compared to the 2-D cosmic shear analysis of the same data (Brown et al. 2003).

The main application of future multi-waveband cosmic shear surveys will be to derive constraints on the equation of state of dark energy, as besides lensing there are only a few methods available to probe it, most noticeably the magnitude-redshift relation of SN Ia. Since dark energy starts to dominate the expansion of the Universe only at relatively low redshifts, little information about its properties is obtainable from the CMB anisotropies alone. For that reason, quite a number of workers have considered the constraints on the dark energy equation of state that can be derived from future cosmic shear surveys (e.g., Huterer 2002; Hu 2002; Munshi and Wang 2003; Hu and Jain

2004; Abazajian and Dodelson 2003; Benabed and van Waerbeke 2003; Song and Knox 2004). The results of these are very encouraging; the sensitivity on the dark energy properties is due to its influence on structure growth. With (photometric) redshift information on the source galaxies, the evolution of the dark matter distribution can be studied by weak lensing, as shown above. van Waerbeke and Mellier (2003) have compared the expected accuracy of the cosmic shear result from the ongoing CFHT Legacy Survey with the variation of various dark energy models and shown that the CFHTLS will be able to discriminate between some of these models, with even much better prospects from future space-based wide-field imaging surveys (e.g., Hu and Jain 2004).

7.7 Discussion

The previous sections have shown that cosmic shear research has matured; several groups have successfully presented their results, which is important in view of the fact that the effects one wants to observe are small, influenced by various effects, and therefore, independent results from different instruments, groups, and data analysis techniques are essential in this research. We have also seen that the results from the various groups tend to agree with each other, with a few very interesting discrepancies remaining whose resolution will most likely teach us even more about the accuracies of data analysis procedures.

Lessons for Cosmology

A natural question to ask is, what has cosmic shear taught us so far about cosmology ? The most important constraint coming from the available cosmic shear results is that on the normalization σ_8, for which only few other accurate methods are available. We have seen that cosmic shear prefers a value of $\sigma_8 \approx 0.8 - 0.9$, which is slightly larger than current estimates from the abundance of clusters, but very much in agreement with the measurement of WMAP. The estimate from the cluster abundance is, however, not without difficulties, since it involves several scaling relations which need to be accurately calibrated; hence, different authors arrive at different values for σ_8 (see, e.g., Pierpaoli, Scott and White 2001; Seljak 2002; Schuecker et al. 2003). The accuracy with which σ_8 is determined from CMB data alone is comparable to that of cosmic shear estimates; as shown in Spergel et al. (2003), more accurate values of σ_8 are obtained only if the CMB measurements are combined with measurements on smaller spatial scales, such as from galaxy redshift surveys and the Lyman alpha forest statistics. Thus, the σ_8-determination from cosmic shear is certainly competitive with other measurements. Arguably, cosmic shear sticks out in this set of smaller-scale constraints due to the fewer physical assumptions needed for its interpretation.

But more importantly, it provides a fully independent method to measure cosmological parameters. Hence, at present the largest role of the cosmic

shear results is that it provides an independent approach to determining these parameters; agreement with those obtained from the CMB, galaxy redshift surveys and other methods are thus foremost of interest in that they provide additional evidence for the self-consistency of our cosmological model which, taken at face value, is a pretty implausible one: we should always keep in mind that we are claiming that our Universe consists of 4.5% normal (baryonic) matter, with the rest being shared with stuff that we have given names to ('dark matter', 'dark energy'), but are pretty ignorant about what that actually is. Insofar, cosmic shear plays an essential role in shaping our cosmological view, and has become one of the pillars on which our standard model rests.

Agreement, or Discrepancies ?

How to clarify the remaining discrepancies that were mentioned before – what are they due to ? One needs to step back for a second and be amazed that these results are in fact so well in agreement as they are, given all the technical problems a cosmic shear survey has to face (see Sect. 3). Nevertheless, more investigations concerning the accuracy of the results need to be carried out, e.g., to study the influence of the different schemes for PSF corrections on the final results. For this reason, it would be very valuable if the same data set is analyzed by two independent groups and to compare the results in detail. Such comparative studies may be a prerequisite for the future when much larger surveys will turn cosmic shear into a tool for precision cosmology.

Joint Constraints from CMB Anisotropies and Cosmic Shear

As mentioned before, the full power of the CMB anisotropy measurements is achieved when these results are combined with constraints on smaller spatial scales. The tightest constraints from WMAP are obtained when it is combined with results from galaxy redshift surveys and the statistics of the Lyα forest absorption lines (Spergel et al. 2003). Instead of the latter, one can use results from cosmic shear, as it provides a cleaner probe of the statistical properties of the matter distribution in the Universe. As was pointed out before (e.g., Hu and Tegmark 1999; see Fig. 34), the combination of CMB measurements with cosmic shear results is particularly powerful to break degeneracies that are left from using the former alone. Contaldi et al. (2003) used the CMB anisotropy results from WMAP (Bennett et al. 2003), supplemented by anisotropy measurements on smaller angular scales from ground-based experiments, and combined them with the cosmic shear aperture mass dispersion from the RCS survey (Hoekstra et al. 2002a). As is shown in Fig. 47, the constraints in the $\Omega_{\rm m}$-σ_8-parameter plane are nearly mutually orthogonal for the CMB and cosmic shear, so that the combined confidence region is substantially smaller than each of the individual regions.

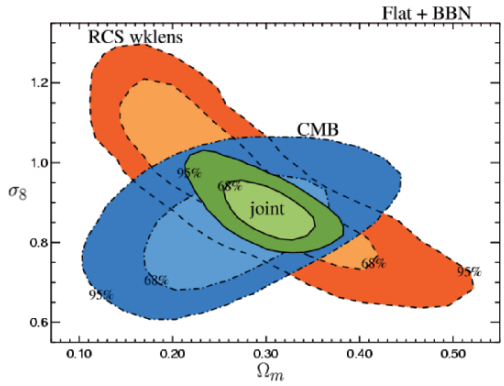

Fig. 47. The confidence region in the $\Omega_{\rm m}$-σ_8-plane obtained from the two-dimensional marginalized likelihood. Shown are the 68% and 95% confidence regions derived individually from the CMB and the RCS cosmic shear survey, as well as those obtained by combining both constraints (Contaldi et al. 2003)

Wide vs. Deep Surveys

In designing future cosmic shear surveys, the survey strategy needs to decide the effective exposure time. For a given total observing time (the most important practical constraint), one needs to find a compromise between depth and area. Several issues need to be considered in this respect:

- The lensing signal increases with redshift, and therefore with increasing depth of a survey; it should therefore be easier to detect a lensing signal in deep surveys. Furthermore, by splitting the galaxy sample into subsamples according to the magnitude (and/or colors), one can study the dependence of the lensing signal on the mean source redshift, which is an important probe of the evolution of the matter power spectrum, and thus of cosmology. If one wants to probe the (dark) matter distribution at appreciable redshifts ($z \sim 0.5$), one needs to carry out deep surveys.
- A wider survey is more likely to probe the linear part of the power spectrum which is more securely predicted from cosmological models than the nonlinear part; on the other hand, measurement of the latter, when compared with precise models (e.g., from numerical simulations), can probe the nonlinear gravitational clustering regime.
- Depending on the intrinsic galaxy alignment, one would prefer deeper surveys, since the relative importance of the intrinsic signal decreases with increasing survey depth. Very shallow surveys may in fact be strongly affected by the intrinsic signal (e.g., Heymans and Heavens 2003). On the other hand, for precision measurements, as will become available in the near future, one needs to account for the intrinsic signal in any case, using redshift information (at least in a statistical sense), and so shallow surveys

lose this potential disadvantage. In fact, the redshift estimates of shallower surveys are easier to obtain than for deeper ones.
- In this context, one needs to compromise between area and the number of fliters in which exposures should be taken. Smaller area means worse statistics, e.g., larger effects of cosmic variance, but this has to be balanced against the additional redshift information. Also, if a fixed observing time is used, one needs to account for the weather, seeing and sky brightness distribution. One should then devise a strategy that the best seeing periods are used to obtain images in the filter which is used for shape measurements, and bright time shall be spent on the longest wavelength bands.
- Fainter galaxies are smaller, and thus more strongly affected by the point-spread function. One therefore expects that PSF corrections are on average smaller for a shallow survey than for a deeper one. In addition, the separation between stars and galaxies is easier for brighter (hence, larger) objects.

The relative weight of these arguments is still to be decided. Whereas some of the issues could be clarified with theoretical investigations (i.e., in order to obtain the tightest constraints on cosmological parameters, what is the optimal choice of area and exposure time, with their product being fixed), others (like the importance of intrinsic alignments) still remain unclear. Since big imaging surveys will be conducted with a broad range of scientific applications in mind, this choice will also depend on those additional science goals.

Future Surveys

We are currently witnessing the installment of square-degree cameras at some of the best sites, among them MegaCam at the CFHT, and OmegaCAM at the newly built VLT Survey Telescope (the 2.6m VST) on Paranal (I present here European-biased prospects, as I am most familiar with these projects). Weak lensing, and in particular cosmic shear has been one of the science drivers for these instruments, and large surveys will be carried out with them. Already ongoing is the CFHT Legacy Survey, which will consist of three parts; the most interesting one in the current context is a $\sim 160\,\mathrm{deg}^2$ survey with an exposure time of $\sim 1\,\mathrm{h}$ in each of five optical filters. This survey will therefore yield a more than ten-fold increase over the current VIRMOS-DESCART survey, with corresponding reductions of the statistical and cosmic variance errors on measurements. The multi-color nature of this survey implies that one can obtain photometric redshift estimates at least for a part of the galaxies which will enable the suppression of the potential contribution to the shear signal from intrinsic alignments of galaxies. A forecast of the expected accuracy of cosmological parameter estimates from the CFHTLS combined with the WMAP CMB measurements has been obtained by Tereno et al. (2005). It is expected that a substantial fraction of the VST observing time will be spend on multi-band wide-field surveys which, if properly designed, will be extremely useful

for cosmic shear research. In order to complement results from the CFHTLS, accounting for the fact that the VST has smaller aperture than the CFHT (2.6m vs. 3.6m), a somewhat shallower but wider-field survey would be most reasonable. For both of these surveys, complementary near-IR data will become available after about 2007, with the WirCam instrument on CFHT, and the newly build VISTA 4m-telescope equipped with a wide-field near-IR camera on Paranal, which will yield much better photometric redshift estimates than the optical data alone. Furthermore, with the PanStarrs project, a novel method for wide-field imaging and a great leap forward in the data access rate will be achieved.

Toward the end of the decade, a new generation of cosmic shear surveys may be started; there are two projects currently under debate which would provide a giant leap forward in terms of survey area and/or depth. One is a satellite project, SNAP/JDEM, originally designed for finding and follow-up of high-redshift supernovae to study the expansion history of the Universe and in particular to learn about the equation of state of the dark energy. With its large CCD array and multi-band imaging, SNAP will also be a wonderful instrument for cosmic shear research, yielding photometric redshift estimates for the faint background galaxies, and it is expected that the observing time of this satellite mission will be split between these two probes of dark energy. The other project under discussion is the LSST, a 8m telescope equipped with a $\sim 9\,\mathrm{deg}^2$ camera; such an instrument, with an efficiency larger than a factor 40 over MegaCam@CFHT, would allow huge cosmic shear surveys, easily obtaining a multi-band survey over all extragalactic sky (modulo the constraints from the hemisphere). Since studying the equation of state of dark energy will be done most effectively with good photometric redshifts of source galaxies, the space experiment may appear more promising, given the fact that near-IR photometry is needed for a reliable redshift estimate, and sufficiently deep near-IR observations over a significant area of sky is not possible from the ground.

8 The Mass of, and Associated with Galaxies

8.1 Introduction

Whereas galaxies are not massive enough to show a weak lensing signal individually (see 19), the signal of many galaxies can be superposed statistically. Therefore, if one considers sets of foreground (lens) and background galaxies, then in the mean, in a foreground–background galaxy pair, the image ellipticity of the background galaxy will be preferentially oriented in the direction tangent to the line connecting foreground and background galaxy. The amplitude of this tangential alignment then yields a mean lensing strength that depends on the redshift distributions of foreground and background galaxies, and on the mass distribution of the former population. This effect is called

galaxy–galaxy lensing and will be described in Sect. 8.2 below; it measures the mass properties of galaxies, provided the lensing signal is dominated by the galaxies themselves. This will not be the case for larger angular separations between foreground and background galaxies, since then the mass distribution in which the foreground galaxies are embedded (e.g., their host groups or clusters) starts to contribute significantly to the shear signal. The interpretation of this signal then becomes more difficult. On even larger scales, the foreground galaxies contribute negligibly to the lens signal; a spatial correlation between the lens strength and the foreground galaxy population then reveals the correlation between light (galaxies) and mass in the Universe. This correlated distribution of galaxies with respect to the underlying (dark) matter in the Universe – often called the bias of galaxies – can be studied with weak lensing, as we shall describe in Sect. 8.3 by using the shear signal, and in Sect. 8.4 employing the magnification effect. It should be pointed out here that our lack of knowledge about the relation between the spatial distribution of galaxies and that of the underlying (dark) matter is one of the major problems that hampers the quantitative interpretation of galaxy redshift surveys; hence, these lensing studies can provide highly valuable input into the conclusions drawn from these redshift surveys regarding the statistical properties of the mass distribution in the Universe.

8.2 Galaxy–Galaxy Lensing

The Average Mass Profile of Galaxies

Probing the mass distribution of galaxies usually proceeds with dynamical studies of luminous tracers. The best-known method is the determination of the rotation curves of spiral galaxies, measuring the rotational velocity of stars and gas as a function of distance from the galaxy's center (see Sofue and Rubin 2001 for a recent review). This then yields the mass profile of the galaxy, i.e. $M(\leq r) \propto v_{\rm rot}^2(r)\, r$. For elliptical galaxies, the dynamics of stars (like velocity dispersions and higher-order moments of their velocity distribution, as a function of r) is analyzed to obtain their mass profiles; as the kinematics of stars in ellipticals is more complicated than in spirals, their mass profiles are more difficult to measure (e.g., Gerhard et al. 2001). In both cases, these dynamical methods provided unambiguous evidence for the presence of a dark matter halo in which the luminous galaxy is embedded; e.g., the rotation curves of spirals are flat out to the most distant point where they can be measured. The lack of stars or gas prevents the measurement of the mass profile to radii beyond the luminous extent of galaxies, that is beyond $\sim 10h^{-1}\,$kpc. Other luminous tracers that have been employed to study galaxy masses at larger radii include globular clusters that are found at large galacto-centric radii (Coté et al. 2003), planetary nebulae, and satellite galaxies. Determining the relative radial velocity distribution of the latter with respect to their suspected host galaxy leads to estimates of the dark matter halo out to distances

of $\sim 100h^{-1}$ kpc. These studies (e.g., Zaritsky et al. 1997) have shown that the dark matter halo extends out to at least these distances.

One of the open questions regarding the dark matter profile of galaxies is the spatial extent of the halos. The dynamical studies mentioned above are all compatible with the mass profile following approximately an isothermal law ($\rho \propto r^{-2}$), which has to be truncated at a finite radius to yield a finite total mass. Over the limited range in radii, the isothermal profile cannot easily be distinguished from an NFW mass profile (see IN, Sect. 6.2), for which measurements at larger distances are needed (the mass distribution in the central parts of galaxies is affected by the baryons and thus not expected to follow the NFW profile; see Sect. 7 of SL).

Weak gravitational lensing provides a possibility to study the mass profiles of galaxies at still larger radii. Light bundles from distant background galaxies provide the 'dynamical tracers' that cannot be found physically associated with the galaxies. Light bundles get distorted in such a way that on average, images of background sources are oriented tangent to the transverse direction connecting foreground (lens) and background (source) galaxy. The first attempt to detect such a galaxy–galaxy lensing signal was reported in Tyson et al. (1984), but the use of photographic plates and the relatively poor seeing prevented a detection. Brainerd et al. (1996) presented the first detection and analysis of galaxy–galaxy lensing. Since then, quite a number of surveys have measured this effect, some of them using millions of galaxies.

Strategy

Consider pairs of fore- and background galaxies, with separation in a given angular separation bin. The expected lensing signal is seen as a statistical tangential alignment of background galaxy images with respect to foreground galaxies. For example, if ϕ is the angle between the major axis of the background galaxy and the connecting line, values $\pi/4 \le \phi \le \pi/2$ should be slightly more frequent than $0 \le \phi \le \pi/4$ (see Fig. 48). Using the fact that the intrinsic orientations of background galaxies are distributed isotropically, one can show (Brainerd et al. 1996) that

$$p(\phi) = \frac{2}{\pi}\left[1 - \gamma_{\rm t}\left\langle \frac{1}{|\epsilon^{\rm s}|}\right\rangle \cos(2\phi)\right] , \tag{133}$$

where $\phi \in [0, \pi/2]$ and $\gamma_{\rm t}$ is the mean tangential shear in the angular bin chosen. Thus, the amplitude of the cos-wave yields the (average) strength of the shear.

The mean tangential ellipticity $\langle \epsilon_{\rm t}(\theta)\rangle$ of background galaxies relative to the direction toward foreground galaxies measures the mean tangential shear at separation θ. Since the signal is averaged over many foreground–background pairs, it measures the average mass profiles of the foreground galaxies. For sufficiently large samples of galaxies, the lens sample can be split into several

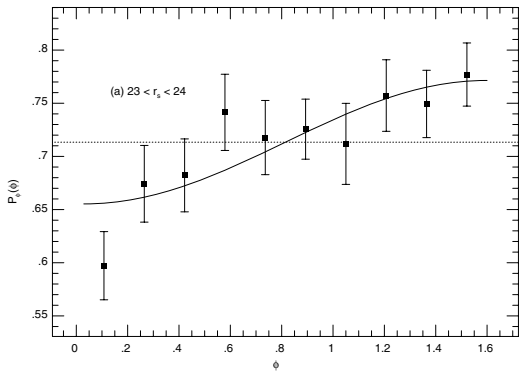

Fig. 48. The probability distribution $p(\phi)$ of the angle ϕ between the major axis of the background galaxy image and the connecting line to the foreground galaxy is plotted for the sample of Brainerd et al. (1996), together with the best fit according to (133). The galaxy pairs have separation $5'' \leq \Delta\theta \leq 34''$, and are foreground-background selected by their apparent magnitudes

subsamples, e.g., according to their color and/or morphology (early-type vs. late-type galaxies), or, if redshift estimates are available, they can be binned according to their luminosity. Then, the mass properties can be derived for each of the subsamples.

The distinction between foreground and background galaxies is ideally performed using redshift information. This is indeed the case for the galaxy-galaxy lensing studies based on the Sloan Digital Sky Survey, for which early results have been reported by McKay et al. (2001); all lens galaxies used there have spectroscopic redshifts, whereas the source galaxies are substantially fainter than the lens galaxies so that they can be considered as a background population. For other surveys, the lack of redshift information requires the separation of galaxies to be based solely on their apparent magnitudes: fainter galaxies are on average at larger distances than brighter ones. However, the resulting samples of 'foreground' and 'background' galaxies will have (often substantial) overlap in redshift, which needs to be accounted for statistically in the quantitative analysis of these surveys.

Quantitative Analysis

The measurement of the galaxy–galaxy lensing signal provides the tangential shear as a function of pair separation, $\gamma_{\rm t}(\theta)$. Without information about the redshifts of individual galaxies, the separation of galaxies into a 'foreground' and 'background' population has to be based on apparent magnitudes only. In the ideal case of a huge number of foreground galaxies, one could investigate the mass properties of 'equal' galaxies, by finely binning them according to redshift, luminosity, color, morphology etc. However, in the real world such a

fine binning has not yet been possible, and therefore, to convert the lensing signal into physical parameters of the lens, a parameterization of the lens population is needed. We shall outline here how such an analysis is performed.

The first ingredient is the redshift probability distribution $p(z|m)$ of galaxies with apparent magnitude m which is assumed to be known from redshift surveys (and/or their extrapolation to fainter magnitudes). This probability density depends on the apparent magnitude m, with a broader distribution and larger mean redshift expected for fainter m. Since the distribution of 'foreground' and 'background' galaxies in redshift is known for a given survey, the probabilities $p(z|m)$ can be employed to calculate the value of $D_{\rm ds}/D_{\rm s}$, averaged over all foreground–background pairs (with this ratio being set to zero if $z_{\rm s} \le z_{\rm d}$). For given physical parameters of the lenses, the shear signal is proportional to this mean distance ratio.

The mass profiles of galaxies are parameterized according to their luminosity. For example, a popular parameterization is that of a truncated isothermal sphere, where the parameters are the line-of-sight velocity dispersion σ (or the equivalent circular velocity $V_{\rm c} = \sqrt{2}\sigma$) and a truncation radius s at which the $\rho \propto r^{-2}$ isothermal density profile turns into a steeper $\rho \propto r^{-4}$ law. The velocity dispersion is certainly dependent on the luminosity, as follows from the Tully–Fisher and Faber–Jackson relations for late- and early-type galaxies, respectively. One therefore assumes the scaling $\sigma = \sigma_*(L/L_*)^{\beta/2}$, where L_* is a fiducial luminosity (and which conveniently can be chosen close to the characteristic luminosity of the Schechter luminosity function). Furthermore, the truncation scale s is assumed to follow the scaling $s = s_*(L/L_*)^{\eta}$. The total mass of a galaxy then is $M \propto \sigma^2 s$, or $M = M_*(L/L_*)^{\beta+\eta}$.

Suppose m and z were given; then, the luminosity of galaxy would be known, and for given values of the parameters σ_*, s_*, β and η, the mass properties of the lens galaxy would be determined. However, since z is not known, but only its probability distribution, only the probability distribution of the lens luminosities, and therefore the mass properties, are known. One could in principle determine the expected shear signal $\gamma_{\rm t}(\theta)$ for a given survey by calculating the shear signal for a given set of redshifts z_i for all lens and source galaxies, and then averaging this signal over the z_i using the redshift probability distribution $p(z_i|m_i)$. However, this very-high dimensional integration cannot be performed; instead, one uses a Monte-Carlo integration method (Schneider and Rix 1997): Given the positions $\boldsymbol{\theta}_i$ and magnitudes m_i of the galaxies, one can draw for each of them a redshift according to $p(z_i|m_i)$, and then calculate the shear at all positions $\boldsymbol{\theta}_i$ corresponding to a source galaxy, for each set of parameters σ_*, s_*, β and η. This procedure can be repeated several times, yielding the expected shear $\langle\gamma_i\rangle$ and its dispersion $\sigma_{\gamma,i}$ for each source galaxy's position. One can then calculate the likelihood function

$$\mathcal{L} = \prod_{i=1}^{N_{\rm s}} \frac{1}{\pi(\sigma_\epsilon^2 + \sigma_{\gamma,i}^2)} \exp\left(-\frac{|\epsilon_i - \langle\gamma_i\rangle\,|^2}{\sigma_\epsilon^2 + \sigma_{\gamma,i}^2}\right)\,, \tag{134}$$

where σ_ϵ is the intrinsic ellipticity dispersion of the galaxies. $\mathcal{L}$ depends on the parameters of the model, and can be maximized with respect to them, thereby yielding estimates of σ_*, s_*, β and η.

First Detection

The galaxy–galaxy lensing effect was first found by Brainerd et al. (1996), on a single $9'.6 \times 9'.6$ field. They considered 'foreground' galaxies in the magnitude range $m \in [20, 23]$, and 'background' galaxies with $m \in [23, 24]$; this yielded 439 foreground and 506 background galaxies, and 3202 pairs with $\Delta\theta \in [5'', 34'']$.[12] For these pairs, the distribution of the alignment angle ϕ is plotted in Fig. 48. This distribution clearly is incompatible with the absence of a lens signal (at the 99.9% confidence level), and thus provides a solid detection.

They analyzed the lens signal $\gamma_t(\theta)$ in a way similar to the method outlined above, except that their Monte-Carlo simulations also randomized the positions of galaxies. The resulting likelihood yields $\sigma_* \approx 160^{+50}_{-60}\,\mathrm{km/s}$ (90% confidence interval), whereas for s_* only a lower limit of $25h^{-1}\,\mathrm{kpc}$ (1σ) is obtained; the small field size, in combination with the relative insensitivity of the lensing signal to s_* once this value is larger than the mean transverse separation of lensing galaxies, prohibited the detection of an upper bound on the halo size.

Galaxy–Galaxy Lensing from the Red-Sequence Cluster Survey (RCS)

Several groups have published results of their galaxy–galaxy lensing surveys since its first detection. Here we shall describe the results of a recent wide-field imaging survey, the RCS; this survey was already described in the context of cosmic shear in Sect. 7.3. 45.5 square degrees of single-band imaging data were used (Hoekstra et al. 2004). Choosing lens galaxies with $19.5 \le R_C \le 21$, and source galaxies having $21.5 \le R_C \le 24$ yielded $\sim 1.2 \times 10^5$ lenses with median redshift of 0.35 and $\sim 1.5 \times 10^6$ sources with median redshift of ~ 0.53, yielding $\langle D_{\rm ds}/D_{\rm s}\rangle = 0.29 \pm 0.01$ for the full sample of lenses and sources. Figure 49 shows the shear signal for this survey.

The lens signal is affected by galaxies counted as lenses, but which in fact are in the foreground. As long as they are not physically associated with lens galaxies, this effect is accounted for in the analysis, i.e., in the value of $\langle D_{\rm ds}/D_{\rm s}\rangle$. However, if fainter galaxies cluster around lens galaxies,

[12] The lower angular scale has been chosen to avoid overlapping isophotes of foreground and background galaxies, whereas the upper limit was selected since it gave the largest signal-to-noise for the deviation of the angular distribution shown in Fig. 48 from a uniform one.

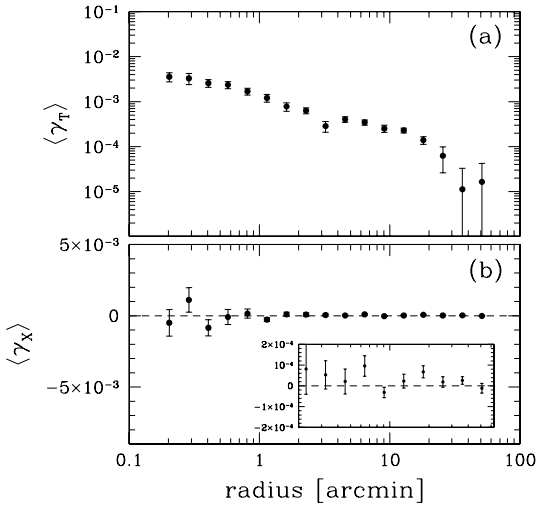

Fig. 49. (**a**) Tangential shear as a function of angular separation, obtained from the RCS survey; the shear signal is detected out to nearly one degree scale. (**b**) Cross shear signal, which is expected to vanish identically in the absence of systematic effects on the ellipticity measurements. As can be seen, the cross signal in indeed compatible with zero. The inset expands the scale, to better show the error bars (from Hoekstra et al. 2003)

this produces an additional effect. Provided the orientation of the associated faint galaxies are random with respect to the separation vector to their bright neighbor, these physical pairs just yield a dilution of the shear signal. The amplitude of this effect can be determined from the angular correlation function of bright and faint galaxies, and easily corrected for. Once this has been done, the corrected shear signal within $10'' \leq \theta \leq 2'$ has been fitted with an SIS model, yielding a mean velocity dispersion of the lens galaxies of $\sqrt{\langle\sigma^2\rangle} = 128 \pm 4\,\mathrm{km/s}$. If the scaling relations between galaxy luminosity and velocity dispersion as described above is employed, with $\beta = 0.6$, the result is $\sigma_* = 140 \pm 4\,\mathrm{km/s}$ for $L_* = 10^{10} h^{-2} L_\odot$ in the blue passband.

To interpret the shear results on larger angular scales, the SIS model no longer suffices, and different mass models need to be employed. Using a truncated isothermal model, the best-fitting values of the scaling parameters $\beta = 0.60 \pm 0.11$ and $\eta = 0.24^{+0.26}_{-0.22}$ are obtained, when marginalizing over all other parameters. Furthermore, $\sigma_* = 137 \pm 5\,\mathrm{km/s}$, in very close agreement with the results from small θ and the SIS model; this is expected, since most of the signal comes from these smaller separations. Most interesting, the analysis also yields an estimate of the truncation scale of $s_* = (185 \pm 30) h^{-1}\,\mathrm{kpc}$, providing one of only a few estimates of the scale of the dark matter halo. Hoekstra et al. also performed the analysis in the frame of an NFW mass model.

These results can then be used to calculate the mass-to-light ratio of an L_* galaxy and, using the scaling, of the galaxy population as a whole. Considering only galaxies with $M \geq 10^{10}h^{-1}M_\odot$, the mean mass-to-light ratio inside the virial radius of galaxy halos is about 100 in solar units.

The Shape of Dark Matter Halos

In the mass models considered before, the mass distribution of galaxies was assumed to be axi-symmetric. In fact, this assumption is not crucial, since the relation between shear and surface mass density, $\gamma_\mathrm{t}(\vartheta) = \bar{\kappa}(\vartheta) - \kappa(\vartheta)$ is true for a general mass distribution, provided γ_t and $\kappa(\vartheta)$ are interpreted as the mean tangential shear and mean surface mass density on a circle of radius ϑ, and $\bar{\kappa}(\vartheta)$ as the mean surface mass density inside this circle (see 24). However, deviations from axial symmetry are imprinted on the shear signal and can in principle be measured. If the mass distribution is 'elliptical', the shear along the major axis (at given distance ϑ) is larger than that along the minor axis, and therefore, an investigation of the strength of the shear signal relative to the orientation of the galaxy can reveal a finite ellipticity of the mass distribution. For that, it is necessary that the orientation of the mass distribution is (at least approximately) known. Provided the orientation of the mass distribution follows approximately the orientation of the luminous part of galaxies, one can analyze the direction dependence of the shear relative to the major axis of the light distribution (Natarajan and Refregier 2000). Hoekstra et al. (2002b) have used the RCS to search for such a direction dependence; they parameterized the lenses with a truncated isothermal profile with ellipticity $\epsilon_\mathrm{mass} = f\epsilon_\mathrm{light}$, where f is a free parameter. The result $f = 0.77 \pm 0.2$ indicates first that the mass distribution of galaxies is not round (which would be the case for $f = 0$, which is incompatible with the data), and second, that the mass distribution is rounder than that of the light distribution, since $f < 1$. However, it must be kept in mind that the assumption of equal orientation between light and mass is crucial for the interpretation of f; misalignment causes a decrease of f. Note that numerical simulations of galaxy evolution predict such a misalignment between total mass and baryons, with an rms deviation of around 20° (van den Bosch et al. 2002). Given the above result on f, it is therefore not excluded that the flattening of halos is very similar to that of the light. Also note that this result yields a value averaged over all galaxies; since the lens efficiency of elliptical galaxies (at given luminosity) is larger than that of spirals, the value of f is dominated by the contributions from early-type galaxies.

Results From the Sloan Survey

The Sloan Digital Sky Survey (e.g., York et al. 2000) will map a quarter of the sky in five photometric bands, and obtain spectra of about one million galaxies. A large fraction of the data has already been taken by SDSS, and parts of this data have already been released (Abazajian et al. 2004). The huge

amount of photometric data in principle is ideal for weak lensing studies, as it beats down statistical uncertainties to an unprecedented low level. However, the site of the telescope, the relatively large pixel size of $0\farcs4$, the relatively shallow exposures of about one minute and the drift-scan mode in which data are taken (yielding excellent flat-fielding, and thus photometric properties, somewhat at the expense of the shape of the PSF) render the data less useful for, e.g., cosmic shear studies: the small mean redshift of the galaxies yields a very small expectation value of the cosmic shear, which can easily be mimicked by residuals from PSF corrections. However, galaxy–galaxy lensing is much less sensitive to larger-scale PSF problems, since the component of the shear used in the analysis is not attached to pixel directions, but to neighboring galaxies, and thus varies rapidly with sky position. Another way of expressing this fact is that the galaxy–galaxy lensing signal would remain unchanged if a uniform shear would be added to the data; therefore, SDSS provides a great opportunity for studying the mass profile of galaxies.

Fischer et al. (2000) reported the first results from the SDSS, and a larger fraction of the SDSS data was subsequently used in a galaxy–galaxy lensing study by McKay et al. (2001), where also the spectroscopic redshifts of the lens galaxies were used. Their sample consists of ∼31000 lens galaxies with measured redshifts, and $\sim 3.6 \times 10^6$ source galaxies selected in the brightness range $18 \le r \le 22$. For this magnitude range, the redshift distribution of galaxies is fairly well known, leaving little calibration uncertainty in the interpretation of the shear signal. In particular, there is very little overlap in the redshift distribution of source and lens galaxies. The data set has been subjected to a large number of tests, to reveal systematics; e.g., null results are obtained when the source galaxies are rotated by 45° (or, equivalently, if $\gamma_\times$ is used instead of γ_t), or if the lens galaxies are replaced by an equal number of randomly distributed points relative to which the tangential shear component is measured. Since the redshifts of the lens galaxies are known, the shear can be measured directly in physical units, so one can determine

$$\Delta\Sigma_+ = \bar{\Sigma}(\le R) - \Sigma(R) \tag{135}$$

in $M_\odot/\mathrm{pc}^2$ as a function of R in kpc.

Figure 50 shows the lensing result from McKay et al. (2001), where the lens sample has been split according to the type of galaxy (early vs. late type) and according to the local spatial number density of galaxies, which is known owing to the spectroscopic redshifts. The fact that most of the signal on small scales is due to ellipticals is expected, as they are more massive at given luminosity than spirals. The large spatial extent of the shear signal for ellipticals relative to that of spirals can be interpreted either by ellipticals having a larger halo than spirals, or that ellipticals are preferentially found in high-density environments, which contribute to the lens signal on large scales. This latter interpretation is supported by the lower panel in Fig. 50 which shows that the signal on large scales is entirely due to lens galaxies in dense environments. This then implies that the galaxy–galaxy lensing signal

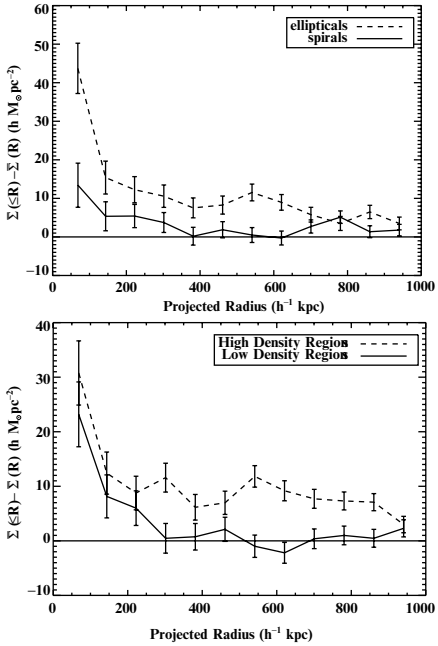

Fig. 50. The galaxy–galaxy lensing signal from the SDSS plotted against physical radius R. The lens sample has been subdivided into early- and late-type galaxies (*upper panel*), and in galaxies situated in dense environments vs. those with a smaller neighboring galaxy density (*lower panel*). The figure clearly shows that the lensing signal is dominated by elliptical galaxies, and by those located in dense environment. Owing to the morphology–density relation of galaxies, these two results are not mutually independent. Note that the lensing signal can be measured out to $1h^{-1}$ Mpc, considerably larger than the expected size of galaxy halos; therefore, the shear at these large separations is most likely caused by the larger-scale mass distribution in which the galaxies are embedded (from McKay et al. 2001)

on large scales no longer measures the density profile of individual galaxies, but gets more and more dominated by group and cluster halos in which these (predominantly early-type) galaxies are embedded.

A separation of these contributions from the data themselves is not possible at present, but can be achieved in the frame of a theoretical model. Guzik and Seljak (2001) employed the halo model for the distribution of matter in the universe (see Cooray and Sheth 2002) to perform this separation. There, the galaxy–galaxy lensing signal either comes from matter in the same halo in which the galaxy is embedded, or due to other halos which are physically associated (i.e., clustered) with the former. This latter contribution is negligible on the scales below $\sim 1h^{-1}$ Mpc on which the SDSS obtained a measurement. The former contribution can be split further into two terms: the first is from the dark matter around the galaxies themselves, whereas the second is due to

the matter in groups and clusters to which the galaxies might belong. The relative amplitude of these two terms depends on the fraction of galaxies which are located in groups and clusters; the larger this fraction, the more important are larger-scale halos for the shear signal. Guzik and Seljak estimate from the radial dependence of the SDSS signal that about 20% of galaxies reside in groups and clusters; on scales larger than about $200h^{-1}\,\mathrm{kpc}$ their contribution dominates. The virial mass of an early-type L_* galaxy is estimated to be $M_{200}(L_*) = (9.3 \pm 2.2) \times 10^{11} h^{-1} M_\odot$, and about a factor of three smaller for late-type galaxies (with luminosity measured in a red passband; the differences are substantially larger for bluer passbands, owing to the sensitivity of the luminosity to star formation activity in late types). From the mass-to-light ratio in red passbands, Guzik and Seljak estimate that an L_* galaxy converts about 10–15% of its virial mass into stars. Since this fraction is close to the baryon fraction in the universe, they conclude that most of the baryons of an L_* galaxy are transformed into stars. For more massive halos, the mass-to-light ratio increases ($M/L \propto L^{0.4\pm0.2}$), and therefore their conversion of baryons into stars is smaller – in agreement with what we argued about clusters, where most of the baryons are present in the form of a hot intracluster gas.

Yang et al. (2003) studied the cross-correlation between mass and galaxies using numerical simulations of structure formation and semi-analytic models of galaxy evolution. The observed dependence of the galaxy–galaxy lensing signal on galaxy luminosity, morphological type and galaxy environment, as obtained by McKay et al. (2001), is well reproduced in these simulations. The galaxy-mass correlation is affected by satellite galaxies, i.e. galaxies not situated at the center of their respective halo. Central galaxies can be selected by restricting the foreground galaxy sample to relatively isolated galaxies. The galaxy–galaxy lensing signal for such central galaxies can well be described by an NFW mass profile, whereas this no longer is true if all galaxies are considered. Combining the measurement with the simulation, they find that an L_*-galaxy typically resides in a halo with a virial mass of $\sim 2 \times 10^{12} h^{-1} M_\odot$.

With the SDSS progressing, larger datasets become available, allowing a more refined analysis of galaxy–galaxy lensing (Sheldon et al. 2004; Seljak et al. 2004). In the analysis of Seljak et al. (2004), more than 2.7×10^5 galaxies with spectroscopic redshifts have been used as foreground galaxies, and as background population those fainter galaxies for which photometric redshifts have been estimated. The resulting signal is shown in Fig. 51, for six different bins in (foreground) galaxy luminosity.

In a further test to constrain systematic effects in the data, Hirata et al. (2004) have used spectroscopic and photometric redshifts to study the question whether an alignment of satellite galaxies around the lens galaxies can affect the galaxy–galaxy lensing signal from the SDSS; they obtain an upper limit of a 15% contamination.

The SDSS already has yielded important information about the mass properties of galaxies; taken into account that only a part of the data of

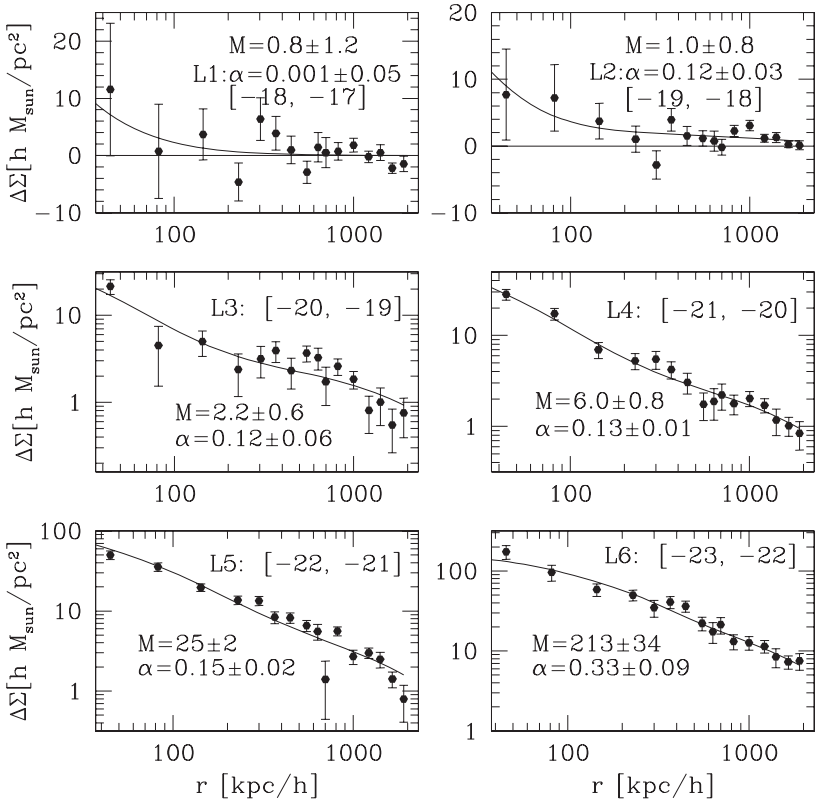

Fig. 51. The galaxy–galaxy lensing signal for six luminosity bins of foreground galaxies, as indicated by the absolute magnitude interval in each panel. The curves show a two-parameter model fitted to the data, based on the halo model, and the fit parameters are indicated: M is the virial mass of the halo (in units of $10^{11}h^{-1}M_{\odot}$) in which the galaxies reside, and α is the fraction of the galaxies which are not central inside the halo, but satellite galaxies (from Seljak et al. 2004)

the complete survey has been used in the studies mentioned above, an analysis of the final survey will yield rich harvest when applied to a galaxy–galaxy lensing analysis.

Lensing by Galaxies in Clusters

As an extension of the method presented hitherto, one might use galaxy–galaxy lensing also to specifically target the mass profile of galaxies in the inner part of clusters. One might expect that owing to tidal stripping, their dark matter halo has a considerably smaller spatial extent than that of the galaxy population as a whole. The study of this effect with lensing is more complicated than galaxy–galaxy lensing in the field, both observationally and

from theory. Observationally, the data sets that can be used need to be taken in the inner part of massive clusters; since these are rare, a single wide-field image usually contains at most one such cluster. Furthermore, the number of massive galaxies projected near the center of a cluster is fairly small. Therefore, in order to obtain good statistics, the data of different clusters should be combined. Since the cores of clusters are optically bright, measuring the shape of faint background galaxies is more difficult than in a blank field. From the theoretical side, the lensing strength of the cluster is much stronger than that of the individual cluster galaxies, and so this large-scale shear contribution needs to be accounted for in the galaxy–galaxy lensing analysis.

Methods for performing this separation between cluster and galaxy shear were developed by Natarajan and Kneib (1997) and Geiger and Schneider (1998). Perhaps the simplest approach is provided by the aperture mass methods, applied to the individual cluster galaxies; there one measures the tangential shear inside an annulus around each cluster galaxy. This measure is insensitive to the shear contribution which is linear in the angular variable $\boldsymbol{\theta}$, which is a first local approximation to the larger-scale shear caused by the cluster. Alternatively, a mass model of the (smoothed) cluster can be obtained, either from strong or weak lensing constraints, or preferentially both, and subtracted from the shear signal around galaxies to see their signal. However, once the mass fraction in the galaxies becomes considerable, this method starts to become biased. Geiger and Schneider (1999) have suggested to simultaneously perform a weak lensing mass reconstruction of the cluster and a determination of the parameters of a conveniently parameterized mass model of cluster galaxies (e.g., the truncated isothermal sphere); since the maximum likelihood method for the mass reconstruction (see Sect. 5.3) was used, the solution results from maximizing the likelihood with respect to the mass profile parameters (the deflection potential on a grid) and the galaxy mass parameters.

Natarajan et al. (1998), by analyzing HST data of the cluster AC 114, concluded that the truncation radius of a fiducial L_* galaxy in this cluster is $\sim 15h^{-1}\,\mathrm{kpc}$; similarly, Geiger and Schneider (1999) showed that the best-fitting truncation radius for early-type galaxies in the cluster A 851 is $\sim 10h^{-1}\,\mathrm{kpc}$ (see Fig. 52). Although the uncertainties are fairly large, these results indicate that indeed galaxies near cluster centers have a halo size considerably smaller than the average galaxy. The sample of clusters which can be investigated using this method will dramatically increase once the cluster sample observed with the new ACS camera onboard HST becomes available and gets properly analyzed.

8.3 Galaxy Biasing: Shear Method

On small scales, galaxy–galaxy lensing measures the mass profile of galaxies, whereas on intermediate scales the environment of galaxies starts to dominate the shear signal. On even larger scale (say, beyond $\sim 1h^{-1}\,\mathrm{Mpc}$), the host halo

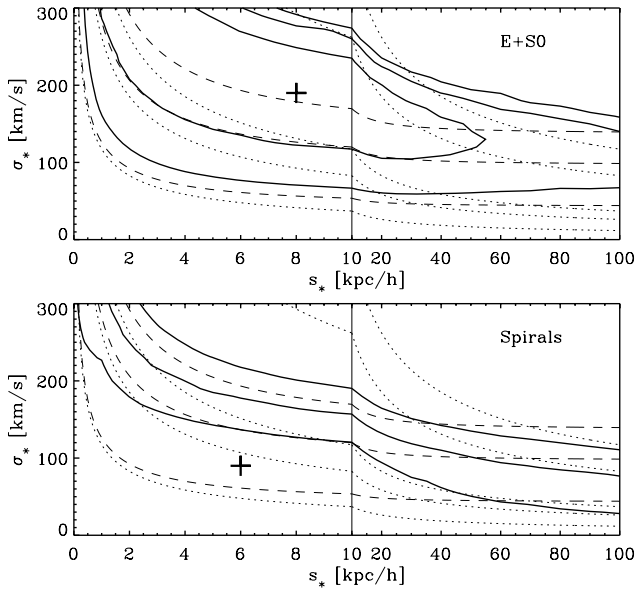

Fig. 52. Significance contours (*solid*) for galaxy properties obtained from galaxy–galaxy lensing of galaxies in the cluster Cl 0939+4713. The parameters are the velocity dispersion σ_* and the halo truncation radius s_* of an L_*-galaxy. Based on HST data (see Fig. 22), a simultaneous reconstruction of the cluster mass profile and the determination of the galaxy mass parameters was performed. No significant lensing signal is seen from the 55 late-type galaxies (*lower panel*), but a clear detection and upper bound to the halo size is detected for the 56 early-types. Dashed and dotted curves connect models with the same mass inside $8h^{-1}$ 1kpc and total mass of an L_*-galaxy, respectively (from Geiger and Schneider 1999)

contribution becomes negligible. Beyond that distance, any signal must come from the correlation of galaxy positions with the mass distribution in the Universe. This correlation, and the related issue of galaxy biasing (see Sect. 6.1 of IN), can ideally be studied with weak lensing. In this section we shall outline how these quantities can be determined from shear measurements, and describe some recent results. As we shall see, this issue is intimately related to galaxy–galaxy lensing. The next section deals with the magnification of distant sources caused by mass overdensities correlated with galaxies and thereby causing an apparent correlation between high-redshift sources and low-redshift galaxies; the amplitude of this signal is again proportional to the correlation between galaxies and the underlying dark matter.

An interesting illustration of the correlation between galaxies and mass has been derived by Wilson et al. (2001). They studied 6 fields with $30' \times 30'$ each, selected bright early-type galaxies from their $V - I$ colors and I magnitudes and measured the shear from faint galaxies. Assuming that mass is strongly correlated with early-type galaxies, these can be used to predict the shear

field, with an overall normalization given by the mean mass-to-light ratio of the early-type galaxies. This correlation has indeed been found, at the 5.2-σ significance level, and a value of $M/L \approx 300h$ in solar units has been obtained, assuming a flat low-density Universe.

The Galaxy–Mass Correlation and the Bias Parameter

First, the concept of the correlation between galaxies and mass shall be described more quantitatively. The mass density inhomogeneities are described, as before, by the dimensionless density contrast $\delta(\mathbf{x}, w)$. In analogy to this quantity, one defines the number density contrast $\delta_{\rm g}(\mathbf{x}, w)$ of galaxies as

$$\delta_{\rm g}(\mathbf{x}, w) := \frac{n(\mathbf{x}, w) - \bar{n}(w)}{\bar{n}(w)} \ , \tag{136}$$

where $n(\mathbf{x}, w)$ is the number density of galaxies at comoving position $\mathbf{x}$ and comoving distance w (the latter providing a parameterization of cosmic time or redshift), and $\bar{n}(w)$ is the mean number density of galaxies at that epoch. Since the galaxy distribution is discrete, the true number density is simply a sum of delta-functions. What is meant by n is that the probability of finding a galaxy in the volume $\mathrm{d}V$ situated at position $\mathbf{x}$ is $n(\mathbf{x})\,\mathrm{d}V$.

The relation between δ and $\delta_{\rm g}$ describes the relative distribution of galaxies and matter in the Universe. The simplest case is that of an *unbiased* distribution, for which $\delta_g = \delta$; then, the probability of finding a galaxy at any location would be just proportional to the matter density. However, one might expect that the relation between luminous and dark matter is more complicated. For example, galaxies are expected to form preferentially in the high-density peaks in the early Universe, which would imply that there are proportionally more galaxies within mass overdensities. This led to the introduction of the concept of biasing (e.g., Bardeen et al. 1986; Kaiser 1984). The simplest form of biasing, called linear deterministic biasing, is provided by setting $\delta_{\rm g} = b\,\delta$, with b being the bias parameter. One might suspect that the relative bias is approximately constant on large scales, where the density field is still in its linear evolution (i.e., on scales $\gtrsim 10h^{-1}\,$Mpc today). On smaller scales, however, b most likely is no longer simply a constant. For example, the spatial distribution of galaxies in clusters seems to deviate from the radial mass profile, and the distributions of different galaxy types are different. Furthermore, by comparing the clustering properties of galaxies of different types, one can determine their relative bias, from which it is concluded that more luminous galaxies are more strongly biased than less luminous ones, and early-type galaxies are more strongly clustered than late-types (see Norberg et al. 2001, and Zehavi et al. 2002 for recent results from the 2dFGRS and the SDSS). This is also expected from theoretical models and numerical simulations which show that more massive halos cluster more strongly (e.g., Sheth et al. 2001; Jing 1998). In order to account for a possible scale dependence of the bias, one considers the Fourier transforms of δ and $\delta_{\rm g}$ and relates them according to

$$\hat{\delta}_{\rm g}(\mathbf{k},w) = b(|\mathbf{k}|,w)\,\hat{\delta}(\mathbf{k},w)\ , \tag{137}$$

thus accounting for a possible scale and redshift dependence of the bias.

Even this more general bias description is most likely too simple, as it is still deterministic. Owing to the complexity of galaxy formation and evolution, it is to be expected that the galaxy distribution is subject to stochasticity in excess to Poisson sampling (Tegmark and Peebles 1998; Dekel and Lahav 1999). To account for that, another parameter is introduced, the correlation parameter $r(|\mathbf{k}|,w)$, which in general will also depend on scale and cosmic epoch. To define it, we first consider the correlator

$$\left\langle \hat{\delta}(\mathbf{k},w)\,\hat{\delta}^*_{\rm g}(\mathbf{k}',w)\right\rangle = (2\pi)^3\,\delta_{\rm D}(\mathbf{k}-\mathbf{k}')\,P_{\delta{\rm g}}(|\mathbf{k}|,w)\ , \tag{138}$$

where the occurrence of the delta function is due to the statistical homogeneity of the density fields, and $P_{\delta{\rm g}}$ denotes the cross-power between galaxies and matter. The correlation parameter r is then defined as

$$r(|\mathbf{k}|,w) = \frac{P_{\delta{\rm g}}(|\mathbf{k}|,w)}{\sqrt{P_\delta(|\mathbf{k}|,w)\,P_{\rm g}(|\mathbf{k}|,w)}}\ . \tag{139}$$

In the case of *stochastic biasing*, the definition of the bias parameter is modified to

$$P_{\rm g}(|\mathbf{k}|,w) = b^2(|\mathbf{k}|,w)\,P_\delta(|\mathbf{k}|,w)\ , \tag{140}$$

which agrees with the definition (137) in the case of $r\equiv 1$, but is more general since (140) no longer relates the phase of (the Fourier transform of) $\delta_{\rm g}$ to that of δ. Combining the last two equations yields

$$P_{\delta{\rm g}}(|\mathbf{k}|,w) = b(|\mathbf{k}|,w)\,r(|\mathbf{k}|,w)\,P_\delta(|\mathbf{k}|,w)\ . \tag{141}$$

We point out again that galaxy redshift surveys are used to determine the two-point statistics of the galaxy distribution, and therefore $P_{\rm g}$; in order to relate these measurements to P_δ, assumptions on the properties of the bias have to be made. As we shall discuss next, weak lensing can determine both the bias parameter and the correlation parameter.

The Principle

In order to determine b and r, the three power spectra defined above (or functions thereof) need to be measured. Second-order cosmic shear measures, as discussed in Sect. 6, are proportional to the power spectrum P_δ. The correlation function of galaxies is linearly related to $P_{\rm g}$. In particular, the three-dimensional correlation function is just the Fourier transform of $P_{\rm g}$, whereas the angular correlation function contains a projection of $P_{\rm g}$ along the line-of-sight and thus follows from Limber's equation as discussed in Sect. 6.2. Finally, the cross-power $P_{\delta{\rm g}}$ describes the correlation between mass and light, and thus

determines the relation between the lensing properties of the mass distribution in the Universe to the location of the galaxies. galaxy–galaxy lensing on large angular scales (where the mass profile of individual galaxies no longer yields a significant contribution) provides one of the measures for such a correlation. Hence, measurements of these three statistical distributions allow a determination of r and b.

As we shall consider projected densities, we relate the density field of galaxies on the sky to the spatial distribution. Hence, consider a population of ('foreground') galaxies with spatial number density $n(\mathbf{x}, w)$. The number density of these galaxies on the sky at $\boldsymbol{\theta}$ is then $N(\boldsymbol{\theta}) = \int \mathrm{d}w\, \nu(w)\, n(f_k(w)\boldsymbol{\theta}, w)$, where $\nu(w)$ is the redshift-dependent selection function, describing which fraction of the galaxies at comoving distance w are included in the sample. Foremost, this accounts for the fact that for large distances, only the more luminous galaxies will be in the observed galaxy sample, but ν can account also for more subtle effects, such as spectral features entering or leaving the photometric bands due to redshifting. The mean number density of galaxies on the sky is $\bar{N} = \int \mathrm{d}w\, \nu(w)\, \bar{n}(w)$; the redshift distribution, or more precisely, the distribution in comoving distance, of these galaxies therefore is $p_\mathrm{f}(w) = \nu(w)\, \bar{n}(w)/\bar{N}$, thus relating the selection function $\nu(w)$ to the redshift distribution. Using the definition (136), one then finds that

$$N(\boldsymbol{\theta}) = \bar{N} \left[1 + \int \mathrm{d}w\, p_\mathrm{f}(w)\, \delta_\mathrm{g}(f_K(w)\boldsymbol{\theta}, w) \right] . \tag{142}$$

We shall denote the fractional number density by $\kappa_\mathrm{g}(\boldsymbol{\theta}) := \left[N(\boldsymbol{\theta}) - \bar{N} \right] / \bar{N} = \int \mathrm{d}w\, p_\mathrm{f}(w)\, \delta_\mathrm{g}(f_K(w)\boldsymbol{\theta}, w)$.

Aperture Measures

We have seen in Sect. 6.3 that the aperture mass dispersion provides a very convenient measure of second-order cosmic shear statistics. Therefore, it is tempting to use aperture measures also for the determination of the bias and the mass–galaxy correlation. Define in analogy to the definition of the aperture mass M_ap in terms of the projected mass density the aperture counts (Schneider 1998),

$$\mathcal{N}(\theta) = \int \mathrm{d}^2\vartheta\, U(|\boldsymbol{\vartheta}|)\, \kappa_\mathrm{g}(\boldsymbol{\vartheta}) , \tag{143}$$

where the integral extends over the aperture of angular radius θ, and $\boldsymbol{\vartheta}$ measures the position relative to the center of the aperture. An unbiased estimate of the aperture counts is $\bar{N}^{-1} \sum_i U(|\boldsymbol{\theta}_i|)$, where the $\boldsymbol{\theta}_i$ are the positions of the galaxies. We now consider the dispersion of the aperture counts,

$$\left\langle \mathcal{N}^2(\theta) \right\rangle = \int \mathrm{d}^2\vartheta\, U(|\boldsymbol{\vartheta}|) \int \mathrm{d}^2\vartheta'\, U(|\boldsymbol{\vartheta}'|) \left\langle \kappa_\mathrm{g}(\boldsymbol{\vartheta})\, \kappa_\mathrm{g}(\boldsymbol{\vartheta}') \right\rangle . \tag{144}$$

The correlator in the last expression is the angular two-point correlation function $\omega(\Delta\vartheta)$ of the galaxies; its Fourier transform is the angular power spectrum

$P_\omega(\ell)$ of galaxies. Using the definition of κ_g together with the result (98) allows us to express P_ω in terms of the three-dimensional power spectrum of the galaxy distribution,

$$P_\omega(\ell) = \int \mathrm{d}w\, \frac{p_\mathrm{f}^2(w)}{f_K^2(w)}\, b^2\left(\frac{\ell}{f_K(w)}, w\right) P_\delta\left(\frac{\ell}{f_K(w)}, w\right)$$
$$= \bar{b}^2 \int \mathrm{d}w\, \frac{p_\mathrm{f}^2(w)}{f_K^2(w)}\, P_\delta\left(\frac{\ell}{f_K(w)}, w\right) , \tag{145}$$

where we made use of (140), and in the final step we defined the mean bias parameter $\bar{b}$ which is a weighted average of the bias parameter over the redshift distribution of the galaxies and which depends on the angular wave number ℓ. To simplify notation, we shall drop the bar on b and consider the bias factor as being conveniently averaged over redshift (and later, also over spatial scale). The aperture count dispersion then becomes

$$\left\langle \mathcal{N}^2(\theta)\right\rangle = \frac{1}{2\pi}\int \mathrm{d}\ell\, \ell\, P_\omega(\ell) W_\mathrm{ap}(\theta\ell) = 2\pi\, b^2\, H_\mathrm{gg}(\theta) , \tag{146}$$

where W_ap is given in (109), and we have defined

$$H_\mathrm{gg}(\theta) = \int \mathrm{d}w\, \frac{p_\mathrm{f}^2(w)}{f_K^2(w)}\, \mathcal{P}(w,\theta) , \tag{147}$$

with

$$\mathcal{P}(w,\theta) = \frac{1}{(2\pi)^2}\int \mathrm{d}\ell\, \ell\, P_\delta\left(\frac{\ell}{f_K(w)}, w\right) W_\mathrm{ap}(\theta\ell) . \tag{148}$$

Using the same notation (following Hoekstra et al. 2002c), we can write the aperture mass dispersion as

$$\left\langle M_\mathrm{ap}^2(\theta)\right\rangle = \frac{9\pi}{2}\left(\frac{H_0}{c}\right)^4 \Omega_\mathrm{m}^2\, H_\kappa(\theta) , \tag{149}$$

with

$$H_\kappa(\theta) = \int \mathrm{d}w\, \frac{g^2(w)}{a^2(w)}\, \mathcal{P}(w,\theta) , \tag{150}$$

where $g(w)$ (see 94) describes the source-redshift weighted efficiency factor of a lens at distance w. One therefore obtains an expression for the bias factor,

$$b^2 = \frac{9}{4}\left(\frac{H_0}{c}\right)^4 \frac{H_\kappa(\theta)}{H_\mathrm{gg}(\theta)}\, \Omega_\mathrm{m}^2\, \frac{\left\langle \mathcal{N}^2(\theta)\right\rangle}{\left\langle M_\mathrm{ap}^2(\theta)\right\rangle} = f_\mathrm{b}(\theta)\Omega_\mathrm{m}^2\, \frac{\left\langle \mathcal{N}^2(\theta)\right\rangle}{\left\langle M_\mathrm{ap}^2(\theta)\right\rangle} . \tag{151}$$

Note that $f_\mathrm{b}(\theta)$ depends, besides the aperture radius θ, on the cosmological parameters Ω_m and Ω_Λ, but for a given cosmological model, it depends only

weakly on the filter scale θ and on the adopted power spectrum P_δ (van Waerbeke 1998; Hoekstra et al. 2002c). This is due to the fact that both, $\langle\mathcal{N}^2(\theta)\rangle$ and $\langle M_{\rm ap}^2(\theta)\rangle$ are linear in the power spectrum, through the functions H, and in both cases they probe only a very narrow range of k-values, owing to the narrow width of the filter function $W_{\rm ap}$. Hence, the ratio $\langle\mathcal{N}^2(\theta)\rangle\,/\,\langle M_{\rm ap}^2(\theta)\rangle$ is expected to be very close to a constant if the bias factor b is scale independent.

Next we consider the correlation coefficient r between the dark matter distribution and the galaxy field. Correlating $M_{\rm ap}(\theta)$ with $\mathcal{N}(\theta)$ yields

$$\begin{aligned}\langle M_{\rm ap}(\theta)\mathcal{N}(\theta)\rangle &= \int {\rm d}^2\vartheta\; U(|\boldsymbol{\vartheta}|)\int {\rm d}^2\vartheta'\; U(|\boldsymbol{\vartheta}'|)\,\langle\kappa(\boldsymbol{\vartheta})\,\kappa_{\rm g}(\boldsymbol{\vartheta}')\rangle \\ &= 3\pi\left(\frac{H_0}{c}\right)^2\,\Omega_{\rm m}\,b\,r\,H_{\kappa{\rm g}}(\theta)\;, \end{aligned} \tag{152}$$

with

$$H_{\kappa{\rm g}}(\theta) = \int {\rm d}w\;\frac{p_{\rm f}(w)\,g(w)}{a(w)\,f_K(w)}\mathcal{P}(w,\theta)\;. \tag{153}$$

It should be noted that $\langle M_{\rm ap}(\theta)\mathcal{N}(\theta)\rangle$ is a first-order statistics in the cosmic shear. It correlates the shear signal with the location of galaxies, which are assumed to trace the total matter distribution. As shown in Schneider (1998), the signal-to-noise of this correlator is higher than that of $\langle M_{\rm ap}^2\rangle$, and therefore was introduced as a convenient statistics for the detection of cosmic shear. In fact, in their original analysis of the RCS, based on $16\,{\rm deg}^2$, Hoekstra et al. (2001) obtained a significant signal for $\langle M_{\rm ap}(\theta)\mathcal{N}(\theta)\rangle$, but not for $\langle M_{\rm ap}^2(\theta)\rangle$. Combining (146) and (149) with (152), the correlation coefficient r can be expressed as

$$r = \frac{\sqrt{H_\kappa(\theta)\,H_{\rm gg}(\theta)}}{H_{\kappa{\rm g}}(\theta)}\;\frac{\langle M_{\rm ap}(\theta)\mathcal{N}(\theta)\rangle}{\sqrt{\langle M_{\rm ap}^2(\theta)\rangle\;\langle\mathcal{N}^2(\theta)\rangle}} = f_{\rm r}(\theta)\;\frac{\langle M_{\rm ap}(\theta)\mathcal{N}(\theta)\rangle}{\sqrt{\langle M_{\rm ap}^2(\theta)\rangle\;\langle\mathcal{N}^2(\theta)\rangle}}\;. \tag{154}$$

As was the case for $f_{\rm b}$, the function $f_{\rm r}$ depends only very weakly on the filter scale and on the adopted form of the power spectrum, so that a variation of the (observable) final ratio with angular scale would indicate the scale dependence of the correlation coefficient.

Whereas the two aperture measures $M_{\rm ap}$ and $\mathcal{N}$ can in principle be obtained from the data field by putting down circular apertures, and the corresponding second-order statistics can likewise be determined through unbiased estimators defined on these apertures, this is not the method of choice in practice, due to gaps and holes in the data field. Note that in our discussion of cosmic shear in Sect. 6.3, we have expressed $\langle M_{\rm ap}^2(\theta)\rangle$ in terms of the shear two-point correlation functions $\xi_\pm(\theta)$ – see (115) – just for this reason. In close analogy, $\mathcal{N}^2(\theta)$ can be expressed in terms of the angular correlation function

$\omega(\theta)$ of the projected galaxy positions, as seen by (144), or more explicitly, when replacing the power spectrum $P_\omega(\ell)$ in (146) by its Fourier transform, which is the angular correlation function, one finds

$$\left\langle \mathcal{N}^2(\theta) \right\rangle = \int_0^{2\theta} \frac{\mathrm{d}\vartheta\, \vartheta}{\theta^2}\, \omega(\vartheta)\, T_+\left(\frac{\vartheta}{\theta}\right) \,, \tag{155}$$

where the function T_+ is the same as that occurring in (115). Correspondingly, we introduce the power spectrum $P_{\mathrm{g}\kappa}(\ell)$, which is defined as

$$\left\langle \hat{\kappa}(\boldsymbol{\ell}) \hat{\kappa}_{\mathrm{g}}^*(\boldsymbol{\ell}') \right\rangle = (2\pi)^2 \delta_{\mathrm{D}}(\boldsymbol{\ell} - \boldsymbol{\ell}')\, P_{\kappa\mathrm{g}}(|\boldsymbol{\ell}|) \,. \tag{156}$$

Applying (98), as well as the definitions of the bias and correlation functions, this projected cross-power spectrum is related to the 3-D density contrast by

$$P_{\kappa\mathrm{g}}(\ell) = \frac{3}{2}\left(\frac{H_0}{c}\right)^2 \Omega_{\mathrm{m}} b r \int \mathrm{d}w \frac{g(w) p_{\mathrm{f}}(w)}{a(w) f_K(w)}\, P_\delta\left(\frac{\ell}{f_K(w)}, w\right) \,. \tag{157}$$

The angular correlation function $\left\langle \kappa(\boldsymbol{\vartheta}) \kappa(\boldsymbol{\vartheta'}) \right\rangle$ occurring in (152) can then be replaced by its Fourier transform $P_{\kappa\mathrm{g}}$. On the other hand, since the Fourier transform of the surface mass density κ is simply related to that of the shear, one can consider the correlation between the galaxy positions with the tangential shear component,

$$\begin{aligned}
\langle \gamma_{\mathrm{t}}(\theta) \rangle &:= \langle \kappa_{\mathrm{g}}(\mathbf{0}) \gamma_{\mathrm{t}}(\boldsymbol{\theta}) \rangle \\
&= -\int \frac{\mathrm{d}^2\ell}{(2\pi)^2} \int \frac{\mathrm{d}^2\ell'}{(2\pi)^2} \mathrm{e}^{2\mathrm{i}(\beta' - \varphi)} \exp\left(-\mathrm{i}\boldsymbol{\theta} \cdot \boldsymbol{\ell}'\right) \left\langle \hat{\kappa}_{\mathrm{g}}(\boldsymbol{\ell}) \hat{\kappa}(\boldsymbol{\ell}') \right\rangle \\
&= \frac{1}{2\pi} \int \mathrm{d}\ell\, \ell\, \mathrm{J}_2(\theta\ell)\, P_{\kappa\mathrm{g}}(\ell) \\
&\Rightarrow P_{\kappa\mathrm{g}}(\ell) = 2\pi \int \mathrm{d}\theta\, \theta\, \langle \gamma_{\mathrm{t}}(\theta) \rangle\, J_2(\theta\ell) \,.
\end{aligned} \tag{158}$$

Note that $\langle \gamma_{\mathrm{t}}(\theta) \rangle$ is just the galaxy–galaxy lensing signal discussed in Sect. 8.2; this shows very clearly that galaxy–galaxy lensing measures the correlation of mass and light in the Universe. In terms of this mean tangential shear, the aperture mass and galaxy number counts can be written as

$$\langle M_{\mathrm{ap}}(\theta) \mathcal{N}(\theta) \rangle = \int_0^{2\theta} \frac{\mathrm{d}\vartheta\, \vartheta}{\theta^2}\, \langle \gamma_{\mathrm{t}}(\vartheta) \rangle\, T_2\left(\frac{\vartheta}{\theta}\right) \,, \tag{159}$$

where the function T_2 is defined in a way similar to $T_\pm$ and given explicitly as

$$T_2(x) = 576 \int_0^\infty \frac{\mathrm{d}t}{t^3}\, \mathrm{J}_2(xt)\, \left[\mathrm{J}_4(t)\right]^2 \,; \tag{160}$$

this function vanishes for $x > 2$, so that the integral in (159) extends over a finite interval only. Hence, all three aperture correlators can be calculated from two-point correlation functions which can be determined from the data directly, independent of possible gaps in the field geometry.

Results from the RCS

Hoekstra et al. (2002c) have applied the foregoing equations to a combination of their RCS survey and the VIRMOS-DESCART survey. The former was used to determine $\langle \mathcal{N}^2 \rangle$ and $\langle M_{\rm ap}\mathcal{N} \rangle$, the latter for deriving $\langle M_{\rm ap}^2 \rangle$. As pointed out by these authors, this combination of surveys is very useful, in that the power spectrum at a redshift around $z \sim 0.35$ can be probed; indeed, they demonstrate that the effective redshift distribution over which the power spectrum, and thus b and r are probed, are well matched for all three statistics for their choice of surveys. 'Foreground' galaxies for the measurement of $\omega(\theta)$ and $\langle \gamma_{\rm t}(\theta) \rangle$ are chosen to have $19.5 \le R_C \le 21$, 'background' galaxies are those with $21.5 \le R_C \le 24$. In Fig. 53 the three aperture statistics are shown as a function of angular scale, as determined from their combined survey, whereas in the right panels, the ratios of these statistics as they appear in (151) and (154) are displayed. Also shown are predictions of these quantities from two cosmological models, assuming $b = 1$ and $r = 1$. The fact that these model predictions are fairly constant in the right-hand panels shows that the factors $f_{\rm b}$ and $f_{\rm r}$ are nearly independent of the radius θ of the aperture, as mentioned before.

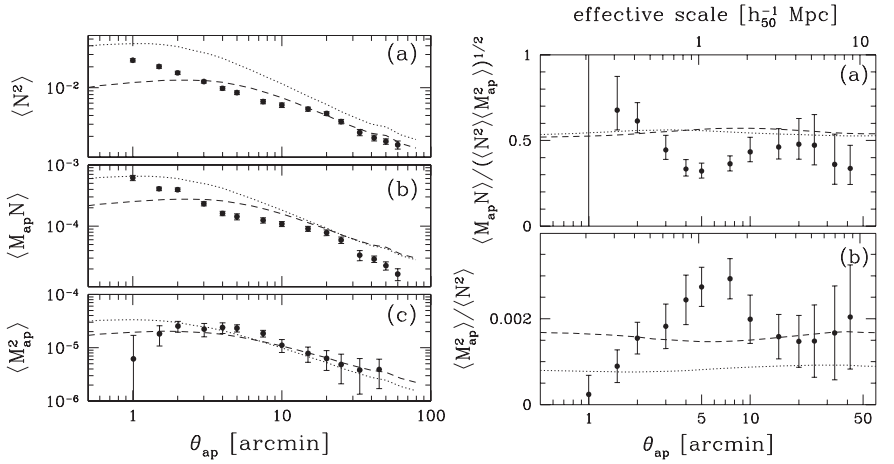

Fig. 53. The left figure displays the three aperture statistics as measured by combining the RCS and the VIRMOS-DESCART survey. Points show measured values, as determined from the correlation functions. The right panels display the ratios of the aperture statistics as they appear in (151) and (154). The dotted and dashed curves in all panels show the predictions for an OCDM and a ΛCDM model, respectively, both with $\Omega_{\rm m} = 0.3$, $\sigma_8 = 0.9$, and $\Gamma_{\rm spect} = 0.21$, for the fiducial values of $b = 1 = r$. The fact that the curves in the right panels are nearly constant show the near-independence of $f_{\rm b}$ and $f_{\rm r}$ on the filter scale. The upper axis in the right panels show the effective physical scale on which the values of b and r are measured (from Hoekstra et al. 2002c)

The results for the bias and correlation factor are shown in Fig. 54, as a function of angular scale and effective physical scale, corresponding to a median redshift of $z \sim 0.35$. The results indicate that the bias factor and the galaxy-mass correlation coefficient are compatible with a constant value on large scales, $\gtrsim 5h^{-1}\,\mathrm{Mpc}$, but on smaller scales both seem to change with scale. The transition between these two regimes occurs at about the scale where the density field at redshift $z \sim 0.35$ turns from linear to non-linear evolution. In fact, in the non-linear regime one does not expect a constant value of both coefficients, whereas in the linear regime, constant values for them appear natural. It is evident from the figure that the error bars are still too large to draw definite conclusions about the behavior of b and r as a function of scale, but the approach to investigate the relation between galaxies and mass is extremely promising and will certainly yield very useful insight when applied to the next generation of cosmic shear surveys. In particular, with larger surveys than currently available, different cuts in the definition of foreground and background galaxies can be used, and thus the redshift dependence of b and r can be investigated. This is of course optimized if (photometric) redshift estimates for the galaxy sample become available.

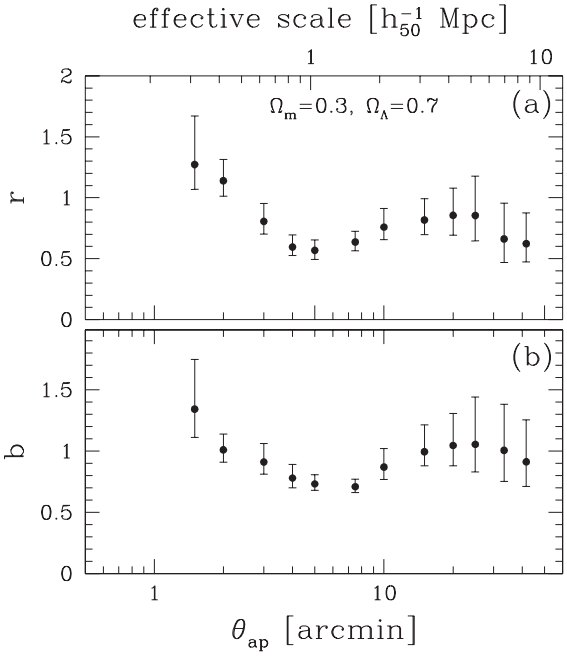

Fig. 54. The values of the bias and correlation coefficient, as determined from (151) and (154) and the results shown in Fig. 53; here, a ΛCDM model has been assumed for the cosmology dependence of the functions f_b and f_r. The upper axis indicates the effective scale on which b and r are measured (from Hoekstra et al. 2002c)

Results from the SDSS

The large sample of galaxies with spectroscopic redshifts already available now from the SDSS permits an accurate study of the biasing properties of these galaxies (see the end of Sect. 8.2). Two different approaches should be mentioned here: the first follows along the line discussed above and has been published in Sheldon et al. (2004). In short, the galaxy–galaxy signal can be translated into the galaxy-mass cross-correlation function $\xi_{\rm gm}$, due to the knowledge of galaxy redshifts. The ratio of $\xi_{\rm gm}$ and the galaxy two-point correlation function $\xi_{\rm gg}$ then depends on the ratio r/b. In Fig. 55 we show the galaxy-mass correlation as a function of linear scale, as well as the ratio b/r. Note that from the SDSS no cosmic shear measurement has been obtained yet, owing to the complex PSF properties, and therefore b and r cannot be measured separately from this data set.

The galaxy-mass correlation function follows a power law over more than two orders-of-magnitude in physical scale, and its slope is very similar to the

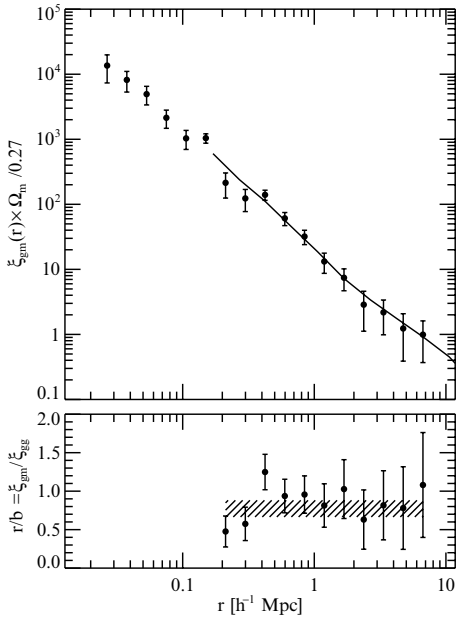

Fig. 55. The galaxy–mass cross-correlation function $\xi_{\rm gm}(r)$, as a function of linear scale (*dots with error bars*), scaled to a matter density parameter of $\Omega_{\rm m} = 0.27$, as well as the two-point galaxy correlation function obtained from the same set of (foreground) galaxies (*solid curve*). The ratio between these two is given in the lower panel, which plots b/r as a function of scale. Over the full range of scales, $\xi_{\rm gm}$ can be well approximated by a power law, $\xi_{\rm gm} = (r/r_0)^{-\gamma}$, with slope $\gamma = 1.79 \pm 0.06$ and correlation length $r_0 = (5.4 \pm 0.7)(\Omega_{\rm m}/0.27)^{-1/\gamma} h^{-1}$ Mpc. The ratio $r/b \approx (1.3 \pm 0.2)(\Omega_{\rm m}/0.27)$ is consistent with being scale-independent

slope of the galaxy two-point correlation function. Hence, the ratio between these two is nearly scale-independent. When splitting the sample into blue and red, and early- and late-type galaxies, the correlation length is larger for the red and the early-type ones. Furthermore, as expected, the lensing signal increases with the velocity dispersion in early-type galaxies.

An alternative approach was taken by Seljak et al. (2004). Their starting point is the fact that the biasing properties of dark matter halos is very well determined from cosmological simulations. This is of course not true for the biasing of galaxies. The bias parameter of galaxies with luminosity L is given as

$$b(L) = \int \mathrm{d}M \; p(M|L)\, b_{\mathrm{h}}(M) \; , \tag{161}$$

where b_{h} is the bias of halos of mass M relative to the large-scale matter distribution, and $p(M|L)$ is the probability that a galaxy with luminosity L resides in a halo of mass M. This latter probability distribution is then parameterized for any luminosity bin, by assuming that a fraction $1-\alpha$ of all galaxies in the luminosity bin considered are at the center of their parent halos, whereas the remaining fraction α are satellite galaxies. For the central galaxies, a unique mass $M(L)$ is assigned, whereas for the non-central ones, a mass distribution is assumed. The values of α and M for six luminosity bins are shown in the various panels of Fig. 51; they are obtained by fitting the galaxy–galaxy lensing signal with the model just described. The main reason why the mass spectrum can be probed is that the numerous low-mass galaxy halos contribute to the lensing signal only at relatively small scales, whereas at larger scales the higher-mass halos dominate the signal; hence, different halo masses appear at different separations in the galaxy–galaxy lensing signal. In this way, $b(L)$ can be determined, which depends on the non-linear mass scale M_* (see Sect. 6.2 of IN). The bias parameter is a relatively slowly varying function of galaxy luminosity for $L \lesssim L_*$, approaching a value $\sim$0.7 for very low-luminosity galaxies, but quickly rises for $L > L_*$.

Seljak et al. combined these measurements of the bias parameter with the clustering properties of the SDSS galaxies and the WMAP results on the CMB anisotropy, and derived new constraints on $\sigma_8 = 0.88 \pm 0.06$ and the bias parameter of an L_*-galaxy, $b_* = 0.99 \pm 0.07$; furthermore, the combination of these datasets is used to obtain new constraints on the standard cosmological parameters. This work has opened up a new way on how to employ the results from galaxy–galaxy lensing as a cosmological tool.

8.4 Galaxy Biasing: Magnification Method

High-redshift QSOs are observed to be correlated on the sky with lower-redshift galaxies and clusters. This topic has indeed an interesting history: The detection of very close associations of high-z QSOs with low-z galaxies (see Arp 1987, and references therein) has been claimed as evidence against

the cosmological interpretation of the QSO redshifts, as the probabilities of observing such close pairs of objects which are physically unrelated were claimed to be vanishingly small. However, these probabilities were obtained a posteriori, and of course, any specific configuration has a vanishingly small probability. Since the cosmological interpretation of QSO redshifts is supported by overwhelming evidence, the vast majority of researchers consider these associations as a statistical fluke.

A physical possibility to generate the association of background sources with foreground objects is provided by the magnification bias caused by lensing: the number counts of background sources is changed in regions where a foreground lens yields magnifications different from unity – see Sect. 5 of IN. Thus, close to a galaxy where $\mu > 1$, the number counts of bright background QSOs can be enhanced since the slope of their counts is steeper than unity. There have been various attempts in the literature to 'explain' the observed QSO-galaxy associations by invoking the magnification bias, either with a smooth galaxy mass distribution or by including the effects of microlensing; see SEF for a detailed discussion of this effect. The bottom line, however, is that the magnification effect is by far not large enough to account for the small (a posteriori) probabilities of the observed individual close associations.

The topic has been revived, though in a different direction, by the finding that high-redshift AGNs are statistically associated with low-redshift galaxies. Fugmann (1990) provided evidence that radio-selected high-z AGNs from the 1-Jansky-catalog are correlated with relatively bright (and therefore low-z) galaxies taken from the Lick catalog, an analysis that later on was repeated by Bartelmann and Schneider (1993), using a slightly different statistics. Different samples of foreground and background populations have been employed in further studies, including the correlation between 1-Jansky AGN with bright IRAS galaxies (Bartelmann and Schneider 1994; Bartsch et al. 1997), high-z QSOs with clusters from the Zwicky catalog of clusters (Rodrigues-Williams and Hogan 1994; Seitz and Schneider 1995b), 1-Jansky AGNs with red galaxies from the APM catalog (Benítez and Martínez-González 1995; see also Norman and Impey 2001), to mention just a few. Radio-selected AGN are considered to be a more reliable probe since their radio flux is unaffected by extinction, an effect which could cause a bias (if the sky shows patchy extinction, both galaxies and QSOs would have correlated inhomogeneous distributions on the sky) or anti-bias (if extinction is related to the lensing matter) for flux-limited optical surveys of AGNs, and which therefore needs to be taken into account in the correlation analysis of optically-selected AGNs. However, most radio source catalogs are not fully optically identified and lack redshifts, and using incomplete radio surveys therefore can induce a selection bias (Benítez et al. 2001). These latter authors investigated the correlation between two completely identified radio catalogs with the COSMOS galaxy catalog, and found a very significant correlation signal.

The upshot of all these analyses is that there seems to be a positive correlation between the high-z sources and the low-z objects, on angular scales

between $\sim 1'$ and about 1°. The significances of these correlations are often not very large, they typically are at the 2–3σ level, essentially limited by the finite number of high-redshift radio sources with a large flux (the latter being needed for two reasons: first, only radio surveys with a high flux threshold, such as the 1-Jansky catalog, have been completely optically identified and redshifts determined, which is necessary to exclude low-redshift sources which could be physically associated with the 'foreground' galaxy population, and second, because the counts are steep only for high fluxes, needed to obtain a high magnification bias). If this effect is real, it cannot be explained by lensing caused by individual galaxies; the angular region on which galaxies produce an appreciable magnification is just a few arcseconds. However, if galaxies trace the underlying (dark) matter distribution, the latter can yield magnifications (in the same way as it yields a shear) on larger scales. Thus, an obvious qualitative interpretation of the observed correlation is therefore that it is due to magnification of the large-scale matter distribution in the Universe of which the galaxies are tracers. This view is supported by the finding (Ménard and Péroux 2003) that there is a significant correlation of bright QSOs with metal absorption systems in the sense that there are relatively more bright QSOs with an aborber than without; this effect shows the expected trend from magnification bias caused by matter distributions associated with the absorbing material.

We therefore consider a flux-limited sample of AGNs, with distance probability distribution $p_{\rm Q}(w)$, and a sample of galaxies with distance distribution $p_{\rm f}(w)$. It will be assumed that the AGN sample has been selected such that it includes only objects with redshift larger than some threshold $z_{\rm min}$, corresponding to a minimum comoving distance $w_{\rm min}$, which is larger than the distances of all galaxies in the sample. We define the AGN-galaxy correlation function as

$$w_{\rm Qg}(\theta) = \frac{\left\langle \left[N_{\rm g}(\boldsymbol{\phi}) - \bar{N}_{\rm g}\right] \, \left[N_{\rm Q}(\boldsymbol{\phi}+\boldsymbol{\theta}) - \bar{N}_{\rm Q}\right] \right\rangle}{\bar{N}_{\rm g}\, \bar{N}_{\rm Q}} \, , \tag{162}$$

where $N_{\rm g}(\boldsymbol{\phi})$ and $N_{\rm Q}(\boldsymbol{\phi})$ are the observed number densities of galaxies and AGNs, respectively. The former is given by (142). The observed number density of AGN is affected by the magnification bias. Provided the unlensed counts can be described (locally) as a power-law in flux, $N_{\rm Q,0}(>S) \propto S^{-\beta}$, then from (108) of IN we find that $N_{\rm Q}(\boldsymbol{\phi}) = N_{\rm Q,0}\, \mu^{\beta-1}(\boldsymbol{\phi})$, where $\mu(\boldsymbol{\phi})$ is the magnification in the direction $\boldsymbol{\phi}$. Then, if the magnifications that are relevant are small, we can approximate

$$\mu(\boldsymbol{\phi}) \approx 1 + 2\kappa(\boldsymbol{\phi}) = 1 + \delta\mu(\boldsymbol{\phi}) \, , \tag{163}$$

and the projected surface mass density κ is given by (93) with p_w in (94) replaced by $p_{\rm Q}$. Assuming that the magnifications do not affect the mean source counts $\bar{N}_{\rm Q}$, the cross-correlation becomes

$$w_{\rm Qg}(\theta) = 2(\beta-1)\bar{b}(\theta)\, \bar{r}(\theta)\, w_{\kappa{\rm g}}(\theta) \, , \tag{164}$$

where $\bar{b}$ and $\bar{r}$ are the effective bias factor of the galaxies and the mean galaxy-mass correlation function just as in Sect. 8.3, and $w_{\kappa g}$ is the correlation between the projected density field κ and the projected number density of galaxies κ_g, defined after (142), which is the Fourier transform of $P_{\kappa g}(\ell)$ defined in (141). Hence, a measurement of this correlation, together with a measurement of the correlation function of galaxies, can constrain the values of b and r (Dolag and Bartelmann 1997; Ménard and Bartelmann 2002).

The observed correlation between galaxies and background AGN appears to be significantly larger than can be accounted for by the models presented above. On scales of a few arcmin, Benítez et al. (2001) argued that the observed signal exceeds the theoretical expectations by a factor of a few. This discrepancy can be attributed to either observational effects, or shortcomings of the theoretical modeling. Obviously, selection effects can easily produce spurious correlations, such as patchy dust obscuration or a physical association of AGNs with the galaxies. Furthermore, the weak lensing approximation employed above can break down on small angular scales. Jain et al. (2003, see also Takada and Hamana 2003) argued that the simple biasing model most likely breaks down for the small scales where the discrepancy is seen, and employed the halo model for describing the large-scale distribution of matter and galaxies to predict the expected correlations. For example, the strength of the signal depends sensitively on the redshifts, magnitudes and galaxy type.

At present, the shear method to determine the bias factor and the galaxy-mass correlation has yielded more significant results than the magnification method, owing to the small complete and homogeneous samples of high-redshift AGNs. As pointed out by Ménard and Bartelmann (2002), the SDSS may well change this situation shortly, as this survey will obtain $\sim 10^5$ homogeneously selected spectroscopically verified AGNs. Provided the effects of extinction can be controlled sufficiently well, this data should provide a precision measurement of the QSO–galaxy correlation function.

9 Additional Issues in Cosmic Shear

9.1 Higher-Order Statistics

On the level of second-order statistics, 'only' the power spectrum is probed. If the density field was Gaussian, then the power spectrum would fully characterize it; however, in the course of non-linear structure evolution, non-Gaussian features of the density field are generated, which show up correspondingly in the cosmic shear field and which can be probed by higher-order shear statistics. The usefulness of these higher-order measures for cosmic shear has been pointed out in Bernardeau et al. (1997), Jain and Seljak (1997), Schneider et al. (1998a) and van Waerbeke et al. (1999); in particular, the near-degeneracy between σ_8 and Ω_m as found from using second-order statistics

can be broken. However, there are serious problems with higher-order shear statistics, that shall be illustrated below in terms of the third-order statistics.

But first, we can give a simple argument why third-order statistics is able to break the degeneracy between $\Omega_{\rm m}$ and σ_8. Consider a density field on a scale where the inhomogeneities are just weakly non-linear. One can then employ second-order perturbation theory for the growth of the density contrast δ. Hence, we write $\delta = \delta^{(1)} + \delta^{(2)} + \ldots$, where $\delta^{(1)}$ is the density contrast obtained from linear perturbation theory, and $\delta^{(2)}$ is the next-order term. This second-order term is quadratic in the linear density field, $\delta^{(2)} \propto \left(\delta^{(1)}\right)^2$. The linear density field is proportional to σ_8, and the projected density $\kappa \propto \Omega_{\rm m}\sigma_8$. Hence, in the linear regime, $\left\langle\kappa^2\right\rangle \propto \Omega_{\rm m}^2\sigma_8^2$, where $\left\langle\kappa^2\right\rangle$ shall denote here any second-order shear estimator. The lowest order contribution to the third-order statistics is of the form

$$\left\langle\kappa^3\right\rangle \propto \left(\delta^{(1)}\right)^2 \delta^{(2)} \propto \Omega_{\rm m}^3\,\sigma_8^4\,,$$

since the term $\left(\delta^{(1)}\right)^3$ yields no contribution owing to the assumed Gaussianity of the linear density field. Hence, a skewness statistics of the form

$$\left\langle\kappa^3\right\rangle / \left\langle\kappa^2\right\rangle^2 \propto \Omega_{\rm m}^{-1}$$

will be independent of the normalization σ_8, at least in this simplified perturbation approach. In more accurate estimates, this is not exactly true; nevertheless, the functional dependencies of the second- and third-order shear statistics on σ_8 and $\Omega_{\rm m}$ are different, so that these parameters can be determined separately.

The Shear Three-Point Correlation Function

Most of the early studies on three-point statistics concentrated on the third-order moment of the surface mass density κ in a circular aperture, $\langle\kappa(\theta)\rangle$; however, this is not a directly measureable quantity, and therefore useful only for theoretical considerations. As for second-order statistics, one should consider the correlation functions, which are the quantities that can be obtained best directly from the data and which are independent of holes and gaps in the data field. The three-point correlation function (3PCF) of the shear has three independent variables (e.g. the sides of a triangle) and 8 components; as was shown in Schneider and Lombardi (2003), none of these eight components vanishes owing to parity invariance (as was suspected before – this confusion arises because little intuition is available on the properties of the 3PCF of a polar). This then implies that the covariance matrix has 6 arguments and 64 components ! Of course, this is too hard to handle efficiently, therefore one must ask which combinations of the components of the 3PCF are most useful for studying the dark matter distribution. Unfortunately, this is essentially unknown yet. An additional problem is that the predictions from theory are less well established than for the second-order statistics.

A further complication stems from a certain degree of arbitrariness on how to define the 8 components of the 3PCF. For the 2PCF, the vector between any pair of points defines a natural direction with respect to which tangential and cross components of the shear are defined; this is no longer true for three points. On the other hand, the three points of a triangle define a set of centers, such as the 'center of mass', or the center of the in- or circum-circle. After choosing one of these centers, one can define the two components of the shear which are then independent of the coordinate frame.

Nevertheless, progress has been achieved. From ray-tracing simulations through a cosmic matter distribution, the 3PCF of the shear can be determined (Takada and Jain 2003a; see also Zaldarriaga and Scoccimarro 2003; furthermore, the three-point cosmic shear statistics can also be determined in the frame of the halo model, see Cooray and Hu 2001; Takada and Jain 2003b), whereas Schneider and Lombardi (2003) have defined the 'natural components' of the shear 3PCF which are most easily related to the bispectrum of the underlying matter distribution. Let $\gamma^{\rm c}(\boldsymbol{\theta}_i) = \gamma_{\rm t} + {\rm i}\gamma_\times = -\gamma\,{\rm e}^{-2{\rm i}\zeta_i}$ be the complex shear measured in the frame which is rotated by the angle ζ_i relative to the Cartesian frame, so that the real and imaginary parts of $\gamma^{\rm c}$ are the tangential and cross components of the shear relative to the chosen center of the triangle (which has to be defined for each triplet of points separately). Then the natural components are defined as

$$\begin{aligned} \Gamma^{(0)} &= \langle \gamma^{\rm c}(\boldsymbol{\theta}_1)\,\gamma^{\rm c}(\boldsymbol{\theta}_2)\,\gamma^{\rm c}(\boldsymbol{\theta}_3)\rangle\ , \\ \Gamma^{(1)} &= \langle \gamma^{\rm c*}(\boldsymbol{\theta}_1)\,\gamma^{\rm c}(\boldsymbol{\theta}_2)\,\gamma^{\rm c}(\boldsymbol{\theta}_3)\rangle\ , \end{aligned} \tag{165}$$

and correspondingly for $\Gamma^{(2)}$ and $\Gamma^{(3)}$. Each of the natural components of the 3PCF constitutes a complex number, which depends just on the three separations between the points. Special care is required for labeling the points, and one should follow the rule that they are labeled in a counter-clock direction around the triangle. If such a unique prescription is not systematically applied, confusing and wrong conclusions will be obtained about the behavior of the shear 3PCF with respect to parity transformations (as the author has experienced painfully enough). In Schneider et al. (2005), explicit relations are derived for the natural components of the shear 3PCF in terms of the bispectrum (that is, the generalization of the power spectrum for the three-point statistics) of the underlying mass distribution κ.

Third-Order Aperture Statistics

Alternatively, aperture measures can be defined to measure the third-order statistics. Schneider et al. (1998a) calculated $\left\langle M_{\rm ap}^3\right\rangle(\theta)$ in the frame of the quasi-linear structure evolution model and showed it to be a strong function of $\Omega_{\rm m}$. van Waerbeke et al. (2001) calculated the third-order aperture mass, using a fitting formula of the non-linear evolution of the dark matter bispectrum obtained by Scoccimarro and Couchman (2001) and pointed out the

strong sensitivity with respect to cosmological parameters. Indeed, as mentioned before, $\langle M_{\rm ap}^3 \rangle$ is sensitive only to the E-modes of the shear field. One might be tempted to use $\langle M_\perp^3 \rangle(\theta)$ as a measure for third-order B-mode statistics, but indeed, this quantity vanishes owing to parity invariance (Schneider 2003). However, $\langle M_\perp^2 M_{\rm ap} \rangle$ is a measure for the B-modes at the third-order statistical level. Jarvis et al. (2004) have calculated $\langle M_{\rm ap}^3(\theta) \rangle$ in terms of the shear 3PCF, for the weight function (110) in the definition of $M_{\rm ap}$. Schneider et al. (2005) have shown that this relation is most easily expressed in terms of the natural components of the shear 3PCF. On the other hand, Jarvis et al. (2004) have expressed $\langle M_{\rm ap}^3(\theta) \rangle$ in terms of the bispectrum of κ, and as was the case for the aperture dispersion in relation to the power spectrum of κ, the third-order aperture mass is a very localized measure of the bispectrum and is sensitive essentially only to modes with three wavevectors with equal magnitudes. For that reason, Schneider et al. (2005) have generalized the definition of the third-order aperture measures, correlating the aperture mass of three different sizes, $\langle M_{\rm ap}(\theta_1) M_{\rm ap}(\theta_2) M_{\rm ap}(\theta_3) \rangle$. This third-order statistics is again a very localized measure of the bispectrum, but this time with wave vectors of different magnitude $\ell_i \approx \pi/\theta_i$, and therefore, by considering the third-order aperture mass for all combinations of θ_i, one can probe the full bispectrum. Therefore, the third-order aperture mass correlator with three independent arguments (i.e., angular scales) should contain essentially the full third-order statistical information of the κ-field, since in contrast to the two-point statistics, the shear 3PCF does not contain information about long-wavelength modes.

Furthermore, the third-order aperture statistics can be expressed directly in terms of the shear 3PCF through a simple integration, very similar to the relations (125) for the two-point statistics. Finally, the other three third-order aperture statistics (e.g., $\langle M_\perp(\theta_1) M_{\rm ap}(\theta_2) M_{\rm ap}(\theta_3) \rangle$) can as well be obtained from the natural components of the shear 3PCF. These correlators are expected to vanish if the shear is solely due to lensing, but intrinsic alignments of galaxies can lead to finite correlators which include B-modes. However, as shown in Schneider (2003), $\langle M_{\rm ap}(\theta_1) M_{\rm ap}(\theta_2) M_\perp(\theta_3) \rangle$, as well as $\langle M_\perp(\theta_1) M_\perp(\theta_2) M_\perp(\theta_3) \rangle$, are expected to vanish even in the presence of B-modes, since these two correlators are not invariant with respect to a parity transformation. Therefore, non-zero results of these two correlators signify the violation of parity invariance and therefore provide a clean check on the systematics of the data and their analysis.

First Detections

Bernardeau et al. (2002) measured for the first time a significant third-order shear from the VIRMOS-DESCART survey, employing a suitably filtered integral over the measured 3PCF (as defined in Bernardeau et al. 2003). Pen et al. (2003a,b) used the aperture statistics to detect a skewness in the same data set. The accuracy of these measurements is not sufficient to derive strong

constraints on cosmological parameters, owing to the limited sky area available. However, with the upcoming large cosmic shear surveys, the 3PCF will be measured with high accuracy. Determining the 3PCF from observed galaxy ellipticities cannot be done by straightforwardly considering any triple of galaxies – there are just too many. Jarvis et al. (2004) and Zhang and Pen (2005) have developed algorithms for calculating the 3PCF in an efficient way.

Based on the halo model for the description of the LSS, Takada and Jain (2003b) studied the dependence of the shear 3PCF on cosmological parameters. For relatively large triangles, the 3PCF provides a means to break the degeneracies of cosmological parameters that are left when using the second-order statistics only, as argued above. For small triangles, the 3PCF is dominated by the one-halo term, and therefore primarily probes the mass profiles of halos. Ho and White (2004) show that the 3PCF on small angular scales also contains information on the asphericity of dark matter halos. The full power of third-order statistics is achieved once redshift information on the source galaxies become available, in which case the combination of the 2PCF and 3PCF provides a sensitive probe on the equation-of-state of the dark energy (Takada and Jain 2004).

Beyond Third Order

One might be tempted to look into the properties of the fourth-order shear statistics (though I'm sure the reader can control her/himself in doing this – but see Takada and Jain 2002). OK, the four-point correlation function has 16 components and depends on 5 variables, not to mention the corresponding covariance or the redshift dependent fourth-order correlator. One can consider correlating the aperture mass of four different angular sizes, but in contrast to the third-order statistics, this is expected not to contain the full information on the trispectrum (which describes the fourth-order statistical properties of κ). Perhaps a combination of this fourth-order aperture mass with the average of the fourth power of the mean shear in circular apertures will carry most of the information. And how much information on cosmological parameters does the fourth-order shear statistics contain ? And even higher orders ?

Already the third-order shear statistic is not acccurately predictable from analytic descriptions of the non-linear evolution of the matter inhomogeneities, and the situation worsens with even higher order.[13] One therefore needs to refer to detailed ray-tracing simulations. Although they are quite time consuming, I do not see a real bottleneck in this aspect: Once a solid

[13] In the limits of small and large angular scales, analytic approximations can be obtained. For small scales, the highly non-linear regime is often described by the hierarchical ansatz and hyperextended perturbation theory (see Munchi and Jain 2001 and references therein), whereas on very large scales second-order perturbation theory can be used. Nevertheless, the range of validity of these perturbation approximations and their accuracy have to be checked with numerical simulations.

and accurate measurement of the three-point correlation function becomes available, certainly considerable effort will be taken to compare this with numerical simulations (in particular, since such a measurement is probably a few years ahead, in which the computer power will increase by significant factors). If we accept this point, then higher-order statistics can be obtained from these simulations, and several can be 'tried out' on the numerical data such that they best distinguish between different models. For example, one can consider the full probability distribution $p(M_{\rm ap};\theta)$ on a given data set (Kruse and Schneider 2000; Reblinsky et al. 1999; Bernardeau and Valageas 2000; Munshi et al. 2004). To obtain this from the observational data, one needs to place apertures on the data field which, as we have argued, is plagued with holes and gaps in the data. However, we can place the same gaps on the simulated data fields and therefore simulate this effect. Similarly, the numerical simulations should be used to find good strategies for combining second- and third-order shear statistics (and potentially higher-order ones) for an optimal distinction between comological model parameters, and, in particular, the equation-of-state of dark energy. Another issue one needs to consider for third- (and higher-)order cosmic shear measures is that intrinsic clustering of sources, and the correlation between galaxies and the dark matter distribution generating the shear field has an influence on the expected signal strength (Bernardeau (1998); Hamana (2001); Hamana et al. (2002)). Obviously, there are still a lot of important studies to be done.

Third-Order Galaxy–Mass Correlations

We have shown in Sect. 8 how galaxy–galaxy lensing can be used to probe the correlation between galaxies and the underlying matter distribution. With the detection of third-order shear statistics already in currently available data sets, one might expect that also higher-order galaxy-mass correlations can be measured from the same data. Such correlations would then probe, on large angular scales, the higher-order biasing parameters of galaxies, and thereby put additional constraints on the formation and evolution of galaxies. Ménard et al. (2003) considered the correlation between high-redshift QSOs and pairs of foreground galaxies, thus generalizing the methods of Sect. 8.4 to third-order statistics. The galaxy–galaxy-shear correlation, and the galaxy-shear-shear correlations have been considered by Schneider and Watts (2005). These correlation functions have been related to the underlying bispectrum of the dark matter and the third-order bias and correlation functions, and appropriate aperture statistics have been defined, that are related in a simple way to the bispectra and the correlation functions.

In fact, integrals of these higher-order correlations have probably been measured already. As shown in Fig. 50, galaxies in regions of high galaxy number densities show a stronger, and more extended galaxy–galaxy lensing signal than more isolated galaxies. Hence there is a correlation between the mean mass profile around galaxies and the local number density of galaxies,

which is just an integrated galaxy–galaxy-shear correlation. In fact, such a correlation is only first order in the shear and should therefore be much easier to measure than the shear 3PCF. Furthermore, the galaxy-shear-shear correlation seems to be present in the cosmic shear analysis of the COMBO-17 fields by Brown et al. (2003), where they find a stronger-than-average cosmic shear signal in the A 901 field, and a weaker cosmic shear signal in the CDFS, which is a field selected because it is rather poor in brighter galaxies.

9.2 Influence of LSS Lensing on Lensing by Clusters and Galaxies

The lensing effect of the three-dimensional matter distribution will contaminate the lensing measurements of localized objects, such as galaxies and clusters. Some of the associated effects are mentioned in this section.

Influence of Cosmic Shear on Strong Lensing by Galaxies

The lensing effect of foreground and background matter in a strong lensing system will affect the image positions and flux ratios. As this 3-D lensing effects are not recognized as such in the lens modeling, a 'wrong' lens model will be fitted to the data, in the sense that the mass model for the lensing galaxy will try to include these additional lensing effects not associated with the galaxy itself. In particular, the corresponding predictions for the time delays can be affected through this effect.

Since the image separation of strong lens systems are less than a few arcseconds, the lensing effect of the LSS can be well approximated by a linear mapping across this angular scale. In this case, the effect of the 3-D matter distribution on the lens model can be studied analytically (e.g., Bar-Kana 1996). The lens equation resulting from the main lens (the galaxy) plus the linearized inhomogeneities of the LSS is strictly equivalent to the single-plane gravitational lens equation without these cosmological perturbations, and the mass distribution of the equivalent single-plane lens can be explicitly derived (Schneider 1997). For example, if the main lens is described by elliptical isopotential curves (i.e., elliptical contours of the deflection potential ψ) plus external shear, the equivalent single-plane lens will be of the same form. The orientation of the ellipticity of the lens, as seen by the observer, will be rotated by the foreground LSS by the same angle as the potential of the equivalent lens, so that no observable misalignment is induced. This equivalence then implies that the determination of the Hubble constant from time-delay measurements is affected by the same mass-sheet degeneracy transformation as for a single plane lens.

LSS Effects on the Mass Determination of Clusters

The determination of mass parameters of a cluster from weak lensing is affected by the inhomogeneous foreground and background matter distribution.

The effect of local mass associated with a cluster (e.g., filaments extending from the cluster along the line-of-sight) will bias the mass determination of clusters toward higher values, since clusters are likely to be located in overdense regions of the LSS, though this effect is considerably smaller than claimed by Metzler et al. (2001), as shown by Clowe et al. (2004a).

Hoekstra (2001, 2003) considered the effect of the LSS on the determination of mass parameters of clusters, using either SIS or NFW models. For the SIS model, the one parameter characterizing this mass profile (σ_v) can be obtained as a linear estimator of the shear. The dispersion of this parameter is then the sum of the dispersion caused by the intrinsic ellipticity of the source galaxies and the cosmic shear dispersion. For the NFW model, the relation between its two parameters (M_{200}, the mass inside the virial radius r_{200}, and the concentration c) and the shear is not linear, but the effect of the LSS can still be estimated from Monte-Carlo simulations in which the cosmic shear is assumed to follow Gaussian statistics with a power spectrum following the Peacock and Dodds (1996) prescription.

For the SIS model, the effect of the LSS on the determination of σ_v is small, provided the cluster is at intermediate redshift (so that most source galaxies are in the background). The noise caused by the finite ellipticity in this case is almost always larger than the effect by the LSS. There is an interesting effect, however, in that the relative contribution of the LSS and shape noise changes as larger aperture fits to the SIS model are considered: The larger the field over which the shear is fitted to an SIS model, the larger becomes the impact of cosmic shear, and this increase compensates for the reduced shape noise. In effect, cosmic shear and shape noise together put an upper limit on the accuracy of the determination of σ_v from shear data. The same is true for the determination of the mass parameters of the NFW model, as shown in Fig. 56. The uncertainties of the mass parameters of NFW profiles are about twice as large as if the effects from the LSS are ignored, whereas the effect is considerably smaller for the one-parameter model of the SIS. One should also note that a decrease of the shape noise, which can be obtained by using data with a fainter limiting magnitude, yields an increase of the noise from the LSS, since the fainter galaxies are expected to be at higher redshift and therefore carry a larger cosmic shear signal. For low-redshift clusters, these two effects nearly compensate.

The Efficiency and Completeness of Weak Lensing Cluster Searches

We take up the brief discussion at the end of Sect. 5.8 about the potential of deriving a shear-selected sample of galaxy clusters. The first studies of this question were based on analytical models (e.g., Kruse and Schneider 1999) or numerical models of isolated clusters (Reblinsky and Bartelmann 1999). Those studies can of course not account for the effects of lensing by the LSS. Ray-tracing simulations through N-body generated LSS were carried out by

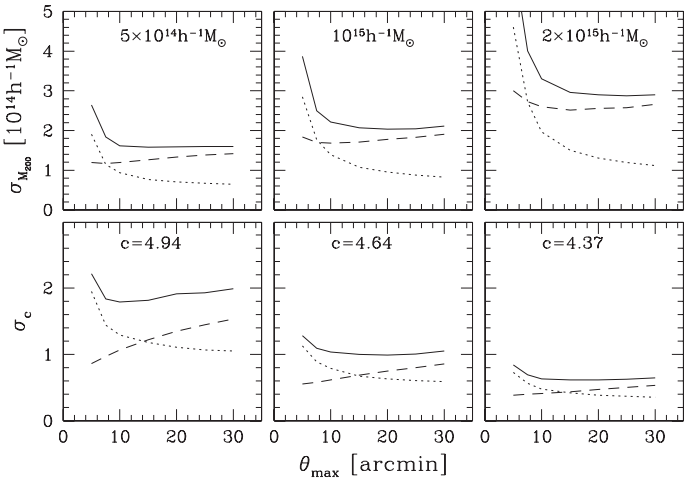

Fig. 56. The dispersion of the determination of the mass and concentration of three NFW halos at redshift $z_{\rm d} = 0.3$. These parameters were derived by fitting an NFW shear profile to the shear simulated from an NFW halo with parameters indicated in the figure and adding shape noise and noise from cosmic shear. The outer angular scale over which the fit was performed is θ_{max}. Dotted curves show the effect from shape noise alone, dashed curves show the dispersion from cosmic shear, and the solid curves contain both effects. Surprisingly, the accuracy of the NFW parameters does not increase once $\theta_{max} \sim 15'$ is reached, as for larger radii, the cosmic shear noise more than compensates for the reduced ellipticity noise. Another way to express that is that the lensing signal at very large distance from the halo center is weaker than the rms cosmic shear and therefore does not increase the signal-to-noise any more (from Hoekstra 2003)

Reblinsky et al. (1999), White et al. (2002), Hamana et al. (2004), Vale and White (2003), Hennawi and Spergel (2005) and others. In these cosmological simulations, halos were identified based on their 3-D mass distribution. They were then compared to the properties of the lensing results obtained from ray tracing, either by considering the (smoothed) surface mass density κ (that could be obtained from a mass reconstruction from the shear field) or by studying the aperture mass $M_{\rm ap}$ which can be obtained directly from the shear. In both cases, noise due to the finite intrinsic source ellipticity can be added.

The two basic quantities that have been investigated in these studies are *completeness* and *efficiency*. Completeness is the fraction of dark matter halos above some mass threshold $M_{\rm min}$ that are detected in the weak lensing data, whereas efficiency is the fraction of significant lensing detections that correspond to a real halo. Both of these quantities depend on a number of parameters, like the mass threshold of a halo and the limiting significance ν of a lensing detection [in the case of the aperture mass, this would correspond to (80)], as well as on the choice of the filter function Q. Hennawi and Spergel

(2005) have pointed out that even without noise (from observations or intrinsic galaxy ellipticities), the efficiency is limited to about 85% – even under these idealized condition, the selected sample will be contaminated by at least 15% of spurious detections, generated by projection effects of the LSS.

To compare these predictions with observations, the six highest-redshift EMSS clusters were all detected at high significance with a weak lensing analysis (Clowe et al. 2000). Clowe et al. (2004b) have studied 20 high-redshift clusters with weak lensing techniques. These clusters were optically selected and are expected to be somewhat less massive (and potentially more affected by foreground galaxies) than the EMSS clusters. Only eight of these 20 clusters are detected with more than 3σ significance, but for none of them does the SIS fit produce a negative σ_v^2. Only for four of these clusters are the lensing results compatible with no shear signal.

10 Concluding Remarks

Weak lensing has become a standard tool in observational cosmology, as we have learned how to measure the shape of faint galaxy images and to correct them for distortions in the telescope and camera optics and for PSF effects. These technical issues are at the very center of any observational weak lensing research. It appears that at present, the accuracy with which shear can be measured is sufficient for the data available today, in the sense that statistical uncertainties are likely to be larger than potential inaccuracies in the measurement of unbiased shear estimates from faint images. This, however, will change quickly. The upcoming large cosmic shear surveys will greatly reduce statistical uncertainties, and then the accuracy of shear measurements from the data will be the essential limiting factor. Alternatives to KSB have been developed, but they need to undergo thorough testing before becoming a standard tool for observers. It should also be noted that the KSB method is applied differently by different groups, in particular with regards to the weighting of galaxies and other details. What is urgently needed is a study in which different groups apply their version of KSB to the same data set and compare the results. Furthermore, starting from raw data, the specific data reduction methods will lead to slightly different coadded images, and shear measurements on such differently reduced imaged should be compared. These technical issues will be a central challenge for weak lensing in the upcoming years.

The ongoing and planned wide-field imaging surveys mentioned at the end of Sect. 7.7 will allow us to investigate several central questions of cosmology. The two aspects that I consider most relevant are the investigation of the equation-of-state of the dark energy and the relation between galaxies and the underlying dark matter distribution. The former question about the nature of dark energy is arguably the central challenge of modern cosmology, and cosmic shear is one of the very few methods how it can be studied empirically.

The relation between dark matter and galaxies is central to our understanding of how galaxies form and evolve, and galaxy–galaxy lensing is the only way how this relation can be investigated without a priori assumptions.

Essentially all weak lensing studies today have used faint galaxies as sources, since they form the densest source population currently observable. The uniqueness of faint optical galaxies will not stay forever, with the currently planned future instruments. For example, there is a rich literature of weak lensing of the cosmic microwave background which provides a source of very accurately known redshift. Weak lensing by the large-scale structure enhances the power spectrum of the CMB at small angular scales, and the Planck satellite will be able to measure this effect. In particular, polarization information will be very useful, since lensing can introduce B-modes in the CMB polarization. The James Webb Space Telescope, with its large aperture of 6.5 meters and its low temperature and background will increase the number density of observable faint sources in the near-IR up to 5μm to several hundred per square arcminute, many of them at redshifts beyond 3, and will therefore permit much more detailed weak lensing studies, in particular of clusters (see Fig. 57; an observation of this huge number of arcs and multiple images will answer questions about the mass distribution of clusters that we have yet not even dared to ask). The envisioned next generation radio telescope Square Kilometer Array will populate the radio sky with very comparable source density as currently the deepest optical images. Since the beam (that is, the point-spread function) of this radio interferometer will be known very accurately, PSF corrections for this instrument will be more reliable than for optical telescopes. Furthermore, higher-order correlation of the shear field with sources in the field will tell us about non-Gaussian properties of galaxy–matter correlations and biasing, and therefore provide important input into models of galaxy formation and evolution.

Acknowledgments

I enjoyed the week of lecturing at Les Diablerets a lot. First, I thank Georges Meylan and his colleagues Philippe Jetzer and Pierre North for organizing this school so efficiently and smoothly; to them also my sincere apologies for not finishing these proceedings much earlier – but sure enough, lecturing is more fun than preparing lectures, and certainly very much more fun than writing them up into something to be published. Second, I thank my fellow lecturers Chris Kochanek and Joe Wambsganss for discussions, great company and good spirits. Third, and foremost, my compliments to the students who patiently sat through these lectures which, I'm sure, were not always easy to follow; nevertheless I hope that they grasped the essential points, and that these lecture notes help to fill in the details. These notes would not have been possible without the many colleagues and students with whom I had the privilege to collaborate over the years on various aspects of weak lensing, among them Matthias Bartelmann, Marusa Bradac, Doug Clowe,

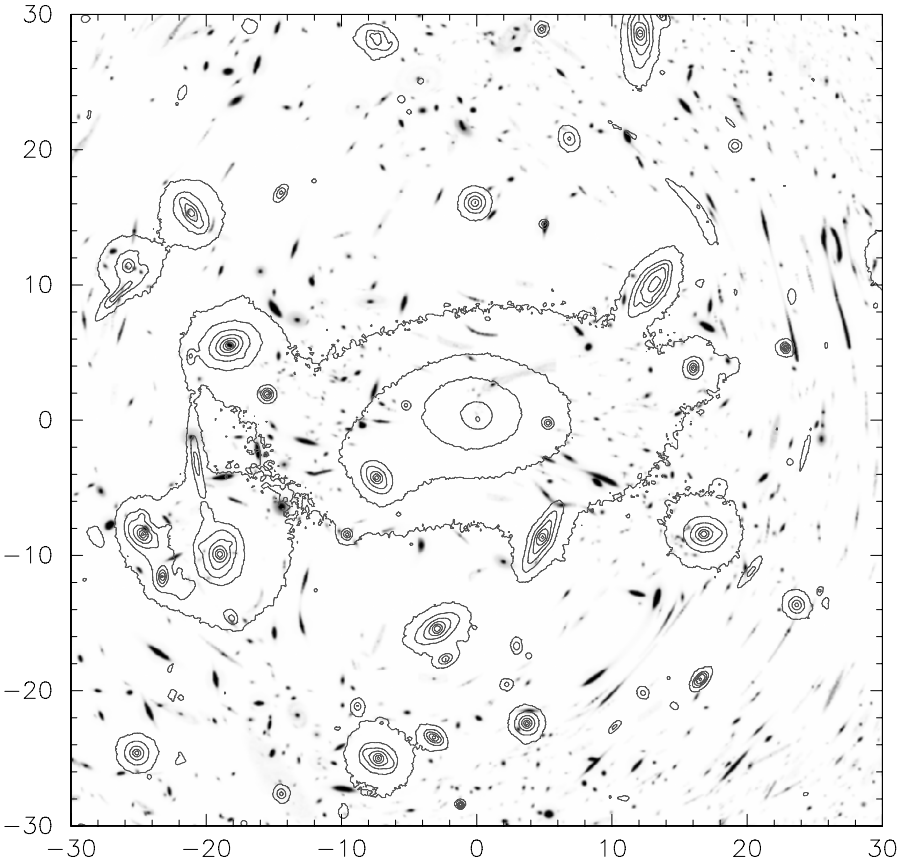

Fig. 57. Simulated image of lensed features in the very central part of the massive cluster A 2218, as observed with the future JWST. For these simulations, the mass profile of the cluster as constrained from HST observations and detailed modeling (Kneib et al. 1996) has been used. The number density of (unlensed) sources was assumed to be $4 \times 10^6 \mathrm{deg}^{-2}$ down to K=29. The redshift distribution assumed is broad and extends to redshift $z \sim 10$ with a median value $z_{\mathrm{med}} \sim 3$. The brighter objects (cluster galaxies and brightest arcs) seen by HST are displayed as contours, to make the faint galaxy images visible on this limited dynamic range reproduction. An enormous number of large arcs and arclets are seen; in particular, numerous radial arcs can be easily detected, which will allow us to determine the 'core size' of the cluster mass distribution. Due to the broad redshift distribution of the faint galaxies, arcs occur at quite a range of angular separations from the cluster center; this effect will become even stronger for higher-redshift clusters. It should be noted that this 1 arcminute field does not cover the second mass clump seen with HST; a JWST image will cover a much larger area, and more strong lensing features will be found which can then be combined with the weak lensing analysis of such a cluster. For this simulation, a pixel size of $0\farcs06$ was used; the JWST sampling will be better by a factor of 2 (from Schneider and Kneib 1998)

Jörg Dietrich, Thomas Erben, Bernhard Geiger, Hannelore Hämmerle, Bhuvnesh Jain, Martin Kilbinger, Lindsay King, Martina Kleinheinrich, Guido Kruse, Marco Lombardi, Yannick Mellier, Hans-Walter Rix, Mischa Schirmer, Tim Schrabback, Carolin Seitz, Stella Seitz, Patrick Simon, Ludovic van Waerbeke and Anja von der Linden. This work was supported by the German Ministry for Science and Education (BMBF) through the DLR under the project 50 OR 0106, by the German Ministry for Science and Education (BMBF) through DESY under the project 05AE2PDA/8, and by the Deutsche Forschungsgemeinschaft under the project SCHN 342/3–1.

References

Abazajian, K., Adelman-McCarthy, J.K., Agüeros, M.A. et al. 2004, AJ 128, 502
Abazajian, K.N. & Dodelson, S. 2003, PRL 91, 041301
Abell, G.O. 1958, ApJS 3, 211
Abell, G.O., Corwin, H.G. & Olowin, R.P. 1989, ApJS 70, 1
Allen, S.W. 1998, MNRAS 296, 392
Andersson, K.E. & Madejski, G.M. 2004, ApJ 607, 190
Arp, H. 1987, Quasars, redshifts, and controversies, Interstellar Media, Berkeley
Athreya, R.M., Mellier, Y., van Waerbeke, L., Pelló, R., Fort, B. & Dantel-Fort, M. 2002, A&A 384, 743
Bacon, D.J., Massey, R.J., Refregier, A.R. & Ellis, R.S. 2003, MNRAS 344, 673
Bacon, D.J., Refregier, A., Clowe, D. & Ellis, R.S. 2001, MNRAS 325, 1065
Bacon, D.J., Refregier, A.R. & Ellis, R.S. 2000, MNRAS 318, 625
Bacon, D.J. & Taylor, A.N. 2003, MNRAS 344, 1307
Bacon, D.J., Taylor, A.N., Brown, M.L. et al. 2004, astro-ph/0403384
Barber, A.J. 2002, MNRAS 335, 909
Barber, A.J., Thomas, P.A., Couchman, H.M.P. & Fluke, C.J. 2000, MNRAS 319, 267
Bardeen, J. M., Bond, J. R., Kaiser, N., Szalay, A. S. 1986, ApJ 304, 15
Bar-Kana, R. 1996, ApJ 468, 17
Bartelmann, M. 1995, A&A 303, 643
Bartelmann, M., Huss, A., Colberg, J., Jenkins, A. & Pearce, F. 1998, A&A 330, 1
Bartelmann, M., King, L.J. & Schneider, P. 2001, A&A 378, 361
Bartelmann, M. & Meneghetti, M. 2004, A&A 418, 413
Bartelmann, M., Meneghetti, M., Perrotta, F., Baccigalupi, C. & Moscardini, L. 2003, A&A 409, 449
Bartelmann, M. & Narayan, R. 1995, ApJ 451, 60
Bartelmann, M., Narayan, R., Seitz, S. & Schneider, P. 1996, ApJ 464, L115
Bartelmann, M., Perotta, F. & Baccigalupi, C. 2002, A&A 396, 21

Bartelmann, M. & Schneider, P. 1993, A&A 271, 421
Bartelmann, M. & Schneider, P. 1994, A&A 284, 1
Bartelmann, M. & Schneider, P. 1999, A&A 345, 17
Bartelmann, M. & Schneider, P. 2001, Physics Reports 340, 291 (BS01)
Bartelmann, M. & Steinmetz, M. 1996, MNRAS 283, 431
Bartelmann, M., Steinmetz, M. & Weiss, A. 1995, A&A 297, 1
Bartelmann, M. & Weiss, A. 1994, A&A 287, 1
Bartsch, A., Schneider, P. & Bartelmann, M. 1997, A&A 319, 375
Beckwith, S., Somerville, R. & Stiavelli, M. 2003, STScI Newsletter 20, Issue 04, p. 1
Benabed, K. & van Waerbeke, L. 2003, PhRvD 70, 123515, also astro-ph/0306033
Benítez, N. 2000, ApJ 536, 571
Benítez, N. & Martínez-González, E. 1995, ApJ 448, L89
Benítez, N., Sanz, J.L. & Martínez-González, E. 2001, MNRAS 320, 241
Bennett, C.L., Halpern, M., Hinshaw, G. et al. 2003, ApJS 148, 1
Bergmann, A.G. & Petrosian, V. 1993, ApJ 413, 18
Bernardeau, F. 1998, A&A 338, 375
Bernardeau, F., Mellier, Y. & van Waerbeke, L. 2002, A&A 389, L28
Bernardeau, F. & Valageas, P. 2000, A&A 364, 1
Bernardeau, F., van Waerbeke, L. & Mellier, Y. 1997, A&A 322, 1
Bernardeau, F., van Waerbeke, L., & Mellier, Y. 2003, A&A 397, 405
Bernstein, G.M. & Jarvis, M. 2002, AJ 123, 583
Bertin, E. & Arnouts, S. 1996, A&AS 117, 393
Blain, A.W., Kneib, J.-P., Ivison, R.J. & Smail, I. 1999, ApJ 512, L87
Blandford, R. & Narayan, R. 1986, ApJ 310, 568
Blandford, R.D., Saust, A.B., Brainerd, T.G. & Villumsen, J.V. 1991, MNRAS 251, 600
Bolzonella, M., Miralles, J.-M. & Pelló, R. 2000, A&A 363, 476
Bonnet, H. & Mellier, Y. 1995, A&A 303, 331
Bradac, M., Lombardi, M. & Schneider, P. 2004, A&A 424, 13
Brainerd, T.G., Blandford, R.D., & Smail, I. 1996, ApJ 466, 623
Bridle, S.L., Hobson, M.P., Lasenby, A.N. & Saunders, R. 1998, MNRAS 299, 895
Broadhurst, T.J., Taylor, A.N. & Peacock, J.A. 1995, ApJ 438, 49
Brown, M.L., Taylor, A.N., Bacon, D.J. et al. 2003, MNRAS 341, 100
Carlberg, R.G., Yee, H.K.C. & Ellingson, E. 1994, ApJ 437, 63
Clowe, D., De Lucia, G. & King, L. 2004a, MNRAS 350, 1038
Clowe, D., Luppino, G.A., Kaiser, N. & Gioia, I.M. 2000, ApJ 539, 540
Clowe, D. & Schneider, P. 2001, A&A 379, 384
Clowe, D. & Schneider, P. 2002, A&A 395, 385
Clowe, D., Schneider, P., Aragon-Salamanca, A. et al. 2004b, A&A, submitted
Connolly, A.J., Csabai, I., Szalay, A.S., Koo, D.C., Kron, R.G., & Munn, J.A. 1995, AJ 110, 2655
Contaldi, C.R., Hoekstra, H. & Lewis, A. 2003, PhRvL 90, 221303

Cooray, A. & Hu, W. 2001, ApJ 548, 7
Cooray, A. & Hu, W. 2002, ApJ 574, 19
Cooray, A. & Sheth, R. 2002. Phys. Rep. 372, 1
Coté, P., McLaughlin, D.E., Cohen, J.G. & Blakeslee, J.P. 2003, ApJ 591, 850
Crittenden, R.G., Natarajan, P., Pen, U.-L. & Theuns, T. 2001, ApJ 559, 552
Crittenden, R.G., Natarajan, P., Pen, U.-L. & Theuns, T. 2002, ApJ 568, 20
Croft, R.A.C. & Metzler, C.A. 2001, ApJ 545, 561
Czoske, O., Kneib, J.-P., Soucail, G., Bridges, T.J., Mellier, Y. & Cuillandre, J.-C. 2001, A&A 372, 391
Czoske, O., Moore, B., Kneib, J.-P. Soucail, G. 2002, A&A 386, 31
Dahle, H., Pedersen, K., Lilje, P.B., Maddox, S.J. & Kaiser, N. 2003, ApJ 591, 662
Dalal, N., Holder, G. & Hennawi, J.F. 2003, ApJ 609, 50, also astro-ph/0310306
de Blok, W.J.G., McGaugh, S.S. & Rubin, V.C. 2001, AJ 122, 2396
De Filippis, E., Schindler, S. & Castillo-Morales, A. 2003, A&A 404, 63
Dekel, A. & Lahav, O. 1999, ApJ 520, 24
Dietrich, J.P., Clowe, D.I. & Soucail, G. 2002, A&A 394, 395
Dietrich, J.P., Schneider, P., Clowe, D., Romano-Diaz, E. & Kerp, J. 2004, A&A submitted, also astro-ph/0406541
Dolag, K. & Bartelmann, M. 1997, MNRAS 291, 446
Donahue, M., Gaskin, J.A., Patel, S.K., Joy, M., Clowe, D. & Hughes, J.P. 2003, ApJ 598, 190
Doré, O., Bouchet, F.R., Mellier, Y. & Teyssier, R. 2001, A&A 375, 14
Dye, S. & Taylor, A. 1998, MNRAS 300, L23
Dye, S., Taylor, A.N., Greve, T.R. et al. 2002, A&A 386, 12
Dye, S., Taylor, A.N., Thommes, E.M. et al. 2001, MNRAS 321, 685
Ebbels, T., Ellis, R., Kneib, J.-P. et al. 1998, MNRAS 295, 75
Ellis, R.S. 1997, ARA&A 35, 389
Erben, T., Miralles, J.M., Clowe, D. et al. 2003, A&A 410, 45
Erben, T., van Waerbeke, L., Mellier, Y., Schneider, P., Cuillandre, J.C., Castander, F.J. & Dantel-Fort, M. 2000, A&A 355, 23
Erben, T., van Waerbeke, L., Bertin, E., Mellier, Y. & Schneider, P. 2001, A&A 366, 717
Ettori, S. & Lombardi, M. 2003, A&A 398, L5
Fabian, A.C. 1994, ARA&A 32, 277
Fahlman, G., Kaiser, N., Squires, G. & Woods, D. 1994, ApJ 437, 56
Fischer, P. 1999, AJ 117, 2024
Fischer, P., McKay, T.A., Sheldon, E. et al. 2000, AJ 120, 1198
Fluke, C.J., Webster, R.L. & Mortlock, D.J. 2002, MNRAS 331, 180
Fort, B. & Mellier, Y. 1994, A&AR 5, 239
Fort, B., Mellier, Y. & Dantel-Fort, M. 1997, A&A 321, 353
Fort, B., Mellier, Y., Dantel-Fort, M., Bonnet, H. & Kneib, J.-P. 1996, A&A 310, 705

Fort, B., Prieur, J.L., Mathez, G., Mellier, Y. & Soucail, G. 1988, A&A 200, L17
Fruchter, A.S. & Hook, R.N. 2002, PASP 114, 144
Fugmann, W. 1990, A&A 240, 11
Gautret, L., Fort, B., & Mellier, Y. 2000, A&A 353, 10
Gavazzi, R., Mellier, Y., Fort, B., Cuillandre, J.-C. & Dantel-Fort, M. 2004, A&A 422, 407
Geiger, B. & Schneider, P. 1998, MNRAS 295, 497
Geiger, B. & Schneider, P. 1999, MNRAS 302, 118
Gerhard, O., Kronawitter, A., Saglia, R.P. & Bender, R. 2001, AJ 121, 1936
Giavalisco, M. & Mobasher, B. 2004, STScI Newletter 21, Issue 01, p. 1
Gioia, I.M., Braito, V., Branchesi, M. et al. 2004, A&A 419, 517
Gladders, M.D., Hoekstra, H., Yee, H.K.C., Hall, P.B. & Barrientos, L.F. 2003, ApJ 593, 48
Gladders, M.D. & Yee, H.K.C. 2000, AJ 120, 2148
Golse, G., Kneib, J.-P. & Soucail, G. 2002, A&A 387, 788
Gray, M.E., Ellis, R.S., Refregier, A. et al. 2000, MNRAS 318, 573
Gray, M., Ellis, R.S., Lewis, J.R., McMahon, R.G. & Firth, A.E. 2001, MNRAS 325, 111
Gray, M., Taylor, A.N., Meisenheimer, K., Dye, S., Wolf, C. & Thommes, E. 2002, ApJ 568, 141
Gunn, J.E. 1967, ApJ 150, 737
Guzik, J. & Seljak, U. 2001, MNRAS 321, 439
Hamana, T. 2001, MNRAS 326, 326
Hamana, T., Colombi, S.T., Thion, A., Devriendt, J.E.G.T., Mellier, Y. & Bernardeau, F. 2002, MNRAS 330, 365
Hamana, T. & Mellier, Y. 2001, MNRAS 327, 169
Hamana, T., Miyazaki, S., Shimasaku, K. et al. 2003, ApJ 597, 98
Hamana, T., Takada, M. & Yoshida, N. 2004, MNRAS 350, 893
Hämmerle, H., Miralles, J.-M., Schneider, P. et al. 2002, A&A 385, 743
Heavens, A. 2003, MNRAS 343, 1327
Heavens, A.F., Refregier, A. & Heymans, C.E.C. 2000, MNRAS 319, 649
Hennawi, J.F. & Spergel, D.N. 2005, ApJ 624, 59, also astro-ph/0404349
Hetterscheidt, M. 2003, Diploma Thesis, Univ. Bonn.
Heymans, C., Brown, M., Heavens, A., Meisenheimer, K., Taylor, A. & Wolf, C. 2004, MNRAS 347, 895
Heymans, C. & Heavens, A. 2003, MNRAS 339, 711
Hirata, C.M., Mandelbaum, R., Seljak, U. et al. 2004, MNRAS 353, 529, also astro-ph/0403255
Hirata, C.M. & Seljak, U. 2004, PhRvD 70, 063526, also astro-ph/0406275
Ho, S. & White, M. 2004, ApJ 607, 40
Hoekstra, H. 2001, A&A 370, 743
Hoekstra, H. 2003, MNRAS 339, 1155
Hoekstra, H. 2004, MNRAS 347, 1337

Hoekstra, H., Franx, M. & Kuijken, K. 2000, ApJ 532, 88
Hoekstra, H., Franx, M., Kuijken, K., et al. 2001, ApJ 548, L5
Hoekstra, H., Franx, M., Kuijken, K., Carlberg, R.G. & Yee, H.K.C. 2003, MNRAS 340, 609
Hoekstra, H., Franx, M., Kuijken, K., & Squires, G. 1998, ApJ 504, 636
Hoekstra, H., Franx, M., Kuijken, K., & van Dokkum, P.G. 2002d, MNRAS 333, 911
Hoekstra, H., van Waerbeke, L., Gladders, M.D., Mellier, Y. & Yee, H.K.C. 2002c, ApJ 577, 604
Hoekstra, H., Yee, H.K.C. & Gladders, M.D. 2001, ApJ 558, L11
Hoekstra, H., Yee, H.K.C. & Gladders, M.D. 2002a, ApJ 577, 595
Hoekstra, H., Yee, H.K.C. & Gladders, M.D. 2004, ApJ 606, 67
Hoekstra, H., Yee, H.K.C., Gladders, M.D., Barrientos, L.F., Hall, P.B. & Infante, L. 2002b, ApJ 572, 55
Hu, W. 1999, ApJ 522, L21
Hu, W. 2002, PhRvD 66, 083515
Hu, W. & Keeton, C.R. 2002, PhRvD 66, 063506
Hu, W. & Jain, B. 2004, PhRvD 70, 043009, also astro-ph/0312395
Hu, W. & Tegmark, M. 1999, ApJ 514, L65
Hu, W. & White, M. 2001, ApJ 554, 67
Huterer, D. 2002, PhRvD 64, 063001
Jain, B., Scranton, R. & Sheth, R.K. 2003, MNRAS 345, 62
Jain, B. & Seljak, U. 1997, ApJ 484, 560
Jain, B., Seljak, U. & White, S.D.M. 2000, ApJ 530, 547
Jain, B. & Taylor, A. 2003, PRL 91, 141302
Jain, B. & van Waerbeke, L. 2000, ApJ 530, L1
Jarvis, M., Bernstein, G.M., Fischer, P. et al. 2003, AJ 125, 1014
Jarvis, M., Bernstein, G.M. & Jain, B. 2004, MNRAS 352, 338
Jing, Y.P. 1998, ApJ 503, L9
Jing, Y.P. 2002, MNRAS 335, L89
Kaiser, N. 1984, ApJ 284, L9
Kaiser, N. 1992, ApJ 388, 272
Kaiser, N. 1995, ApJ 439, L1
Kaiser, N. 1998, ApJ 498, 26
Kaiser, N. 2000, ApJ 537, 555
Kaiser, N. & Squires, G., 1993, ApJ 404, 441
Kaiser, N., Squires, G. & Broadhurst, T. 1995, ApJ 449, 460
Kaiser, N., Squires, G., Fahlman, G. & Woods, D. 1994, in *Clusters of galaxies, proc. XIVth Moriond astrophysics meeting, Méribel, France, 1994*, p. 269
Kaiser, N., Wilson, G. & Luppino, G. 2000, astro-ph/0003338
Kaiser, N., Wilson, G., Luppino, G. et al. 1998, astro-ph/9809268
Kilbinger, M. & Schneider, P. 2004, A&A 413, 465
King, L.J., Clowe, D.I., Lidman, C., Schneider, P., Erben, T., Kneib, J.-P. & Meylan, G. 2002a, A&A 385, L5
King, L.J., Clowe, D.I. & Schneider, P. 2002b, A&A 383, 118

King, L. & Schneider, P. 2001, A&A 369, 1
King, L. & Schneider, P. 2002, A&A 396, 411
King, L. & Schneider, P. 2003, A&A 398, 23
King, L., Schneider, P. & Springel, V. 2001, A&A 378, 748
Kleinheinrich, M. 2003, Ph.D. Thesis, University of Bonn
Kneib, J.-P., Ellis, R.S., Santos, M.R. & Richard, J. 2004, ApJ 607, 697
Kneib, J.-P., Ellis, R.S., Smail, I., Couch, W.J. & Sharples, R.M. 1996, ApJ 471, 643
Kneib, J.-P., Hudelot, P., Ellis, R.S. et al. 2003, ApJ 598, 804
Kochanek, C.S. 1990, MNRAS 247, 135
Kruse, G. & Schneider, P. 1999, MNRAS 302, 821
Kruse, G. & Schneider, P. 2000, MNRAS 318, 321
Kuijken, K. 1999, A&A 352, 355
Limber, D.N. 1953, ApJ 117, 134
Link, R. & Pierce, M.J. 1998, ApJ 502, 63
Lombardi, M. & Bertin, G. 1998, A&A 335, 1
Lombardi, M. & Bertin, G. 1999, A&A 342, 337
Lombardi, M. & Schneider, P. 2001, A&A 373, 359
Lombardi, M. & Schneider, P. 2002, A&A 392, 1153
Luppino, G.A., Gioia, I.M., Hammer, F., Le Fèvre, O. & Annis, J.A. 1999, A&AS 136, 117
Luppino, G.A. & Kaiser, N. 1997, ApJ 475, 20
Lynds, R. & Petrosian, V. 1989, ApJ 336, 1
Mackey, J., White, M. & Kamionkowski, M. 2002, MNRAS 332, 788
Maoli, R., van Waerbeke, L., Mellier, Y. et al. 2001, A&A 368, 766
Markevitch, M., Gonzalez, A.H., Clowe, D. et al. 2004, ApJ 606, 819
Marshall, P.J., Hobson, M.P., Gull, S.F. & Bridle, S.L. 2002, MNRAS 335, 1037
Marshall, P.J., Hobson, M.P. & Slosar, A. 2003, MNRAS 346, 489
McKay, T.A., Sheldon, E.S., Racusin, J. et al. 2001, astro-ph/0108013
Mellier, Y. 1999, ARA&A 37, 127
Mellier, Y., Fort, B., Soucail, G., Mathez, G. & Cailloux, M. 1991, ApJ 380, 334
Ménard, B. & Bartelmann, M. 2002, A&A 386, 784
Ménard, B., Bartelmann, M. & Mellier, Y. 2003, A&A 409, 411
Ménard, B. & Péroux, C. 2003, A&A 410, 33
Meneghetti, M., Bartelmann, M., Dolag, K. et al. 2005, NewAR 49, 111, also astro-ph/0405070
Meneghetti, M., Yoshida, N., Bartelmann, M. et al. 2001, MNRAS 325, 435
Metzler, C.A., White, M. & Loken, C. 2001, ApJ 547, 560
Miralda-Escudé, J. 1991, ApJ 380, 1
Miralles, J.-M., Erben, T., Hämmerle, H. et al. 2002, A&A 388, 68
Miralles, J.-M., Erben, T., Hämmerle, H. et al. 2005, A&A 432, 797, also astro-ph/0310716
Miyazaki, S., Hamana, T., Shimasaku, K. et al. 2002, ApJ 580, L97

Mould, J., Blandford, R., Villumsen, J., Brainerd, T., Smail, I., Small, T., & Kells, W. 1994, MNRAS 271, 31
Mulchaey, J.S., Dressler, A. & Oemler, A. 2004, eds, Clusters of Galaxies: Probes of Cosmological Structure and Galaxy Evolution, Carnegie Observatories Astrophysics Series, Vol. 3., (Cambridge University Press: Cambridge)
Munchi, D. & Jain, B. 2001, MNRAS 322, 107
Munshi, D., Valageas, P. & Barber, A.J. 2004, MNRAS 350, 77
Munshi, D. & Wang, Y. 2003, ApJ 583, 566
Narayan, R. & Nityananda, R. 1986, ARA&A 24, 127
Natarajan, P. & Kneib, J.-P. 1997, MNRAS 287, 833
Natarajan, P., Kneib J.-P., Smail, I. & Ellis, R.S. 1998, Ap 499, 600
Natarajan, P. & Refregier, A. 2000, ApJ 538, L113
Norberg, P., Baugh, C.M., Hawkins, E. et al. 2001, MNRAS 328, 64
Norman, D.J. & Impey, C.D. 2001, AJ 121, 2392
Oguri, M., Lee, J. & Suto, Y. 2003, ApJ 599, 7
Ota, N., Pointecouteau, E., Hattori, M. & Mitsuda, K. 2004, ApJ 601, 120
Peacock, J.A. & Dodds, S.J. 1996, MNRAS 280, L19
Pelló, R., Kneib, J.P.; Le Borgne, J.F. et al. 1999, A&A 346, 359
Pelló, R., Schaerer, D., Richard, J., Le Borgne, J.-F. & Kneib, J.-P. 2004, A&A 416, L35
Pen, U.-L., Lu, T., van Waerbeke, L. & Mellier, Y. 2003a, MNRAS 346, 994
Pen, U.-L., Zhang, T., van Waerbeke, L., Mellier, Y., Zhang, P. & Dubinski, J. 2003b, ApJ 592, 664
Pierpaoli, E., Scott, D. & White, M. 2001, MNRAS 325, 77
Premadi, P., Martel, H., Matzner, R. & Futamase, T. 2001, ApJS 135, 7
Press, W.H., Flannery, B.P., Teukolsky, S.A. & Vetterling, W.T. 1986, Numerical Recipes, (Cambridge: University Press)
Press, W.H., Teukolsky, S.A., Vetterling, W.T., Flannery, B.P. 1992, Numerical Recipes, (Cambridge: University Press)
Reblinsky, K. 2000, A&A 364, 377
Reblinsky, K. & Bartelmann, M. 1999, A&A 345, 1
Reblinsky, K., Kruse, G., Jain, B. & Schneider, P. 1999, A&A 351, 815
Refregier, A. 2003a, ARA&A 41, 645
Refregier, A. 2003b, MNRAS 338, 35
Refregier, A. & Bacon, D. 2003, MNRAS 338, 48
Refregier, A. Rhodes, J. & Groth, E.J. 2002, ApJ 572, L131
Refsdal, S. 1970, ApJ 159, 357
Rhodes, J., Refregier, A., Collins, N.R., Gardner, J.P., Groth, E.J. & Hill, R.S. 2004, ApJ 605, 29
Richards, E.A., Kellermann, K.I., Fomalont, E.B., Windhorst, R.A. & Partridge, R.B. 1998, AJ 116, 1039
Rix, H.-W., Barden, M., Beckwith, S.V.W. et al. 2004, ApJS 152, 163
Rögnvaldsson, Ö.E., Greve, T.R., Hjorth, J. et al. 2001, MNRAS 322, 131
Rodrigues-Williams, L.L. & Hogan, C.J. 1994, AJ 107, 451

Sand, D.J., Treu, T. & Ellis, R.S. 2002, ApJ 574, L129
Sand, D.J., Treu, T., Smith, G.P. & Ellis, R.S. 2004, ApJ 604, 88
Sarazin, C.L. 1986, RvMP 58, 1
Schirmer, M. 2004, PhD Dissertation, Univ. Bonn
Schneider, P. 1995, A&A 302, 639
Schneider, P. 1996, MNRAS 283, 83
Schneider, P. 1997, MNRAS 292, 673
Schneider, P. 1998, ApJ 498, 43
Schneider, P. 2003, A&A 408, 829
Schneider, P. & Bartelmann, M. 1997, MNRAS 286, 696
Schneider, P., Ehlers, J. & Falco, E.E. 1992, Gravitational Lenses (New York: Springer) (SEF)
Schneider, P., Kilbinger, M. & Lombardi, M. 2005, A&A 431, 9, also astro-ph/0308328
Schneider, P., King, L. & Erben, T. 2000, A&A 353, 41
Schneider, P. & Kneib, J.-P. 1998, in The Next Generation Space Telescope, Proceedings of the 34th Liège International Astrophysics Colloquium, ESA Sp-429, p. 89
Schneider, P. & Lombardi, M. 2003, A&A 397, 809
Schneider, P. & Rix, H.-W. 1997, ApJ 474, 25
Schneider, P. & Seitz, C. 1995, A&A 294, 411
Schneider, P., van Waerbeke L., Jain B., Kruse G., 1998a, MNRAS, 296, 873
Schneider, P., van Waerbeke, L. & Mellier, Y. 2002a, A&A 389, 729
Schneider, P., van Waerbeke, L., Mellier, Y., Jain, B., Seitz, S. & Fort, B. 1998b, A&A 333, 767
Schneider, P., van Waerbeke, L., Kilbinger, M. & Mellier, Y. 2002b, A&A 396, 1
Schneider, P. & Watts, P. 2005, A&A 432, 783
Schneider, P. & Weiss, A. 1988a, ApJ 327, 526
Schneider, P. & Weiss, A. 1988b, ApJ 330, 1
Schrabback, T. 2004, Diploma Thesis, Univ. Bonn
Schramm, T. & Kayser, R. 1995, A&A 299, 1
Schuecker, P., Böhringer, H., Collins, C.A. & Guzzo, L. 2003, A&A 398, 867
Scoccimarro, R. & Couchman, H. 2001, MNRAS 325, 1312
Seitz, C., Kneib, J.-P., Schneider, P. & Seitz, S. 1996, A&A 314, 707
Seitz, C. & Schneider, P. 1995a, A&A 297, 287
Seitz, C. & Schneider, P. 1997, A&A 318, 687
Seitz, S., Saglia, R., Bender, R., Hopp, U., Belloni, P. & Ziegler, B. 1998, MNRAS 298, 325
Seitz, S. & Schneider, P. 1995b, A&A 302, 9
Seitz, S. & Schneider, P. 1996, A&A 305, 383
Seitz, S. & Schneider, P. 2001, A&A 374, 740
Seitz, S., Schneider, P. & Bartelmann, M. 1998, A&A 337, 325
Seitz, S., Schneider, P. & Ehlers, J. 1994, Class. Quantum Grav. 11, 2345
Seljak, U. 1998, ApJ 506, 64

Seljak, U. 2002, MNRAS 337, 769
Seljak, U., Makarov, A., Mandelbaum, R. et al. 2004, PhRvD 71, 043511, also astro-ph/0406594
Sheldon, E.S., Johnston, D.E., Frieman, J.A. et al. 2004, AJ 127, 2544
Sheth, R.K., Mo, H.J. & Tormen, G. 2001, MNRAS 323, 1
Simon, P., King, L.J. & Schneider, P. 2004, A&A 417, 873
Smith, R.E., Peacock, J.A., Jenkins, A. et al. 2003, MNRAS 341, 1311
Sofue, Y. & Rubin, V. 2001, ARA&A 39, 137
Song, Y.-S. & Knox, L. 2004, PhRvD 70, 063510, also astro-ph/0312175
Soucail, G., Fort, B., Mellier, Y. & Picat, J.P. 1987, A&A 172, L14
Soucail, G., Kneib, J.-P. & Golse, G. 2004, A&A 417, L33
Soucail, G., Ota, N., Böhringer, H., Czoske, O., Hattori, M. & Mellier, Y. 2000, A&A 355, 433
Spergel, D.N. & Steinhardt, P.J. 2000, PRL 84, 3760
Spergel, D.N., Verde, L., Peiris, H.V. et al. 2003, ApJS 148, 175
Squires, G. & Kaiser, N. 1996, ApJ 473, 65
Takada, M. & Hamana, T. 2003, MNRAS 346, 949
Takada, M. & Jain, B. 2002, MNRAS 337, 875
Takada, M. & Jain, B. 2003a, MNRAS 340, 580
Takada, M. & Jain, B. 2003b, MNRAS 344, 857
Takada, M. & Jain, B. 2004, MNRAS 348, 897
Takada, M. & White, M. 2004, ApJ 601, L1
Taruya, A., Takada, M., Hamana, T., Kayo, I. & Futamase, T. 2002, ApJ 571, 638
Taylor, A.N. 2001, astro-ph/0111605
Taylor, A.N., Bacon, D.J., Gray, M.E. et al. 2004, MNRAS 353, 1176, also astro-ph/0402095
Taylor, A.N., Dye, S., Broadhurst, T.J., Benítez, N. & van Kampen, E. 1998, ApJ 501, 539
Tegmark, M. & Peebles, P.J.E. 1998, ApJ 500, L79
Tereno, I., Doré, O., van Waerbeke, L. & Mellier, Y. 2005, A&A 429, 383, also astro-ph/0404317
Torri, E., Meneghetti, M., Bartelmann, M., Moscardini, L., Rasia, E. & Tormen, G. 2004, MNRAS 349, 476
Trager, S.C., Faber, S.M., Dressler, A. & Oemler, A. 1997, ApJ 485, 92
Trentham, N. & Tully, R.B. 2002, MNRAS 335, 712
Tyson, J.A. 1988, AJ 96, 1
Tyson, J.A. & Fischer, P. 1995, ApJ 446, L55
Tyson, J.A., Valdes, F., Jarvis, J.F. & Mills Jr., A.P. 1984, ApJ 281, L59
Tyson, J.A., Valdes, F. & Wenk, R.A. 1990, ApJ 349, L1
Umetsu, K. & Futamase, T. 2000, ApJ 539, L5
Valdes, F., Jarvis, J.F. & Tyson, J.A. 1983, ApJ 271, 431
Vale, C. & White, M. 2003, ApJ 592, 699
van den Bosch, F.C., Abel, T., Croft, R.A.C., Hernquist, L. & White, S.D.M. 2002, ApJ 576, 21

van Kampen, E. 1998, MNRAS 301, 389
van Waerbeke, L. 1998, A&A 334, 1
van Waerbeke, L. 2000, MNRAS 313, 524
van Waerbeke, L., Bernardeau, F. & Mellier, Y. 1999, A&A 342, 15
van Waerbeke, L., Hamana, T., Scoccimarro, R., Colombi, S. & Bernardeau, F. 2001, MNRAS 322, 918
van Waerbeke, L. & Mellier, Y. 2003, astro-ph/0305089
van Waerbeke, L., Mellier, Y., Erben, T. et al. 2000, A&A 358, 30
van Waerbeke, L., Mellier, Y. & Hoekstra, H. 2005, A&A 429, 75, also astro-ph/0406468
van Waerbeke, L., Mellier, Y., Pello, R., et al. 2002, A&A 393, 369
van Waerbeke, L., Mellier, Y., Radovich, M. et al. 2001, A&A 374, 757
von der Linden, A. 2004, Diploma Thesis, Univ. Bonn
Wambsganss, J., Bode, P. & Ostriker, J.P. 2004, ApJ 606, L93
Wambsganss, J., Cen, R. & Ostriker, J.P. 1998, ApJ 494, 29
Weinberg, N.N. & Kamionkowski, M. 2002, MNRAS 337, 1269
Weinberg, N.N. & Kamionkowski, M. 2003, MNRAS 341, 251
White, M. & Hu, W. 2000, ApJ 537, 1
White, M., van Waerbeke, L. & Mackey, J. 2002, ApJ 575, 640
White, S.D.M., Navarro, J.F., Evrard, A.E. & Frenk, C.S. 1993, Nat 366, 429
Williams, R.E., Blacker, B., Dickinson, M. et al. 1996, AJ 112, 1335
Wilson, G., Kaiser, N. & Luppino, G. 2001, ApJ 556, 601
Wittman, D. 2002, in Gravitational Lensing: An Astrophysical Tool, F. Courbin & D. Minniti (eds.) (Springer-Verlag: Berlin), Lecture Notes in Physics, 608, 55
Wittman, D., Margoniner, V.E., Tyson, J.A., Cohen, J.G., Becker, A.C. & Dell'Antonio, I. 2003, ApJ 597, 218
Wittman, D.M., Tyson, J.A., Kirkman, D., Dell'Antonio, I. & Bernstein, G. 2000, Nat 405, 143
Wittman, D., Tyson, J.A., Margoniner, V.E., Cohen, J.G. & Dell'Antonio, I. 2001, ApJ 557, L89
Yang, X.H., Mo, H.J., Kauffmann, G. & Chu, Y.Q. 2003, MNRAS 339, 387
York, D.G., Adelman, J., Anderson, J.E. et al. 2000, AJ 120, 1579
Zaldarriaga, M. & Scoccimarro, R. 2003, ApJ 584, 559
Zaritsky, D. & Gonzalez, A.H. 2003, ApJ 584, 691
Zaritsky, D., Smith, R., Frenk, C. & White, S.D.M. 1997, ApJ 478, 39
Zaroubi, S., Squires, G., Hoffman, Y. & Silk, J. 1998, ApJ 500, L87
Zaroubi, S., Squires, G., de Gasperis, G., Evrard, A.E., Hoffman, Y. & Silk, J. 2001, ApJ 561, 600
Zehavi, I., Blanton, M.R., Frieman, J.A. et al. 2002, ApJ 571, 172
Zhang, L.L. & Pen, U.-L. 2005, New Astronomy 10, 569, also astro-ph/0305447
Zwicky, F. 1933, Helv. Phys. Acta 6, 110